MASTER

3 2 5
6-5-61

ORNL-3102
UC-80 – Reactor Technology

GAS-COOLED REACTOR PROJECT
QUARTERLY PROGRESS REPORT
FOR PERIOD ENDING MARCH 31, 1961

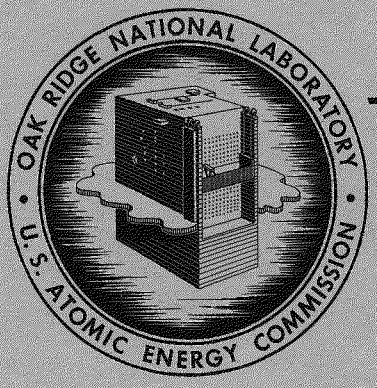

OAK RIDGE NATIONAL LABORATORY
operated by
UNION CARBIDE CORPORATION
for the
U.S. ATOMIC ENERGY COMMISSION

Printed in USA. Price $4.00. Available from the

Office of Technical Services
Department of Commerce
Washington 25, D.C.

DISCLAIMER

ORNL-3102

Reactor Technology
TID-4500 (16th ed.)

Contract No. W-7405-eng-26

GAS-COOLED REACTOR PROJECT

QUARTERLY PROGRESS REPORT

For Period Ending March 31, 1961

Staff
Oak Ridge National Laboratory

DATE ISSUED

MAY 26 1961

OAK RIDGE NATIONAL LABORATORY
Oak Ridge, Tennessee
operated by
UNION CARBIDE CORPORATION
for the
U. S. ATOMIC ENERGY COMMISSION

CONTENTS

PART 2. MATERIALS RESEARCH AND TESTING

SUMMARY

Part 1. Design Investigations

1. Reactor Physics

Criticality calculations have been made for the EGCR without experimental loops. The calculational methods applied to the finite reactor study were checked for accuracy by application to measurements of k_∞ for the EGCR lattice. The k_∞ measurements were made at Hanford with the Physical Constants Test Reactor. For a fuel enrichment of 1.8 wt % U^{235}, the calculated k_∞ was 1.1424 and the measured value was 1.146 ± 0.004; for an enrichment of 2.6 wt % U^{235}, the values were 1.2659 and 1.264 ± 0.008, respectively. For the finite reactor calculations, it was assumed that there were no experimental loops, that the lattice positions assigned to the small loops were filled with fuel, that the positions of the large loops were filled with graphite, and that the graphite sleeves on the fuel elements were uncoated. Calculations were made for three enrichments (2.1, 2.2, and 2.4 wt % U^{235}) and for room temperature and operating temperature.

The results of these calculations were then used to determine a base value for EGCR fuel enrichment. The value established after compensating for the reactivity effects of coating the sleeves and adding steel to support graphite plugs in the deferred loop positions was 2.46 wt % U^{235}. The condition of maximum reactivity will occur during room-temperature operation at the beginning of life of the first core. Calculations indicate an average exposure of the initial core of 7000 Mwd/MT.

The fast neutron flux distribution was computed for a central core column of the EGCR without experimental loops based on an equation developed to determine the degree to which the lattice fine structure is separable from the smooth variation caused by leakage. The information developed has been useful in calculations of graphite stresses from radiation-induced dimensional changes.

2. Reactor Design Studies

Estimates of the bowing that will result from temperature asymmetries in an EGCR fuel cluster were made. The permanent deflection was found to be less than 0.010 in., and it was established that at the time of interchanging the positions of the fuel assemblies the permanent deflection will be in the direction to reduce the thermal gradients. The effect of the bowing on the temperature differences was considered, and it was found that a 0.001-in. deflection will cause an increase of about 1°F in the temperature difference. Thus the effect will be small.

A parametric study was made of the performance under EGCR conditions of beryllium-clad fuel elements in a 19-element assembly as a function of element spacing and fin height. The power and surface temperatures are strong functions of the element spacing, and the sensitivity increases as the fin height increases.

Heat transfer correlations were determined for EGCR fuel elements in order to obtain data needed in the design of alternate fuel assemblies. It was found that the rate of decay of the Nusselt number increased with increases in the uninterrupted length-to-diameter ratio as the Reynolds number decreased.

Additional calculations were made of the effect of off-design operating conditions and assumed control rod properties on the thermal performance of EGCR control rods. An adequate safety factor was found to be available even for extreme transient conditions.

A determination was made of the EGCR moderator temperature distribution and the coolant flow required to keep the maximum moderator temperature below 1100°F. It was found that a total moderator coolant flow of 32 000 lb/hr, which would remove 5400 kw of energy, would be about 5000 lb/hr in excess of that which would give an average gas exit temperature of 1050°F from the annuli.

The second phase of the experimental investigation of the EGCR pressure vessel stresses was completed. The configurations throughout the cluster region and the vessel itself were found to be structurally adequate. The primary and the primary-plus-secondary stress intensities for the burst-slug detection and gas outlet nozzles were found to be

within the allowable limits. Complete design evaluations of these units cannot be made until the temperature distributions are known.

Experimental and calculational studies of the structural integrity of the EGCR experimental through-tubes were continued. The second and third of a series of four 8-in.-o.d., 9-ft-long tubes and the third and fourth in a series of 4-in.-o.d. tubes were collapsed. The data for both instantaneous and time-dependent collapse are being correlated with various proposed theories.

Bimetallic hemispherical shell collapse tests were performed as a means for evaluating the structural stability of the thermal barrier for the EGCR pressure vessel. The tests showed that thermal strains induced across the walls of the hemispherical shells neither increased nor decreased their resistance to instantaneous collapse under external pressure.

A study was made of the irradiation-induced stresses in an EGCR graphite column. For the particular column and conditions studied it was found that cracking might occur after 8.1 years and that the crack-free period might be increased by subdividing the column. Temperature distributions in the graphite columns are being calculated in order to evaluate the thermal stresses that will exist during refueling operations.

Additional data were obtained on the oxidation of hydrogen in a flowing stream of helium at 300 psia by fixed beds of 1/8-in.-diam CuO pellets. The data being obtained will be used to determine the reaction-controlling mechanism and to develop design equations.

Preliminary studies have indicated that the EGCR containment system may be operated in the event of the maximum credible accident by sealing the building rapidly or by venting the building for several minutes before sealing. Operation by venting before sealing would place the containment system in a less hazardous condition and would permit evacuation of plant personnel before the activity was contained and spread throughout the building.

Theoretical and experimental investigations of the possibility of a runaway graphite fire in the EGCR are under way. It has been established that, with the present design, natural convection alone would be insufficient to remove the decay heat after a loss-of-pressure accident and

that therefore a graphite fire is a possibility. Means for providing an independent heat sink to assure adequate removal of decay heat are being studied.

3. Experimental Investigations of Heat Transfer and Fluid Flow

The investigation of the source of the flow asymmetries which caused skewed temperature patterns in the seven-tube cluster simulating the EGCR fuel assembly was continued. A series of experiments with the channel inlet screens removed led to no clear decision as to whether the flow maldistribution originated in (1) the plenum or transition piece or (2) a misalignment of either the central or peripheral tubes. A comparison with previous experiments showed that the flow was sensitive to plenum conditions. On the other hand, velocity-distribution measurements indicated that small displacements of the central tube had noticeable effects. These studies have been discontinued in favor of an investigation of the effect of cluster orientation on the temperature distributions in a heated-tube apparatus.

Data were obtained on surface-temperature profiles and heat-transfer coefficient variations for the situation in which only a single peripheral tube of a seven-tube cluster was heated (corresponding to experiments with a single naphthalene-coated rod). The circumferential temperature profiles showed a more than 100% increase in the diametral temperature difference in the upstream region of the cluster and a reversal of the pattern in the downstream section with respect to previous profiles with all tubes heated. These features are ascribed to the lower sink temperature in the inner region resulting from the absence of heating from the central tube. The discrepancy in the heat-transfer coefficient as compared with previous results has been resolved on the assumption that the heating is confined only to the region surrounding the heated tube.

The evaluation of gas properties at film temperatures rather than mixed-mean temperatures and the inclusion of an L/d_e correction have eliminated the previously noted 23% deviation between heat-transfer and mass-transfer results. Thus, it is felt, to within the limits of the experimental techniques used, that the application of mass-transfer measurements

to the prediction of heat transfer in seven-tube clusters is valid. It was found that slight, permanent deformations of the naphthalene-coated tubes had an appreciable effect on the mass-removal profiles. Correction of the data to include this factor resulted in excellent agreement with previous results for straight tubes.

The accumulation of data for delineating the velocity field in the downstream element of two seven-tube clusters as a function of relative cluster rotation was continued. The influence of the spiders was most noticeable just downstream of the cluster inlet. Contour mapping of a 120-deg segment of the flow passage showed quite similar patterns for the 0- and 90-deg (tubes inline) and the 30- and 60-deg (tubes staggered) rotations. The observed differences were related to the shifted location of the central web.

A study of the contribution of the mid-cluster spacers to the pressure loss in the EGCR fuel assemblies was initiated using a flow channel containing both inlet and outlet dummies and three EGCR Title II assemblies with graphite sleeves. Preliminary data for bare-tube regions (sections devoid of spacers or spiders) were in good agreement with earlier results for seven-tube clusters; the friction-factor curve showed a reduced dependency on the Reynolds modulus for data obtained for short sections.

Analyses of data on gas-mixing (using a helium-tracer technique) in the vicinity of the mid-cluster spacer indicated, through the progressive narrowing of the concentration profiles and the displacement of the concentration peaks with respect to the injection point, that there existed a radially outward component to the flow in this region. The influence of the spiders on gas-mixing was more pronounced than for the mid-cluster spacer; essentially complete mixing occurred in a full-cluster length.

4. Materials Development

Sintering conditions were established for the production of UO_2 shapes of controlled grain size, and specimens were produced having average grain sizes of 20 and 60 μ and densities approximately 97% of theoretical. The conditions required for preparing high-density material with a controlled oxygen-to-uranium ratio of about 2.10 are being investigated. The

preparation and inspection of disks of UO_2 for use in thermal-conductivity tests were completed. Additional testing was performed with specimens of INOR-8 alloy to improve the thermal-conductivity apparatus.

The method of measuring the bulk density of small irregular particles of UO_2 by embedment in plastic was further developed by the addition of a technique involving deep etching of a polished section of the embedment. The extent of infiltration of the pore structure of the UO_2 particles by the plastic material can thus be determined. The bulk density of particles of sintered UO_2 (density, 96% of theoretical) was measured with a precision of ± 0.01 g/cm^3 by this method.

The release of fission-product gases from bulk UO_2 at temperatures of 400 to 1000°C was investigated. Results obtained at 1000°C agreed with the value found by extrapolation of data taken at higher temperatures. The rate of release at 600°C was below the limits of detection. At 400°C, however, release was higher than at 1000°C and proportional to time. A surface reaction, such as slight oxidation at the low pressures, is presumed to have caused this surprising result.

The binders proposed for use in fabricating fueled BeO were evaluated on the basis of gas evolution and residue after heating. The polyvinyl alcohol selected as most suitable was found to inhibit the sintering of BeO bodies to some extent. By shielding specimens from the furnace lining and by heating slowly on a programed sintering cycle, fueled bodies of BeO containing 30 vol % UO_2 as 100- to 150-μ particles were fabricated to a density of 93% of theoretical. The high release rate of fission-product gases previously observed for fueled BeO at high temperatures is believed to have been due to significant changes in the microstructure. Specimens of BeO containing 30 vol % UO_2 heated for various times at 1600 and 1800°C showed extensive agglomeration of the BeO and redistribution of the UO_2 phase. Sublimation of UO_2 at 1800°C was also observed.

A specimen of fueled BeO calculated to contain 13 vol % UO_2 and 13 vol % ThO_2 was examined by the combined techniques of petrography, metallography, and x-ray diffraction. Pure BeO, a ThO_2-UO_2 solid solution containing an estimated 57% ThO_2, and a small amount of pure UO_2 (<5%) were identified.

The evaluation of coated fuel particles by thermal cycling and leaching tests was initiated. Samples of "UC_2" spheres coated with pyrolytic carbon were received from two vendors. Particles coated by High Temperature Materials, Inc., were found to have lower initial surface contamination and lower loss of material by leaching after thermal cycling to 1800°C. These particles were selected for the initial irradiation test.

The compatibility of UC with beryllium is being determined at various temperatures. Preliminary results of a 66-hr test at 1100°C indicated formation of a reaction layer 0.006 in. thick.

Coatings applied to full-size graphite support sleeves were inspected and tested for permeability, adherence, and oxidation resistance. Permeability measurements indicate that all the coatings (SiC, siliconized SiC, and pyrolytic carbon) reduce the permeability of sleeves to helium. Adherence tests conducted with high-velocity air showed that some material could be removed from all SiC-base coatings, while the pyrolytic carbon coatings seemed to be completely adherent. Oxidation tests performed on sections of sleeves showed that, with the exception of coated sleeves of grade 901-S graphite, the coatings provided only slight protection at 600°C. The effectiveness of the coatings increased with increasing temperatures until, at 900°C, on one sample the fractional weight loss was only about 6% of that of an uncoated specimen. An eddy-current procedure for measuring the thickness of SiC-base coatings was developed. Measurements performed on the various coated sleeves have not yet been verified on polished sections. A technique was developed for determining the integrity of SiC coatings by use of a galvanic cell. Correlation of the area of exposed graphite with the emf generated in the cell was demonstrated on specimens of grade 901-S graphite coated with siliconized SiC.

The mechanical properties of EGCR moderator graphite are being determined by tensile and transverse bending creep tests. Tensile creep tests at room temperature and at 750 and 1100°F show a very slight initial creep rate, which quickly saturates. A slight amount of creep also occurs in bend tests, causing the compressive and tensile strains to become equal. The strength in bend tests is higher, but the strains at fracture are similar to those in tensile tests. Results from all testing to date

The sample of UO_2 clad in low-permeability graphite with an outer coating of pyrolytic carbon that was used in an instantaneous fission-gas-release experiment was removed from the ORR and examined. The coating had blistered and flaked away in several places, and a pin hole was found in the graphite cladding. A thin-plate UO_2 sample shielded with ThO_2 is now being used for the instantaneous fission-gas-release experiments. The fission-gas release from this ThO_2-shielded sample is essentially the same as from the unshielded sample. This demonstrates that back diffusion from the metal capsule is not a significant contribution to the fission-gas release. The fission-gas release from the UO_2 is highly temperature dependent down to 700°C. A method for measuring the formation of Xe^{138} was developed and some data were obtained at 1100°C. The perturbed thermal-neutron flux within the capsule was determined by using argon as the sweep gas and then measuring the activation of the argon. The measurements demonstrated the variation of flux that may be expected at an experiment location and therefore the need for continuous monitoring. Electrical conductivity measurements were made on the UO_2 thin plates by using the spring-loaded thermocouples as electrical contacts. In-pile measurements of resistivity made up to a dose of about 10^{18} neutrons/cm^2 fall very close to the values obtained for the unirradiated material. Measurements made during irradiation to doses greater than 10^{18} neutrons/cm^2 fall on an almost parallel line of lower resistivity.

The third high-temperature beryllium swelling experiment was completed using tubular specimens instead of coupons. The results indicate that swelling becomes significant above 700°C at exposures of 3.6×10^{20} neutrons/cm^2 (>1 Mev). Annealing studies were performed on specimens previously irradiated at low temperatures. Bend tests on these specimens show that ductility is recovered rapidly by annealing at temperatures above 700°C.

In-pile tube-burst tests of beryllium were conducted in two different positions in the ORR at 600°C. Comparison of results for tubing from hot-pressed block with previous out-of-pile results showed that the stress to

produce rupture in times of 5 to 100 hr was reduced by about 2000 psi at an exposure of approximately 3×10^{20} neutrons/cm^2 (>1 Mev).

6. Out-of-Pile Testing of Materials and Components

An isothermal test of AGOT graphite and metal specimens in static helium at 1700°F was conducted. Comparison of the results with those of similar tests at 1100 and 1400°F indicated consistent weight gains for austenitic stainless steel specimens and decreases in the weight gains of ferritic materials. Decarburization was apparent at the surfaces of low-alloy steel specimens tested at 1400 and 1700°F. The test at 1700°F gave further evidence that CO-CO_2 concentrations in helium in a closed stainless steel system containing graphite can become decarburizing as a result of gas-metal reactions.

Two 900-hr thermal-convection loop tests at 1100°F were completed in which the CO-CO_2 concentrations were controlled. In test TCL 14, in which the CO-CO_2 concentration was approximately 100 ppm, the metal specimens showed weight gains similar to those of specimens tested in helium containing 450 to 1800 ppm CO + CO_2. In test TCL 15, in which the impurities simulated the EGCR specification (10 000 ppm CO_2 and 2500 ppm CO), low- and medium-alloy steels showed much higher weight gains, but steels containing 7% or more chromium had only slightly higher weight gains than in tests with lower concentrations of CO-CO_2.

A test has been initiated in the forced-circulation loop to investigate the effect on graphite and structural materials of controlled additions of H_2O to high-temperature helium. In another series of experiments a systematic study has been initiated of the effects of temperature, contact pressure, atmosphere, and surface treatments on the rate of carburization of type 304L stainless steel in contact with graphite. Preparations are also being made for materials compatibility studies of high-pressure hydrogen systems.

Experimental studies were made of the degassing behavior of two specimens of graphite prepared from needle coke by the National Carbon Company for use in the EGCR at Oak Ridge and the NPR at Hanford. Evidence was obtained that specimens cut from near the surface of the 16-in. by 16-in.

by 20-ft EGCR extrusions contained less gas than specimens from the central region. The specimens released, during heating from 30 to 1000°C, about two-thirds of the total amount of gas released during heating from room temperature to 1800°C.

Techniques are being studied for determining the permeability coefficients of graphite samples that exhibit low values of porosity and forced-flow rates. It appears that it will be necessary to determine both the diffusion coefficient and the permeability coefficient to characterize flow behavior within the graphite. The porosity of type CEY graphite pipe was determined by two methods.

A thermionic ionization gage is being developed as a sensitive detector for use in analyzing helium. In addition to providing improved sensitivity, a successful thermionic ionization detector would permit the simplification of other chromatograph components.

Investigations of the removal of radioactive fission-product gases from helium and other carrier gases have been continued. Several types of activated charcoal have been studied for the removal of iodine vapor from helium at high temperatures. A charcoal impregnated with salts of silver, copper, and chromium (Whetlerite ASC) has demonstrated the ability to adsorb and retain iodine vapor with an efficiency exceeding 99.99%. Studies of the removal of krypton and xenon have included additional dynamic adsorption measurements, additional calculations of apparent diffusion coefficients for krypton in charcoal, statistical analysis of equilibrium krypton and xenon adsorption data, possible retention of fission-product gases by Linde molecular sieves type 4A, and measurement of apparent thermal conductivities for five types of charcoal with various gases in the voids.

Work has continued on the study of abnormal emf drifts of Chromel-P vs Alumel thermocouples in helium atmospheres. Additional tests with other chromium-nickel alloys have shown that the special Chromel-P alloy undergoes selective oxidation such as that of Chromel-P under the experimental conditions used. Alloys of the 80% nickel–20% chromium type (Geminol-P, Chromel-A, and Chromel-AA) do not show the abnormal negative emf drifts.

Additional tests of emf drifts of sheathed Chromel-P vs Alumel thermocouples in a graphite-helium atmosphere have shown that the products from outgassing graphite are important in explaining the negative drifts. Couples sheathed in type 304 stainless steel appear to be more susceptible to the drift than those sheathed in type 310 stainless steel. In addition there seemed to be differences in drift rates between materials obtained from different vendors. Metallographic studies show that the drift was due to selective oxidation of chromium in the thermal-gradient region of the Chromel-P leg.

A high-temperature furnace with a helical graphite resistance heater has been constructed and partially tested. Temperatures in excess of 2500°C have been reached for short periods, and 2000°C has been maintained for over 200 hr with no furnace damage.

7. Development of Test Loops and Components

Title II drawings for the bottom-nozzle tee sections of the four EGCR experimental through-tubes that are to be installed were completed. Title I designs of the four top-nozzle tee sections were completed and 90% of the Title II detail drawings have been made. Studies of the nozzle loadings have shown the bending moments to be below the allowable limits. Work continued on component designs and the preparation of the preliminary hazards summary report.

Electrical breakdown tests of a microswitch for use in the EGCR were completed. The test results indicate that the switch can be expected to operate satisfactorily in helium at a pressure of 125 to 300 psig at temperatures from 70 to 530°F.

Tests of 1/4- and 6-in. globe valves for use in the EGCR experimental loops are being conducted, and facilities are being constructed for testing the through-tube bearing surface and the orifice-type flow restrictors required to maintain the desired temperatures in the through-tubes. Service tests of mechanical joints were continued, and assembly and disassembly of a "Conoseal" joint by remote operation were demonstrated.

Design and construction work on GCR-ORR loop No. 2 continued. The shakedown of the loop, without the test section, is now scheduled for

the period August through October 1961. The shakedown of the test section is scheduled for November and December 1961. Tests were conducted on a multiple-cylinder experimental slip joint and on filters for the coolant stream. The out-of-pile test loop is being modified for additional component tests.

The two regenerative compressors installed in GCR-ORR loop No. 1 have logged a total of 3100 hr of satisfactory operation. A centrifugal compressor was examined after 5500 hr, and the condition of the bearings indicated that it could have operated for a much longer period. Apparently grease-lubricated bearings can be operated for periods considerably in excess of the specified 2000 hr without relubrication.

Bristol Siddeley has continued to have difficulties with instabilities in gas-lubricating bearings applied to compressors operating at speeds in excess of 11 000 rpm. Installation of a test loop for gas-bearing compressors was completed.

Part 1. Design Investigations

1. REACTOR PHYSICS

A. M. Perry

Criticality Calculations for the EGCR Without Loops

C. A. Preskitt, E. A. Nephew

The Physical Constants Test Reactor (PCTR) at Hanford has been used to measure[1] k_∞ for the EGCR lattice at fuel enrichments of 1.8 and 2.6 wt % U^{235}. The fuel element and lattice geometry for these experiments differed from the final EGCR design in certain minor details in the end-cap region and, in addition, the experimental assemblies had an over-all length of 21 7/8 in. as compared with 29 in. in the reactor. The results of these measurements have been used to check the accuracy of calculational methods which have then been applied to the finite reactor.

Any formulation of the problem of calculating k_∞ for a reactor is intimately tied to the particular neutron flux model adopted, since, in any case, the multiplication factor is deduced from a detailed accounting of neutron fates. Neutron thermalization calculations have been made for infinite homogeneous media using the free-gas approximation for graphite scattering to determine the neutron energy spectrum below 2 ev for amounts of 1/v absorption in the range from 0.05 barn per carbon atom to 0.5 barn per carbon atom.[2] In each calculation the effective neutron temperature is determined by obtaining a least-squares fit of a Maxwellian function to the total flux in the range below ~1.5 kT_N. When this Maxwellian is subtracted from the total flux, the residue is found to be very nearly independent of the moderator temperature or the magnitude of the absorption cross section. An example of this decomposition of the spectrum is shown in Fig. 1.1. The residue, which represents the epithermal spectrum, is similar to that proposed by Campbell and Freemantle,[3] but with modified parameters, and in all calculations presented here this residue has been

---

[1] Nuclear Physics Research Quar. Rep. Oct., Nov., Dec. 1959, HW-63576.

[2] E. A. Nephew and J. S. Howland, unpublished work.

[3] C. G. Campbell and R. G. Freemantle, Effective Cross Section Data for Thermal Reactor Calculations, AERE RP/P 2031 and Supplement 1 (Aug. 1956 and July 1957).

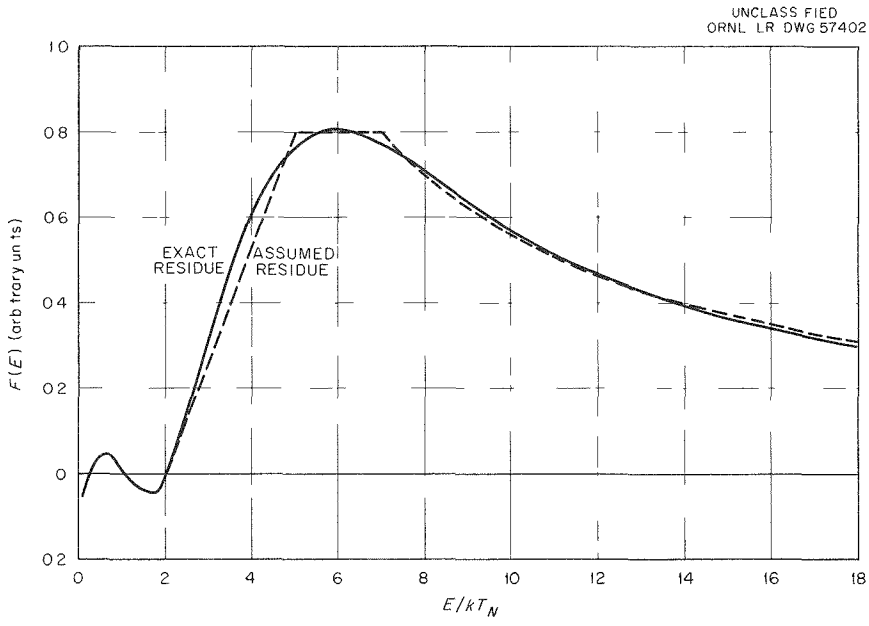

Fig. 1.1. Comparison of Exact and Assumed Residue for a Moderator Temperature of 600°K and an Absorption Cross Section of 0.15 Barn per Carbon Atom.

assumed to be zero below $2kT_N$, to rise linearly between $2kT_N$ and $5kT_N$, to contain a flat portion from $5kT_N$ to $7kT_N$, and to be 1/E in shape above $7kT_N$.

The neutron temperature deduced from any calculation of the total neutron flux spectrum will depend on the upper limit of the energy range over which the Maxwellian fit is obtained if this range extends into the region where the flux shows significant deviations from a Maxwellian form. This was avoided in the calculations described here, and the resulting correlation between neutron temperature and moderator temperature for graphite was found to be

$$\frac{T_N}{T_M} = 1 + 1.40\ \sigma_a \left(\frac{T_o}{T_M} \right)^{1/2} ,$$

where σ_a is in units of barns per carbon atom and σ_s for graphite is taken as 4.8 barns. The corresponding correlation, as deduced by Coveyou et al.,[4]

[4]R. R. Coveyou, R. R. Bate, and R. K. Osborn, J. Nuclear Energy, 2: 153 (1956).

is

$$\frac{T_N}{T_M} = 1 + 2.67\ \sigma_a \left(\frac{T_o}{T_M}\right)^{1/2} \quad .$$

Since this expression was obtained by fitting the spectrum to a Maxwellian up to a quite high energy ($4.8\ kT_M$), the epithermal spectrum which must be used to reproduce the total flux spectrum is quite different from that described here.

In terms of the spectral model described above, all reaction rates are calculated separately for the thermal (Maxwellian) and epithermal components. The thermal reaction rate is obtained in terms of an average cross section $\bar{\sigma}$ such that

$$\bar{\sigma} \int \phi_T(E)\ dE = \int \sigma(E)\ \phi_T(E)\ dE \quad ,$$

where $\phi_T(E)$ is Maxwellian. For the epithermal reaction rate, a total resonance integral is defined as

$$I = \int \sigma(E)\ \phi_e(E)\ dE \quad ,$$

where $\phi_e(E)$ is the epithermal flux described above. A resonance escape probability is then calculated from this resonance integral in the usual way. It should be noted that the resonance integrals defined in this way must include the $1/v$ part of the cross section, as well as the specific resonance structure.

Based on these definitions of reaction rates, the infinite multiplication factor is defined as

$$k_\infty = \eta_T \epsilon p f + \eta_e^{25} \epsilon p' (1 - p_{25}) \quad ,$$

where

$\eta_T = \dfrac{\nu\bar{\Sigma}_f}{\bar{\Sigma}_a}$ for thermal (Maxwellian) neutrons in fuel,

ϵ = total number of fast neutrons produced per neutron produced by fission of U^{235},

$p = p_{28}p_{25}p_{ss}p_{gr}$, resonance escape probability in slowing down to thermal energy (including 1/v) for U^{238}, U^{235}, stainless steel, and graphite,

f = thermal utilization, ratio of total thermal (Maxwellian) fuel absorptions to total thermal absorptions,

$\eta_e^{25} = \nu I_f / I_a$ for U^{235},

$p' = p'_{28}p'_{ss}p'_{gr}$, resonance escape probability (including 1/v) for slowing down to 6 ev for U^{238}, stainless steel, and graphite.

The value 6 ev which enters into the calculation of p' was selected on the basis that it lies just below the lowest resonance of U^{238}, although the calculation is not greatly sensitive to the exact energy used. The only significant assumption incorporated in the above expression for k_∞ is that all U^{235} absorptions occur below 6 ev; that is, the product $\epsilon p'$ gives the number of neutrons which arrive below the last U^{238} resonance, and $\epsilon p'(1 - p_{25})$ is then the number of nonthermal U^{235} absorptions. If this is multiplied by η_e^{25}, the number of neutrons produced by all nonthermal U^{235} fissions is obtained. For epithermal neutrons, it is assumed that there is no flux fine structure in the lattice cell. For thermal neutrons the P-3 approximation is used to determine the radial fine structure, and two-dimensional diffusion theory is used to determine the axial fine structure. The results given in Table 1.1 were obtained by applying the above formulation to the analysis of the PCTR experiments.

After having verified the accuracy of the method established for calculating k_∞, the analysis was extended to the finite reactor. The values of k_{eff} were calculated using one-dimensional two-group calculations in cylindrical geometry. The axial leakage was computed by specifying an axial buckling which included the reflector savings of the end reflectors. The radial leakage was computed explicitly through specification of the diffusion coefficient in each group.

Table 1.1. Summary of Calculated Results from Analysis of PCTR Measurements and Comparison of Calculated and Measured Values of k_∞

	For an Enrichment of 1.8 wt %	For an Enrichment of 2.6 wt %
η_T	1.6988	1.8004
ϵ	1.017	1.017
p_{28}	0.8162	0.8169
p_{25}	0.8629	0.8076
p_{ss}	0.9584	0.9584
p_{gr}	0.9951	0.9951
p	0.6717	0.6292
f	0.8032	0.8425
p'_{28}	0.8378	0.8384
p'_{ss}	0.9840	0.9840
p'_{gr}	0.9999	0.9999
p'	0.8243	0.8249
η_e^{25}	1.830	1.830
k_∞ (calculated)	1.1424	1.2659
k_∞ (measured)	1.146 ± 0.004	1.264 ± 0.008

For both groups the diffusion coefficient is defined as

$$\overline{D} = \frac{\int D(E)\ \phi(E)\ dE}{\int \phi(E)\ dE} ,$$

and the method of Behrens[5] is used to determine the streaming corrections to account for voids. The other cross sections which are required are determined by the analogy between the two-group equations and the equation for k_∞ given above. For an infinite homogeneous medium, the two-group equations are

[5]D. J. Behrens, The Migration Length of Neutrons in a Reactor, AERE T/R 877 (1956).

$$\Sigma_1\phi_1 + \Sigma_R\phi_1 = 1 \quad ,$$

$$\Sigma_2\phi_2 = \Sigma_R\phi_1 \quad ,$$

$$k_\infty = \nu\Sigma_1^f\phi_1 + \nu\Sigma_2^f\phi_2 \quad ,$$

where Σ_1 and Σ_2 are the fast and thermal absorption cross sections, Σ_R is the fast group removal cross section, and Σ_1^f and Σ_2^f are the fast and thermal group fission cross sections. If Σ_1^f and Σ_2^f are obtained by volume and flux averaging within the lattice cell and the conditions that

$$\frac{\nu\Sigma_2^f}{\Sigma_2} = \eta_T\epsilon f = \eta_2$$

and

$$\Sigma_R\phi_1 = p$$

are used, it is straightforward to show from the above two-group equations that

$$\Sigma_R = \frac{\dfrac{\nu\Sigma_1^f}{k_\infty}}{\dfrac{1-p}{p} - \dfrac{\eta_2 - k_\infty}{k_\infty}}$$

and

$$\Sigma_1 = \frac{1-p}{p}\,\Sigma_R \quad .$$

This method has been applied to the analysis of the EGCR for the condition in which no loops are present and the lattice positions assigned to the small loops are filled with fuel. The positions of the large loops were assumed to be filled with graphite and no coating was assumed to be

on the fuel element sleeves. The results of these calculations are given in Table 1.2 for three enrichments.

Table 1.2. Summary of EGCR Criticality Calculations

	At Operating Temperature and Indicated Enrichment			At Room Temperature and Indicated Enrichment		
	2.1 wt %	2.2 wt %	2.4 wt %	2.1 wt %	2.2 wt %	2.4 wt %
η_T	1.717	1.730	1.754	1.745	1.758	1.781
ϵ	1.017	1.017	1.017	1.017	1.017	1.017
p_{28}	0.792	0.792	0.792	0.801	0.801	0.801
p_{25}	0.880	0.875	0.864	0.828	0.821	0.806
p_{ss}	0.969	0.969	0.969	0.958	0.958	0.958
p_{gr}	0.997	0.997	0.997	0.995	0.995	0.995
p	0.673	0.669	0.662	0.632	0.627	0.616
f (clean)	0.833	0.838	0.846	0.831	0.836	0.844
f (Xe poisoned)	0.814	0.818	0.826	0.820	0.824	0.832
p'_{28}	0.805	0.805	0.805	0.824	0.824	0.824
p'_{ss}	0.984	0.984	0.984	0.984	0.984	0.984
p'_{gr}	0.999	0.999	0.999	0.999	0.999	0.999
p'	0.791	0.791	0.792	0.810	0.810	0.811
η_e^{25}	1.737	1.737	1.737	1.828	1.828	1.828
k_∞ (clean)	1.147	1.162	1.189	1.191	1.206	1.234
k_∞ (Xe poisoned)	1.124	1.139	1.165	1.178	1.193	1.220
k_{eff} (clean)	1.082	1.097	1.124	1.129	1.144	1.172
k_{eff} (Xe poisoned)	1.061	1.075	1.102			

Specification of EGCR Fuel Enrichment

C. A. Preskitt

The reactivity considerations for the initial core loading which determine the fuel enrichment are based on the requirements that satisfactory fuel cycle economics should be obtained with the first core and that an adequate shutdown margin must exist for the highest reactivity

condition of the core. This condition of maximum reactivity occurs during room-temperature operation at the beginning of life of the first core.

The calculations described in the preceding section have been used to determine a base value for the enrichment, and the actual enrichment has been specified relative to this base value by estimating the effects of probable differences in core makeup from this base configuration.

These differences are small and consist of a 2.5 wt % silicon carbide coating on the fuel element sleeves and some additional stainless steel components required for the support of graphite plugs at the positions of the deferred loop facilities.

For the base condition an enrichment of 2.40% has been chosen, and the actual enrichment which must be specified to compensate for the reactivity effects of the coatings and additional steel has been determined to be 2.46%. The initial core will then have the reactivity characteristics shown in Table 1.3.

Table 1.3. Reactivity Characteristics of the EGCR Without Loops for the Specified Fuel Enrichment of 2.46%

Core Condition	k_{eff}
Hot, equilibrium Xe and Sm	1.095
Hot, clean	1.124
Cold, clean	1.172
Cold, clean, 21 control rods	0.911

The reactivity lifetime of the initial core will depend on the fuel management program which is followed, but present calculations indicate that an average exposure of 7000 Mwd/MT should result.

Separability of Neutron Flux in a Heterogeneous System

C. A. Preskitt

In a heterogeneous reactor it is often necessary to obtain considerable detail in determining the neutron fine structure distributions in the core. For an infinite reactor there is no variation of the average flux from one lattice cell to the next, and this fine structure may be

obtained through calculations on a single lattice cell. For a finite reactor, the leakage of neutrons produces an over-all gradient which is superimposed on the infinite lattice fine structure. Although it is possible, through the use of two-dimensional cell calculations, to obtain values of the neutron flux on a closely spaced grid of points over a single lattice cell, the memory capacity of present digital computers usually requires the use of a coarse mesh when calculating an entire heterogeneous reactor. One such calculation has been done,[6] however, and this has been used to determine the degree to which the lattice fine structure is separable from the smooth variation caused by leakage.

For the cylindrical reactor, an attempt was made to fit the calculated flux for the heterogeneous core with a function of the form

[6]GCR Quar. Prog. Rep. Sept. 30, 1959, ORNL-2835, p. 3.

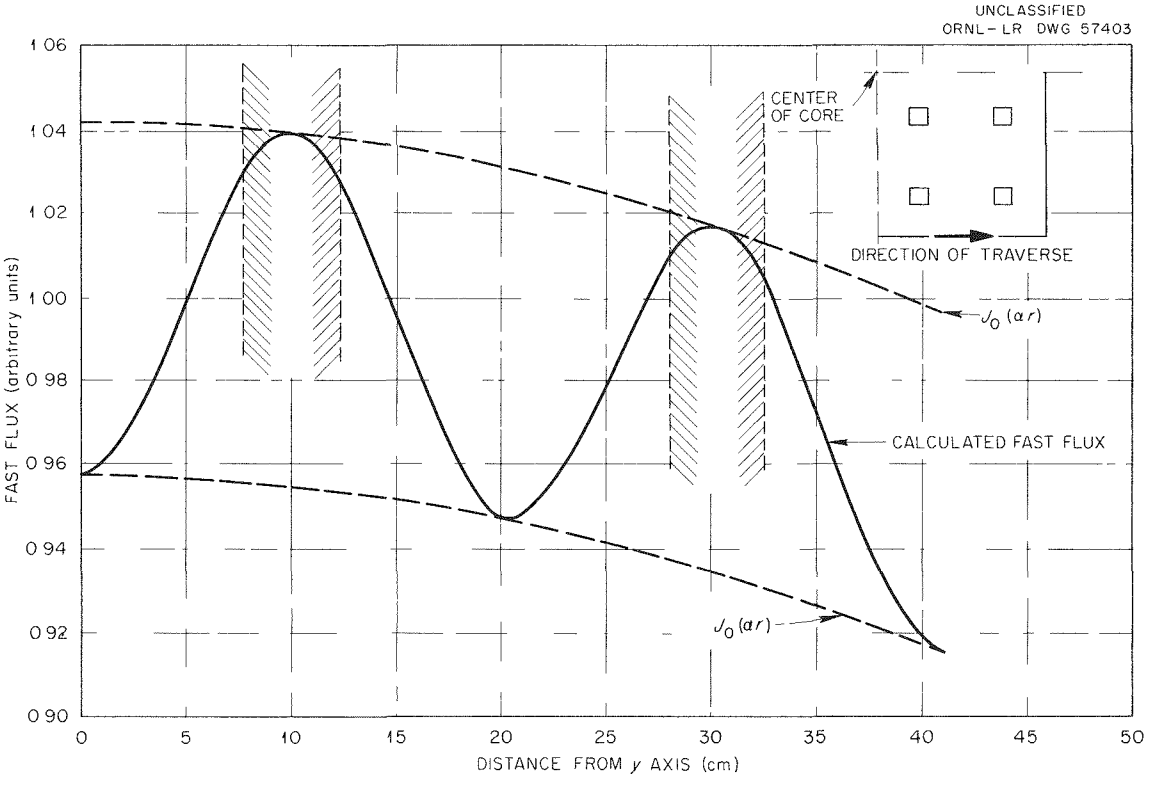

Fig. 1.2. Comparison of Calculated Fast Flux Distribution in a Heterogeneous Reactor with the Bessel Function Variation Produced by Neutron Leakage.

$$\Phi(x,y) = J_o(\alpha r)\ \phi(x,y) \quad ,$$

where

$$\alpha = \frac{2.405}{R_{eff}}$$

and $\phi(x,y)$ is the fine structure distribution in a lattice cell of the infinite reactor. An excellent fit was obtained for a value of R_{eff} equal to the actual reactor radius plus the radial reflector savings. A comparison between the calculated heterogeneous fast flux and the Bessel function variation resulting from neutron leakage is shown in Fig. 1.2.

The equation given above for $\Phi(x,y)$ has been used to compute the fast neutron flux distribution on a closely spaced grid of points for a central core column of the EGCR without loops. This information has been useful in calculations of graphite stresses from radiation-induced dimensional changes.

2. REACTOR DESIGN STUDIES

Thermal Analyses of Core Components

G. Samuels

EGCR Fuel Elements (G. Samuels, M. E. Lackey, R. S. Holcomb)

The thermal stability of the elements of the cluster has been of primary concern in the design of the EGCR fuel assemblies. Sufficient experimental data are now available for reasonably good estimates to be made for the temperature asymmetries within the cluster and the resulting bowing of the elements.

In calculating the local temperatures within the cluster, the geometry of the system was segmented as shown in Fig. 2.1. The effects considered were (1) the radial and axial heat generation gradients, (2) thermal radiation within the cluster, (3) the variable heat transfer coefficient around the element and along the channel, (4) gas temperature differences between the various flow passages, (5) eddy diffusivity mixing between flow regions 3 and 4, and (6) circumferential heat conduction around the graphite sleeve. The eddy diffusivity mixing from regions 1 and 2 to regions 3 and 4 was neglected, and conduction through the elements was not considered; that is, the flow of heat in the UO_2 pellets was assumed to be radial only. Regions 1 and 2 were assumed to have the same gas temperature.

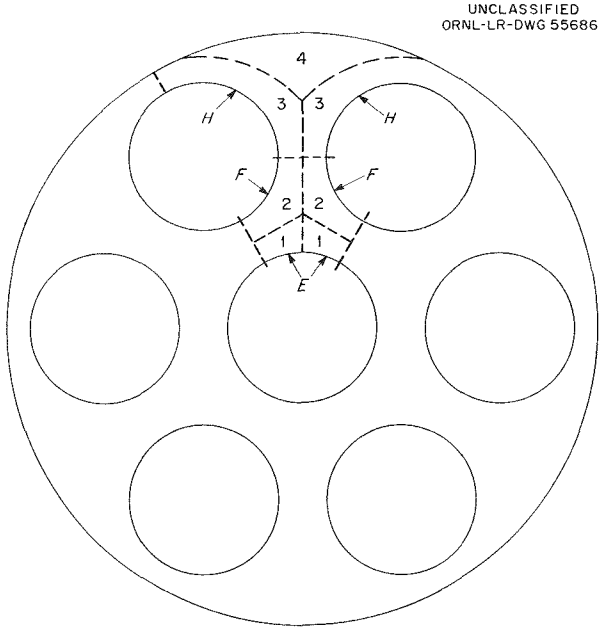

Fig. 2.1. Flow and Surface Sections Considered in Analysis of Seven-Element Cluster.

The net thermal radiation from the three surfaces was discussed previously,[1] and the local heat transfer coefficients used have been reported.[2] The eddy-diffusivity mixing between regions 3 and 4 was determined from experimental mixing studies. It was found that (1) neither the mid-cluster spacers nor the top and bottom hangers in the aligned orientation induced any gross mixing in the channel and (2) the mixing found agreed with that predicted from the turbulence or eddy diffusivity type of mixing in turbulent streams. For the EGCR configuration the following equation was derived:

$$K = k - \mu C_p + 0.243\rho V \quad ,$$

where K is total conductivity, k is thermal conductivity, μ is viscosity, C_p is specific heat, ρ is density, and V is velocity. In determining the conduction between regions 3 and 4, a mean distance x for heat flow between the two regions was determined from the geometry of the system, and the value of K/x was then treated as a heat transfer coefficient between the two regions. The results of calculations combining all these effects are presented in Fig. 2.2.

The temperature of surface E is not shown, because it was found to be very close to that of surface F. The difference in temperatures F and H gives the temperature difference across the outer elements that leads to bowing of these elements. It is interesting to note that the bowing forces on the elements are such that in the lower assemblies the bowing is outward and at the top of the channel the bowing is inward. This reversal of the temperature gradients emphasizes the problem of choosing the optimum location of the elements and shows that it is not possible to balance the temperature by the location of the assembly.

The actual temperature gradients across the element will not be as large as shown in Fig. 2.2. The mixing between the inner two and outer two regions will considerably reduce the difference in the gas temperature between these regions and thus reduce the difference in surface

---

[1]GCR Quar. Prog. Rep. June 30, 1960, ORNL-2964, Fig. 2.7, p. 28.

[2]GCR Quar. Prog. Rep. Dec. 31, 1960, ORNL-3049, pp. 118–20.

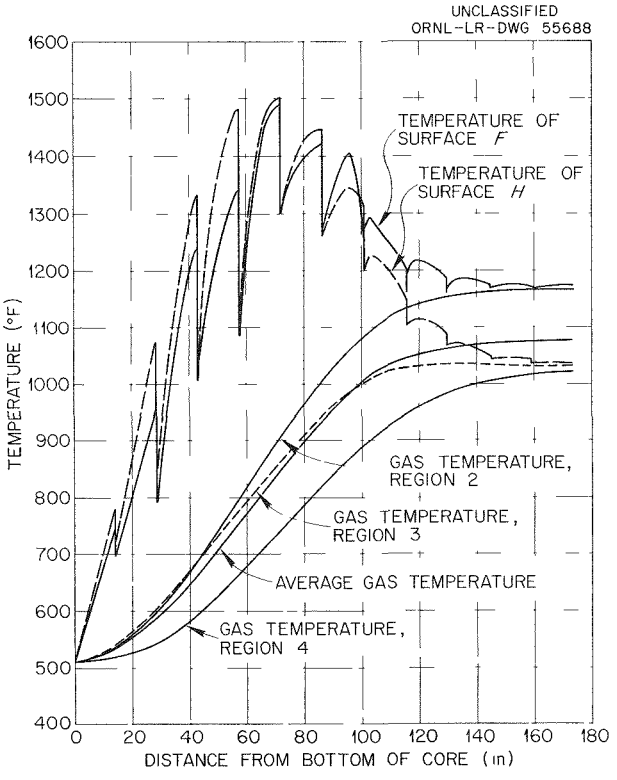

Fig. 2.2. Local Surface and Gas Temperatures for Uniform Exit Gas Temperature and Bank Insertion of Control Rods to 62 in.

temperatures of F and H at the top of a channel. At the end of the second assembly, where the heat generation is highest, the conduction through the element will reduce the temperature across the element by about 30 or 40°F so that the maximum difference will be 80 to 90°F. At the top of a channel the difference will be well under 100°F.

Studies[3,4] have been made to determine the effect of a temperature gradient across an element for both restrained and unrestrained cases. The deflection of an element as a function of time for a constant temperature difference of 100°F along its entire length is shown in Figs. 2.3 and 2.4 taken from ref. 3. Curves for the 1100°F case, which correspond to the temperatures of the elements near the exit of a channel, were not calculated because of the very low creep rates and lack of creep data at this temperature.

The fuel loading scheme for the reactor is such that the upper three and lower three assemblies will be interchanged at their half life or after about 500 days. Assuming a 100°F constant temperature difference across the upper assemblies, it can be seen from Fig. 2.3 that the maximum deflection for a mean temperature of 1200°F would be about 0.023 in. At 1100°F this deflection would be much lower and less than 0.020 in. The

---

[3]J. M. Corum and W. A. Shaw, Restrained Thermal Bowing of Beams Accomplished by Creep with Application to the Experimental Gas-Cooled Reactor Fuel Elements, ORNL CF-60-9-1, Dec. 6, 1960.

[4]GCR Quar. Prog. Rep. March 31, 1960, ORNL-2929, pp. 27–28.

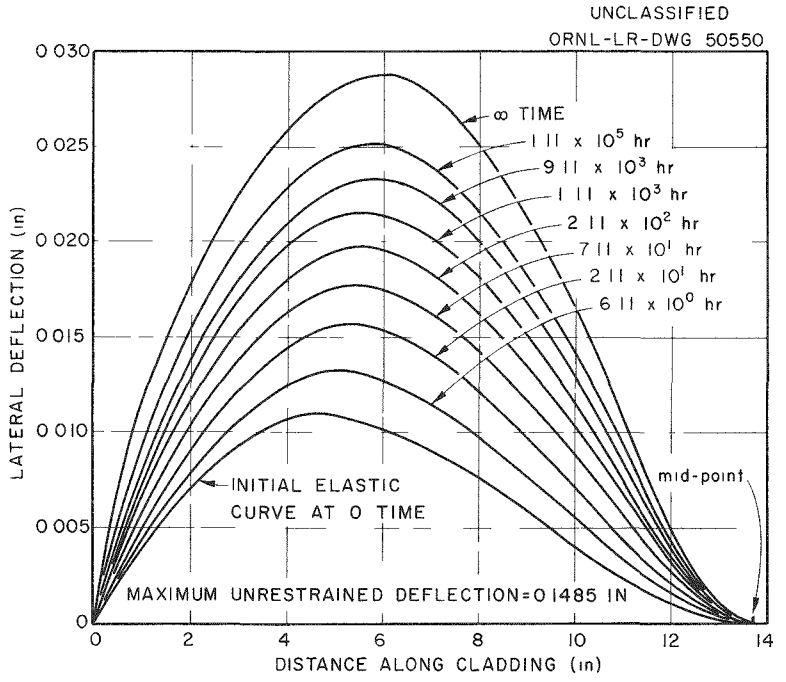

Fig. 2.3. Deflection of EGCR Fuel Rod vs Distance Along Cladding for a Mean Temperature of 1200°F and a Diametral Temperature Difference of 100°F.

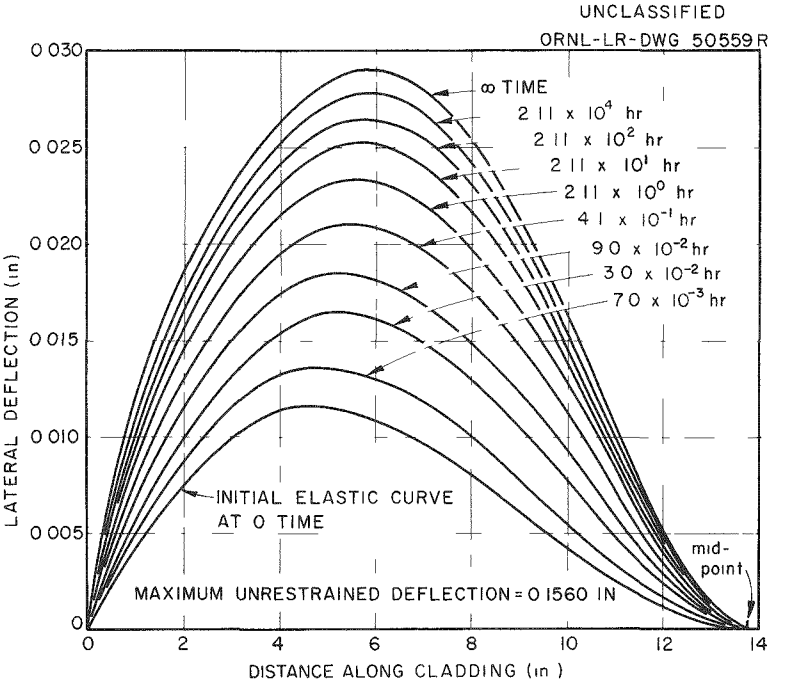

Fig. 2.4. Deflection of EGCR Fuel Rod vs Distance Along Cladding for a Mean Temperature of 1500°F and a Diametral Temperature Difference of 100°F.

permanent deflection is the difference between the final deflection and the initial elastic curve and will be less than 0.010 in. For the second assembly from the bottom the temperature difference across the element varies from 50 to 70°F in the first half and from 40 to 90°F in the second half. The maximum deflection will be 0.020 to 0.025 in. and the permanent deflection about 0.010 in. At the time of interchanging the positions of the assemblies the permanent deflection of the elements will be in the direction to reduce the thermal gradients shown in Fig. 2.2.

In considering the effect of the bowing on the temperature differences, it has been estimated that a 0.001-in. deflection of an element will cause an additional temperature difference of about 1°F. Thus, the increase in temperature and additional bowing will be small.

Beryllium-Clad Fuel Elements (R. S. Holcomb)

A parametric study has been made of the performance of beryllium-clad fuel elements in a 19-element assembly as a function of element spacing and fin height. The fuel assembly consists of nineteen 0.5-in.-o.d. elements arranged on an equilateral triangular pitch in a hexagonal hole with rounded corners in the graphite sleeve. The fin configuration studied was six longitudinal rectangular fins per element, with the fin thickness held constant at 0.040 in. and the fin height varied. A cross section through a typical fuel assembly is shown in Fig. 2.5.

The channel power and the maximum nominal surface temperatures were determined for an exit gas temperature of 1050°F and the total available EGCR pressure drop across the fuel column for several combinations of fin height and element pitch. The results are shown in Fig. 2.6. The range of pitch of 0.6 to 0.8 in. corresponds to a range of 3.0 to 4.0 in. in the distance across corners of the hole in the graphite sleeve. The channel power is relative to the average channel power of the EGCR.

The power and surface temperatures are strong functions of the element pitch for a particular fin height, with the sensitivity decreasing as the fin height increases. The power increases as the fin height increases for a fixed value of surface temperature. The high thermal conductivity of beryllium gives good fin efficiency for fairly high fins.

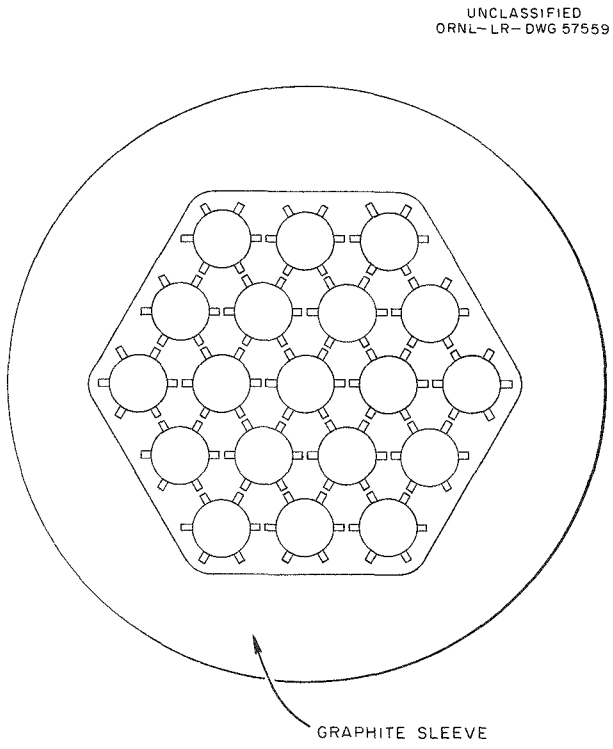

Fig. 2.5. Cross Section Through 19-Element Fuel Assembly with Finned Beryllium-Clad Elements.

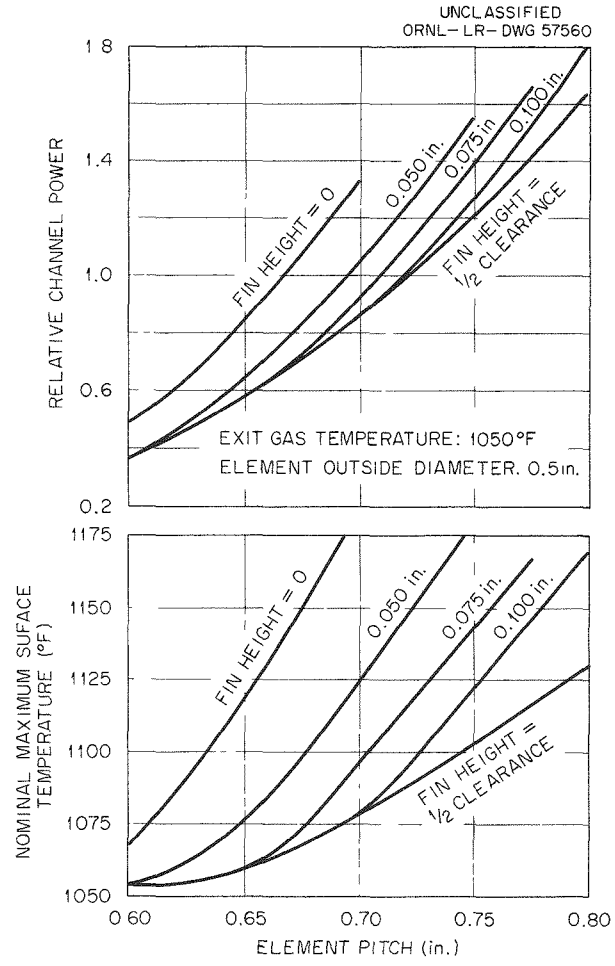

Fig. 2.6. Channel Power and Surface Temperature for Variable Fin Height and Element Pitch in a 19-Element Assembly of Beryllium-Clad Fuel Elements.

The temperature for the finned element is the calculated temperature at the fin base. There will be a small temperature difference between the fin base and the element surface mid-way between fins, which will be a penalty to the finned rods as compared with bare rods.

Over the range studied it would appear that the way to achieve the highest channel power is to increase the pitch and fin height until the limiting surface temperature is reached. Since a small change in temperature results in a large change in power, there is quite an incentive to operate as closely as possible to the maximum surface temperature of 1300°F. In order to be able to reduce the allowance for uncertainties in the surface temperature to a minimum, it will be necessary to know quite accurately the heat transfer coefficient and the flow distribution in the cluster. The fins will eliminate the need for mid-cluster spacers; hence, the local heat transfer coefficient for length-to-diameter ratios up to 100 will have to be determined.

Heat Transfer Correlations for EGCR Fuel Elements (M. E. Lackey)

The design of alternate fuel assemblies for the EGCR requires a knowledge of the effect of the uninterrupted element length-to-diameter ratio on the local heat transfer. This effect has been determined for the average conditions of the reference EGCR element, which has an uninterrupted length-to-diameter ratio of approximately 20. In an attempt to reduce the number of experimental investigations required to determine the effects of ratios greater than 20 for various elements, a correlation has been made of the local heat transfer data obtained for 0.124- and 0.402-in.-i.d. tubes[5-7] and for a seven-element bundle with 60-deg mid-cluster spacers.[8]

---

[5]M. F. Taylor and T. A. Kirchgessner, Measurements of Heat Transfer and Friction Coefficients for Helium Flowing in a Tube at Surface Temperatures Up to 5900°R, NASA Report TND-133 (1959).

[6]W. F. Weiland and W. H. Lowdermilk, Measurements of Heat Transfer and Friction Coefficients for Air Flowing in a Tube of Length-Diameter Ratio of 15 at High Surface Temperatures, NACA Report RME53E04 (1953).

[7]L. V. Humble, W. H. Lowdermilk, and M. Grele, Heat Transfer from High-Temperature Surfaces to Fluids I — Preliminary Investigation With Air in Inconel Tube With Rounded Entrance Inside Diameter of 0.4 in. and Length of 24 in., NACA Report RM No. E7L31 (1948).

[8]Allis-Chalmers, Run 212-C, unpublished data.

The local heat transfer data are shown in Fig. 2.7, where the local surface Nusselt number, Nu_{sx}, is plotted as a function of the local surface Reynolds number, Re_{sx}. The data are in fair agreement with the line given by the following equation:

$$Nu_{sx} = 0.0975\ Re_{sx}^{0.724}\ Pr_{sx}^{0.4}\left(\frac{x}{D}\right)^{-0.5576\ Re_{sx}^{-0.109}},$$

where D is the hydraulic diameter of the system and x is the distance

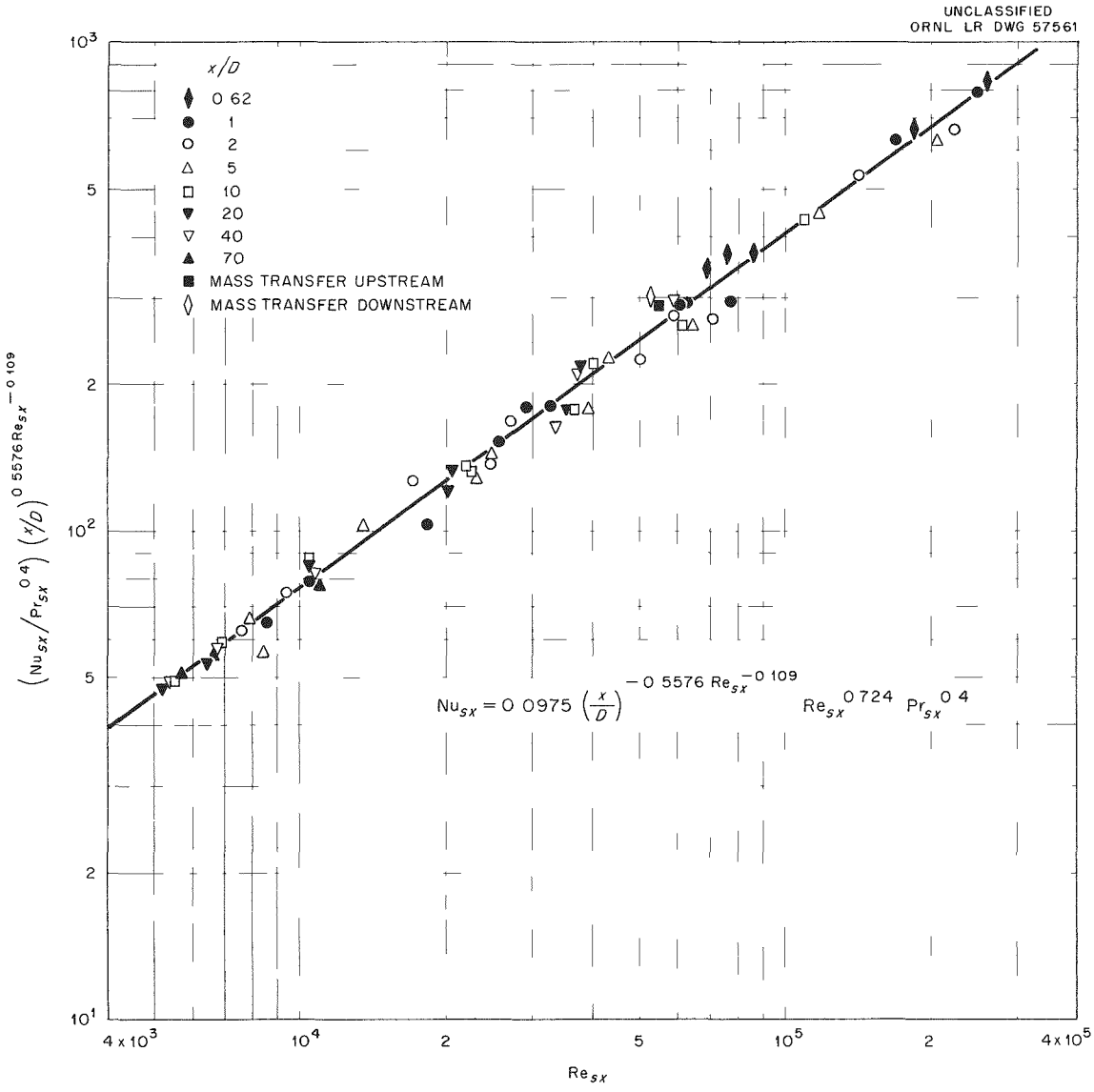

Fig. 2.7. Correlation of Local Heat and Mass Transfer Coefficients.

from the last interruption to the point in question. Included in Fig. 2.7 are the equivalent heat transfer values obtained from the mass transfer experiments on a seven-rod bundle.[9]

The variation of the local heat transfer performance, as characterized by the variation in the local Nusselt number, is shown in Fig. 2.8 as a

[9]GCR Quar. Prog. Rep. Sept. 30, 1960, ORNL-3015, pp. 53–63.

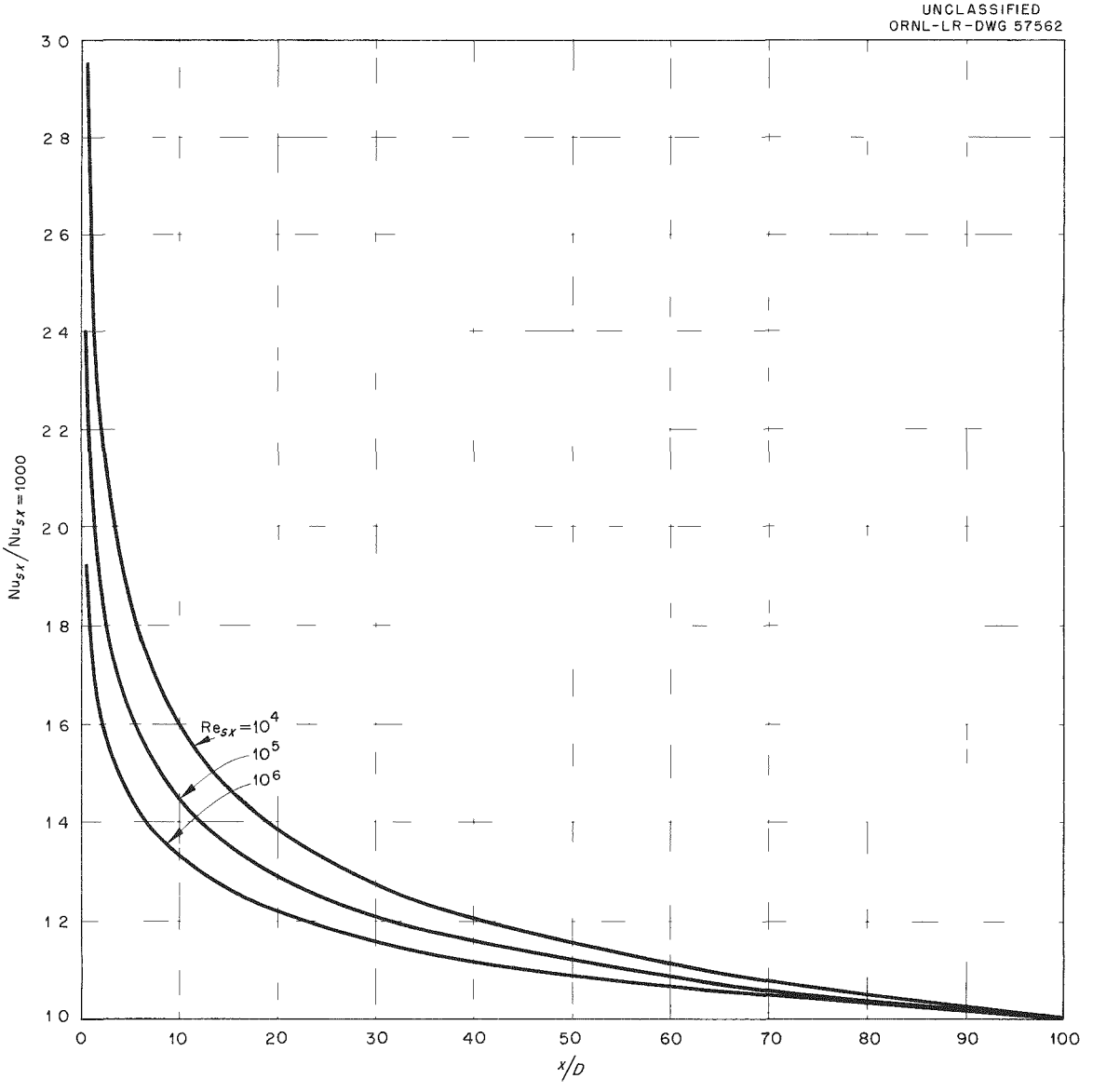

Fig. 2.8. Variation of Local Nusselt Number at Constant Values of Reynolds Number.

function of x/D at constant values of local Reynolds number. The values used in Fig. 2.8 were obtained by evaluating the above equation at constant Reynolds numbers. The data in Fig. 2.8 indicate that the rate of decay of the Nusselt number with x/D increases as the Reynolds number decreases.

EGCR Control Rods (J. W. Michel)

Additional calculations have been made of the effect of off-design operating conditions and assumed control rod properties on the thermal performance of the EGCR control rods. The parameters studied were the emissivity of the outside tubing and the coolant flow rate. The effects of variations of these parameters on the maximum control rod temperatures were determined. The results of this study are plotted as peak stainless steel cladding temperature versus emissivity of the outside cladding in Fig. 2.9. For the design coolant flow rate of 75 lb/hr, it may be seen that an emissivity, ϵ, of 0.47 is required to maintain the peak temperature below the maximum allowable value of 1600°F. Achieving an emissivity of at least this value by oxidizing the surface appears to be possible.[10] It should be noted that even at $\epsilon = 0.3$, the central support rod,[11] which is the structural element in the control rod design, only reaches a peak temperature of 1140°F.

An examination of the consequences of coolant flow stoppage was made, although this event is considered to be unlikely. For the worst case of emissivity of 0.3 and no coolant flow, the peak temperature is about 2230°F. The reactor would be shut down in this case, since the source of the control rod cooling is the same as for the pressure vessel. The stress developed in the central support rod in supporting the weight of the control rod is about 1200 psi, while the yield strength of type 347 stainless steel at 2230°F is about 4200 psi. Thus an adequate safety factor is available even for this extreme transient condition.

---

[10] W. H. McAdams, Heat Transmission, p. 475, 3rd ed., McGraw-Hill.

[11] GCR Quar. Prog. Rep. Dec. 31, 1960, ORNL-3049, pp. 118–22.

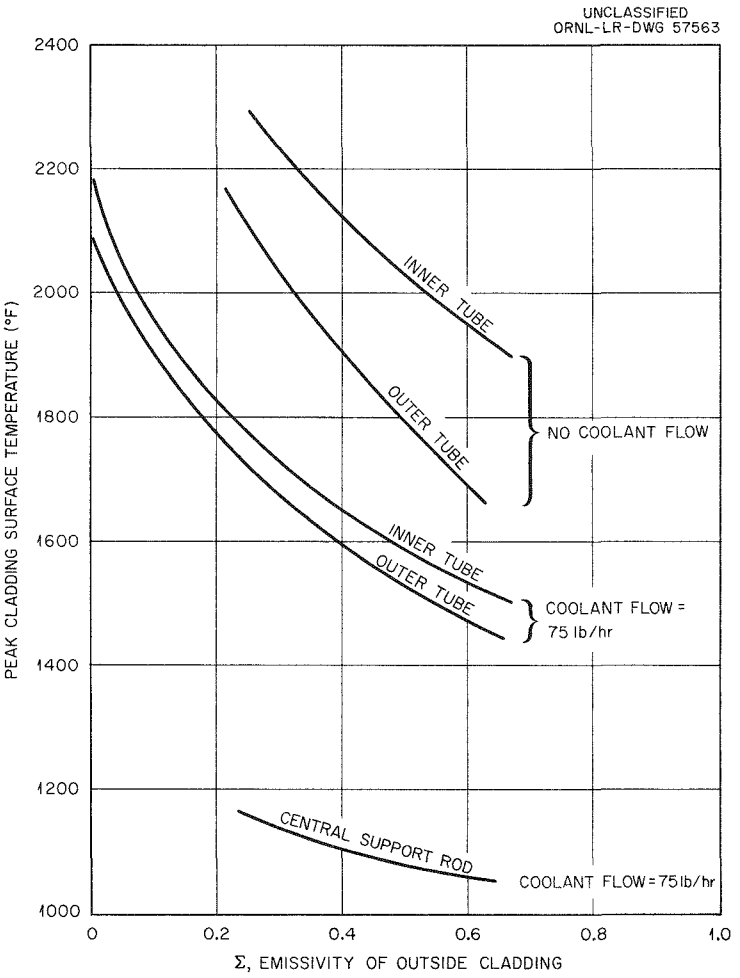

Fig. 2.9. Peak Surface Temperature Versus Emissivity of EGCR Control Rod with Center Control Rod Fully Inserted and an Average Heat Generation Rate of 7500 Btu/hr·ft.

EGCR Moderator Temperatures (E. G. Beasley)

A determination was made of the EGCR moderator temperature distribution and the coolant flow required to keep the maximum moderator temperature below 1100°F. The moderator is to be cooled by reactor coolant flowing in the annuli formed by the outsides of the fuel element sleeves and the 5 1/4-in.-diam channels in the moderator. The amount of flow is fixed by flow restrictors in the bottom dummy assembly. The power distribution and thus the gamma and fast-neutron heat deposition will vary with time and core loading. Since it will be difficult to change the size of the flow restrictor in the bottom dummy after initial operation, it is

planned to set the flow at a rate which will cool the moderator when the heat deposition is at the maximum in each channel. Consequently, there will always be some of the moderator that will be over-cooled.

The study was based on the heat deposition rates published by Nephew[12] and the peak-to-average power distribution shown in Table 2.1. In the calculations, each unit cell was considered individually. It was assumed that all the energy deposited in the fuel sleeve and the moderator in each unit cell was removed by the coolant in the annulus. This is not exactly accurate, but the results will be conservative. The channels were divided in three groups based on the predicted peak-to-average heat deposition ratio. Group I is for peak-to-average ratios of 1.3 and 1.35, group II for 1.15, 1.20, and 1.25, and group III for 1.05 and 1.10. The coolant flow required was 147, 136, and 118 lb/hr for groups I, II, and III, respectively.

These flow rates are sufficient to keep the graphite temperature below 1100°F, except in some channels adjacent to a 1.5-Mw experiment in a through-tube, where the experimental element would cause heating to a temperature in excess of 1100°F by a small amount; with 1.0-Mw experiments, none of the graphite will exceed a temperature of 1100°F.

Based on these assumptions, the total moderator coolant flow is 32 000 lb/hr, which removes 5400 kw of energy. This flow is about 5000

[12]E. A. Nephew, Gamma-Ray and Fast-Neutron Heat Deposition in EGCR Core, ORNL CF-60-10-122, Oct. 28, 1960.

Table 2.1. EGCR Power Distribution

y	Peak-to-Average Power Distribution in Indicated Channel (x,y)[a]								
	x = 4	x = 12	x = 20	x = 28	x = 36	x = 44	x = 52	x = 60	x = 68
4	1.35	1.35	1.35	1.35	1.35	1.25	1.20	1.10	1.05
12	1.35		1.35	1.35	1.35	1.25	1.25	1.15	1.05
20	1.35	1.35	1.35	1.35	1.35	1.30	1.25	1.15	
28	1.35	1.35	1.35	1.35	1.35	1.35	1.20	1.10	
36	1.35	1.35	1.35	1.35	1.35	1.35	1.25	1.10	
44	1.25	1.25	1.30	1.35	1.35				
52	1.20	1.25	1.25	1.20	1.25				
60	1.10	1.15	1.15	1.10	1.10				
68	1.05	1.05							

[a]x and y are coordinates of channel in inches from center of reactor.

lb/hr in excess of that which would give an average gas exit temperature of 1050°F from the annuli.

The calculated temperature at the center of each 16-in.-square moderator block is given in Fig. 2.10. It may be seen that the temperature of block b, which is adjacent to a small through-tube that was assumed to be loaded with a 1.5-Mw experiment, exceeds 1100°F. It was assumed that the large experimental channels were loaded with graphite rather than experiments; hence, some of the blocks were grossly over-cooled.

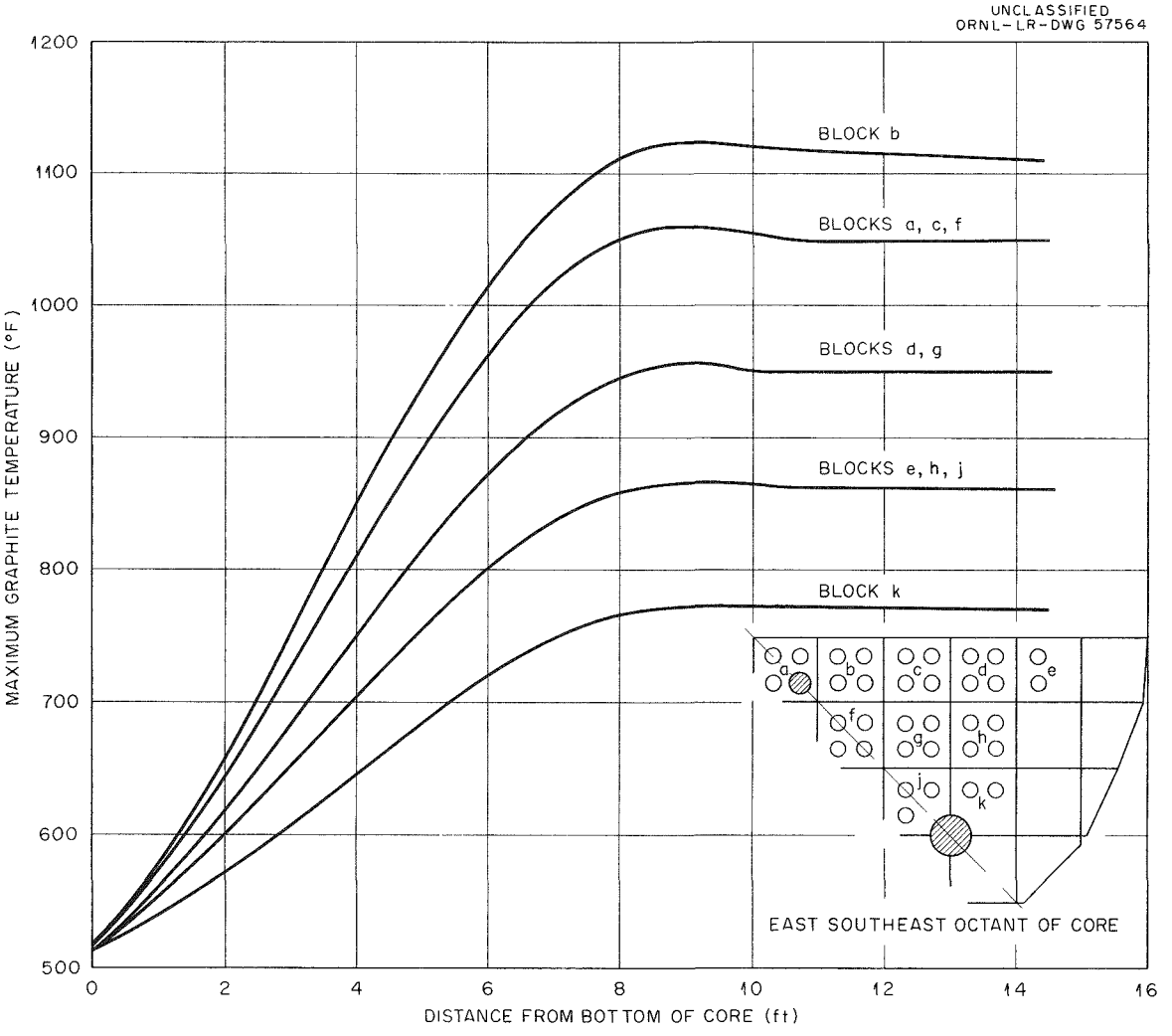

Fig. 2.10. Maximum Graphite Temperatures at Centerlines of Moderator Blocks in EGCR Core.

Structural Investigations

B. L. Greenstreet

Stress Analysis of EGCR Pressure Vessel (B. L. Greenstreet, F. J. Witt)

The second phase of the experimental investigation[13] of the EGCR pressure vessel was completed. This phase of the study consisted of translating the experimental data into quantities applicable to the full-scale vessel and utilizing the results in making design evaluations. The design pressure and the magnitudes of the forces and moments to be applied to the nozzles were provided by Kaiser Engineers, except for the pipe reactions on the experimental loop nozzles, which were determined at ORNL.

These data, together with the experimental results, were combined with the theoretically determined thermal stress distributions to make complete evaluations for the nozzles in the cluster region. The temperature distributions for the gas outlet and burst-slug detection nozzles were not known, however, and complete evaluations of these units could not be made.

The experimental results were used to obtain the stress profiles along the nozzles and to estimate the maximum stresses in the sphere based on the assumption that the distributions are correctly given by existing theoretical models. This assumption was made despite discrepancies between predicted and measured magnitudes. In the case of the sphere the use of this assumption was limited to the immediate vicinity of each nozzle. The profiles along the nozzles were obtained for each separate loading so that the total stresses could be determined for any combination of loads given by the design specifications.

It was found that the stresses determined analytically for a single nozzle radially attached to a spherical segment were in approximate agreement with the experimental results for a nozzle loaded by an axial force. Much less agreement was found to exist for pressure stresses. From these observations the simplified model appeared to be valid for localized loadings, and the thermal stresses were calculated on this basis.

---

[13]GCR Quar. Prog. Rep. Sept. 30, 1960, ORNL-3015, pp. 35–42.

The profiles along the nozzles were obtained by considering each nozzle as an independent structural unit. For an infinitely long, symmetrically loaded, cylindrical shell, the principal stresses are given by

$$\sigma_x = \frac{N_x}{h} \pm \frac{6M_x}{h^2}$$

and

$$\sigma_c = \frac{N_c}{h} \pm \frac{6M_c}{h^2} \quad ,$$

where h is wall thickness, N is membrane force, and M is bending moment. The subscripts x and c refer to the axial and circumferential directions, respectively. The positive signs in the equations correspond to the outer surface and the negative ones to the inner surface. The M's and N's are functions of the axial coordinates,[14] and when the expressions for these quantities are substituted into the equations they become

$$\sigma_x = \frac{ap}{2h} \pm \frac{3e^{-\beta x}}{ah^2\beta^2} (-C_1 \cos \beta x + C_2 \sin \beta x)$$

and

$$\sigma_c = \frac{ap}{h} - \frac{e^{-\beta x}}{h} (C_1 \sin \beta x + C_2 \cos \beta x)$$

$$\pm \frac{3\mu e^{-\beta x}}{ah^2\beta^2} (-C_1 \cos \beta x + C_2 \sin \beta x) \quad ,$$

[14] F. J. Stanek, Stress Analysis of Cylindrical Shells, ORNL CF-58-9-2 (July 1959), p. 2, 26.

for internal pressure loading. In these expressions a is the radius of the middle surface, C_1 and C_2 are integration constants, p is pressure, x is axial distance, and

$$\beta = \left[\frac{3(1 - \mu^2)}{a^2h^2}\right]^{1/4} ,$$

where μ is Poisson's ratio. Hence, the distributions are completely defined if the constants C_1 and C_2 are known.

The axial membrane stress, ap/2h in the above case, may be calculated or obtained from strain gage readings in those regions where no bending occurs (the so-called membrane regions). In obtaining the stress profiles, preference was given to the gage readings. Once the axial membrane stress was determined, the two integration constants were evaluated using two of the experimentally determined stresses in the region where bending occurred. Whenever possible the experimental stress values nearest the junction were used because the higher stresses occurred in these regions, and, in general, greater accuracy was obtained. However, the lack of reliable data dictated the use of other points in some cases. After these evaluations were made the stress distributions were completely determined.

In most cases the nozzles are not subjected to axisymmetrical edge forces. Asymmetries arise because of the proximity of adjacent nozzles or other structural discontinuities and because of nonradial attachment to the shell. Although the assumption of symmetrical edge loading is unrealistic, except perhaps for the nozzle at the apex (nozzle A), it is reasonable to assume that in the region of a particular axial element the cylinder behaves the same as one with a symmetrical edge load and may be analyzed according to this premise. Thus, the stress profiles along the instrumented elements of all nozzles were obtained using the procedure described above. [Note: Each nozzle in the cluster region was given a letter designation corresponding to the radius from the apex to its center.

With this means of identification, only the designation A applies to a single nozzle.]

In all cases the profiles were calculated using experimental stress values for the outside surface only. Hence, the accuracy of the method may be examined by comparing the calculated stresses for the inner surface with the experimental values. Since the inner surface of the gas outlet nozzle was instrumented, the comparisons were made for this unit. The experimental points and the stress profile for the outer surface of an axial element located on the side nearest the apex of the sphere (uphill side) are shown in Fig. 2.11. It may be seen that an excellent fit of the experimental points with the profile was obtained. Similar data for the inner surface are shown in Fig. 2.12. The agreement is good, with the fit being better for the axial than for the circumferential stress distribution. This comparison demonstrates that the method is sufficiently accurate for use in finding the peak stresses along the nozzles.

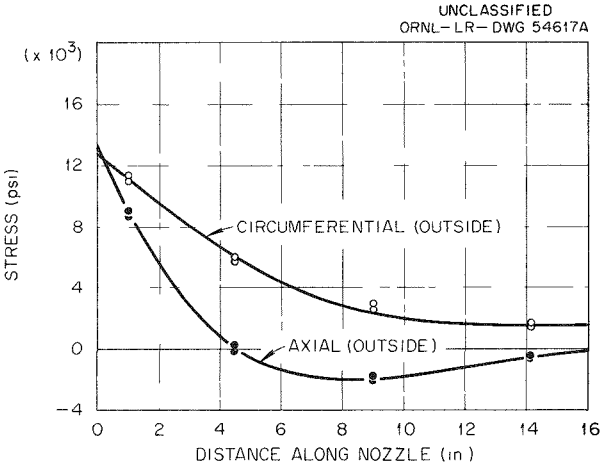

Fig. 2.11. Stress Distributions on Outer Surface of Gas Outlet Nozzle Resulting from 350-psi Pressure Loading (Uphill Side).

The profiles along the outside surface of the control rod nozzle at the apex (nozzle A) for internal pressure and for an axial load on the nozzle are shown in Figs. 2.13 and 2.14. This nozzle is centrally located and radially attached to the shell; therefore, the stress distribution was assumed to have axial symmetry. In order to illustrate the effect of nonradial attachment, the stress profiles for nozzle K under an internal pressure loading are shown in Figs. 2.15 and 2.16. Nozzle K is a large experimental loop nozzle, but it has the same dimensions as nozzle A.[15] From the

[15]The reference circle radii and the nozzle types are given in Table 2.5, p. 41, GCR Quar. Prog. Rep. Sept. 30, 1960, ORNL-3015, and the nozzle dimensions are given in Table 2.4, p. 35.

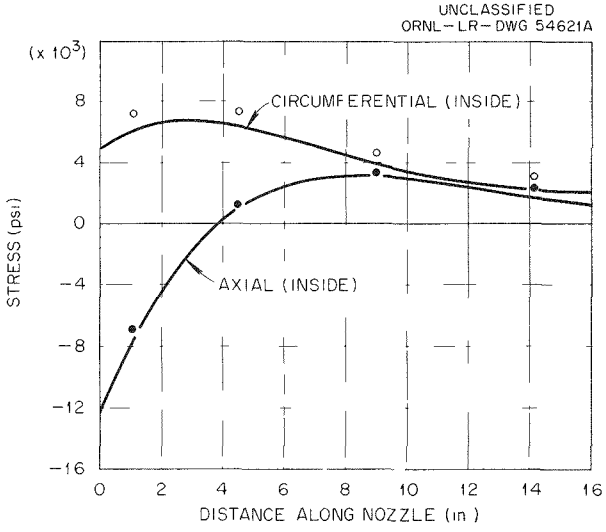

Fig. 2.12. Stress Distributions on Inner Surface of Gas Outlet Nozzle Resulting from 350-psi Pressure Loading (Uphill Side).

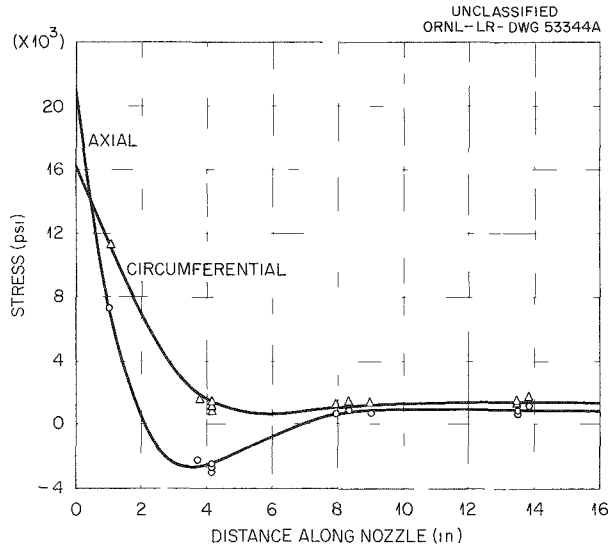

Fig. 2.13. Stress Distributions on Outer Surface of Nozzle A Resulting from 350-psi Pressure Loading.

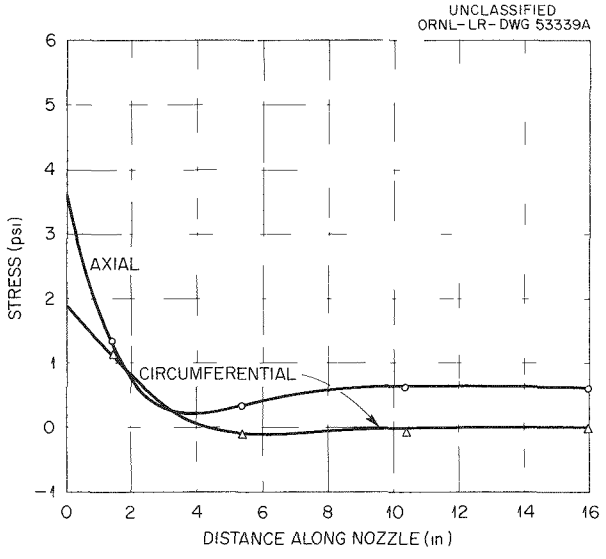

Fig. 2.14. Stress Distributions on Outer Surface of Nozzle A Resulting from Axial Tensile Loading of 1 lb/in. Along Mean Circumference.

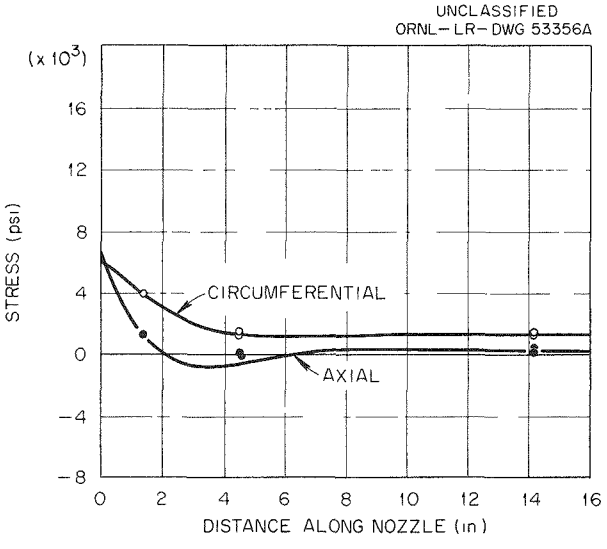

Fig. 2.15. Stress Distributions on Outer Surface of Nozzle K Resulting from 350-psi Pressure Loading (Uphill Side).

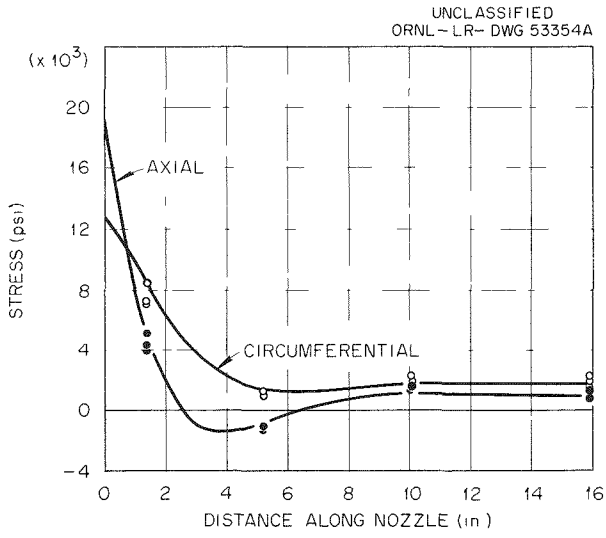

Fig. 2.16. Stress Distributions on Outer Surface of Nozzle K Resulting from 350-psi Pressure Loading (Downhill Side).

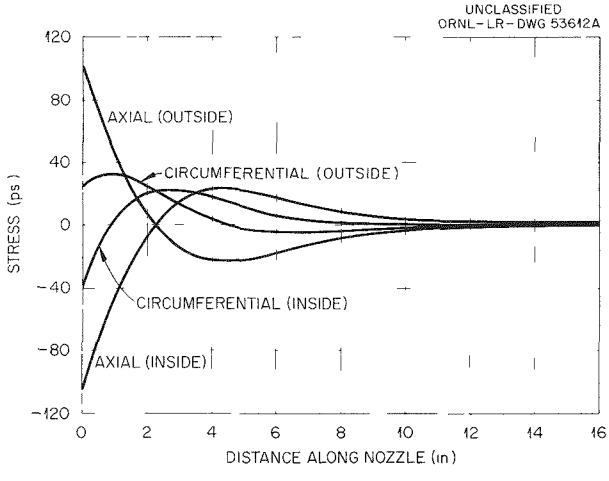

Fig. 2.17. Thermal Stresses (Theoretical) in Exterior Control Rod or Large Experimental Loop Nozzle Assuming a Single Nozzle-to-Shell Attachment.

figures it may be seen that the highest stresses occur on the downhill side. The profiles for this side are very similar to those for nozzle A, but the peak stresses are less. A comparison of the profiles for the two sides gives a graphic illustration of the effects associated primarily with nonradial attachment.

The temperature distributions along the external portions of the nozzles in the cluster region are given by

$$T = T_0(e^{-bx} - 1) \quad ,$$

where T_0 is the temperature excess above the reference temperature, b is a constant, and x is axial distance. The calculated thermal stresses along nozzle A for a T_0 of unity are given in Fig. 2.17. Since this nozzle is subjected only to an axial loading and the maximum stresses occur on the outer surface, the data contained in Figs. 2.13, 2.14, and 2.17 complete the information required for a structural evaluation of this unit.

The maximum pressure stresses are in the nozzles, with one exception. This exception applies to the regions of the shell in the vicinities of the B nozzles, where the maximum stresses are approximately equal to the maximum nozzle stress. For other types of loadings, the B nozzles are more highly

stressed than the head. However, this exception is not of major significance, since the highest stresses for critical design loadings in the cluster region are not in the B nozzles or the head regions in their vicinities.

The circumferential and the meridional or axial stresses versus the profile of a section of the experimental model are shown in Fig. 2.18. Also shown are the stresses along a burst-slug detection (BSD) nozzle and along nozzle L, which is one of the nozzles in the cluster. All the stress values are based on the full-scale pressure vessel being subjected to an internal pressure of 350 psi. The effects of the structural discontinuity at the junction between the hemispherical head and the cylindrical body may be seen. The mean stresses in the cylindrical portion of the shell are lower than the theoretical values. These are 7720 psi for the axial stress and 15 440 psi for the circumferential stress. In addition, the experimental values show that the axial stress on the outer surface is less than one-half the circumferential stress, but this may be attributed to axial bending in the shell.

The structural evaluations of the upper head of the vessel, including all nozzles except the burst-slug detection and gas-outlet nozzles, were made using the procedures outlined in "Tentative Structural Design Basis for Reactor Pressure Vessels and Directly Associated Components," PB 151987, 1 December 1958 Revision, Department of Commerce, Office of Technical Services. The configurations throughout the cluster region and the vessel itself were found to be structurally adequate. The primary and the primary-plus-secondary stress intensities for the burst-slug detection and gas-outlet nozzles are within the allowable limits. However, the complete design evaluations of these units cannot be made until the temperature distributions are known.

Structural Integrity of EGCR Through-Tubes (J. M. Corum)

Instantaneous and time-dependent collapse tests on types 304 and 347 stainless steel cylindrical shells are being made to provide collapse data applicable to the experimental through-tubes in the EGCR. As

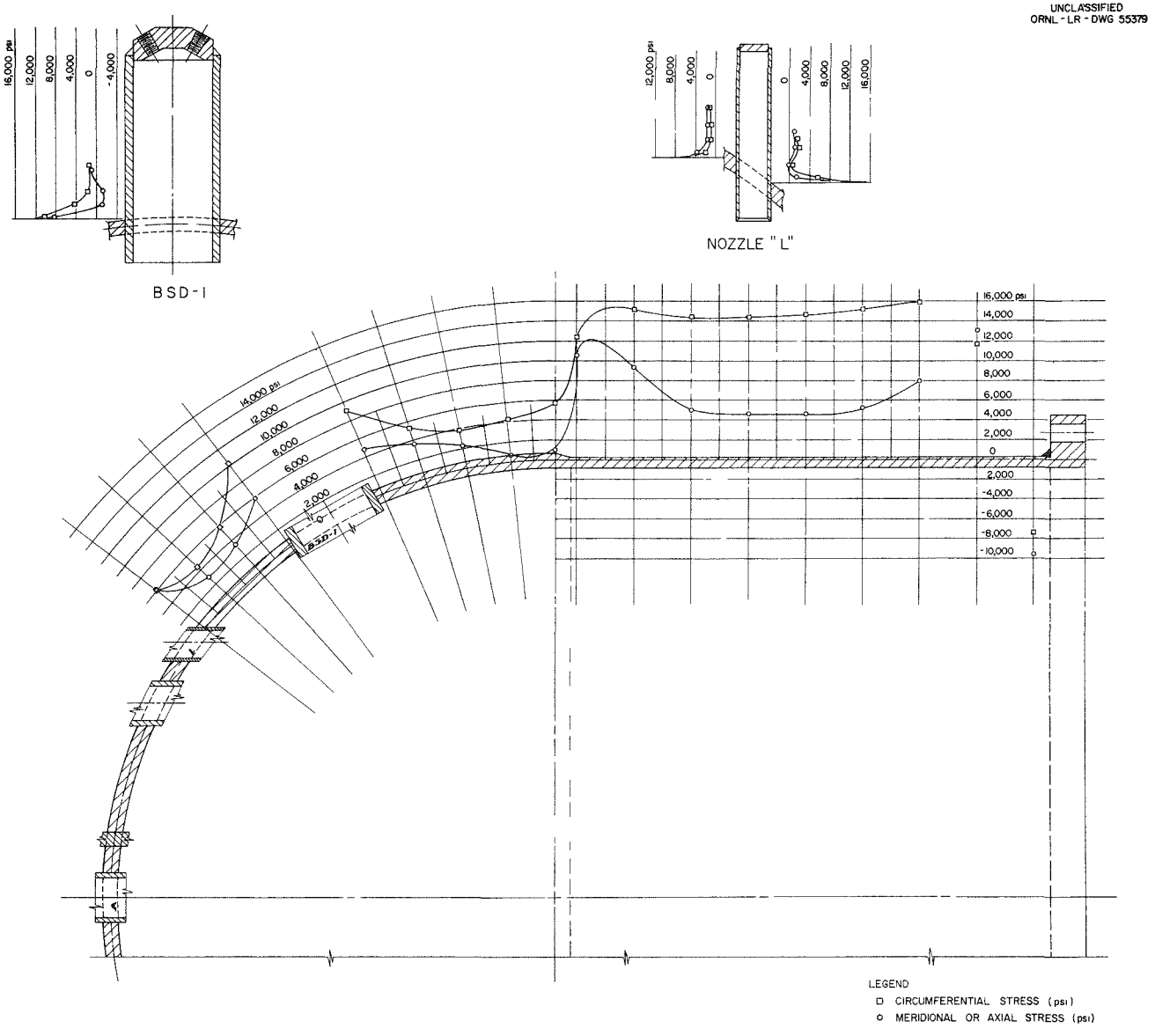

Fig. 2.18. Circumferential and Meridional or Axial Stresses on Outside Surface of Head BSD Nozzle, and Nozzle L on a Diametral Section Through BSD Nozzle.

previously reported,[16] the test program includes the use of two sets of large-diameter units made from commercial tubing in addition to tests using model tubes. In one case the outside diameter and wall thickness are 8.0 and 0.25 in., respectively, while in the other 4.0-in.-o.d., 0.12-in.-wall tubes are used. The material for the larger specimens is type 304 stainless steel, but the smaller ones are made using both types 304 and 347 stainless steel so that the behavior of the two materials may be compared.

The second and third of a series of four 8.0-in.-o.d. tubes were collapsed. Both specimens were type 304 stainless steel tubing purchased in accordance with ASTM A-213 TP-304 specifications and were tested at 1200°F. Modifications of the furnace heater arrangement and controls permitted control of the temperatures to ±20°F along the length of the specimens, except at the upper extremities.

Both specimens were approximately 9 ft long; the mean radius-to-thickness ratio of the second tube was 15.84 and the ovality ratio was 0.9868, while for the third tube these quantities were 15.71 and 0.9865, respectively. The second tube failed instantaneously in the characteristic two-lobe mode under an external pressure of approximately 780 psi, which is within the scatter band of the results from model tests. This critical pressure compares favorably with that for a similar type 304 stainless steel tube previously collapsed under an external pressure of 805 psi with a maximum temperature of 1200°F near the center of the specimen.[16]

The third specimen was subjected to an external pressure loading of 595 psi and collapsed after 60 hr. This specimen also failed in a two-lobe mode. As was expected, the cross-sectional configuration was not as distorted as for the instantaneous-collapse specimens.

The differences in distortion occur because of differences in the compressive stresses. The mean compressive stresses in the walls of the tubes which buckled instantaneously exceeded the proportional limit of the material. Thus, collapse of the specimens was initiated through

---

[16]GCR Quar. Prog. Rep. Dec. 31, 1960, ORNL-3049, pp. 144–54.

inelastic action, and the initial resistance to bending deformation was smaller than it would have been if the mean stresses had been below the proportional limit. For the creep collapse specimen, the mean stress was below the proportional limit, and collapse was initiated through elastic action with a subsequent higher initial resistance to deformation.

The third and fourth in the series of 4.0-in.-o.d. tubes were collapsed instantaneously at 1200°F in tests conducted by the University of Tennessee. The third specimen was type 304 stainless steel tubing and the fourth was type 347. Both specimens were approximately 5 ft long and were purchased in accordance with ASTM A312-58T specifications.

The type 304 specimen had an average measured mean radius-to-thickness ratio of 16.37 and an ovality ratio of 0.9973. This specimen collapsed under an external pressure of 540 psi. The temperature variation did not exceed ±15°F along the length of the tube. The specimen collapsed against the inside insert in a single-lobe mode with the thinner regions of the tube wall moving outward to form the lobe, as in the other cases. Here again, the collapse pressure is comparable with the collapse pressures of the model tests and with the collapse pressure for a similar type 304 stainless steel tube previously collapsed under an external pressure of 590 psi at a temperature of 1200°F.[16]

The type 347 stainless steel specimen had an average measured mean radius-to-thickness ratio of 15.43 and an ovality ratio of 0.9982. This unit collapsed under an external pressure of 900 psi at a temperature of 1200°F at one end, 1170°F at the center, and 1130°F at the other end. This specimen also collapsed against the inside insert in a single lobe mode with the thinner regions of the tube wall moving outward to form the lobe. The critical pressure and deformed geometry again compared favorably with those for a similar type 347 stainless steel tube previously collapsed under an external pressure of 990 psi with a temperature of 1200°F at one end and 920°F at the other.

The data for both instantaneous and time-dependent collapse are being correlated with various proposed theories which are both "exact" and semi-empirical in nature. Results from instantaneous collapse tests which have been performed on type 304 stainless steel tubes at 1200°F were correlated

with collapse pressures predicted from the classical instability formula for long ideal tubes which collapse into a two-lobe mode:

$$P_{cr} = \frac{E}{4(1 - \mu^2)} \left(\frac{t}{r}\right)^3 ,$$

where t is the tube thickness, r is the mean radius, μ is Poisson's ratio, and E is the modulus of elasticity. For mean circumferential stresses above the proportional limit, E was replaced by the tangent modulus (slope of the compressive stress-strain diagram) corresponding to the mean stress. As a first approximation, the tangent moduli were obtained from tensile stress-strain diagrams at 1200°F which, in turn, were obtained from specimens cut from the wall of one of the 8-in.-o.d. instantaneous collapse specimens after it was collapsed.

It was found that the critical pressures for the model tests varied from approximately 78% of the calculated pressures for low mean radius-to-thickness ratios ($r/t \approx 12$) to 82% for high ratios ($r/t \approx 26$). The values for the two instantaneously collapsed 8-in.-o.d. tubes were approximately 93% of the predicted critical pressure. The predicted values may be lowered when the tangent moduli are obtained from compressive rather than tensile stress-strain diagrams. In addition, the predicted values are applicable only to perfectly round tubes. It is almost impossible to obtain such a perfect tube, and, in actuality, the out-of-roundness reduces the critical pressure.

As a first approximation for predicting time-dependent collapse, the concept of isochronous-stress-strain curves was used. An isochronous-stress-strain curve gives the total strain (elastic + time-independent plastic + time-dependent plastic) which will occur at any stress level during the time period for which the curve is constructed. The curves for different time periods appear to be stress-strain diagrams but actually are not in the usual sense. An isochronous-stress-strain diagram for type 304 stainless steel at 1200°F and for 60 hr was constructed using the tensile data previously mentioned and tensile creep data for type 304 stainless steel at 1200°F. The tangent moduli at different stress levels were

used in the classical formula for instantaneous collapse to predict the time-dependent collapse behavior. For the 8-in.-o.d. time-dependent collapse specimen, the predicted value was 92% of the actual pressure that caused collapse after 60 hr. The effects of stress biaxially were neglected in the calculations. The close agreement between the predicted and actual pressures is better than expected because, in actuality, the pressure predicted by the time-dependent tangent modulus is only an approximation to a conservative estimate.[17]

Bimetallic Hemispherical Shell Collapse Tests (J. M. Corum, B. L. Greenstreet)

In evaluating the structural stability of the thermal barrier for the EGCR pressure vessel, a basic question arose regarding the effect of a temperature difference across the wall of a thin spherical shell upon the buckling pressure for the structure. The evaluation of the thermal strain influence is important to design in general. Therefore, an experimental investigation was initiated under contract at Syracuse University Research Institute.

Since there are many difficulties and undesirable features associated with imposing a temperature differential across a spherical shell, specimens made from bimetallic sheet were used. By selecting two materials with unequal thermal expansion coefficients, thermal strains were induced by merely changing the temperature level. This scheme was advantageous because each specimen was at a constant temperature during the test period. The strain distributions as functions of thickness were not the same as for the case of constant heat flow. In the heat flow case the strains are linearly distributed with zero strain at the mid-surface, but for the bimetallic sheet the strain in each material was almost uniform. However, the strain distribution is not the important factor, since, in either case, the influence of thermal strains is being evaluated, and the gross effects are the same.

---

[17]R. L. Carlson, Time-Dependent Tangent Modulus Applied to Column Creep Buckling, J. Appl. Mechanics, 23(3): 390 (1956).

The metal chosen for the test shells was Truflex A-1 thermostat metal, which is a brass-Invar type that is manufactured by Metals and Controls Division of Texas Instruments, Inc., as a commercial item. The applicable physical and mechanical properties of brass and Invar are listed in Table 2.2. The thicknesses of the two materials that make up a sheet are proportional to obtain the maximum effects from a thermostat element. These maximum effects are obtained when the thicknesses of the components are inversely proportional to the square roots of the moduli of elasticity. On this basis, the relative percentage thicknesses of the brass and Invar were 55 and 45, respectively.

The sheets were formed into two types of hemispherical shells; one had brass on the outside, while the other had Invar. All the shells were 8.5 in. in diameter with a total wall thickness of 0.022 in., giving a radius-to-thickness ratio of 193.2.

The test results are shown in Fig. 2.19, where the buckling pressure is given as a function of temperature for the two types of shells. Each shell tested exhibited a symmetrical collapse configuration, and the points for the specimens with Invar on the outside always fell above those for shells with brass on the outside. The relative data scatter exhibited in Fig. 2.19 is smaller than that observed in the results from instantaneous buckling tests on copper shells.[18]

Theoretical stress distributions based on no bending in the shells are illustrated in Fig. 2.20. Schematic representations of the pressure and thermal stress distributions in the EGCR thermal barrier subjected to an external pressure are shown in Fig. 2.20a. The temperature on the inside surface is greater than that on the outside surface because heat is flowing out of the hemisphere, as indicated. The schematic stress distributions in a brass-Invar shell, with Invar on the outside, under an external pressure and at a temperature above that corresponding to the stress-free state are shown in Fig. 2.20b. It may be seen that this

[18]K. N. Tong, Creep Buckling of Hemispherical Copper Shells, Syracuse University Research Institute Report No. ME 659-596A (June 1959), pp. 20–21.

condition approximates that in Fig. 2.20a. If the temperature of the shell in Fig. 2.20b were below the stress-free temperature, the thermal stresses would be changed in sign, and the condition of the shell would

Table 2.2. Composition and Properties of Brass and Invar

	Invar	Brass (Muntz)
Composition	36% Ni–64% Fe	60% Cu–40% Zn
Tensile strength, psi	75 000	54 000
Yield strength, psi	50 000	21 000
Elongation, %	35	51
Modulus of elasticity, psi	21.4×10^6	15×10^6
Coefficient of thermal expansion, in./in.·°F	2×10^{-6}	9×10^{-6}

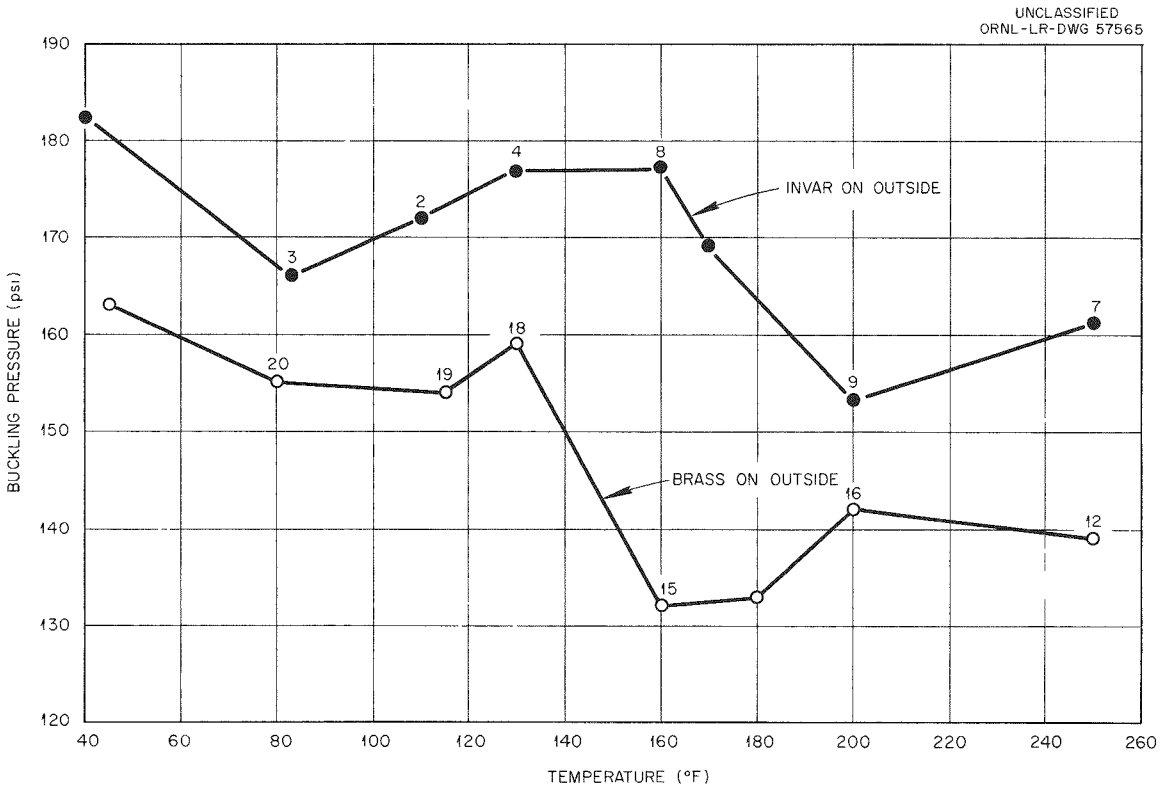

Fig. 2.19. Buckling Pressure Versus Temperature for Brass-Invar Bimetallic Hemispherical Shells (Mean Radius-to-Thickness Ratio = 193.2).

correspond to that in Fig. 2.20a with reversed heat flow. The stress distributions for a shell with brass on the outside are shown schematically in Fig. 2.20c. Again the thermal stresses are those for a temperature above the stress-free state. The simulated heat flow is inward in this case, but for a temperature below that corresponding to the stress-free state, the condition in Fig. 2.20a would again be approximated.

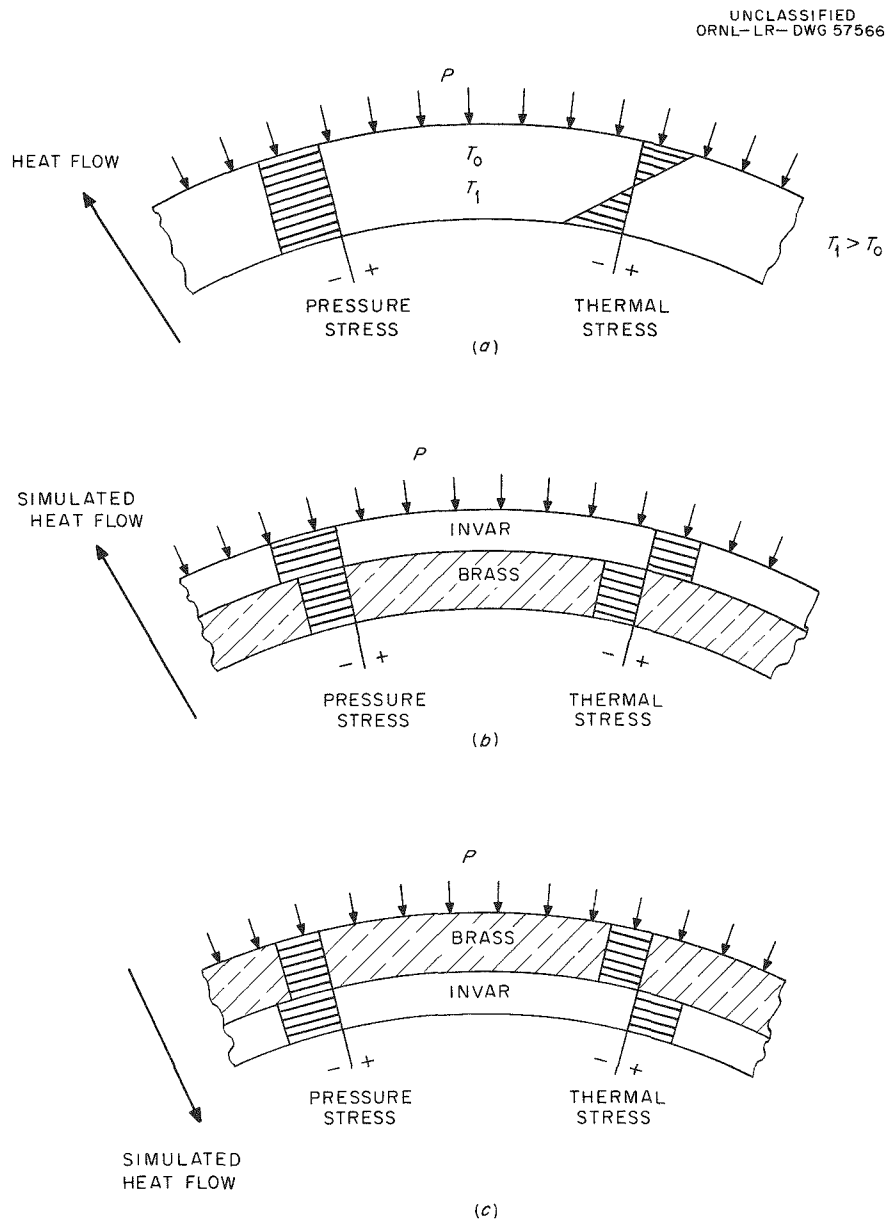

Fig. 2.20. Theoretical Stress Distributions in the EGCR Thermal Barrier and in Brass-Invar Hemispherical Shells.

It is difficult to evaluate the stresses in a thermostat metal because there are many unknown factors. In addition to stresses resulting from thermal changes and mechanical loading, internal stresses are induced from bonding, rolling, heat treating, and, in the case of the hemispherical shells, from forming the shell. Thus, only hypothetical thermal and mechanical stresses based on the elastic properties of the materials may be calculated. The theoretical compressive membrane stresses from external pressure in the brass-Invar shells are shown in Fig. 2.21 as a function of external pressure. The stresses and strains from temperature changes were calculated for a sheet restrained from lateral deflections. These are equivalent to the stresses and strains existing in regions of

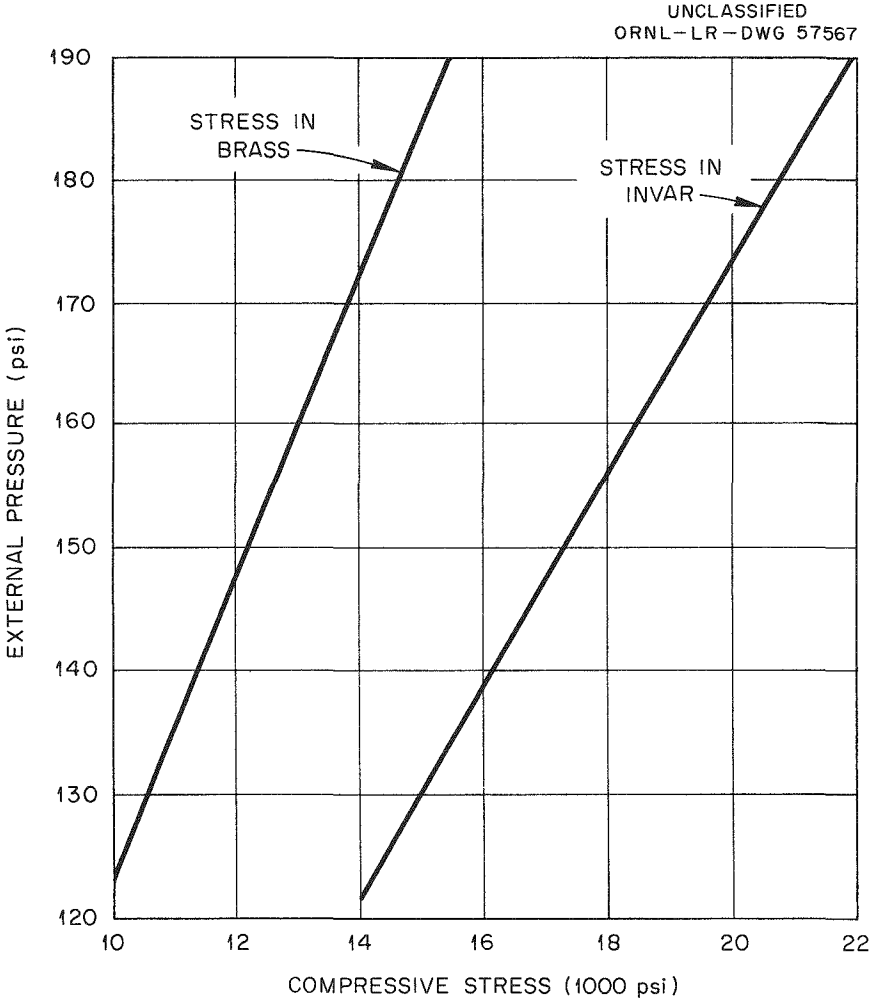

Fig. 2.21. Membrane Stresses in Brass-Invar Hemispherical Shells Versus External Pressure.

the shells away from the edges. The free thermal strain which would occur in the components if they were not bonded together, the total thermal strain of the composite metal, and the thermal stress in each component are shown in Fig. 2.22 as a function of temperature. It was assumed that the material was stress free at 75°F. It should be kept in mind that these are theoretical values applicable to an unworked, stress-free sheet.

By reference to Figs. 2.20 through 2.22, the results of the buckling tests, as shown in Fig. 2.19, can be interpreted. The thermal stresses

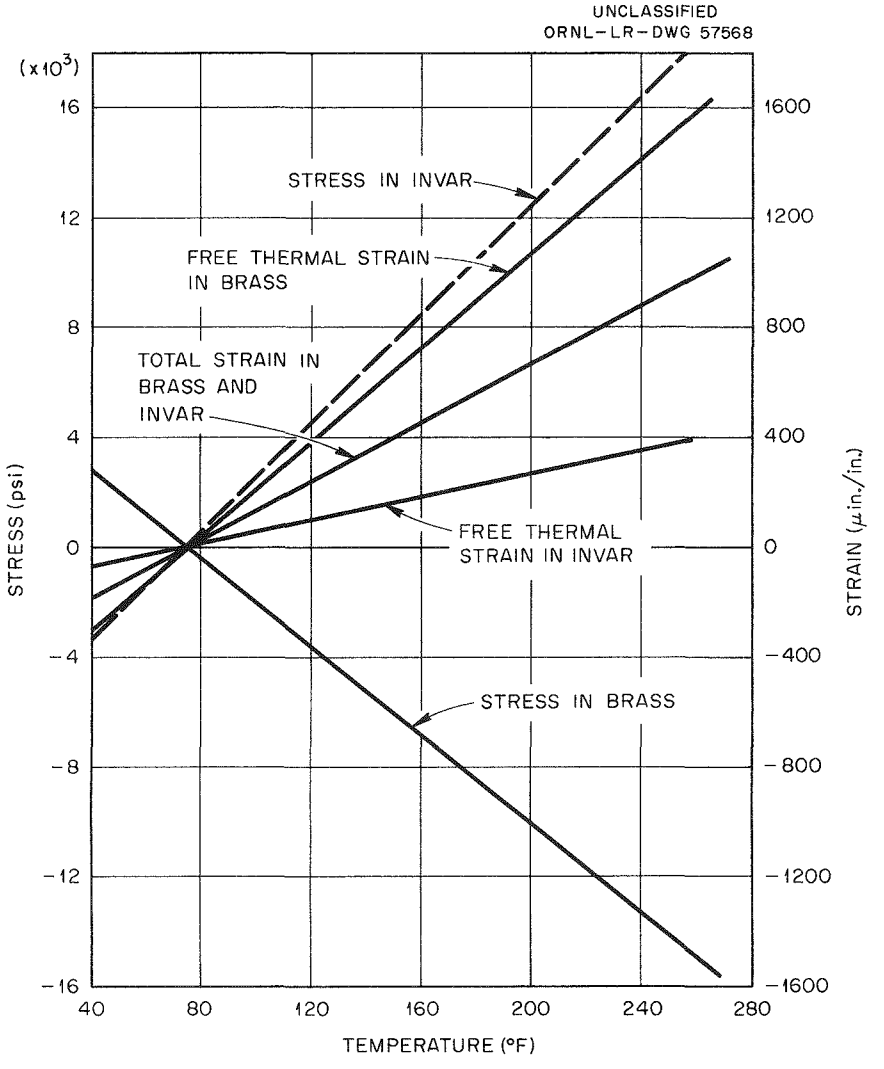

Fig. 2.22. Stresses and Strains Versus Temperature for Uniformily Restrained Brass-Invar Bimetallic Sheet (Thickness of Brass = 0.0121 in., Thickness of Invar = 0.0099 in.).

shown in Fig. 2.22 for the higher temperatures are of the same order of magnitude as the membrane pressure stresses shown in Fig. 2.21. Hence, the thermal changes have a very definite effect on the stress distribution. If these thermal changes affected the buckling pressure, the two curves in Fig. 2.19 should either converge or diverge with increasing temperature, and an opposite effect would be expected as the temperature was decreased below the stress-free temperature. However, these effects do not occur, and the downward trend of both curves as the temperature increases can be attributed to the normal reduction in strength of the materials.

The higher buckling pressures for the shells with Invar on the outside may be explained by considering only the strains induced by the external pressure loading. Since a local increase in radius is required for buckling to occur, the uniform compressive strains for the inner material are partially offset by tensile bending strains, while the strains are additive for the material of the outer portion. Also, Invar has a higher resistance to deformation than brass. Hence, the Invar was in a more effective position when it was located on the outer surface.

In conclusion, it may be stated that a change in temperature affected the buckling pressure of the bimetallic hemispherical shells only by the small amount attributable to the normal decrease in strength with increasing temperature. Thus, the thermal strains induced across the walls of the hemispherical shells neither increased nor decreased their resistance to instantaneous collapse under external pressure.

Irradiation-Induced Stresses in EGCR Graphite Columns (F. J. Stanek)

A study was made to determine the stresses that would occur in column 67 of the graphite core of the EGCR from irradiation shrinkage if this column had four fuel channels. The cross section of column 67 and its position in the core are shown in Fig. 2.23. The exposure distribution used was symmetrical about the line $y = x$ and is shown in Figs. 2.24a and 2.24b as a function of y for several constant values of the coordinate x. The unit of exposure, Mwd/AT, is proportional to the integrated fast (above 0.18 Mev) neutron flux. The fast-neutron flux was obtained by numerical calculations using two-dimensional diffusion theory for a core

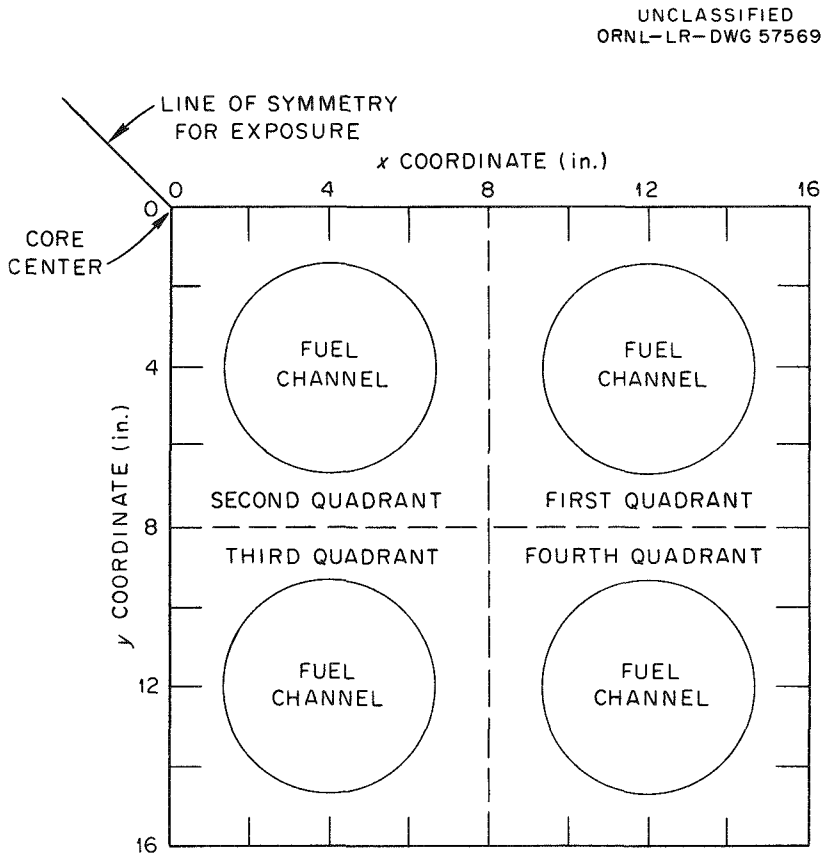

Fig. 2.23. Cross Section of Graphite Column 67 in EGCR Core.

without experimental loops and with fuel in all channels (see chap. 1, this report).

The exposure stresses were obtained by numerical calculations using plane thermoelasticity theory. A section near the mid-height of the column was examined for three specific problems: (1) the region was the entire 16- by 16-in. block, as shown in Fig. 2.23, (2) the region was an 8- by 8-in. block (one quadrant of the 16- by 16-in. block) subjected to the exposure of the fourth quadrant where the exposure distribution is symmetrical about the diagonal, and (3) the region was an 8- by 8-in. block subjected to the exposure of the third quadrant where the exposure distribution has no symmetry. The numerical calculations were made with a program which was written by the Battelle Memorial Institute under contract

for use on an IBM 7090 computing machine. The smallest size of the mesh was 8/15 by 8/15 in., requiring 602 equations (unknowns) for the 16- by 16-in. block, and 4/15 by 4/15 in. for each of the 8- by 8-in. blocks, requiring 563 and 1000 equations, respectively.

The graphite was assumed to be transversely isotropic; that is, the mechanical and physical properties of the material are independent of

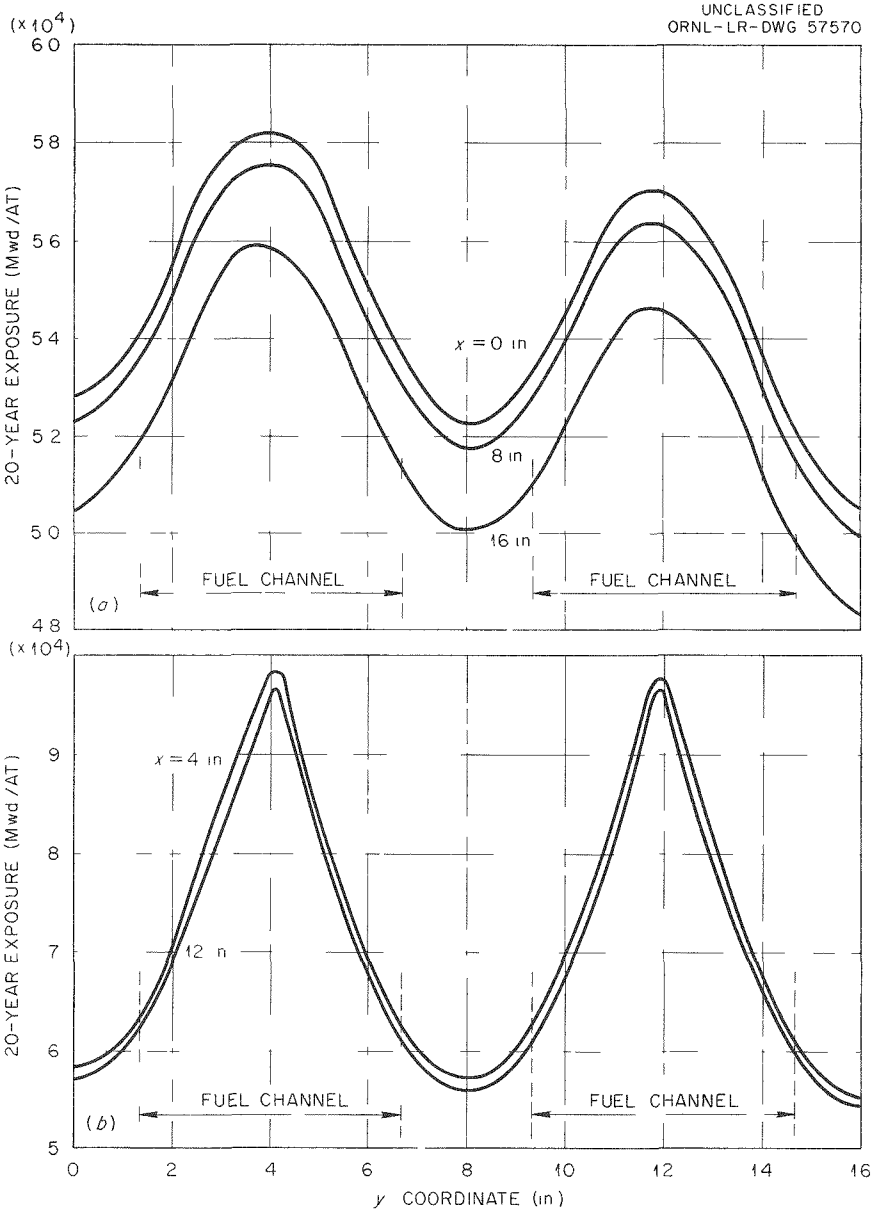

Fig. 2.24. Mid-Plane Exposure of Graphite Column 67 in EGCR Without Experimental Channels in Core.

direction in the x-y plane but they may differ from those in the axial, or z, direction. It can be shown by plane thermoelasticity theory that the coplanar stresses are proportional to a parameter D, which is defined as follows:

$$D = \frac{E_Z \alpha_Z (\alpha + \beta_3)}{\beta_1 - \beta_3^2} ,$$

where

E = Young's modulus of elasticity, psi,

α_Z = coefficient of exposure expansion in the axial direction, in./in. per Mwd/AT,

$\alpha = \alpha_X/\alpha_Z$ = ratio of the expansion coefficients (the subscript x denotes any direction in the x-y plane),

$\beta_1 = E_Z/E_X$ = ratio of the two moduli,

$\beta_3 = \delta_{ZX}$ = ratio of the unit strains, ϵ_X/ϵ_Z, when stressed in the x direction,

$\beta_2 = E_Z \delta_{XY}/E_X$ = β_1 multiplied by Poisson's ratio in the x-y plane (used in displacement relationships).

When the two normal coplanar stresses σ_X and σ_Y are known, the axial stress, σ_Z, is obtained from the following expression:

$$\sigma_Z = E_Z \alpha_Z \left[\left(\frac{\beta_3}{E_Z \alpha_Z} \right) (\sigma_X + \sigma_Y) - t + \left(\frac{\epsilon_Z}{\alpha_Z} \right) \right] ,$$

where t represents the exposure function and ϵ_Z is an arbitrary unit strain in the axial direction which may be superimposed onto the final results. The magnitude of ϵ_Z was determined so that the end force was zero, or, more precisely, the integral $\int \sigma_Z dA$ was zero when evaluated over the entire cross-sectional area of the material.

The following numerical values were used for the properties of the graphite:

$E_z = 1.5 \times 10^6$ psi,

$E_x = 1.11 \times 10^6$ psi,

$\alpha_z = -3.4 \times 10^{-7}$ in./in. per Mwd/AT per year (the negative sign denotes contraction or shrinkage),

$\alpha_x = -1.3 \times 10^{-7}$ in./in. per Mwd/AT per year,

$\delta_{zx} = 0.35$,

$\delta_{xy} = 0.50$.

Hence, $D = -304.3$ psi per 1000 Mwd/AT per year.

The accuracy of the values for the shrinkage coefficients is unknown, since they were obtained by extrapolation. Obviously the values of the stresses may be changed when more accurate values become known; however, this will not change the values of the stress ratios (given in tables which are discussed later) for the coplanar stresses (see Tables 2.3 and 2.4). A slight change may occur in the values of the ratios of the axial stresses to the coplanar stresses.

The significant stresses are presented in Tables 2.3 and 2.4 for a 20-year exposure period. Table 2.3 gives the four significant stresses (the two coplanar principal stresses and the maximum and the minimum axial stresses) for each of the three problems considered. The values of the x and y coordinates of the physical points at which the stresses occurred are also given. Each stress ratio was obtained by merely dividing the value of the stress in the 16- by 16-in. block by the value of the corresponding stress in the 8- by 8-in. block.

Table 2.4 gives the stresses in the third and fourth quadrants of the 16- by 16-in. block at each point that is significant for that quadrant. The value of each significant stress is indicated. The first three points of Table 2.4 are located in the third quadrant, while the last four points are located in the fourth quadrant. It should be noted that a point which is significant in an integral quadrant of the 16- by 16-in. block does not necessarily remain a significant point when the quadrant is considered as an individual 8- by 8-in. block. This may be verified by comparing the locations of the coordinates of the points listed in Table 2.4 with those in Table 2.3.

Table 2.3. Significant Exposure Stresses for Each Region for a 20-Year Period

	16- by 16-in. Block	8- by 8-in. Block	
		Exposed with Diagonal Symmetry	Exposed with No Symmetry
Maximum coplanar stress, psi	4308	1444	2691
Coordinates[a] of point of maximum coplanar stress, in.	0, 4.8	12.0, 14.67	2.13, 13.87
Stress ratio relative to 16- by 16-in. block		2.98[b]	1.6[b]
Minimum coplanar stress, psi	−6702	−796	−1645
Coordinates of point of minimum coplanar stress, in.	10.67, 14.4	12.27, 16.0	5.87, 10.13
Stress ratio relative to 16- by 16-in. block		8.42	4.07
Maximum axial stress, psi	4423	3729	3572
Coordinates of point of maximum axial stress, in.	2.13, 2.13	9.6, 10.93	6.13, 10.4
Stress ratio relative to 16- by 16-in. block		1.19	1.24
Minimum axial stress, psi	−3920	−3213	−2935
Coordinates of point of minimum axial stress, in.	16, 16	16, 16	7.73, 16.0
Stress ratio relative to 16- by 16-in. block		1.22	1.34

[a]The x and y coordinates given refer to the orientation and position of the axis shown in Fig. 2.23; hence, it must be noted that the stresses are for the individual 8- by 8-in. block rather than for an integral quadrant of the 16- by 16-in. block.

[b]The stress ratio multiplied by the stress will yield the corresponding stress in the 16- by 16-in. block.

Table 2.4. Exposure Stresses at the Significant[a] Points in the Third and the Fourth Quadrant of the 16- by 16-in. Block for a 20-yr Period

Coordinate		Maximum Coplanar Stress (psi)	Stress Ratio[b]	Maximum Coplanar Stress (psi)	Stress Ratio[b]	Axial Stress (psi)	Stress Ratio[b]
x (in.)	y (in.)						
5.87	10.13	[3994]	0.12	−335	4.9	[4321]	0.35
0	12.8	1	338	[−2864]	0	−446	−0.41
7.47	8.0	−863	−0.18	−1259	0.02	[−1599]	0.73
10.13	10.13	3372	0.33	−254	0.10	[3764]	0.57
10.67	16.0	[4273]	0	−12	34.4	308	−1.49
10.67	14.40	1557	0.517	[−6702]	−0.06	−97	−15.7
16.0	16.0	−228	−0.21	−247	0.24	[−3920]	0.82

[a]The important stress value at a point is indicated by brackets.

[b]The stress ratio is the value which multiplied by the adjacent stress will yield the value of the corresponding stress at the same point when the quadrant is considered as an individual 8- by 8-in. block.

The stress ratio given in Table 2.4 is defined differently than that given in Table 2.3. In this case, it is the value of the stress which was obtained at the point when the quadrant was considered as an individual 8- by 8-in. block divided by the value of the corresponding stress at the same point for the quadrant as an integral part of the 16- by 16-in. block. This was done in order to present the most pertinent information in a concise manner. There should be no confusion on this if it is noted that the product of the value of the ratio and the value of the stress shown is the stress with which it is compared. The physical significance of these ratios should also be noted; in Table 2.3 they are merely the ratio of the corresponding significant stresses for each of the regions considered, whereas in Table 2.4 they are the ratio of the corresponding stresses at a point which is subjected to the same exposure but surrounded by a different geometrical body.

For graphite in the EGCR temperature range the critical stress is the maximum (tensile) principal stress. These stresses are summarized in Table 2.5 for the two quadrants considered.

The data of Table 2.3 show that the maximum calculated tensile stress in the 16- by 16-in. section is at the surface of the fuel channel adjacent to the vertical centerline of the core and that its magnitude for a 20-year

Table 2.5. Comparison of the Maximum Principal Tensile Stresses in the Third and Fourth Quadrants

	Maximum Tensile Stress (psi)		
	When the Quadrant is an Integral Part of the 16- by 16-in. Block	When the Quadrant is an Individual 8- by 8-in. Block	Stress Ratio
Third quadrant	4321	3572	0.83
Fourth quadrant	4273[a]	3729	0.87

[a]This is a coplanar stress; all others are axial stresses.

exposure is 4423 psi. Therefore, if the fracture stress for the EGCR graphite is 1800 psi, cracking may occur in a column with the exposure distribution used in this analysis after 8.1 years. An increased crack-free period could be achieved by subdividing the column. The data in Table 2.5 show that the maximum tensile stress for a quadrant of the 16- by 16-in. column may be reduced by a factor of about 0.83 to 0.87 if the quadrant is made into an individual column. The stress reduction factor is dependent, however, on the damage distribution for each unit, and caution should be used in applying these results to all columns in the EGCR core.

Thermal Stresses in EGCR Graphite Columns (M. E. LaVerne, S. E. Moore)

During normal power operation the temperature distributions in the EGCR graphite are not expected to produce large thermal stresses.[19] However, during refueling operations at power, there will be a short time interval, on the order of minutes, when cold (510°F) helium will wash the graphite surface of a fuel channel. This gas is admitted at the time the charge machine is connected and the control of the gas flow is transferred from the bottom dummy assembly and seal to the charge machine.

[19]F. Cheng, Temperature Distributions, Moderator and Reflector for Reactor Core, Experimental Gas-Cooled Reactor, Allis-Chalmers Study II-226, Aug. 31, 1960.

The cold gas flowing through the channel being refueled causes increased temperature gradients in the graphite, and the thermal stresses associated with these gradients may be important.

In order to calculate these stresses, detailed temperature distributions in a graphite column must be calculated. These distributions depend upon the coolant gas flow rate and temperature and the nuclear heat deposition in the graphite. As a preliminary to determining temperature distributions in the graphite blocks, neutron and gamma heat depositions were determined for (1) all fuel channels filled and (2) one channel empty. The calculations were based on an infinite array of sources operating at average reactor power and centered in the fuel channels. Only one half of a column was completely analyzed, because diagonal symmetry exists even with one channel empty. The total heat deposition (neutron plus gamma) along selected axes in the graphite block is shown in Fig. 2.25. After the temperature distributions have been calculated, the Battelle machine code used in calculating the irradiation-induced stresses will be used to compute the stresses corresponding to these temperature distributions.

Helium Purification Studies

J. C. Suddath, C. D. Scott

Useful data were obtained in 20 additional tests of the oxidation of hydrogen in a flowing stream of helium at 300 psia by fixed beds of 1/8-in.-diam CuO pellets. The helium purification test facility described previously[20] was used for these tests. Two-inch thicknesses of 3-mm-diam pyrex-glass beads were placed above and below the CuO bed in the 2-in.-diam oxidizers to develop full gas turbulence prior to contact of the gas and the CuO.

Helium flow was metered and controlled by an instrumented orifice meter and the hydrogen flow was metered by a high-pressure rotameter.

---

[20]GCR Quar. Prog. Rep. March 30, 1960, ORNL-2929, pp. 54–56.

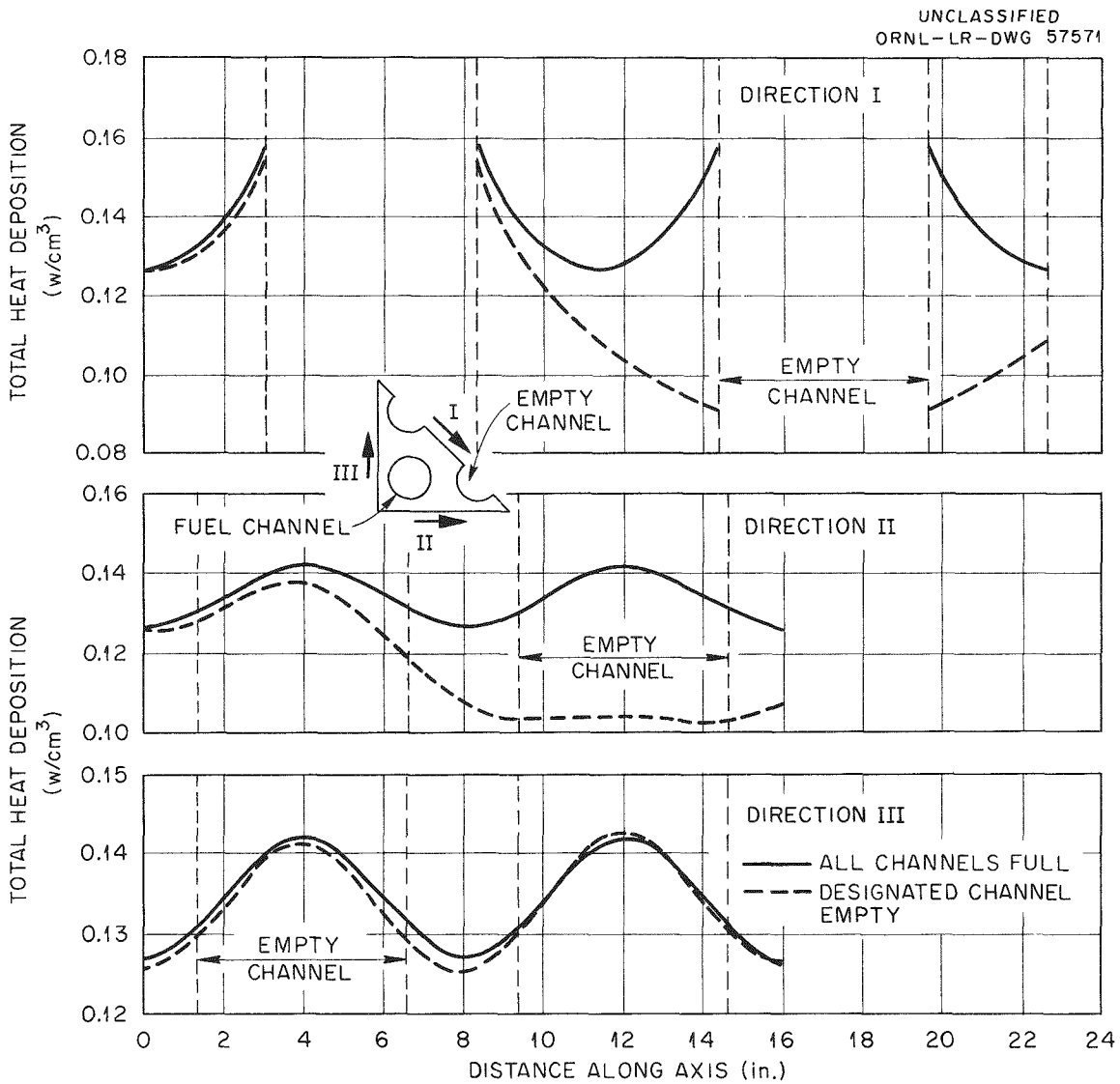

Fig. 2.25. Total Heat Deposition Curves for EGCR Graphite Columns.

The effluent gas stream was sampled automatically and periodically by a gas-adsorption chromatograph to determine the hydrogen content.

The CuO pellets, as received from the Harshaw Chemical Co., are nominally 1/8 in. in diameter and 1/8 in. thick. They contain 0.15 to 0.50% carbon; the specific surface area ranges from 1.8 to 3.5 m^2/g; and the tap density is approximately 1.8 g/cm^3. It was found that repeated use of the CuO by reduction to Cu and then regeneration to CuO by exposure to air resulted in a decrease in the pellet particle size, the specific

surface area, and the carbon content. These effects appeared to diminish after a few runs, and, after approximately 10 cycles, changes in the various physical properties were small. After 10 cycles, typical average dimensions of the pellets were 0.093 in. in diameter and 0.097 in. in thickness; the specific surface area was 0.77 m^2/g; the carbon content was 0.10%; and the tap density was 3.1 g/cm^3.

It was found that these physical properties could be closely approached if the original CuO pellets were sintered in air at 1000°C for 12 to 16 hr prior to use. The sintered CuO typically had dimensions of 0.095 in. in diameter and 0.096 in. in thickness; the specific surface area was 0.68 m^2/g; the carbon content was 0.15%; and the tap density was 3.1 g/cm^3. Thus the sintered material was used for kinetic tests so that the experimental results would be similar to those to be expected from CuO which had been through several cycles of use.

Each run was made by first activating the CuO bed by a 1-min exposure to helium containing 5% H_2 at 300 psia. Then a preheated He-H_2 gas mixture was sent through the CuO bed at a constant rate, and the H_2 concentration of the effluent stream was measured every 6 to 10 min by a gas-adsorption chromatograph. This procedure resulted in an effluent hydrogen-concentration history for each run which can be used to determine the reaction-controlling mechanism and to develop reactor design equations.

The 20 experimental tests completed a series in which three initial hydrogen concentrations (~1.0, ~0.5, and ~0.1%), three helium flow rates (~36.3, 72.2, and 109 slpm), and three CuO bed temperatures (~400, ~500, and ~600°C) at 300 psia were investigated. The data obtained in these tests are summarized in Table 2.6. A limited amount of experimental data will be obtained at two other operating pressures, 150 and 450 psia, in order to determine the effects of pressures on the rate of reaction, and an attempt will be made to fit the data to a gas-phase diffusion control model, a solid-phase diffusion model, and a combination of both models.

Table 2.6. Operating Conditions for Kinetic Tests of Oxidation of Hydrogen in a Flowing Stream of Helium at 300 psia by a Fixed Bed of 1/8-in.-diam CuO Pellets

Run No.	Average CuO Bed Temperature (°C)	Helium Flow Rate (slpm)	Initial H_2 Concentration (vol %)	CuO Bed Depth in 2-in.-diam Oxidizer (in.)
3	480	36.3	0.93	2.0
4	465	36.3	0.98	1.0
5	480	72.2	1.18	2.0
6	500	109.0	1.09	2.0
7	400	36.3	1.01	1.0
8	400	72.2	1.14	2.0
9	410	109.0	0.97	2.0
10	500	36.3	0.80	1.0
11	500	109.0	0.105	0.5
12	500	109.0	0.097	1.0
13	600	36.3	0.99	1.0
14	500	36.3	0.132	1.0
15	400	36.3	0.49	1.0
16	500	36.3	0.51	1.0
17	600	36.3	0.52	1.0
18	500	36.3	0.142	0.5
19	500	72.2	0.47	1.0
20	400	109.0	0.67	1.0
21	500	109.0	0.59	1.0
22	500	72.2	0.49	1.0

EGCR Hazards Evaluation

W. B. Cottrell

Containment System for EGCR (H. N. Culver)

The design of a containment system for a reactor is strongly influenced by the transient behavior of the reactor following the maximum credible accident (mca). Of particular importance is the ability of the fuel to retain fission products during the period following the mca, since this determines the required integrity of the other physical barriers and mechanical devices that may be provided to alleviate the consequences of the accident.

The containment of activity in the EGCR is accomplished through a system of multiple barriers, or devices, each having the ability to either retain or delay the escape of fission products. At the time of the mca, the only effective barriers for reducing activity escape are the fuel material and the containment building. During normal operation, the primary system and the cladding on the fuel elements also act as effective barriers for retaining activity. The requirements of the overall containment system may be established from basic design information such as power level, site location, fuel lifetime, meteorological conditions at the site, and the rules and regulations governing the allowable exposure to the general public for emergency conditions. However, the requirements of a given part of the containment system may be varied to reflect the degree of confinement achieved by other parts of the system.

The exposure dose downwind from the EGCR has been investigated for a number of cases which represent various methods of operating the containment system. In evaluating these various proposed methods of operation, three factors have been investigated: (1) the rate of release of the activity, (2) the importance of deposition of iodine, and (3) the importance of removing iodine and solids by recirculating the gases inside the containment building. For all the cases investigated, it has been assumed that the meteorological conditions during the period of interest are represented by inversion conditions.

The effects of the three factors listed above have been examined for each of the following three periods of activity release:

Case 1 – activity release during the period of depressurization of the primary system,

Case 2 – activity release following the period of depressurization of the primary system but prior to sealing of the containment building,

Case 3 – activity release from the sealed containment building.

Activity Release from the Fuel. In all three cases, it was assumed that 100% of the fuel elements in the reactor core would fail during the period of primary system depressurization. A fuel element failure was defined as the loss of the integrity of the cladding on the fuel.

Therefore for case 1, the activity that had diffused from the fuel during normal operation would escape instantly, and, for cases 2 and 3, additional activity would escape as the fuel oxidized. The escape rate for cases 2 and 3 was varied over a wide range to illustrate the extreme importance of this factor. The maximum amount of release due to oxidation was determined experimentally to be 100% of the noble gases, 30% of the iodine, and 1% of the solids, such as strontium.

Activity Removal in Containment Building. For cases 1 and 2, the escape of activity from the building by leakage would be so rapid that removal of activity inside the building by deposition or cleanup was neglected. In discharging activity from the stack (case 2), however, it was assumed that the filter would be effective in removing 99% of the iodine and solid fission products. For case 3, the activity was assumed to be removed by leakage, deposition, and purification. Calculations have been made with and without deposition to illustrate the importance of deposition. Only iodine was assumed to deposit, and only iodine and the solids were assumed to be removed by the cleanup system.

Activity Release from Building. In case 1, it was assumed that the activity escaped from the open penetrations in the containment building. For case 2, it was assumed that all activity was discharged at the height of the stack. For case 3, it was assumed that all activity was released at ground level. All cases of ground level release were modified to reflect the dilution of activity by air turbulence at or adjacent to the building.

The exposure doses for these three cases and as a function of the indicated factors are presented in Figs. 2.26 through 2.31. Figure 2.26 shows the exposure dose to the bone and thyroid for the activity released during the period of depressurization of the primary system (case 1). The submersion exposure dose is not shown, since it is small by comparison with the bone and thyroid exposure doses. In arriving at the exposure levels for case 1, it was assumed that 50% of the activity released from the fuel escaped from the containment building. It was further assumed that the activity would be discharged from all openings at the same rate. The fraction of the activity released through the stack (exhaust lines in

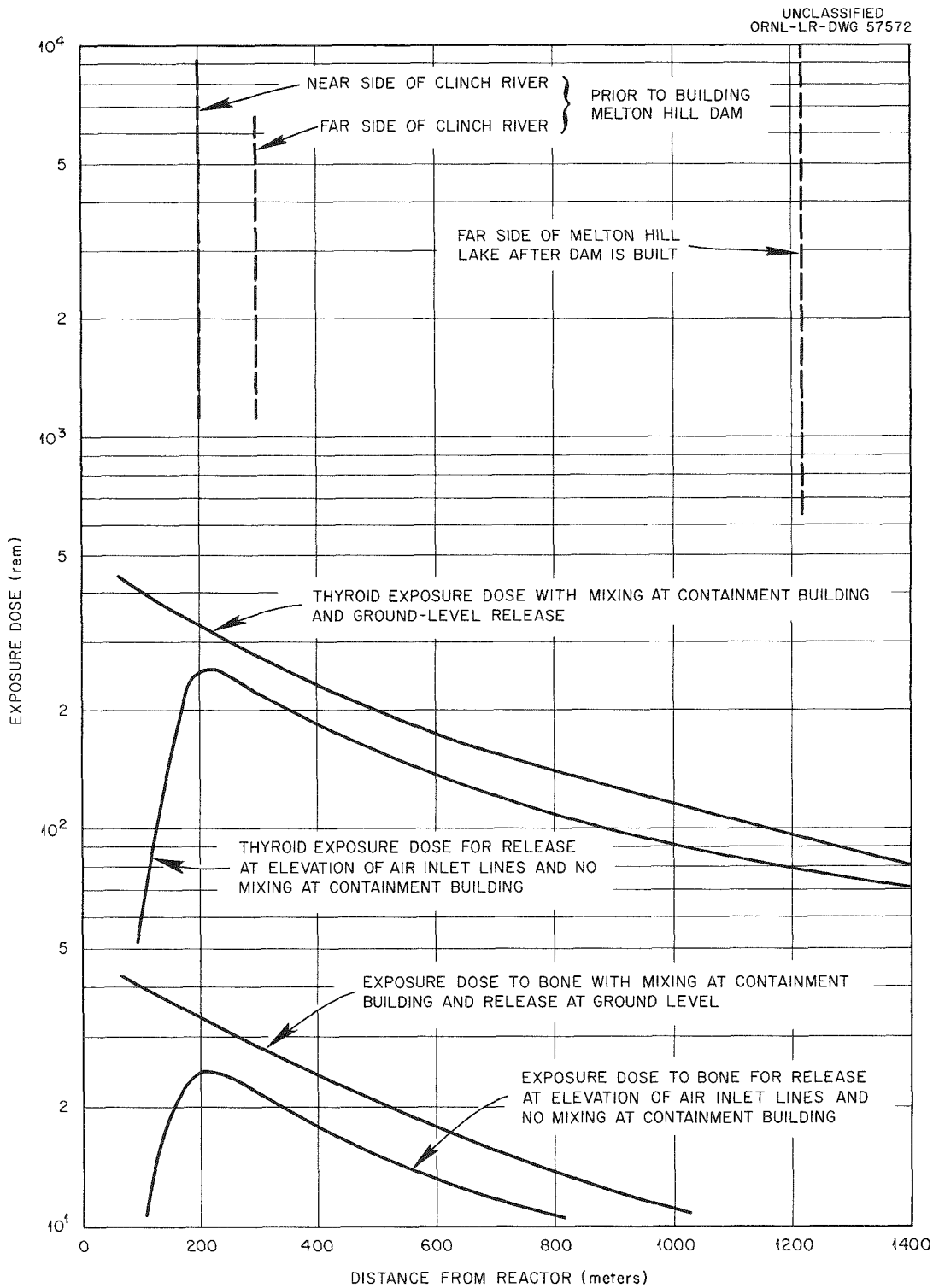

Fig. 2.26. Exposure Dose Downwind from Activity Released During Period of Depressurization of EGCR Following Maximum Credible Accident; Atmospheric Inversion Conditions Assumed.

the ventilation system) was neglected, since the exposure resulting from the elevated release would be small compared with the release at or near ground level. In Fig. 2.26, the exposure dose to the bone and thyroid is shown for release with and without mixing adjacent to the building. With no mixing the activity is discharged at the elevation of the air-ventilation inlet lines. If in this case it were assumed that the activity was discharged at ground level, the exposures would be considerably

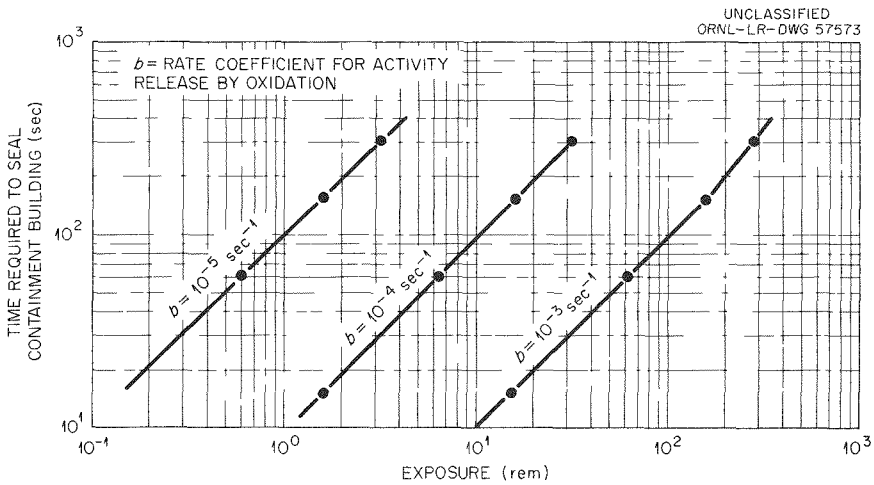

Fig. 2.27. Inhalation Exposure to the Thyroid at 4000 ft from Reactor for Activity Released Following Depressurization of Primary System But Prior to Sealing Containment Building.

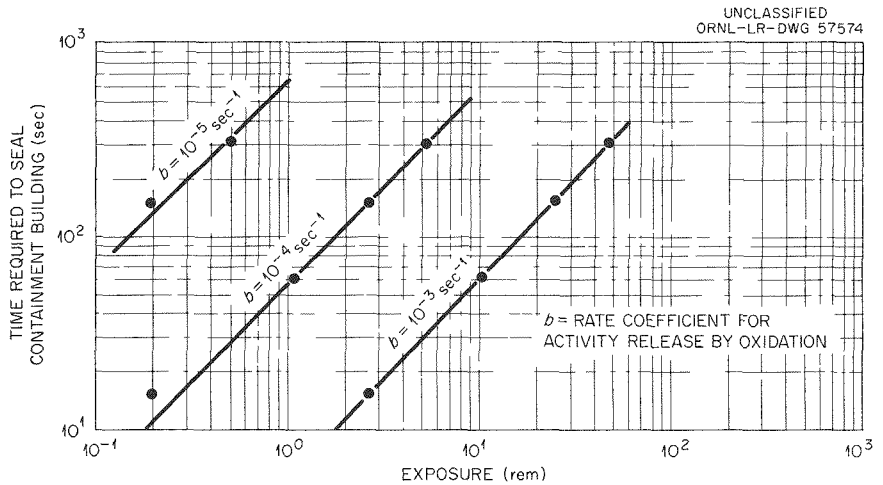

Fig. 2.28. Inhalation Exposure to the Bone at 4000 ft from Reactor for Activity Released Following Depressurization of the Primary System But Prior to Sealing the Containment Building.

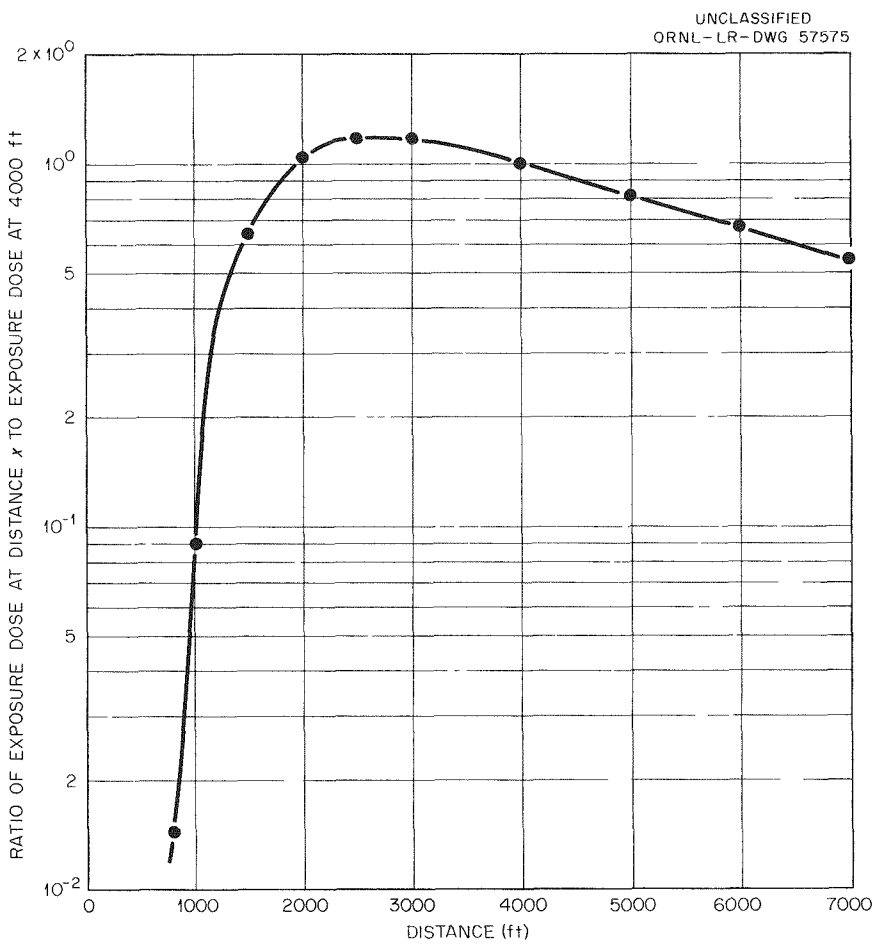

Fig. 2.29. Exposure Dose as a Function of Dose at 4000 ft.

higher. With mixing it was assumed that the activity might be discharged at any elevation of the containment vessel.

The exposure values given in Fig. 2.26 represent extreme upper limits. If the depressurization of the primary system is rapid (5 to 10 sec), the discharge of activity from the openings in the containment building will be rapid. By diverting the activity release upward, the release would not be at ground level, and the exposure would be decreased by several orders of magnitude. If, on the other hand, the depressurization of the primary system was relatively slow, the number of fuel element failures would be decreased, and it would be possible to control the release from the openings in the containment building at or near ground level.

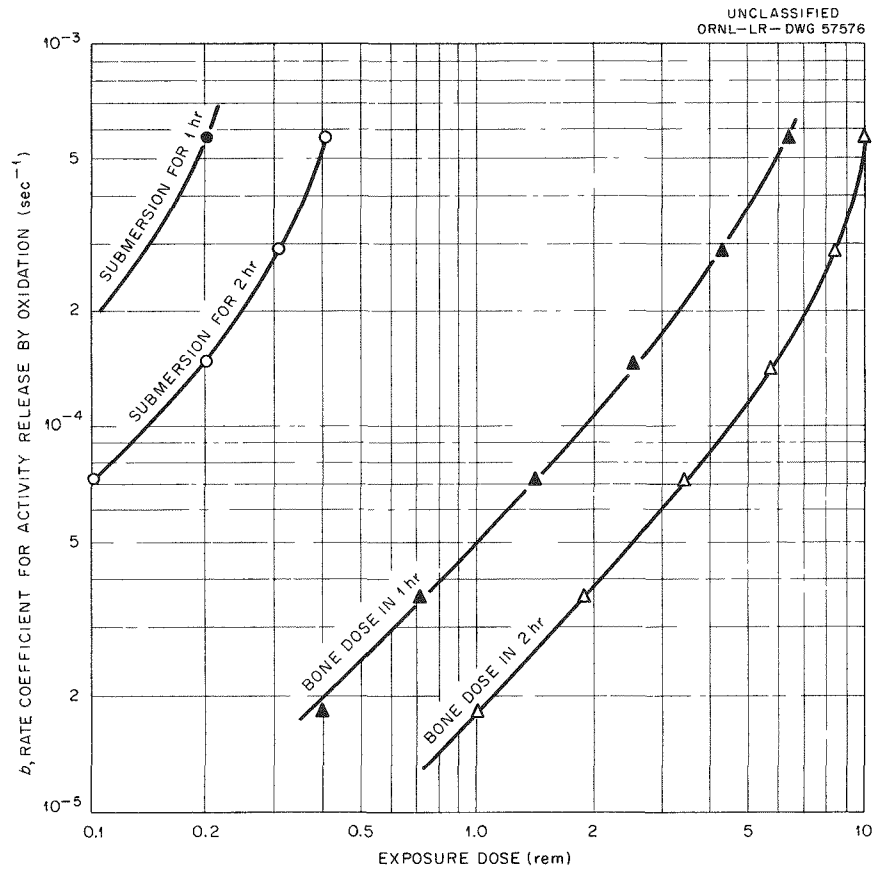

Fig. 2.30. Exposure Dose at 4000 ft from Reactor for Activity Released Following Sealing of the Containment Building.

Figures 2.27 and 2.28 show the exposure dose to the thyroid and bone from activity released following depressurization of the primary system but prior to sealing of the containment building (case 2). The exposure dose is given as a function of the rate of release of activity from the fuel and as a function of the time required to seal the containment building. As may be seen, if the release of activity from the fuel is slow, there is no need to immediately seal the containment building in order to limit the exposure to the bone and thyroid to acceptable levels. The values shown are the doses at a distance of 4000 ft from the reactor. The exposure doses at other distances may be obtained from the curve of Fig. 2.29.

Figures 2.30 and 2.31 give the exposure dose to the thyroid and bone, as well as the submersion exposure dose to the total body, for activity

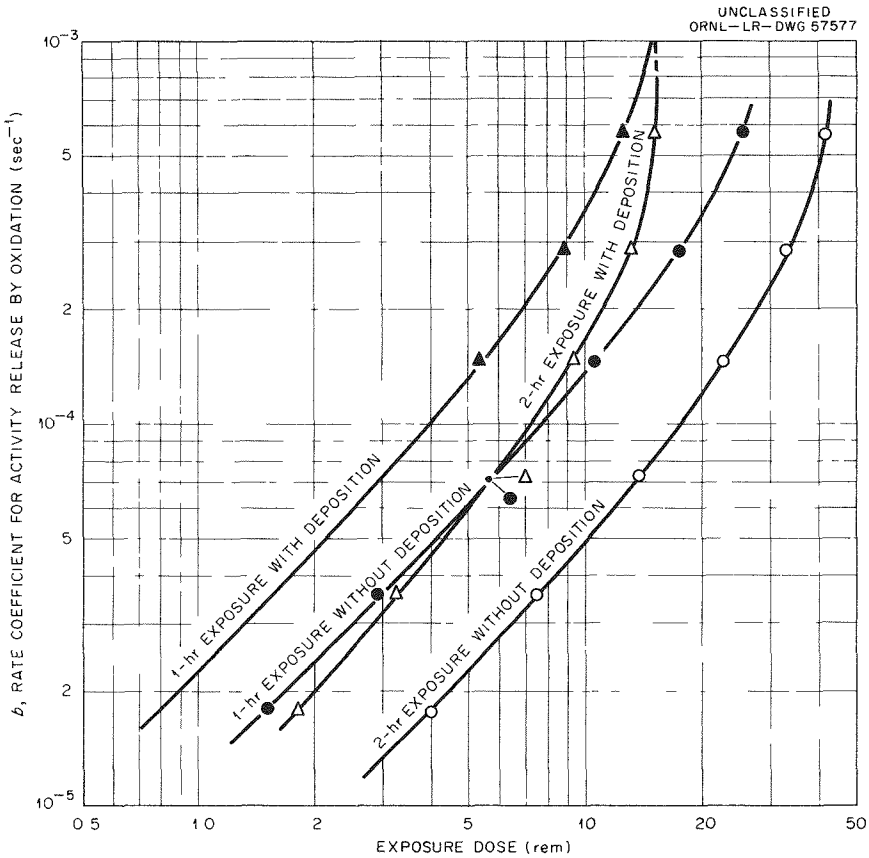

Fig. 2.31. Exposure Dose to Thyroid at 4000 ft from Reactor for Activity Released Following Sealing of the Containment Building.

released following the sealing of the containment building (case 3). These exposure values are shown for 1- and 2-hr exposure periods. The values shown are for a distance of 4000 ft from the reactor and are based on the assumption that there would be dilution of the activity adjacent to the containment building. Exposure values at other distances and for the case of no dilution at the containment building may be obtained by comparison with the values given in Fig. 2.26. Figure 2.31 shows the importance of deposition in reducing the exposure dose to the thyroid.

The data presented in Figs. 2.26 through 2.31 indicate that there are several important factors which must be considered in determining how the containment system should be operated. During the period of depressurization of the primary system, there are two factors of importance in determining the exposure at a given location: (1) the depressurization

rate of the primary system and (2) the dilution of activity at or near the containment building due to turbulence. At distances greater than 200 meters, the dilution factor is not of great significance. On the other hand, the rate of depressurization will have a large influence on the exposure dose at distances between 200 and 1200 meters. If the depressurization rate is rapid, the gases escaping from the containment building will exit at a high velocity. It is therefore possible to design the air inlet lines so that, when gases were exhausted, they would be discharged into a jet extending in the vertical direction. The resultant jet would be more than adequate to reduce the exposure levels at the distances of importance. If the depressurization of the primary system is slow, two factors assume great importance. First, the activity release from the primary system would be reduced or eliminated during the initial phases of depressurization. During the final stages of depressurization, the valves in the air inlet lines could be closed to prevent the escape of activity at ground level.

Following the period of depressurization of the primary system, but prior to the sealing of the containment building, there are two major factors in determining the exposure levels at a given distance. The exposure will be approximately proportional to the time required to seal the building, but it will depend mainly on the rate of release of activity from the fuel. The release rate will be closely related to the type of failure in the primary system, since the size and location of the failure in the primary system will influence the oxidation of the fuel. Experimental information on the oxidation rate of a failed fuel element, assuming sufficient oxygen is available at the surface of the fuel element cladding to cause oxidation, indicates that the release rate coefficient will be of the order of $b = 10^{-5}$ to 10^{-6} sec^{-1}. With a release rate of this magnitude, there does not appear to be any undue hazard in allowing the containment building to be vented for times of up to 5 min.

During the period following the sealing of the containment building, three factors influence the exposure levels at a particular location: (1) the rate of release of activity from the fuel, (2) the recirculating gas purification rate, and (3) the activity deposition rate. None of

these factors is as important, however, as the time required to seal the containment building. If the containment building is sealed after the pressure inside the building is released, the subsequent exposure dose at a particular location as a result of leakage will be insignificant. If, however, the building is sealed rapidly and contains the pressure, all the factors cited become important. However, as in the other cases with a release rate coefficient of about 10^{-5} to 10^{-6} sec^{-1}, the exposure levels are not excessive.

These preliminary studies therefore indicate that the containment system may be operated by sealing the building rapidly or by venting the building for a period of several minutes. Operation by venting for several minutes offers two main advantages: (1) it would place the containment system in a less hazardous condition, since there would be no appreciable pressure to be contained, and (2) it would allow a short but significant time period for evacuation of plant personnel from the containment building before the activity was contained and spread throughout the building.

Graphite Oxidation (M. Fontana)

A computer calculation of graphite oxidation in the EGCR following the mca was performed by Allis-Chalmers on the Bendix G-15, using the rate equation presented by Prados.[21] The results showed that a runaway graphite fire would not occur in the EGCR if one blower remained operative and a 95% effective coating was maintained on the sleeves. It was reported that the coating would have to remain effective for more than 42 min, after which the temperatures would continue to decrease if blower operation was maintained. The effect of oxidation of the uncoated ends of the sleeves, which could cause increased leakage of air from the main channel to the annulus, was not considered, although such oxidation could lead to quite different results. Additional computer calculations of the graphite oxidation problem are being undertaken on the IBM 7090 by ORNL. The required program is currently undergoing debugging.

[21]J. W. Prados, Estimation of Reaction and Heat Release Rates for Graphite Oxidation, ORNL CF-60-10-31, Oct. 19, 1960.

Two tests have been run at Hanford in the experimental phase of this investigation. In one test in the burning rig, a steel pipe was inserted to simulate a nonreactive coated graphite sleeve. Although the only form of heat removal was the air flow in the annulus adjacent to the simulated moderator graphite, runaway combustion did not occur until the initial temperatures approached 600°C. The rig blowers were then modified to provide sufficient flow so that full-size graphite sleeves could be tested at the expected conditions in the EGCR. The fuel elements were simulated by seven 3/4-in.-diam rods in the center of the sleeves to give approximately equivalent EGCR gas velocities in the channel. Available sleeves, although poorly coated, were used, since it was reasoned that, if runaway combustion did not occur with these, it would not occur for sleeves with coatings of good quality. Preliminary runs showed that runaway combustion did not occur with initial graphite temperatures less than 665°C, but it did occur with initial temperatures in excess of 675°C. Extensive damage to the sleeves was found at the conclusion of the tests, but the bulk of the damage was thought to have occurred during two extremely high-temperature runs. Considerable damage was evident in areas near the ends of the sleeves, which were uncoated. Completely coated sleeves of good quality are being manufactured and will be sent to Hanford for testing in the burning rig. It is expected that the coatings will be effective in preventing oxidation.

From the information available at this time, it appears that blower operation must be maintained for long periods after the loss-of-pressure accident and that subsequent failure of the blowers because of an independent accident is a possibility that must be considered. The present philosophy is that only one coolant loop must be available after the loss-of-pressure accident. Calculations on the effectiveness of natural convection of air at atmospheric pressure under these conditions, allowing the outlet temperature to reach 2000°F and the inlet temperature 150°F, show that the heat removal is insufficient to remove the afterheat until 70 days after shutdown. At natural-convection flow rates, the heat released by oxidation of the graphite is negligible if the sleeve coatings remain effective. A rough, transient calculation based on the inlet

air temperature being maintained at 200°F (a requirement which implies that the steam generators are effective at natural-convection flow rates) and the air outlet temperature being that of the core average temperature shows that the air outlet (and core) temperature reaches a peak of 2500°F at 19 days after shutdown.

Clearly, with the present design, natural convection alone is insufficient to remove the decay heat after the loss-of-pressure accident. The alternatives include (1) modification of the design to attain adequate natural convection, (2) a guarantee of blower and steam generator operation for the order of months after shutdown without maintenance inside the containment vessel, or (3) an independent heat sink. The rate of temperature rise in the reactor is slow enough so that time is available to restore power if the loss is caused by an electrical failure external to the containment vessel. However, the situation can be serious if the failure is in the blower, blower bearings, or associated equipment; if the failure is in the feedwater supply; or if the steam generator gas-side flow characteristics are such that it is ineffective at low flow rates.

Any alternative heat removal system must meet the following requirements: (1) It must be reliable in that it can be expected to operate at any time within the lifetime of the reactor. The system must therefore be extremely simple or it must be possible to test it at regular intervals without disrupting the operation of the reactor. (2) It must be reliable in that it must not operate inadvertently during the lifetime of the reactor if such inadvertent operation would result in damage to the reactor system or result in an inordinate nuisance to the everyday operation of the plant. (3) It should be as independent as possible of the operating systems in the reactor.

These criteria can be met by a backup emergency heat dump consisting of water tubes installed underneath the insulation external to the reactor pressure vessel. These tubes would normally be dry but would be supplied with ordinary plant water in the event of a loss-of-power accident subsequent to the loss-of-pressure accident. Heat would be removed by conduction through the core and by combined conductive and radiative heat

transfer to and through the pressure vessel wall to the water flowing in the tubes. Preliminary calculations for 1 1/4-in. tubes on 3 1/4-in. spacing on the cylindrical surface of the pressure vessel show that at 0.5% afterheat, that is, 53 hr after shutdown according to the Way-Wigner formula, the core edge temperature would be approximately 1560°F, and, at steady state, the core center temperatures would be between 2500 and 2800°F. The rough, transient calculation referred to previously, which considered natural-convection heat removal concurrent with decay heat input, showed that the average core temperature would be approximately 1500°F at 53 hr after shutdown. Calculations will be made on concurrent heat removal by natural convection and the water tubes to determine the expected peak central core temperature.

The Way-Wigner decay heat equation was used for all these calculations, except the Allis-Chalmer's computer study, for which the Untermeyer decay curves were used. Studies presently under way at ORNL may show that the actual decay heat will be somewhat in excess (~30%) of that given by the Way-Wigner equation for short times after shutdown and somewhat less than that given by the Way-Wigner equation for long times after shutdown. It is not expected, however, that the heat generation rates will be as high as those predicted by Untermeyer.

Decontamination of EGCR Components

A. B. Meservey

Experimental work was continued in an effort to improve the stability of oxalate-peroxide mixtures and to decrease corrosion, and the decontamination effectiveness of a mixture prepared from an improved formula was tested on metal coupons in a modified household dishwasher to simulate liquid spraying in the charge and service machines.

Stability studies showed that oxalate-peroxide mixtures should not be allowed to contact brass or copper because of rapid corrosion and peroxide decomposition. Instability under other conditions is proportional to the area of metal surface contacted, the concentration of dissolved iron, and the amount of suspended matter, such as rust, as is well known

in hydrogen peroxide technology. Pyrophosphate, 8-hydroxy quinoline, and Na_2EDTA showed little promise as peroxide stabilizers in the presence of 100 ppm of dissolved iron.

The biggest improvement in stability resulted from lowering the peroxide concentration. For example, the useful life at 95°C of 0.3 M $(NH_4)_2C_2O_4$ with 1.0 M H_2O_2 and 100 ppm Fe^{+++}, with the pH initially 4.5 and allowed to rise, was about 1.5 hr. With 0.3 M H_2O_2, the life was 3.5 hr, and, with 0.15 M H_2O_2, the life was 5 hr. Peroxide is also more stable at about pH 4, and formula development is currently proceeding at pH 4 instead of the formerly recommended pH 5.

A third improvement in peroxide stability resulted from the addition of citrate to the oxalate-peroxide mixture. The beneficial effect probably comes both from iron complexing and greater buffering action or resistance to an increase in pH. For example, when 0.1 M ammonium citrate was added to 800 ml of 0.30 M $(NH_4)_2C_2O_4$–0.07 M $H_2C_2O_4$–0.34 M H_2O_2–100 ppm Fe^{+++} at pH 4.0 and a temperature of 95°C in the presence of 36 $in.^2$ of mild steel, and the pH was again lowered to 4.0, the useful life without pH adjustment was raised from 2.5 to 6 hr. Increasing the citrate to 0.22 M by adding 0.1 M citrate and then lowering the pH to 4.0 with citric instead of oxalic acid decreased the useful life again to 2.5 hr, showing that much yet remains to be learned about optimum formulation.

Oxalic acid corrosion inhibitors, such as Rodine 115 and 130, phenylthiourea, and 2-mercaptobenzothiazole, failed to inhibit the corrosion of mild steel in the presence of hydrogen peroxide. Sumco SP-2 (0.1%) reduced corrosion by depositing an oily film on the metal but at the same time decreased decontamination by a factor of 1000. The hydrogen peroxide itself, which had already been shown to inhibit stainless steel attach by oxalic, sulfuric, and hydrofluoric acids, proved to be the best corrosion inhibitor for carbon steel in oxalate-peroxide mixtures at pH 4.0. Comparative figures in mils/hr at pH 4.0 and 95°C in 0.3 M $(NH_4)_2C_2O_4$ with and without 0.3 M H_2O_2 were: type A-109 carbon steel, 0.13 vs 0.015; type 1020 carbon steel, 0.24 vs 0.016; annealed type 440C stainless steel, 1.00 vs 0.001; type 440C stainless steel ball bearings, 0.32 vs 0.001; high-carbon ball bearings, 1.6 (at pH 5.1) vs 0.010 (at 4.0); type 304 stainless steel,

0.015 vs 0.001; and Inconel <0.001 vs <0.001. Aluminum corrodes at 0.12 to 0.24 mils/hr in oxalate-peroxide solutions. Preliminary data show some decrease in corrosion rates on steel when citrate-oxalate-peroxide mixtures are used. When 0.2 M fluoride was included in the oxalate-peroxide formula, corrosion on carbon steel was 136 mils/hr, and peroxide decomposition occurred in only a few minutes because of the greatly increased iron content in the solution.

The liquid spraying of decontamination solutions in the charge and service machines was simulated by the use of a modified household dishwasher. Fifty-four coupons of carbon steel, type 347 stainless steel, and aluminum were contaminated with pure fission products and with mixed fission

Table 2.7. Decontamination by Exposure in Dishwasher to Simulate Solution Spraying in EGCR Service Machine

Isotope	Average β–γ Activity (mr/hr)	Metal Coupon	Decontamination Factor	
			Top Location	Bottom Location
Ru^{106}	36	Carbon steel	730	1.7×10^4
		Type 347 stainless steel	32	420
		Aluminum	1.8×10^4	1.1×10^4
Zr^{95}–Nb^{95}	72	Carbon steel	2.5×10^4	2.3×10^5
		Type 347 stainless steel	1.9×10^4	3.3×10^3
		Aluminum	2.7×10^4	130
Sr^{90}	460	Carbon steel	3.9×10^5	9.0×10^4
		Type 347 stainless steel	3.7×10^4	1.1×10^5
		Aluminum	5.3×10^4	1.9×10^5
Cs^{137}	31	Carbon steel	1.2×10^5	4.9×10^3
		Type 347 stainless steel	8.6×10^3	120
		Aluminum	3.7×10^4	6.5×10^3
Y^{91}	60	Carbon steel	3.3×10^3	2.0×10^4
		Type 347 stainless steel	2.8×10^3	7.5×10^3
		Aluminum	2.4×10^3	3.2×10^4
Ce^{144}	1030	Carbon steel	8.5×10^5	2.5×10^5
		Type 347 stainless steel	1.7×10^5	9.6×10^4
		Aluminum	2.4×10^4	1.8×10^5
Mixed fission products	93	Carbon steel	6.6×10^4	1.8×10^4
		Type 347 stainless steel	5.9×10^3	2.3×10^3
		Aluminum	7.1×10^4	1.7×10^5
I^{131a}	185	Carbon steel	520	980
		Type 347 stainless steel	2.0×10^3	5.1×10^3
		Aluminum	1.6×10^4	1.6×10^4
Ba^{140}–La^{140a}	1600	Carbon steel	8.8×10^4	2.1×10^4
		Type 347 stainless steel	2.9×10^4	1.5×10^4
		Aluminum	2.7×10^5	2.1×10^5

[a]Formula contained 0.1 M citrate.

products by a drying and baking technique, washed with hot water, gamma-counted, and then exposed for 90 min in the washer at 75 to 95°C with 0.3 M $(NH_4)_2C_2O_4$ + 0.36 to 0.28 M H_2O_2 at pH 4.1 to 4.4. Decontamination was very satisfactory, as shown in Table 2.7. A literature review on equipment decontamination was completed and published.[22]

---

[22]A. B. Meservey, Procedures and Practices for the Decontamination of Plant and Equipment, ORNL CF-60-12-71, Jan. 16, 1961.

3. EXPERIMENTAL INVESTIGATIONS OF HEAT TRANSFER AND FLUID FLOW

H. W. Hoffman

Resistance-Heated-Tube Heat Transfer Experiment

W. J. Stelzman

The previously discussed data of the series 4B experiment,[1,2] in which a seven-tube cluster at a 2:1 ligament-ratio spacing with a 60-deg-pad mid-cluster spacer[3] and a pair of nonmetallic screens at the channel inlet[2] was studied, indicated, as in the series 2 studies,[4] the existence of asymmetry in the flow within the channel. Experiments to date involving altered plenum and channel-inlet screen arrangements have suggested that the source of the skewed flow was in the geometry of the upper plenum or in the geometry of the transition piece joining the gas supply to the plenum. The investigation of this situation in the model 3 apparatus[5] has been concluded with a study made with the inlet screens completely removed. Other conditions were maintained as in the series 4B experiment; that is, N_{Re} = 50 500 and an over-all mean heat flux for the peripheral tubes of 6500 Btu/hr·ft^2. An error, arising from the voltmeter used in controlling the central tube, resulted in approximately 3% lower heat generation for the central tube than for the peripheral tubes in this study (designated series 4C). The data have been adjusted to a common inlet air temperature of 99°F.

The axial variation of the mean inside surface temperature of each of the seven tubes of the series 4C experimental cluster is presented in Table 3.1. It may be seen that tubes 4 through 6 have somewhat higher mean surface temperatures than tubes 1 through 3; this observation is in conformity with the cooling patterns found in previous experiments (series 2,

---

[1]GCR Quar. Prog. Rep. Sept. 30, 1960, ORNL-3015, pp. 48–53.

[2]GCR Quar. Prog. Rep. Dec. 31, 1960, ORNL-3049, pp. 169–73.

[3]GCR Quar. Prog. Rep. Dec. 31, 1959, ORNL-2888, pp. 27–28.

[4]GCR Quar. Prog. Rep. March 31, 1960, ORNL-2929, pp. 65–70.

[5]GCR Semiann. Prog. Rep. June 30, 1959, ORNL-2767, pp. 75–77.

Table 3.1. Axial Variation in Mean Inside Surface Temperatures for Tubes of Experiment 4-C

Axial Position, L/d_e	Temperature (°F)						
	Peripheral Tube No.						Central Tube No. 7
	1	2	3	4	5	6	
0	273	273	279	275	280	296	280
5	362	358	367	370	383	376	356
10	401	396	410	414	424	424	396
15	425	425	433	443	448	454	427
17.9	427	429	435	445	454	457	435
20	278	283	282	286	289	293	291
22.5	345	345	346	348	353	361	362
25	388	385	384	388	395	403	417
30	452	444	446	448	458	469	465
35	484	480	477	479	494	498	488
38	485	484	481	485	498	496	491

4A, and 4B). Except near the inlet and exit, tube 6 temperatures are the highest for the peripheral tubes and tube 1 temperatures, the lowest. Two possible explanations for this consistent asymmetry have been advanced; namely, a maldistribution in flow originating in (1) the plenum or the transition piece and (2) a misalignment of either the central or peripheral tubes. An examination of the available data leads to no clear choice between these two postulates. Thus, circumferential temperature distributions around tube 4 near the channel inlet ($L/d_e = 5$) for series 4A and 4C experiments are similar with regard to shape, amplitude, and location of the temperature minimum but display contradictory displacement of the temperature with respect to the 0- to 180-deg diametral axis. This is shown in Fig. 3.1. Since the two experiments differed only in the screens used in the plenum region (a single, 16-mesh, 0.023-in. wire screen surrounding the weir in 4A and a pair of 40-mesh, 0.011-in. wire screens in 4C), it appears that the flow in the channel is indeed sensitive to plenum conditions. On the other hand, measurements[6] of the velocity

[6]GCR Quar. Prog. Rep. Sept. 30, 1960, ORNL-3015, pp. 63–67.

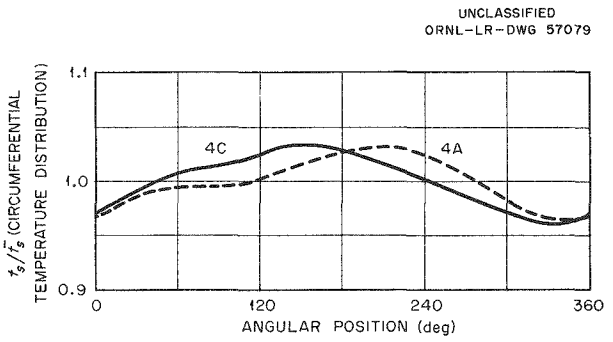

Fig. 3.1. Comparison of Circumferential Temperature Distributions for Series 4A and 4C. Tube 4; L/d_e = 5; N_{Re} = 50 500.

distribution in the vicinity of the central tube in another apparatus of similar geometry indicated that small displacements of the central tube had noticeable effects. Initial attempts to detect and to establish the magnitude of such dislocations in the model 3 heat-transfer apparatus have been unsuccessful because of difficulties in introducing measuring devices into the assembled test section. In view of the near completion of the model 4 apparatus (see below), a definitive experiment to answer this question as to the source of the temperature asymmetries will not be attempted.

A comparison between the mean temperature of the central tube and the average of the mean temperatures for the peripheral tubes in the series 4 experiments is made in Table 3.2. It may be observed that in

Table 3.2. Comparison Between Mean Tube-Surface Temperatures for the Series 4 Experiments

Axial Position, L/d_e	Temperature (°F)					
	Average for Peripheral Tubes			Central Tube		
	Series 4A[a]	Series 4B	Series 4C	Series 4A[a]	Series 4B	Series 4C
0	260	246	279		262	280
5	372	408	369		587	356
10	413	401	411		633	396
15	438	418	438		540	427
17.9	441	425	441		498	435
20	285	282	285		305	291
22.5	347	347	350		388	362
25	390	387	391		442	417
30	452	450	453		476	465
35	486	483	485		492	488
38	491	489	488		495	491

[a]Data obtained for tubes 4 and 6 only.

the upper portion of the channel ($L/d_e < 19$) the average temperatures for the peripheral tubes of series 4B are less than the corresponding temperatures for series 4C (except at $L/d_e = 5$); whereas for the central tube, the situation is reversed. The reduction in power generation in the central tube for the 4C experiment is not sufficient to account for a discrepancy as large as that observed between the middle tube temperatures of 4B and 4C. A preliminary analysis[2] of the series 4B data, in relation to the series 2 results, suggests that the higher central tube temperatures resulted from diminished flow in the inner region of the channel because of the restriction of the flow into this area by the close packing of the electrodes passing through the plenum chamber. The series 4C results indicate that, in addition, the screens at the channel entrance in experiment 4B have a significant effect. Below the mid-cluster spacer, the cumulative effect of a radial transfer of fluid into the inner region and some displacement of the fluid by the spacer itself leads to reasonable agreement between the 4B and 4C data. The average peripheral temperatures for series 4A and 4C are in very close correspondence. However, since only tubes 4 and 6 were used in obtaining the 4A average, it may be presumed, in view of the over-all temperature patterns for 4B and 4C, that the mean based on all the outer tubes for 4A will be 8 to 10°F lower than the tabulated values for the upstream portion of the channel (in relation to the mid-cluster spacer) and 4 to 5°F lower for the downstream section. Near the inlet ($L/d_e < 10$), the flow deficiency in the inner region for experiment 4B, which resulted in abnormally high temperatures for the central tube, also caused excessive temperatures on the inner side of the peripheral tubes. This is illustrated by the typical temperature profile shown in Fig. 3.2 (tube 4 at $L/d_e = 5$). Thus, despite the enhanced cooling in the outer region, the mean tube temperatures are higher than those calculated for series 4A and 4C.

A final set of experiments (labeled 4D) were performed with the model 3 heat-transfer apparatus in which only a single tube (No. 4) was heated. The situation thus created corresponds to that for the mass-transfer studies with a single naphthalene-coated rod. The experimental

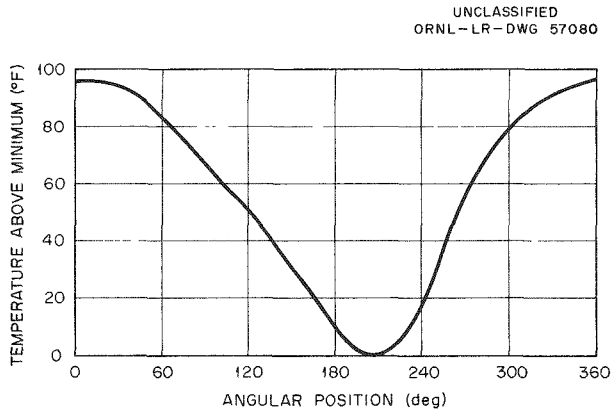

Fig. 3.2. Circumferential Temperature Profile for Series 4B. Tube 4; $L/d_e = 5$; $N_{Re} = 50\ 500$.

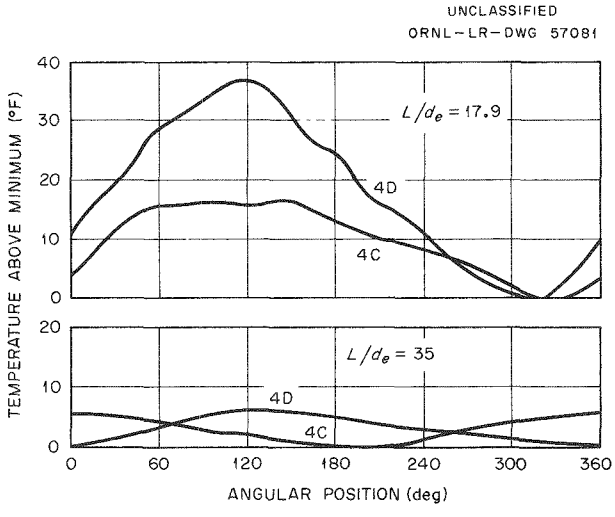

Fig. 3.3. Comparison of Circumferential Temperature Profiles for Series 4C and 4D at Two Axial Levels. Tube 4; $N_{Re} = 50\ 500$.

conditions were the same as those of the previous series 4 investigations ($N_{Re} = 50\ 500$ and mean surface heat flux of 6500 Btu/hr·ft^2); there were no channel-inlet screens.

Temperature traverses were made at 11 axial levels for (1) the heated tube, (2) the three immediately adjacent unheated tubes (Nos. 3, 5, and 7), and (3) a more remote tube (No. 6). Typical circumferential distributions are shown in Fig. 3.3 for tube 4 at two levels, along with similar results from series 4C. In comparison with the 4C traverses, the 4D curves show a more than 100% increase in the maximum diametral temperature difference at $L/d_e = 17.9$ and a complete reversal in the profile at $L/d_e = 35$. Both these features derive from the lower sink temperature in the inner region as a result of the absence of heating from the central tube; the effects of the adjacent peripheral tubes are cancelled, since they supply heat to both the inner and outer regions. Analyses of the data for the adjacent tubes have not been completed.

Mean heat-transfer coefficients calculated from the tube 4 data for the series 4 experiments (based on a uniform gas temperature at every level) are compared in Table 3.3. Downstream of the mid-cluster spacer, the agreement between series 4A, 4B, and 4C data is excellent (an average

Table 3.3. Axial Variation in Mean Heat-Transfer Coefficient for Tube 4 (Model 3)

Axial Position, L/d_e	Mean Heat-Transfer Coefficient (Btu/hr·ft^2·°F)			
	Series 4A	Series 4B	Series 4C	Series 4D
0	40.1	42.8	36.5	37.3
4	27.0	22.0	26.3	25.3
8	24.8	22.7	24.5	22.7
12	23.6	23.6	22.7	21.1
16	23.2	23.7	22.5	20.6
18	23.5	23.9	22.8	20.7
20	48.8	47.3	45.8	37.7
24	31.2	30.8	30.5	26.6
28	26.2	26.3	26.0	22.9
32	24.3	24.1	24.0	20.4
36	23.6	23.5	23.6	19.6
38	23.6	23.4	23.7	19.6

deviation of 1.3%); in the upstream region, where the effects of the different entrance arrangements are still present, the variation is larger (2.8% between 4A and 4C and 8.2% over-all). The coefficients evaluated from the 4D experiment are significantly below those obtained from series 4C, ranging from 7 to 10% low in the upstream region to 13 to 19% low in the downstream section. Since in calculating the heat transfer coefficient it was assumed that the heat added to the fluid was uniformly distributed over the full cross section of the channel at each level, the temperature difference (surface to fluid mean) was larger, and hence the coefficient smaller, than actually existed. From studies on mixing in the seven-rod cluster geometry,[7] it appears that for the single-heated-tube situation it is more reasonable to consider the heat addition as being confined to the immediate vicinity of tube 4 (1/6 of the total flow area). On this basis, the 4D results agree well with the 4C data; this is shown in Fig. 3.4.

[7]GCR Quar. Prog. Rep. Dec. 31, 1960, ORNL-3049, p. 184.

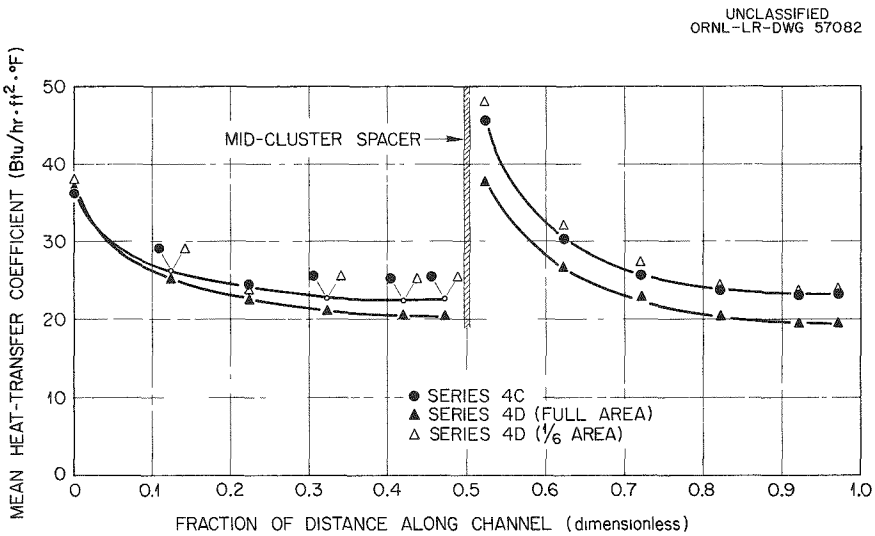

Fig. 3.4. Comparison of Axial Variation in Heat-Transfer Coefficients for Series 4C and 4D.

Fabrication and assembly of the model 4 apparatus[1,2] have been completed. In the course of construction, it has been necessary to make a number of modifications in the test section to correct fabrication errors; this has resulted in some delay. The upper and lower spiders for the upstream cluster have been altered slightly from the Title II design to provide for reasonable power connections; the gas distribution should not be seriously influenced. It will be possible to obtain with this apparatus information on circumferential and radial gas-temperature distributions in both clusters (at four axial locations in the downstream element and one in the upstream unit) and in the region between the clusters. Surface temperatures will be measured in the downstream cluster only. Operation of this apparatus will begin shortly.

Mass-Transfer Measurements

J. L. Wantland

The investigation of the discrepancy between the previously reported heat-transfer and mass-transfer experimental measurements[8,9] has been

[8]GCR Quar. Prog. Rep. Dec. 31, 1959, ORNL-2888, pp. 54–58.

[9]GCR Quar. Prog. Rep. Dec. 31, 1960, ORNL-3049, pp. 174–5.

continued. Based on measurements of surface temperatures of heated tubes and mass removal from naphthalene-coated tubes in the model 3 heat transfer apparatus at the $L/d_e = 17.9$ level, the j factors for heat transfer (j_H) and mass transfer (j_M) were 0.0027 and 0.0035, respectively, at $N_{Re} = 75\ 000$. (The mass-transfer value was based on three separate runs which, while exhibiting widely different circumferential patterns, yielded nearly identical mean values.) When the film temperature, t_f (the arithmetic average between the surface temperature, t_s, and the mixed-mean gas temperature, t_g), rather than t_g is used in evaluating the thermal properties of the coolant in the heat-transfer experiment,[10] a value of 0.0031 is obtained for j_H. The initial 23% difference is thus reduced to 12%.

A further correction can be made by considering the geometric differences between the two experiments. For the heat-transfer study, where the entire tube length was heated, the hydrodynamic and thermal boundary layers were initiated identically at the channel entrance. In contrast, the hydrodynamic entrance for the mass-transfer investigation was $L/d_e = 9.2$ upstream of the beginning of the naphthalene-coated region. Since in both experiments the measurements were at $L/d_e = 17.9$, this corresponds to a mass-transfer entrance region of only $L/d_e = 8.7$. When the data are adjusted to take this difference into account [assuming $j \sim (l/d_e)^{0.1}$, as developed by Humble et al.,[10] where l is now the length over which heat or mass transfer is actually occurring], it is found that the mass-transfer experiments predict a value of j_H 3% lower than measured directly in the heated-tube study. Further, Boelter et al.[11] found, for flow in a circular tube, that the presence of a long hydrodynamic entry ($L/d_e = 11.2$) upstream of a heated section resulted in an approximately 9% reduction in the heat-transfer coefficient with respect to that obtained either without or with only short ($L/d_e = 2.8$) hydrodynamic entry sections. Thus, it is felt,

---

[10]L. V. Humble, W. H. Lowdermilk, and D. G. Desman, Measurement of Average Heat-Transfer and Friction Coefficients for Subsonic Flow of Air in Smooth Tubes at High Surface and Fluid Temperatures, NACA Report 1020, 1951.

[11]L. M. K. Boelter, G. Young, and H. W. Iverson, Distribution of Heat-Transfer Rate in the Entrance Region of a Circular Tube, NACA Technical Note 1451, 1948.

to within the limits of the experimental techniques used in these studies, that the application of mass-transfer measurements to the prediction of heat transfer in rod clusters is valid.

In the course of these studies, it has been assumed that the free-stream naphthalene concentration was negligible. More recently it has been realized that, while the concentration of naphthalene in the gas stream is small on an absolute basis, the inclusion of this factor in calculating the concentration driving force results in a significant correction to the j-factor. In view of the quantity of data involved, the determination of a precise correction has not been attempted. Instead, a set of approximate multipliers has been estimated which is applicable to the peripheral tubes of the previous studies;[12] these multipliers are listed in Table 3.4. Similar estimates for the central tube have not been completed; preliminary calculations indicate that the multipliers will not be as large as those found for the peripheral tubes. These corrections have been included on an absolute basis in the discussion above concerning the discrepancy between the heat-transfer and mass-transfer results.

It was proposed earlier[12] that some of the observed abnormalities in the circumferential mass-transfer profiles resulted from a slight, though permanent, bending of the rods during installation or removal of

[12]GCR Quar. Prog. Rep. Sept. 30, 1960, ORNL-3015, pp. 53–57.

Table 3.4. Approximate j-Factor Corrections for Peripheral Tubes[a]

L/d_e	Multiplier	L/d_e	Multiplier
3.8	1.007	23.2	1.006
6.1	1.02	25.7	1.02
9.8	1.03	28.1	1.04
13.6	1.05	30.8	1.05
17.4	1.07	35.0	1.07
19.6	1.08	39.3	1.09
21.8	1.09	41.2	1.11

[a]These corrections apply to the previously reported results[12] on mass transfer in full-scale models of EGCR Title II elements.

the test cluster. Since this would occur subsequent to the initial profilometer traverse of the rod, a consistent bias (varying from zero at each end to a maximum in the middle) would be introduced. In view of the small amount of naphthalene lost from the rod in the course of a run (maximum observed changes in the rod radius were of the order of 0.010 in.), a limited, fixed displacement of the rod would be sufficient to overshadow completely the real variations in the mass-removal profiles. The magnitude and direction of the warp was found by traversing the aluminum section at the rod midpoint both before and after each run. This information was then used to correct the mass-removal data. For the first run made following this procedure, it was found that the distortion at the rod center was 0.0015 in.; the effect of this less than 1/2% deformation (ratio of rod displacement to rod radius) on the j-factor profile near the mid-plane is shown by the uncorrected-data curve of Fig. 3.5 obtained for rod 6 at L/d_e = 21.8, 0-deg relative cluster orientation, and N_{Re} = 50 000. After adjustment, the profile shows the anticipated shape, and the data are closely comparable with previous data obtained for other rods under similar conditions (for example, Fig. 3.4 of ref. 12).

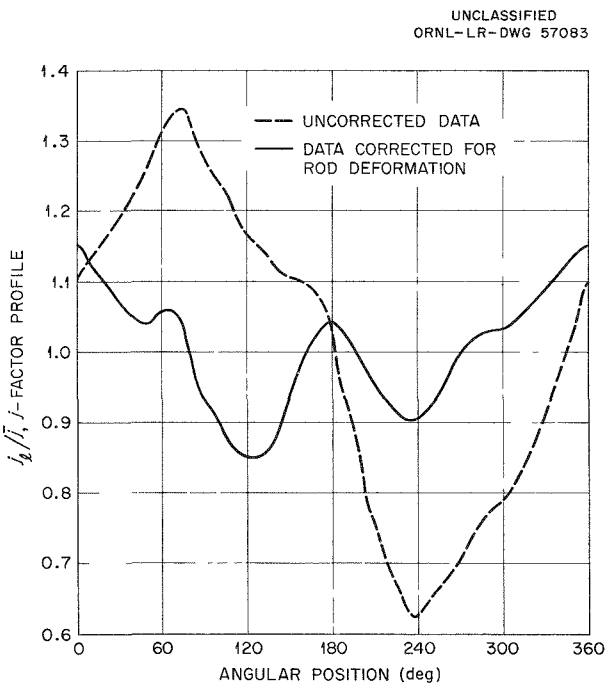

Fig. 3.5. Effect of Rod Warping on j-Factor Profiles. Rod 6; L/d_e = 21.8; 0-deg relative cluster orientation; N_{Re} = 50 000; 0.0015-in. displacement at rod center.

Velocity Distribution Studies

F. E. Lynch

The accumulation of data for delineating the velocity field in the downstream element of two EGCR clusters was continued.[13] The model 3

[13]GCR Quar. Prog. Rep. Dec. 31, 1960, ORNL-3049, pp. 174–81.

velocity apparatus was used in determining the profiles at $L/d_e = 3.9$, while models 4A and 4B were used for studies further downstream.

Contour maps of the velocity distribution in the 120-deg channel segment containing rods 1, 2, 3, and 7 (see Fig. 3.6 for rod location and cluster orientation schematic) have been completed at the $L/d_e = 3.9$ and $L/d_e = 26$ levels of the upstream cluster for five relative cluster orientations (0, 15, 30, 60, and 90 deg). A typical portrayal of the results is given in Fig. 3.7 for $L/d_e = 3.9$, 0-deg orientation, and $N_{Re} = 50\,000$; this figure replaces Fig. 4.7 of ref. 13 in which there is an error in the contours drawn near the central rod.

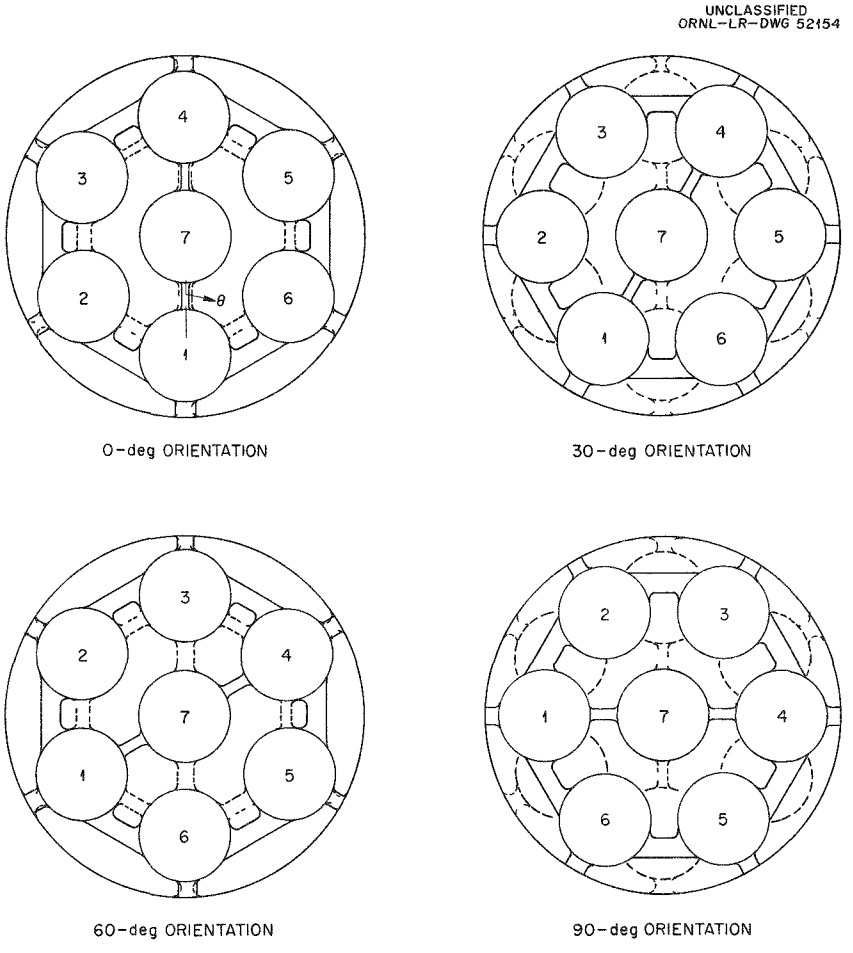

Fig. 3.6. Designation of Rod Positions and Relative Cluster Orientations of Adjacent Title II Design Spiders as Examined in Experimental Studies with EGCR Clusters.

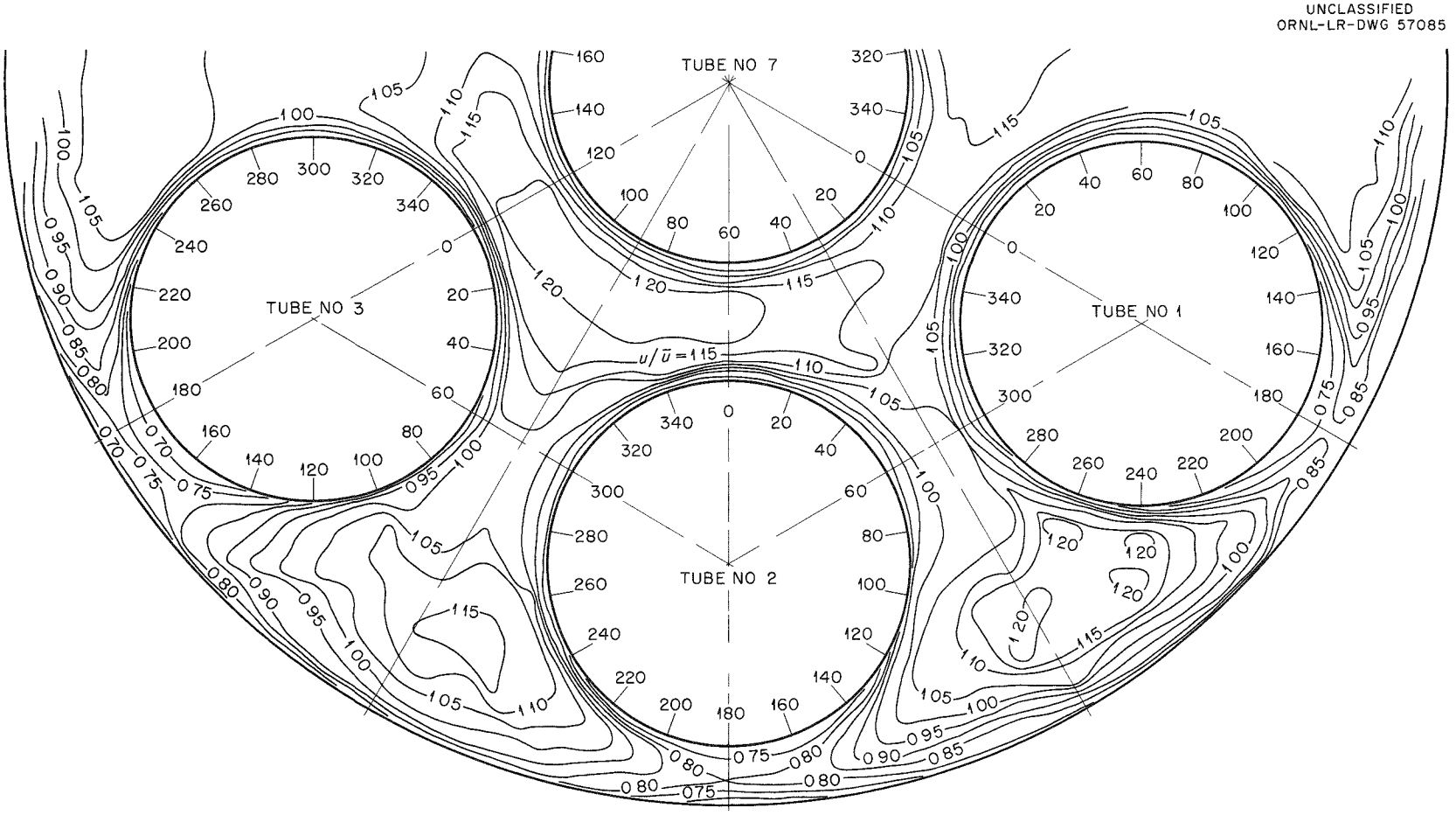

Fig. 3.7. Velocity Contours in an EGCR Channel. L/d_e = 3.9; 0-deg relative cluster orientation; $N_{Re} \sim 50\,000$.

An examination of the velocity distributions of the $L/d_e = 3.9$ level leads to the following comparisons:

1. The contour maps for the 0- and 60-deg cluster rotations are quite similar in appearance, with the only differences deriving from the shift in locations of the webs supporting the central rod (see Fig. 3.6). Thus, the low velocity region between rods 1 and 7 at the 0-deg orientation is replaced by two such areas (between rods 1 and 7 and rods 1 and 3) at the 60-deg rotation.

2. In like fashion, the distributions for the 30- and 90-deg orientations may be paired; in both arrangements the peripheral rods of the lower cluster completely block the gaps between the peripheral rods of the upper element. This results primarily in a reduction in the velocities in the outer flow region bounded by adjacent peripheral tubes and the channel wall to a value about 15% lower than that observed for the inline arrangements (0 to 30 deg). Some differences also appear in the inner flow region due to the locations of the central webs with respect to the area studied (see Fig. 3.6).

3. At the 15-deg rotation, the partial blocking of the outer flow region by the rods of the downstream cluster causes a counter-clockwise shift in the locations of the velocity maxima.

The data for all cluster orientations at the $L/d_e = 26.0$ level are similar. It thus appears that velocity distributions downstream of the mid-cluster spacer are not strongly influenced by cluster rotations. Some effect of the 60-deg-pad spacers is noted.

Measurements just upstream of the mid-channel spacer and of the channel exit are in progress.

Pressure-Loss Measurements in EGCR Clusters

G. J. Kidd

A pressure-drop flow section previously used by the Allis-Chalmers Manufacturing Company in their support studies on the EGCR fuel element has been reassembled and connected to existing gas supply facilities. The channel (pictured in Fig. 3.8) consisted of an inlet dummy, three Title II

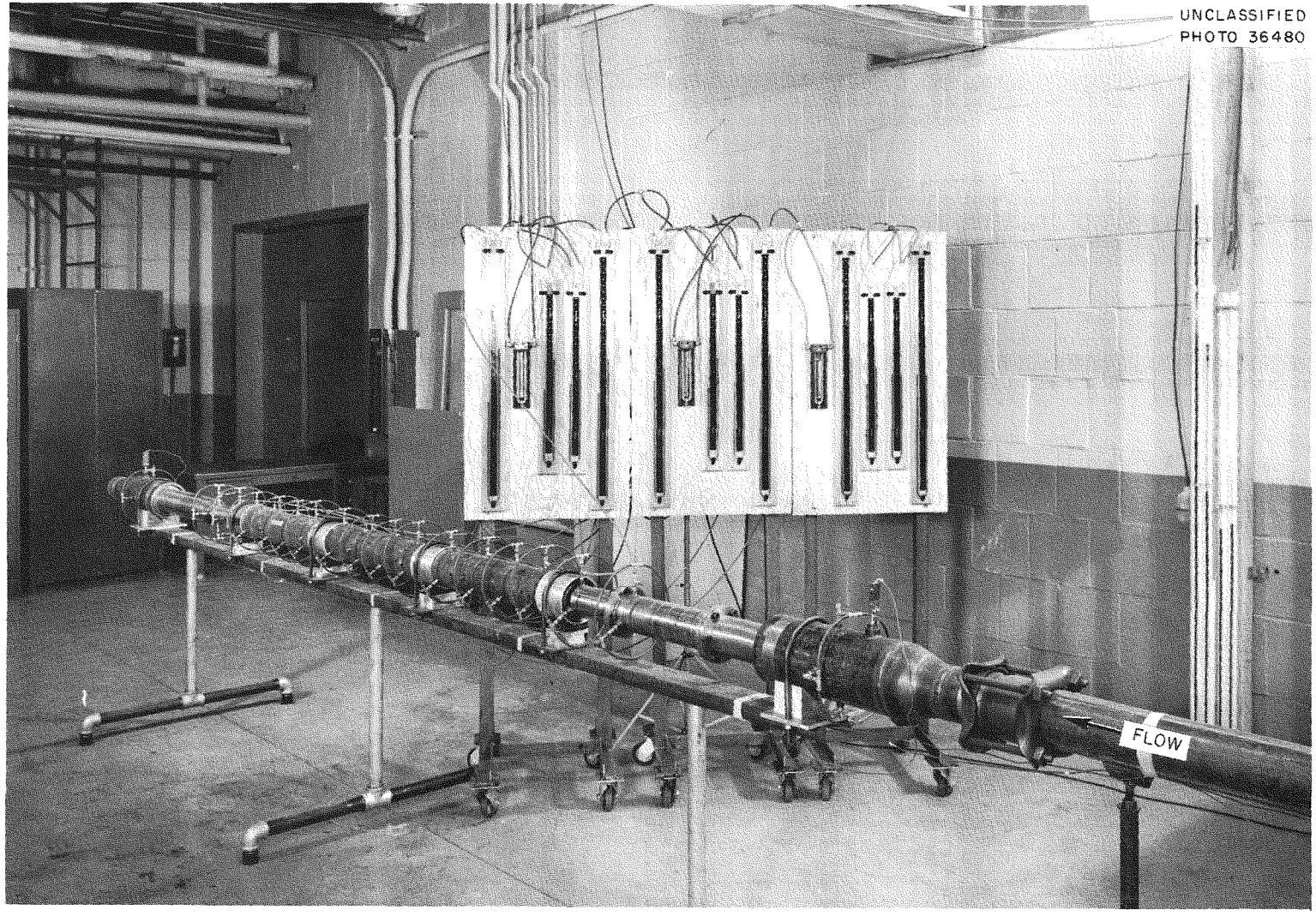

Fig. 3.8. EGCR Title II Pressure-Drop Assembly.

EGCR fuel-element clusters, including graphite sleeves, and an outlet dummy. The original instrumentation was extended by the inclusion of a number of additional static-pressure taps so that the pressure losses attributable to the mid-cluster spacers could be determined. Three static taps (joined by a piezometric ring) were located at four axial positions in each cluster: station 1, downstream of the inlet spider; station 2, upstream, and station 3, downstream of the mid-cluster spacer; and station 4, upstream of the outlet spider.

The pressure losses between stations can be expressed by the equation:

$$\Delta p = \left(f_B \frac{L}{d_e} + K \right) \frac{\rho \bar{u}^2}{2g_c} \quad ,$$

where f_B is the Blasius friction factor and K is a pressure-loss coefficient associated with the spiders and spacers. Thus, between stations 1 and 2 and between stations 3 and 4, which do not include spiders or spacers, $K = 0$.

Preliminary data have been obtained on friction factors in the bare-tube sections of the clusters (stations 1–2 and 3–4) over the Reynolds modulus range 20 000 to 80 000. The results are compared in Fig. 3.9 with previous data for seven-rod geometries taken over (1) a long ($L/d_e \sim 280$) bare-tube section at 4:1 (curve A) and 1:4 (curve B) ligament-spacing ratios[14] and (2) a short ($L/d_e \sim 42$) section in a slotted, circular channel (curve C).[15] For the EGCR Title II channel, the unobstructed length between pressure taps is only $L/d_e = 12$. Despite these differences, there is good agreement between the four sets of data. There is some question as to the EGCR Title II cluster points near $N_{Re} = 20\,000$ and $N_{Re} = 30\,000$; these will be rechecked. With these two values omitted, the short L/d_e data show a flatter characteristic than do the data taken over longer tube lengths.

In view of the inconsistencies in the Title II element data, the apparatus was taken apart, and the surface of the graphite channels was

[14] GCR Semiann. Prog. Rep. Dec. 31, 1958, ORNL-2676, pp. 26–36.

[15] GCR Semiann. Prog. Rep. June 30, 1959, ORNL-2767, pp. 58–63.

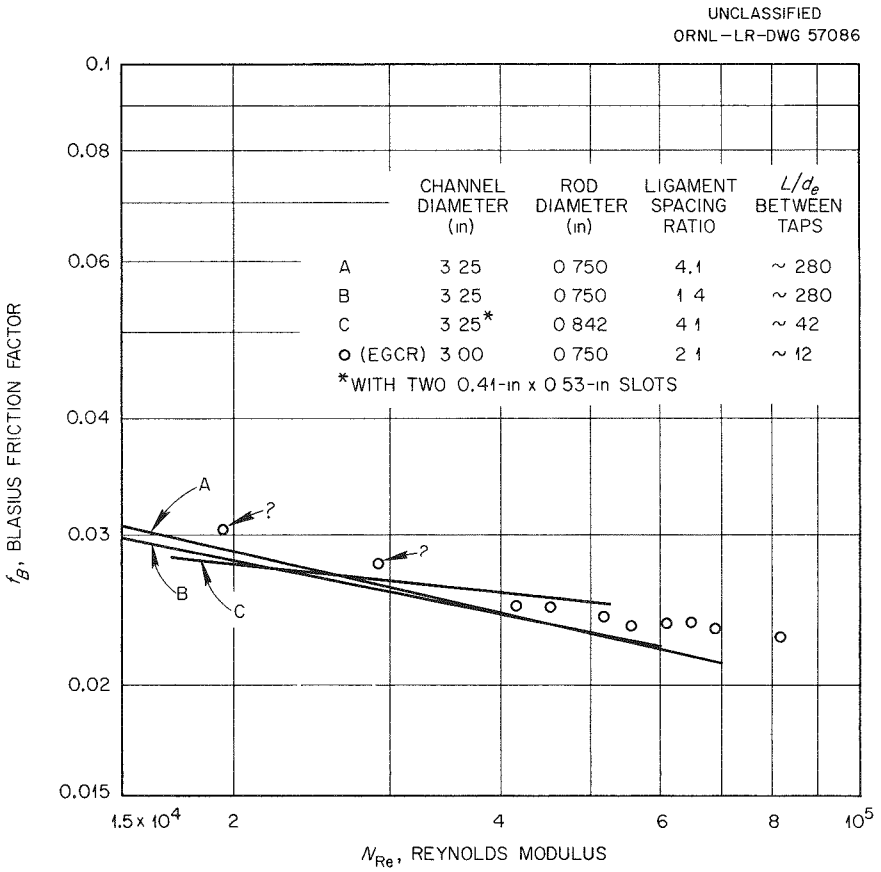

Fig. 3.9. Preliminary Bare-Tube Friction Factors Obtained in EGCR Title II Pressure-Drop Studies.

examined in the vicinity of the pressure taps. It was found that the surface roughness of the graphite was of the same order of magnitude as the diameter of the static-pressure holes. All taps have been enlarged to 1/16 in. in diameter. Measurements to establish the variation between the pressure taps at any level (with respect to a far-removed hole) are in progress; the determination of the loss coefficients for the mid-cluster spacers has been deferred until more consistent data can be obtained.

Gas-Mixing Experiments

G. J. Kidd

The experimental portion of the initial gas-mixing studies has been completed using the previously described experimental system.[16] A modified

[16]GCR Quar. Prog. Rep. Dec. 31, 1960, ORNL-3049, pp. 177–85.

probe that permits easy, continuous, and rapid variation of the sampling location has been substituted for the original, fixed position pickup. The modified probe is shown in Fig. 3.10. The inclusion of sampling-injection ports at three additional levels in the central cluster (see Fig. 3.11) enabled a more detailed study of mixing within the element confines, with particular emphasis on the influence of the mid-cluster spacer.

An extensive set of data, encompassing the measurement of the effect of mid-cluster spacers, end spiders, and full clusters on the circumferential and radial distribution of the helium-tracer concentration, has been accumulated. Analysis is proceeding with the eventual goal of integrating these results with previous information on heat and mass transfer in rod-cluster geometries.

Typical normalized results on mixing across the mid-cluster spacer (between stations IIC and IID) are shown in Fig. 3.12 along the radius at $\theta = -15$ deg. The locations of the sampling and injection probes are referred to a polar grid wherein the radial position is given by the dimensionless distance r/R (ratio of distance from the channel centerline to the channel radius) and the angular position, θ, by the positive or negative displacement from rod 1 (arbitrarily selected as lying on the web supporting the center rod, see Fig. 3.11a). The center of the probe is taken as

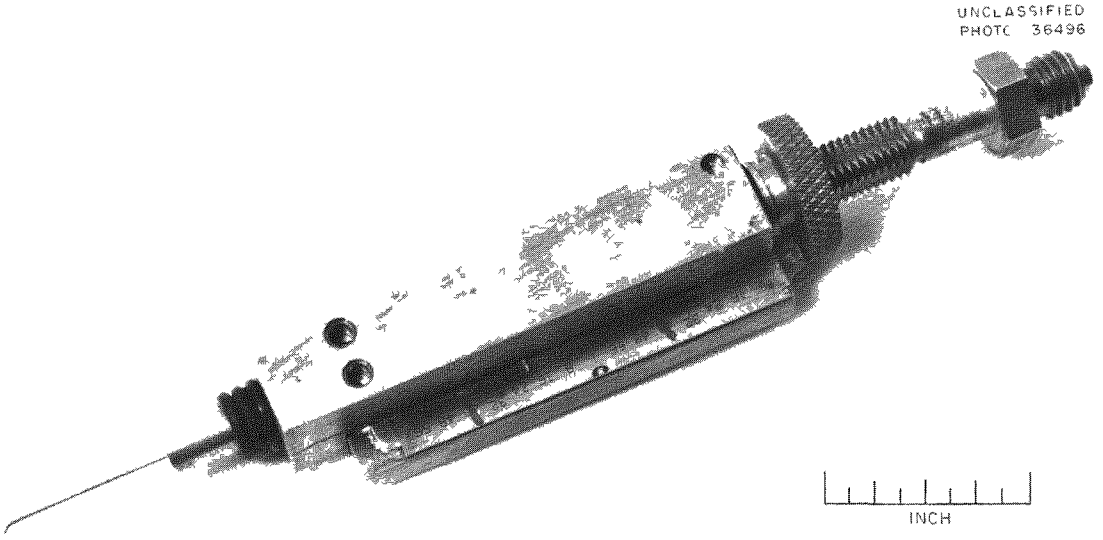

Fig. 3.10. Continuously Adjustable Sampling Probe for Gas-Mixing Studies.

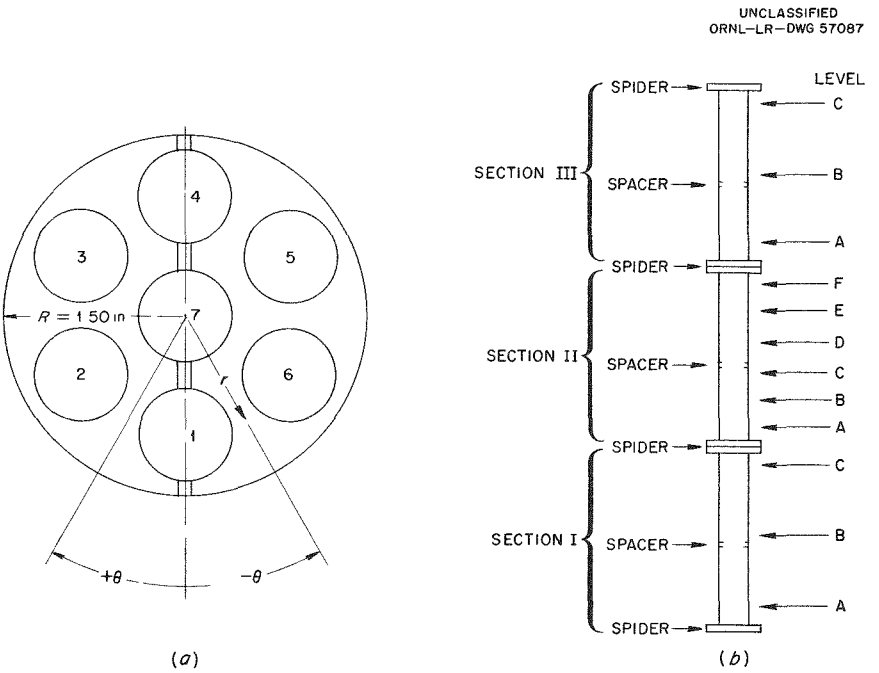

Fig. 3.11. Schematic Diagram of Gas-Mixing Apparatus Showing Injection and Sampling Stations.

the reference point. Since the probes have a diameter of 0.050 in., injection with the probe contacting the central tube corresponds to the location r/R = 0.267, and similarly, at the channel wall, to r/R = 0.983. The degree of mixing may be characterized by the width of the concentration profile at the level at which the concentration has dropped to half the peak value; this is symbolized by the parameter ρ, the ratio of the concentration profile width on either side of the peak to the passage width. Thus, $\rho = 0$ corresponds to no mixing and $\rho = \infty$, to complete mixing; the extent of skewness is measured by the positive and negative variation around the $\rho = 0$ line. For example, in Fig. 3.12, with injection at R = 0.85, $\rho = {}^{+0.14}_{-0.08}$ (passage width = 1.125 in.). The general pattern of the profiles (the shift of the concentration peaks to the left of the injection points and the narrowing of the profiles as the injection point approaches the channel wall) suggests that the flow in this region has an outward component.

A comparison of concentration profiles at $\theta = -15$ deg and r/R = 0.58 for the spider pair (IC-IIA), the mid-cluster spacer (IIC-IID), and a full

element (IC-IIF) is given in Fig. 3.13. The stronger influence of the spiders on mixing in relation to the spacers is apparent ($\rho = \pm 0.3$ versus $\rho = \pm 0.16$); essentially complete mixing occurs across a full cluster.

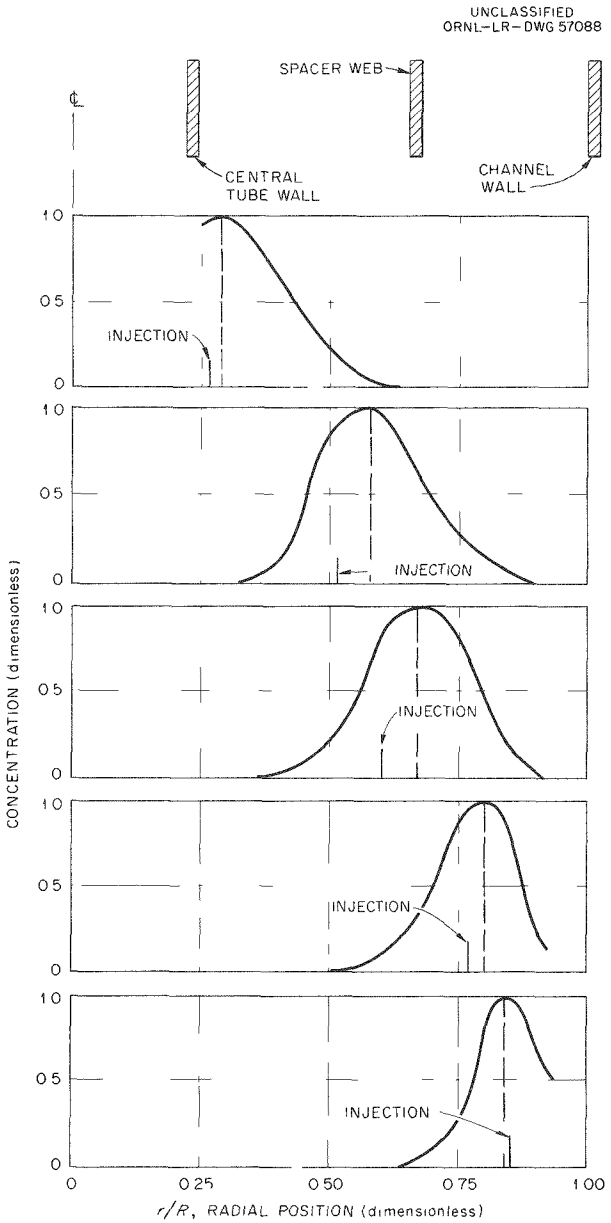

Fig. 3.12. Influence of Mid-Cluster Spacer on Gas-Mixing Profiles. A comparison along radius at $\theta = -15$-deg, with injection at level IIC and sampling at level IID.

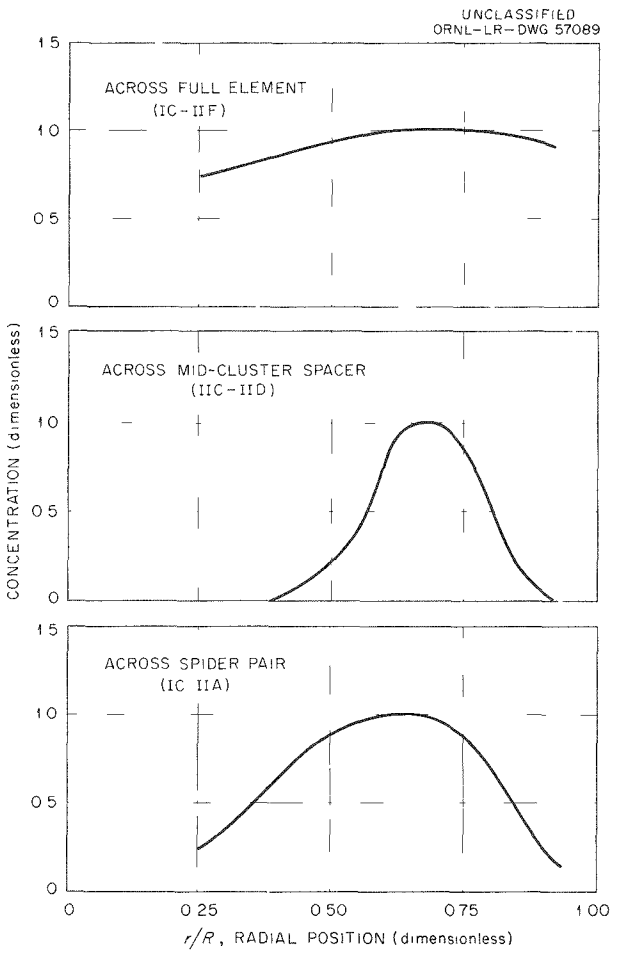

Fig. 3.13. Effect of Spacers and Spiders on Gas-Mixing Profiles. A comparison with injection at r/R = 0.58 on the $\theta = -15$-deg radius.

Part 2. Materials Research and Testing

4. MATERIALS DEVELOPMENT

J. H. Coobs

Fabrication and Physical Properties of UO_2

Fabrication of UO_2 (A. J. Taylor, J. M. Robbins)

Controlled-grain-size miniature UO_2 specimens have been fabricated for LITR capsule irradiations. One set was fabricated with a grain size of approximately 20 μ and an average bulk density of 10.64 g/cm^3; the second set had a grain size of approximately 60 μ and an average bulk density of 10.70 g/cm^3. Both sets are matched with respect to dimensions. Inspection was completed on both sets of pellets, except for precise grain-size measurements.

It was determined that the sintering of flat, thin UO_2 disks for use in experiments on in-pile fission-gas release is feasible under conditions identical to those used in sintering the specimens described above. This observation resulted in the fabrication of a set of disks from 4%-enriched UO_2 with diameters of 0.6036 ± 0.0035 in., thicknesses of 0.0295 ± 0.0005 in., and an average bulk density of 10.28 g/cm^3. These disks will have a grain size of approximately 20 μ.

Development work has been started on the fabrication of depleted UO_2 specimens for Be-UO_2 compatibility studies. Disks 0.6 in. in diameter by approximately 1/8 in. are required, representing densities between 90 and 98% of theoretical and oxygen-to-uranium ratios up to 2.10. In a furnace run designed to investigate the conditions required to produce material with the high oxygen-to-uranium ratio, it was observed that after sintering at 1750°C in argon for 1 hr, the oxygen-to-uranium ratio was reduced from its initial value of 2.18 to 2.003. The gas-purification system was renewed, and a different supply of argon was used in a subsequent run, but the oxygen-to-uranium ratio was still reduced to 2.066. A systematic study of the effect of temperature on the oxygen-to-uranium ratio during sintering in inert atmospheres has been initiated.

Thermal-Conductivity Studies (T. G. Godfrey, D. L. McElroy)

The UO_2 disks for which the radial-heat-flow apparatus was originally designed have been successfully fabricated by the Y-12 Development Group. These disks (3 in. o.d., 0.65 in. i.d., 1/2 in. thick) were rigorously inspected and characterized as to dimensional tolerances and densities. The densities of 28 disks ranged from 92.73 to 93.60% of theoretical. The 18 best disks were surface ground, and six of these were chosen on the basis of size and density to be incorporated into the critical 3-in. section of the specimen stack. Blind thermocouple wells (0.067 in. in diameter) with radial entry grooves were drilled into these six disks. Final inspections are being made to characterize all disks as to density, microstructure, stoichiometry, and purity.

In the interim the radial-heat-flow apparatus is being operated using INOR-8 specimens to determine the effects of a number of variables on its operation. The purpose of these studies is to establish criteria for purely radial heat flow under steady-state conditions in order to reap the full potential of this apparatus. A magnet-regulated, transistorized, direct-current power supply has been successfully used for the core heater in place of the previously used storage batteries. Present difficulties center around small differences in the thermal emf's of the measuring thermocouples in the system. The data obtained consistently yield higher thermal-conductivity values for the center plane than for the top and bottom detection planes. Possible causes for this are being studied.

Bulk-Density Measurements on Small Irregular Particles (Mary P. Haydon, A. J. Taylor)

The solid-embedment technique[1] was used to measure the bulk density of 20 different batches of microspheres and crushed fused UO_2 of particle sizes of 150 to 200 μ. An additional technique was developed to ascertain the validity of each bulk-density determination. This technique involves the low-power stereomicroscopic analysis of another plastic embedment of the same material as that being tested for bulk density. The bottom

[1]GCR Quar. Prog. Rep. Dec. 31, 1960, ORNL-3049, pp. 191–2.

surface of the embedment is ground on a series of waterproof silicon carbide abrasive papers, sizes 60 to 600, so that a smooth surface is obtained across sections of the embedded grains. This surface is then deeply etched with 20% HNO_3 solution. When the acid corrosion products are washed from the surface of a porous sample, a filamentous plastic skeleton of the pore structure remains in the cavities. This pore skeleton gives an excellent model of the surface-connected pore structure down to about 1/2 μ and shows at a glance the validity of the bulk-density value determined in the embedment.

The UO_2 particles used in the study on BeO-UO_2 fuel fabrication were measured by the two embedment techniques. Oxide No. 198, prefired at 950°C in H_2, was then crushed to −60 +120 mesh and fired in H_2 at 1750°C. The bulk-density values determined on three different samples from two runs are presented in Table 4.1. The ground and etched section of this

Table 4.1. Bulk Density of Sintered Particles of Oxide No. 198

Sample No.	Run No.	Density	
		g/cm^3	Percentage of Theoretical
198-A	1	10.521	96.08
	2	10.515	96.03
198-B	1	10.531	96.18
	2	10.512	96.00
198-C	1	10.524	96.11
	2	10.511	96.00

material showed no penetration of the plastic, which indicates that the above densities, averaging 10.519 g/cm^3 (96.07% of theoretical), are valid bulk-density values for this material.

Fission-Gas-Release Studies (J. L. Scott, D. F. Toner)

A series of measurements was made of the rates of release of Xe^{133} from various types of UO_2 by using the neutron-activation technique

described previously.[2] The types of UO_2 studied included pressed and sintered pellets of nominal 95% density and fused and ground powder of the type used to fabricate the swaged fuel elements being irradiated in the ORR. The experiments covered a temperature range of 400 to 1600°C, with results as shown in Table 4.2.

The values of the release rate parameter (D′) at 1400°C for 95% dense pellets, shown in Table 4.2, are in agreement with previously reported results for similar pellets,[3] and the D′ values at 1000°C are in agreement with calculated values obtained by extrapolation from 1400°C by use of an activation energy of 70 kcal/mole. The value of D′ for pellet 50-6 at 1600°C is higher than the value obtained by extrapolation of the 1000 and 1400°C data, but this was expected, because the sintering temperature of the particular batch of oxide was 1630°C. Thus, some additional sintering with attendant high fission-gas-release rates would be expected to occur.

The rates of release of Xe^{133} from pellet 1173 at 600 and 400°C illustrate two problems associated with measurements at low temperatures. At 600°C the total amount of Xe^{133} released after an initial burst of 0.015%, which occurred during heatup, was below the limits of detection even after three days. At 400°C, on the other hand, a linear rate of release of Xe^{133} was observed following an incubation period of approximately 29 hr, with the total amount of Xe^{133} released being much higher than at 600 or 1000°C. The linear rate leads us to believe that the mechanism of release at 400°C is the oxidation of the UO_2 to form a new phase which spalls off. Such an effect would be expected if the thermodynamic data of Belle and Lustman[4] for the oxygen-uranium system were considered. According to these data, oxygen at a partial pressure of 1×10^{-3} μ Hg is reducing to $UO_{2.00}$ above 1000°C but is oxidizing below 1000°C. The partial pressure of oxygen in the system during the tests was not known, but it would be expected to be very low, because the total pressure in the system was less than 0.05 μ Hg, and the samples were contained in a tantalum crucible, which acts as

---

[2]GCR Quar. Prog. Rep. Dec. 31, 1959, ORNL-2888, p. 68.

[3]GCR Quar. Prog. Rep. Dec. 31, 1960, ORNL-3049, pp. 192–5.

[4]J. Belle and B. Lustman, Properties of UO_2, WAPD-184, Sept. 1957.

Table 4.2. Results of Fission-Gas-Release Rate Measurements on UO_2

Sample Designation	Manufacturer	Bulk Density (% of theoretical)	BET Surface Area (cm^2/g)	Test Temperature (°C)	Time of Test (hr)	Fraction of Xe^{133} Released	Release Rate Parameter (sec^{-1})
						$\times 10^{-3}$	
Pellet 50-6	Babcock and Wilcox	91.7	58.0	1600	2.0	8.52	
					18.0	49.3	
					22.0	90.3	
					25.0	96.5	9.25×10^{-9}
Pellet 50-6	Babcock and Wilcox	91.7	58.0	1400	2.0	3.47	
					16.0	5.80	
					18.0	5.87	
					20.0	5.93	1.89×10^{-12}
Pellet 50-6	Babcock and Wilcox	91.7	58.0	1000	0.35	0.72	
					0.75	0.82	
					2.3	0.89	
					19.3	0.96	
					42.9	1.00	1.07×10^{-14}
Ground-fused UO_2 powder	Spencer	100	200	1600	2.0	5.01	
					3.5	6.40	
					19.5	15.0	
					24.5	16.7	2.66×10^{-10}
Ground-fused UO_2 powder	Spencer	100	200	1400	1.5	3.51	
					17.5	5.71	
					19.5	5.79	
					22.5	5.91	1.13×10^{-11}
Pellet 1173	ORNL	95.4	89.3	1400	2.0	7.60	
					6.0	9.64	
					23.0	11.81	
					25.0	12.20	2.42×10^{-11}
Pellet 1173	ORNL	95.4	89.3	1000	1.0	0.065	
					17.0	0.68	
					19.0	0.71	4.59×10^{-14}

Table 4.2 (Continued)

Sample Designation	Manufacturer	Bulk Density (% of theoretical)	BET Surface Area (cm^2/g)	Test Temperature (°C)	Time of Test (hr)	Fraction of Xe^{133} Released	Release Rate Parameter (sec^{-1})
						$\times 10^{-3}$	
Pellet 1173	ORNL	95.4	89.3	1000	0.40	0.45	
					1.08	0.49	
					18.0	0.59	
					24.5	0.62	
					45.3	0.66	2.34×10^{-14}
Pellet 1173	ORNL	95.4	89.3	600	0.32	0.138	
					1.30	0.146	
					5.00	0.145	
					21.8	0.154	
					45.0	0.151	$<1 \times 10^{-16}$
Pellet 1173	ORNL	95.4	89.3	400	0.25	0.0037	
					1.00	0.0041	
					2.00	0.0051	
					19.1	0.105	
					27.0	0.157	
					43.7	0.77	
					51.2	1.13	
					67.4	1.86	
					72.5	2.07	Not applicable

an oxygen getter. The results indicate, however, that at 400°C the environment was sufficiently oxidizing to UO_2 to result in the formation of a second phase. Since the rate of release of Xe^{133} was thereby determined by the rate at which oxygen was supplied to the sample instead of the rate of diffusion of Xe^{133}, no D′ value was computed from the data at 400°C.

Values of D′ for fused and ground UO_2 at 1400 and 1600°C were comparable to those for pressed and sintered pellets. Thus, the rates of release of fission gases in swaged fuel elements using this powder would not be excessive unless the swaged powders have a markedly lower thermal conductivity than pressed and sintered pellets of the same density.

Advanced Fuel Materials Development

Fabrication of Fueled BeO Bodies (R. L. Hamner)

Fabrication development of BeO bodies containing large UO_2 particles was continued with specific attention to the problems of microscopic cracking and densification of specimens. Emphasis was placed on studies of binder characteristics, programing of the sintering cycle, and the effect of particle size.

Binder Studies. The decomposition behavior of three polyvinyl alcohol binder materials was observed as a function of time and temperature in atmospheres of argon, carbon dioxide, and hydrogen. Based on bonding characteristics, gaseous evolution during decomposition, and quantity of residue, "PVA 71-24" was tentatively selected as the binder and CO_2 as the atmosphere for binder removal. This information was then used to program the heating cycle so that cracking of specimens during binder removal was eliminated.

Additional fabrication studies using "PVA 71-24" showed that it tended to inhibit the sintering of BeO. For instance, the fired bulk density of samples of pure BeO compacted to the same green density with and without 4 wt % binder was 93 and 96% of theoretical, respectively. Attempts to use paraffin as an alternate binder were discouraging. It was found to be inferior to the polyvinyl alcohols as a means for minimizing segregation of the BeO powder and the UO_2 particles; further, it did not produce significant improvement in densification.

Programing of the Sintering Cycle. Sintering studies were conducted with varying heating schedules in atmospheres of hydrogen and of argon with subsequent hydrogen treatment in an effort to eliminate microscopic cracking during sintering. The following observations were made:

1. Cracking was reduced by shielding the specimens with an alumina muffle and slowing the heating rate from approximately 30 to 15°C/min.

2. A slow heating rate to 1100°C was shown to be of particular importance, indicating that cracks were propagated in the initial stages of sintering.

3. Under the same sintering conditions, specimens containing UO_2 incorporated as 100- to 150-μ particles were less prone to crack than specimens containing particles in the size range 150 to 250 μ.

In summary, it can be stated that crack-free BeO specimens containing 30 vol % UO_2 introduced as 100- to 150-μ particles preshrunk approximately 24 vol % have been fabricated to 93% of theoretical density. However, the microstructure of the specimens examined showed a large portion of the fuel grains to be fractured. Voids were observed around fuel grains indicating that shrinkages of fuel and matrix were not adjusted properly, as calculated according to shrinkage profiles.[5] This leads to the hypothesis that BeO containing a large volume fraction of large fuel particles does not shrink to the same extent, based on green density, as unfueled BeO. Attempts are being made to adjust shrinkages by increasing the shrinkage of fuel particles before incorporation.

Fission-Gas Release and Microstructural Changes in Fueled BeO (J. L. Scott, D. F. Toner)

It was shown previously[6] that fine-grained BeO-UO_2 sintered pellets release nearly all their fission gas in about 30 hr at 1800°C. At the time it was suspected that the reason for the high fission-gas release was a chemical reaction between the tantalum crucible and the BeO-UO_2 pellet. Subsequent metallographic investigation of an unirradiated specimen

[5]GCR Quar. Prog. Rep. Dec. 31, 1960, ORNL-3049, pp. 196–202.

[6]GCR Quar. Prog. Rep. Dec. 31, 1960, ORNL-3049, p. 204.

indicated that no chemical reaction occurred but that there was a marked change in the microstructure.

Microstructural changes that might occur at high temperatures probably affect the mechanism of fission-gas release. In order to investigate the extent of microstructural rearrangement, a series of heat treatments were performed on BeO-UO_2 pellets containing 30 vol % UO_2 and 70 vol % BeO. The as-fabricated structure is shown in Fig. 4.1. The pellet shown was cold pressed and sintered 1 hr at 1750°C in argon and then 1/2 hr in hydrogen to reduce the oxygen-to-uranium ratio to 2.00. Subsequently, two specimens were heat treated for 8 and 92 hr at 1600°C in a vacuum of 10^{-4} mm Hg. The resulting microstructures are also shown in Fig. 4.1. It may be seen that even after 8 hr at 1600°C some moderate microstructural rearrangement was present.

A similar heating experiment at 1800°C produced more marked changes in the microstructure, as shown in Fig. 4.2. The as-fabricated microstructure is presented again for comparison. It may be seen that UO_2 might become the continuous phase after heating for long periods. Further, it is evident that the high fission-gas release previously reported at 1800°C may be explained on the basis of this gross structural rearrangement.

One other phenomenon was noted during the 30-hr heat treatment at 1800°C. Some UO_2 particles were vaporized, and they left void regions within about 0.02 in. of the surface, as shown in Fig. 4.3. The dark spots near the surface are voids from which UO_2 was vaporized. One surface was unaffected because it was in contact with the tantalum crucible.

Phase Identification in BeO-UO_2-ThO_2 Bodies (C. K. H. DuBose)

Metallographic examinations were conducted and phase identification studies were made on a pellet of UO_2-ThO_2-BeO. The pellet was 3/16 in. in diameter and 1/4 in. long and it consisted of 13 vol % UO_2, 13 vol % ThO_2, and 74 vol % BeO; it had been sintered at 1750°C in hydrogen for 1 hr. This material is representative of samples being irradiated as part of the program on development of fuels for high-temperature breeder reactors.

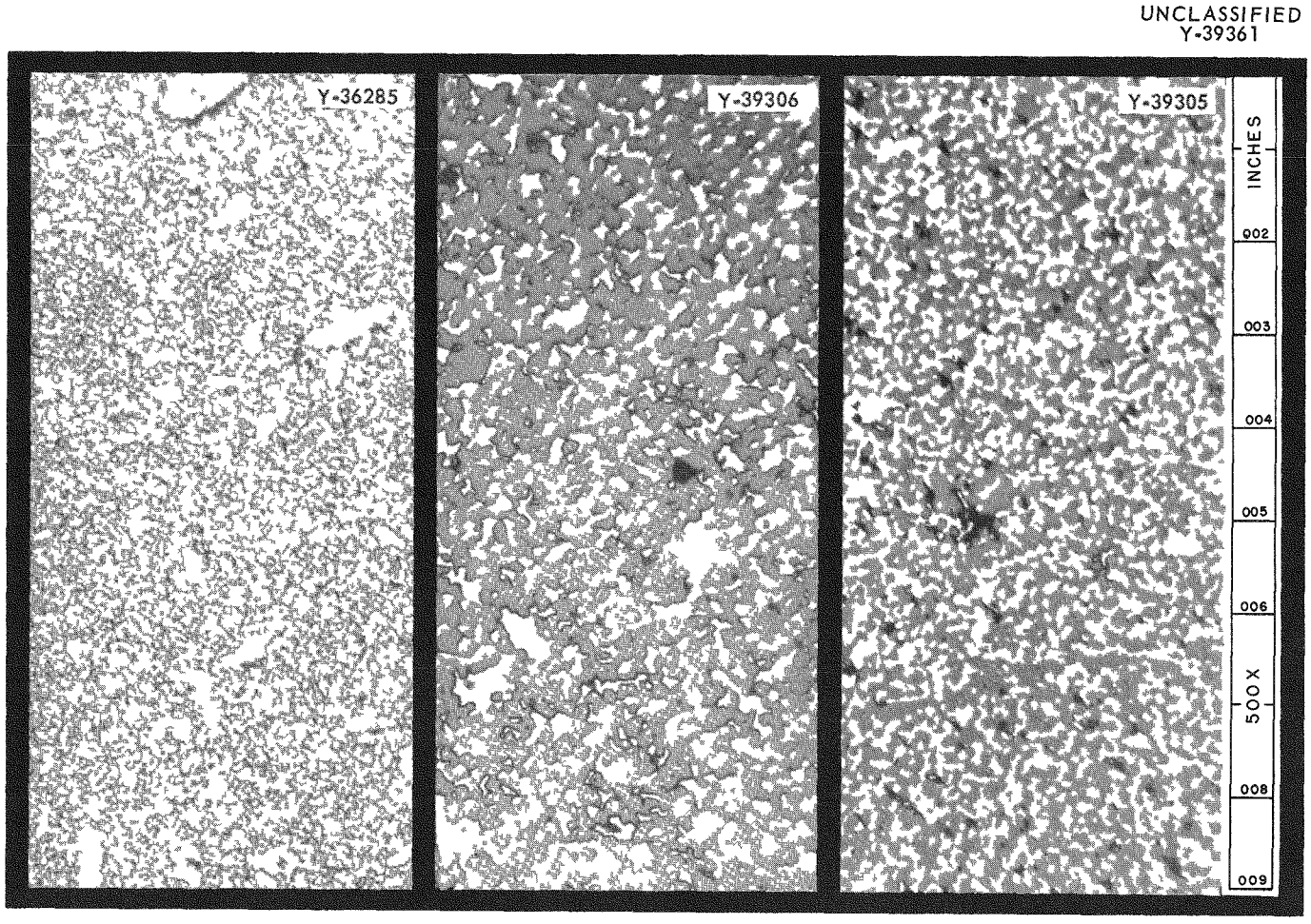

Fig. 4.1. Microstructures of a BeO-UO_2 Pellet As-Fabricated and After 8- and 92-hr Heat Treatments at 1600°C in Vacuum.

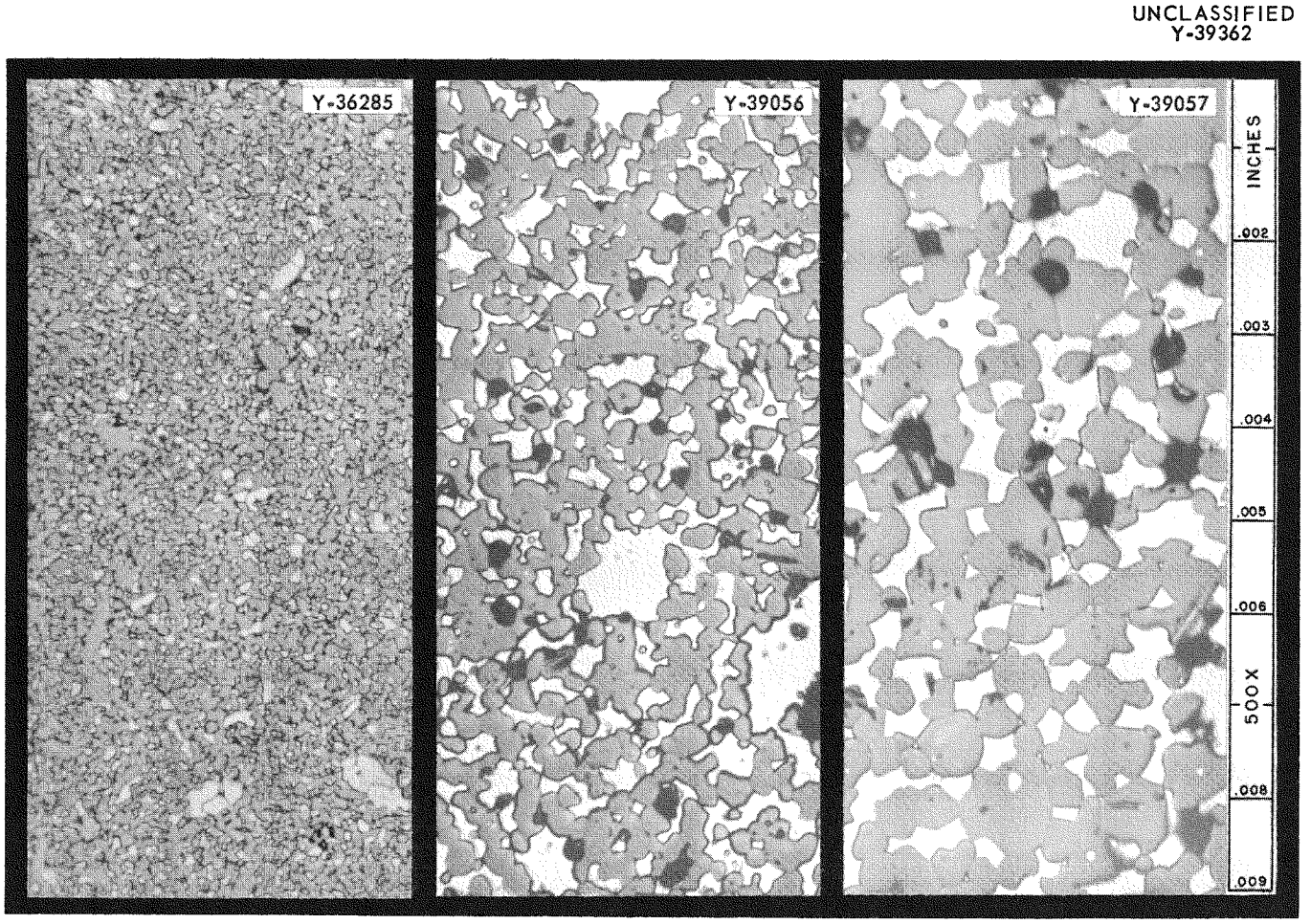

Fig. 4.2. Microstructures of a BeO-UO_2 Pellet As-Fabricated and After 9- and 30-hr Heat Treatments at 1800°C in Vacuum.

Metallographic examination of a polished sample revealed the three phases indicated in Fig. 4.4. The BeO appears as the darkest phase, and the free UO_2 particles are somewhat lighter in color. The lightest phase is a heterogeneous UO_2-ThO_2 solid solution. Although distinguishable with the microscope, the photomicrograph does not distinguish the difference

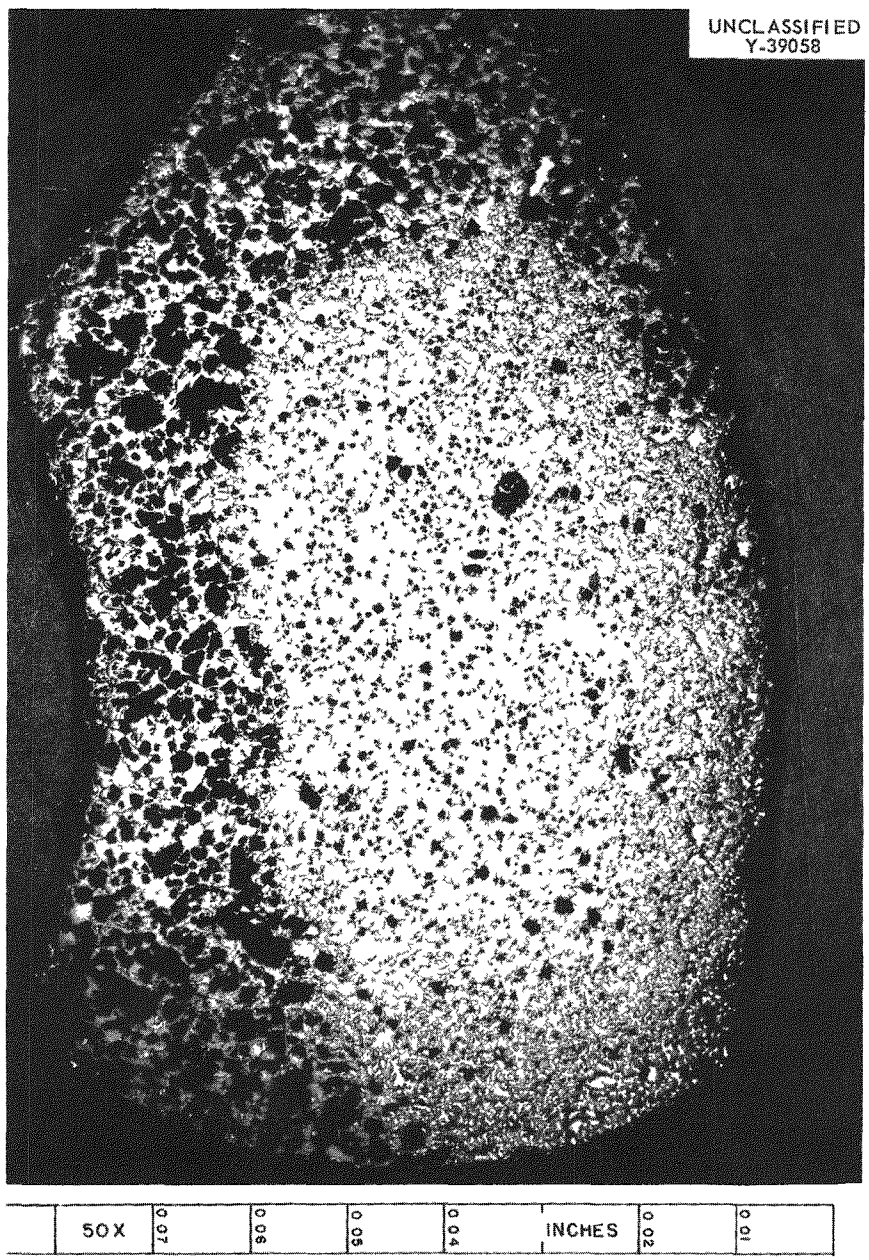

Fig. 4.3. Voids Left by Vaporization of UO_2 from a BeO-UO_2 Pellet During Heating for 30 hr at 1800°C.

in shading between the UO_2-ThO_2 solid solution and free UO_2 particles in any great detail.

Identification of these three phases required a combination of metallographic, petrographic, and x-ray diffraction techniques. Petrographic analysis of a thin section showed a large amount of the sample to be highly birefringent BeO, while a trace of free UO_2 and an unidentified phase (not

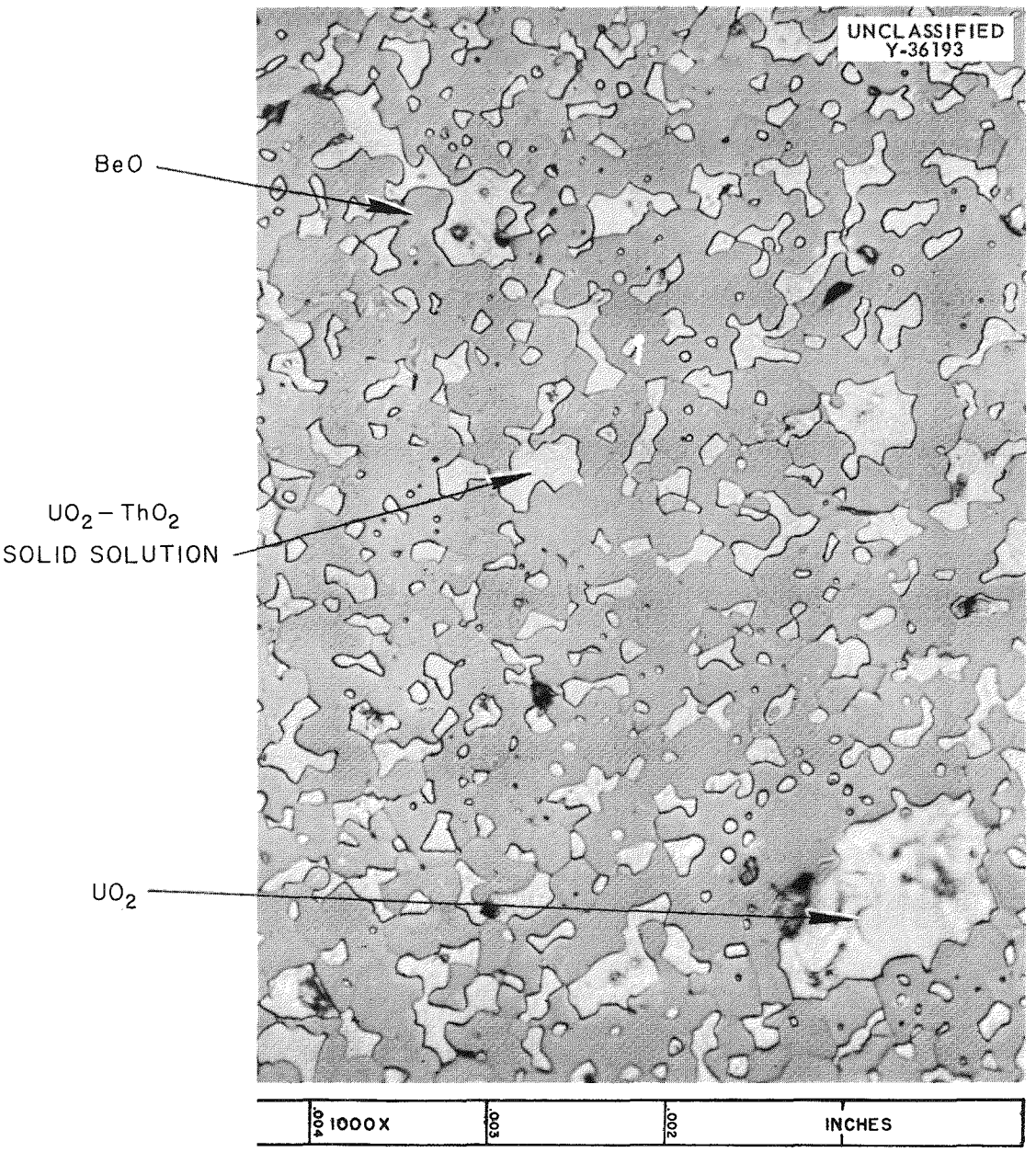

Fig. 4.4. Microstructure of Sintered Pellet Consisting of 13 vol % ThO_2, 13 vol % UO_2, and 74 vol % BeO. Etchant: 1:1 HF and H_2O. 1000X.

ThO_2) were also detected. By crushing a small portion of the sample the dark gray phase outlined in Fig. 4.4 was found to match the indices of refraction for BeO (wD 1.719, eD 1.733) when suitable oils were applied. A sulfur-selenium melt was used to match the index of refraction of UO_2 (n = 2.34). The very small amount of dark red particles found in the petrographic section were matched by this refractive index, thus verifying the presence of free UO_2.

No free ThO_2 was detected, either by petrographic examination or by matching indices of refraction. Therefore, it was speculated that the ThO_2 had formed a solid solution with the UO_2. A similar observation has been reported by Reeve.[7] Although some free UO_2 was found, it was present in much less than the original 13 vol %. Examination of a crushed and ground sample of the material by x-ray diffraction showed strong lines for BeO and a second phase with a lattice parameter of a = 5.5355 Å. No lines for UO_2 could be detected in the pattern, indicating that less than 5% UO_2 was present.

The measured lattice parameter (a = 5.5355 Å) of the second phase was compared with the parameters for UO_2 and ThO_2. If it is assumed that the lattice parameter of the UO_2-ThO_2 system is a straight-line function, the observed phase would have an average composition of approximately (43% U–57% Th)O_2. This uranium-to-thorium ratio in the UO_2-ThO_2 solid solution also indicates that part of the UO_2 did not react with the ThO_2.

Coated-Particle Evaluation (J. M. Kerr, F. L. Carlsen, Jr., T. Hikido)

Spherical, coated fuel particles incorporated into graphite matrices are under consideration for use in unpurged all-ceramic reactor systems. Before a fuel element of this type can be used, a thorough evaluation of the composite materials must be made. The coated fuel particles must be tested for fission-gas retention, coating integrity, stability under thermal cycling, and stability during irradiation. Thus, a rigid evaluation that includes both preirradiation examinations and testing as well as irradiation experiments is required.

---

[7]K. D. Reeve, An Exploratory Study of the BeO-UO_2-ThO_2 System, AERE-MR-2727 (1959).

The out-of-pile evaluation of the coated particles must include, in sequence, (1) alpha assay of the as-received particles, (2) metallographic examination of representative particles, (3) leaching in a 1:1 HNO_3-H_2O solution, (4) chemical analysis for uranium in the leach liquid, (5) alpha assay of the leached particles, (6) thermal cycling of the particles three times to an elevated temperature, (7) leaching again in the acid solution, (8) chemical analysis for uranium in the leach liquid, (9) alpha assay of the particles, and (10) final metallographic examination.

Samples of spherical uranium carbide with a pyrolytically deposited coating of carbon have been received from Minnesota Mining and Manufacturing Company (3M) and High Temperature Materials, Inc. (HTM) for evaluation. Typical microstructures of products from these vendors are shown in Fig. 4.5. The marked difference in structure of the coatings is the result of differences in processing techniques. The carbide cores in both cases were supplied by 3M and contain UC_2, UC, and graphite flakes. The relative amounts vary, but as much as 50 vol % UC and 40 vol % graphite flakes have been observed in the particles.

In the out-of-pile evaluation, the uranium contamination at the surface of the spheres and the uranium leached from the surface are determined relative to the total uranium in the samples. The thermal cycling gives an indication of the ability of the coatings to withstand the stresses set up by differential thermal expansion. Initial studies have shown that in the as-received condition the alpha assay indicates a surface uranium contamination of 1.8×10^{-3}% on the 3M particles and less than 1.7×10^{-4}% on the HTM particles. Essentially the same values were obtained after leaching. Chemical analysis of the leach liquid indicated that approximately 3.6×10^{-2}% of the total uranium in the 3M sample was leached from the surface and that 3.3×10^{-3}% was leached from the surface of the HTM sample.

During thermal-cycling tests, a 3M sample was cycled to 2170°C, and the coating cracked. Samples of both types of particles were also cycled three times between 200 and 1800°C. Results of the chemical analysis for uranium in the leach liquid from the 3M sample indicated that 1.4×10^{-1}% of the total uranium had been leached from the particles, while no uranium was detected in the leach liquid from the HTM sample. The alpha assay

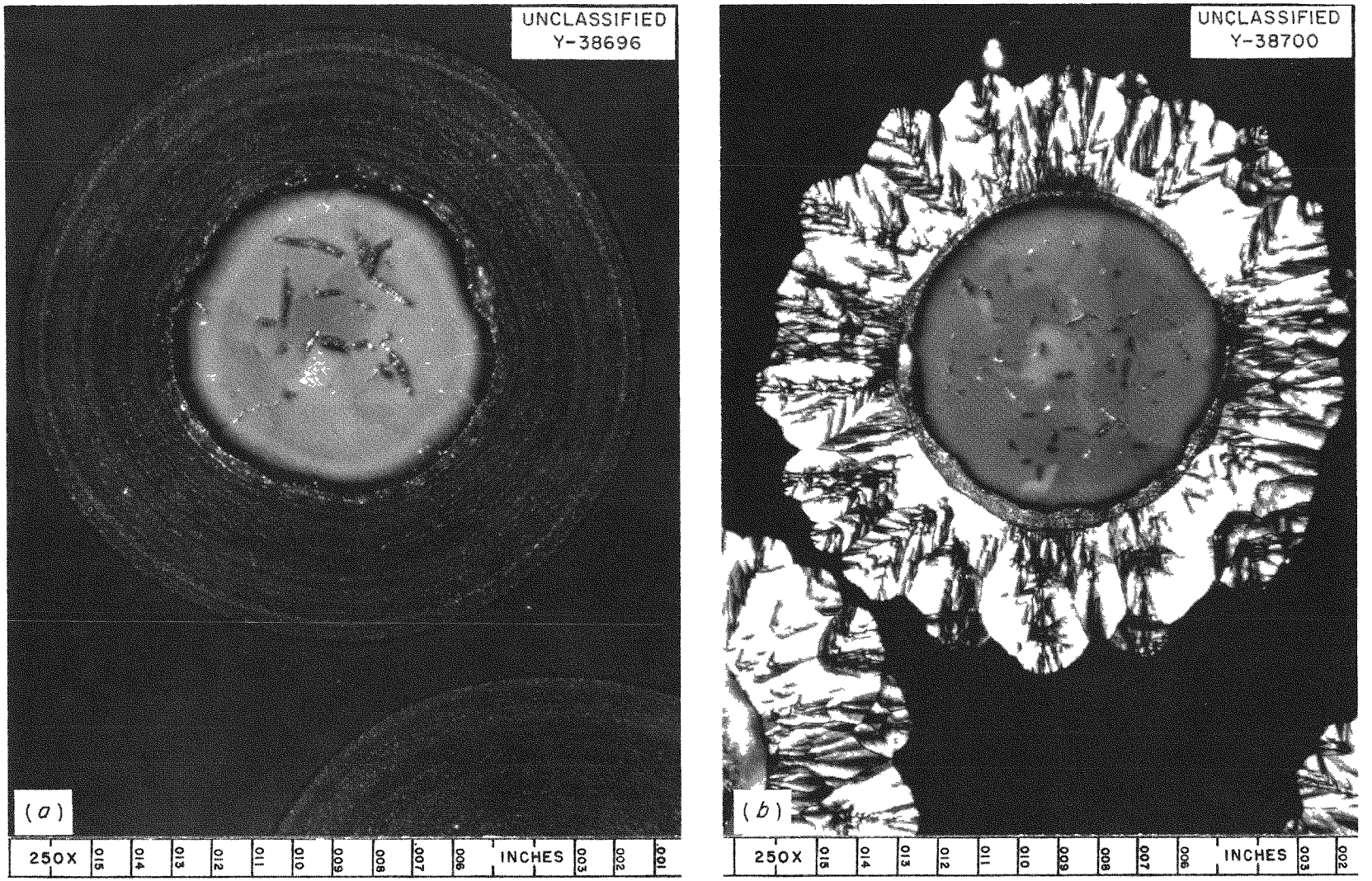

Fig. 4.5. Typical Pyrolytic-Carbon-Coated Uranium Carbide Particles As-Coated by Two Vendors and Viewed Using Polarized Light. Note the difference in structure of the coatings. The carbide core contains UC_2, UC, and graphite flakes, the latter being apparent in these photomicrographs. The material at the interface has not been positively identified. As polished.

indicated surface contamination of $3.7 \times 10^{-2}\%$ and $1.2 \times 10^{-2}\%$ for the 3M and HTM products, respectively. The inconsistencies in results of alpha assay and chemical analysis of the leach liquid are at present unexplained.

A small tantalum capsule was designed for irradiation of the coated particles in LITR static capsule tests (see chap. 6). The capsule is approximately 1 in. long and 0.287 in. in diameter, and it consists of an outside sleeve in which a hollow central pin is spaced by end caps, leaving an annulus of 0.085 in. The hollow central pin and one end cap are constructed so that a thermocouple may be placed in the center of the capsule. The coated particles are contained in the annulus bound by the sleeve, the central pin, and the two end caps. The HTM material was selected for the initial irradiation experiment because it showed a lower initial surface contamination, less uranium in the leach solution, and a uranium density per given volume which was better adapted to the particular capsule design selected.

Another capsule to be used in the coated-particle in-pile evaluation tests was designed to fit in the C-1 facility of the ORR. This capsule is made of graphite and "Carbocel" (a porous carbon insulation material), and it consists of an outer shell of "Carbocel" 1 in. long and 3/4 in. in diameter surrounding a graphite sleeve in which a graphite central pin is spaced. The annulus between the graphite sleeve and the central pin accommodates a one-particle-thick layer of particles.

Shape Casting of Uranium Monocarbide (D. T. Bourgette)

The development program on the melting and casting of uranium monocarbide has been completed. Techniques have been developed for arc-melting and casting crack-free high-purity UC cylinders, 0.25 to 0.5 in. in diameter and 3 in. long. However, small shrinkage cavities which occur in the top 20% of the casting cannot be eliminated. The cavity is formed because the molten alloy "drops" into the mold and simultaneously freezes in the outer regions of the casting. A solidification pattern results that allows very little molten alloy to act as a feeding head.

Compatibility of UC with Beryllium (J. F. Murdock)

A program was initiated for determining the compatibility of UC with beryllium in the temperature range 600 to 1000°C and for studying the effect of the uranium-to-carbide ratio on the reactions with beryllium. Samples are being heat-treated as diffusion couples in a capsule of the type shown in Fig. 4.6. The capsule consists of an Inconel shell with a central type 347 stainless steel rod to insure contact between the specimens. The capsules will be welded in an argon atmosphere and heated isothermally.

A preliminary experiment was conducted using crushed UC in the diffusion couple instead of a wafer. The UC contained 4.80 wt % carbon, which is very nearly the stoichiometric quantity. A small amount of alpha uranium was present in the structure. The capsule was heat treated 66 hr at 1000°C and then water quenched to room temperature. Since the inside of the capsule remained bright, it appears that the inert atmosphere in the capsule was pure.

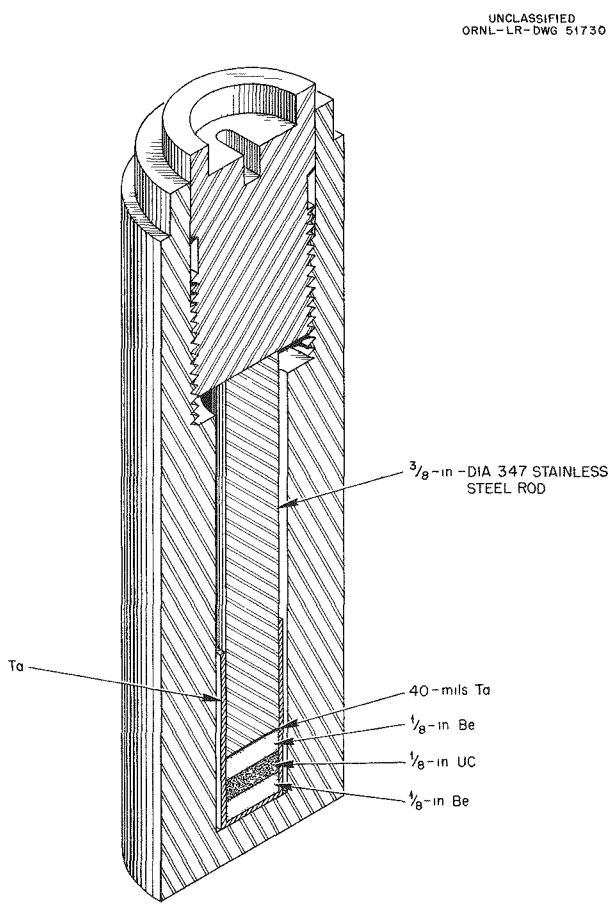

Fig. 4.6. Capsule for Diffusion Couple Compatibility Studies.

The tantalum crucible and the diffusion couple were sectioned and examined microscopically. A layer 0.006 to 0.010 in. thick of an intermetallic compound was found near both beryllium wafers. A typical area of the interface region is shown in Fig. 4.7. In all cases the reaction layer separated from the beryllium. The interface between the reaction layer and the UC is shown in more detail in Fig. 4.8. In this figure the lines in the intermetallic phase which appeared to be cracks at the lower magnification (Fig. 4.7) are shown to be a precipitate within the

intermetallic compound. The identities of the intermetallic compound and the precipitate were not learned during examination of this sample. Additional capsules containing polished wafers of beryllium and UC are being tested at 700 and 1000°C.

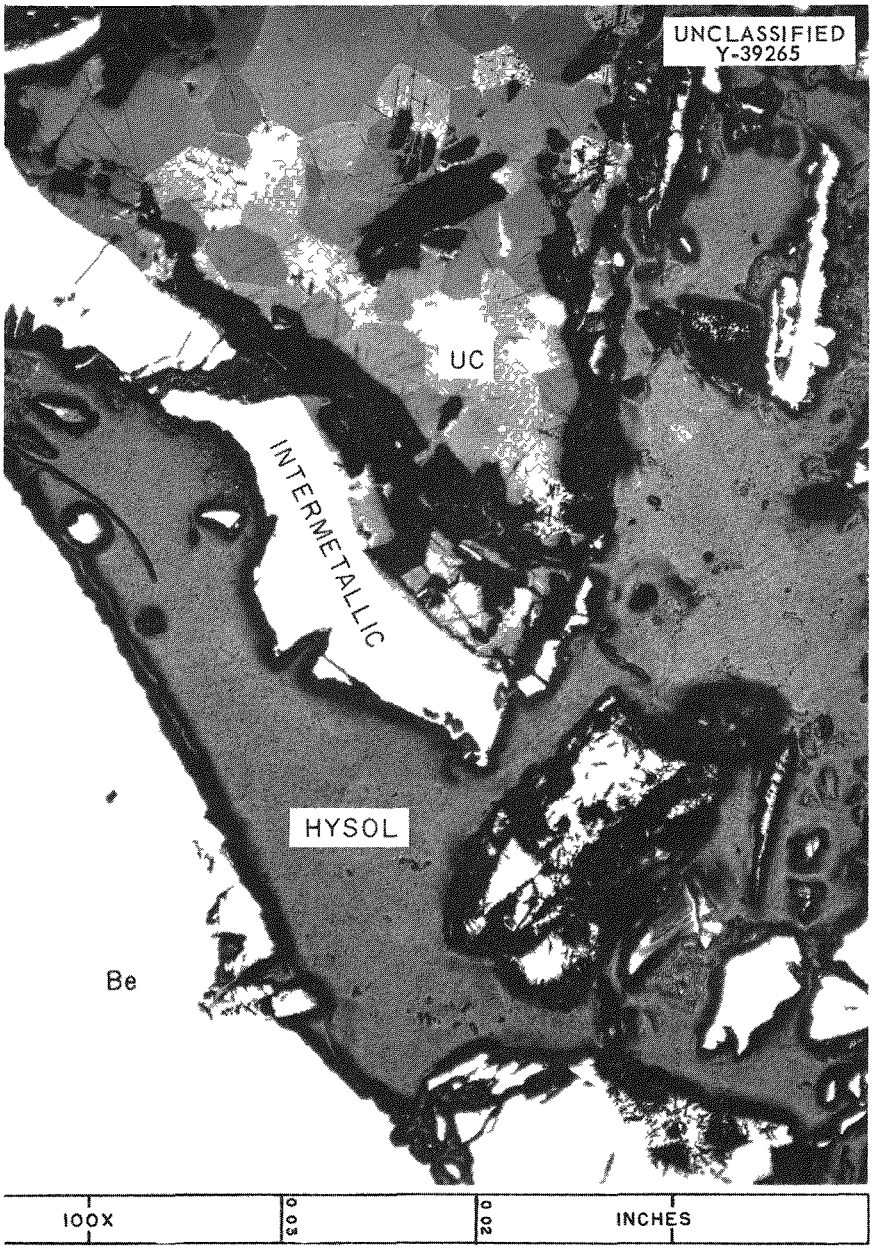

Fig. 4.7. Intermetallic Reaction Zone Between UC Fragments and a Beryllium Wafer After 66 hr at 1000°C. Etchant: H_2O, HNO_3, and acetic acid.

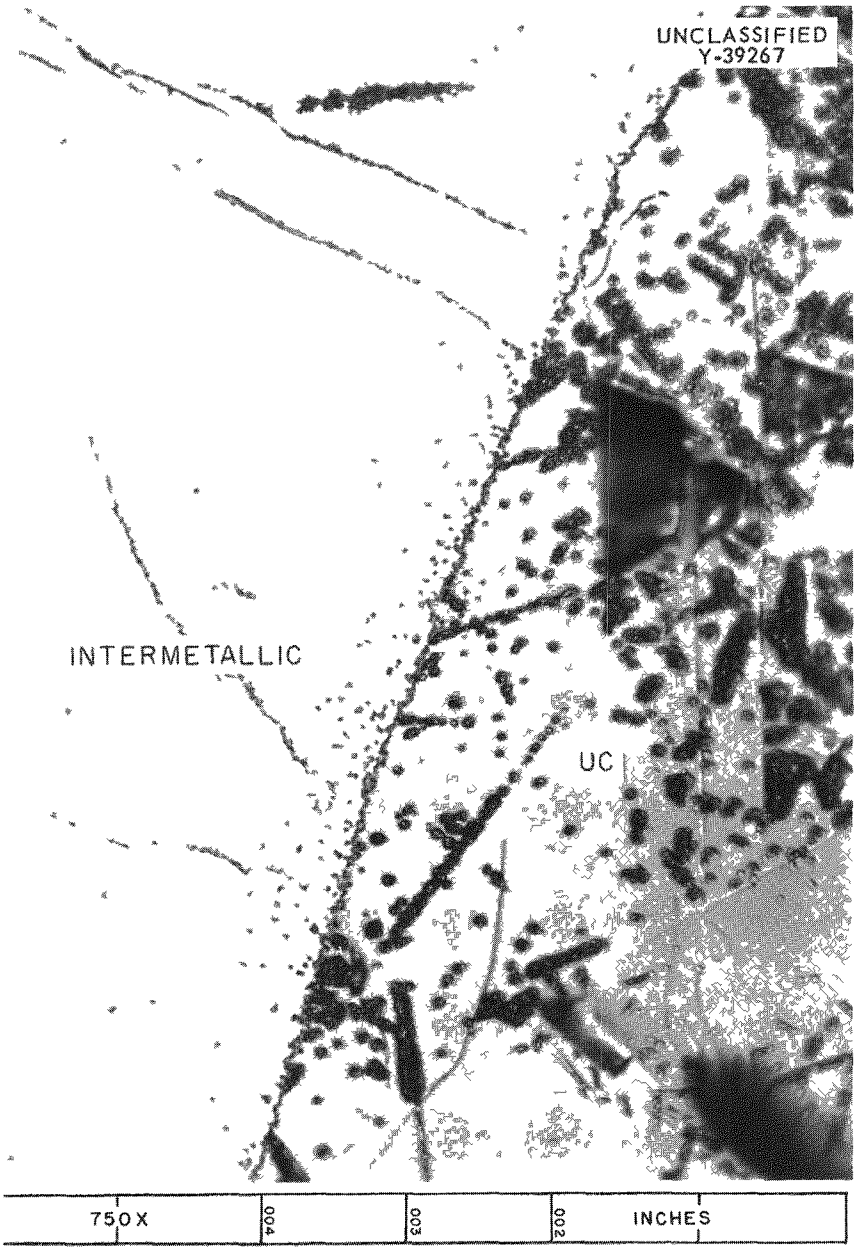

Fig. 4.8. Interface Between UC and Intermetallic Phase. Note the finely dispersed precipitate within the intermetallic matrix.

Structural Materials Evaluation

Coatings for EGCR Graphite Support Sleeves (F. L. Carlsen, K. V. Cook, R. W. McClung, N. V. Smith)

Various types of coatings applied to full-size EGCR graphite support sleeves have been partially evaluated. Tests were performed using coatings of silicon carbide, siliconized silicon carbide, and pyrolytic

graphite applied to three representative samples of nuclear grades of graphite, as well as two samples of special grades of graphite. The evaluation included coating thickness and integrity, permeability measurements, adherence tests, and oxidation tests.

Permeability Measurements. The effect of the coating on room-temperature helium permeability was measured on several of the coated sleeves. The information obtained is summarized in Table 4.3. The data show that each type of coating is effective in lowering the permeability of the sleeve. In the case of the pyrolytic graphite coatings, however, the low permeability of the base AHDG-1A graphite and uncertainties due to experimental limitations make this conclusion less definite than for SiC-base coatings. It is in order to note that the apparatus used in these measurements[8] was designed to measure permeabilities greater than 1 millidarcy.

Adherence Tests. The apparatus for testing the adherence of the coatings to the graphite was designed to direct high-velocity air perpendicular to the coated surfaces and thereby remove any nonadherent material. Air velocities of up to 1000 fps through a 3/16-in.-diam nozzle were used during the tests.

[8]N. V. Smith and Jack Truitt, EGCR Graphite Permeability Tests: Results of Forced Flow Experiments on EGCR Fuel Element Sleeves and Sleeve Material, ORNL CF-60-7-101, June 29, 1960.

Table 4.3. Permeability of Full-Size EGCR Graphite Sleeves to Helium at Two Atmospheres

Graphite Grade	Coating Type	Coating Vendor	Permeability to Helium at 2 atm (millidarcy)	Number of Tests
AHDG-1A	Uncoated		0.016–0.39	3
	Pyrolytic graphite	American Metal Products Company	0.0025–0.021	4
AGOT	Uncoated		45–300	3
	SiC	National Carbon Company	3.8	1
	Si-SiC	American Lava Corporation	1.8	1
R1-HLM	Uncoated		9–14	3
	SiC	National Carbon Company	1.5	1
	Si-SiC	American Lava Corporation	0.93	1
NG-2	Uncoated		12	1
	SiC	National Carbon Company	5.1	1
	Si-SiC	American Lava Corporation	1.1	1
Unknown	SiC	Norton Company	3.0–8.3	3

The tests showed that there was a considerable amount of nonadherent SiC on the sleeves coated by both the National Carbon Company and the Norton Company. The siliconized SiC coating applied by the American Lava Corporation was much more adherent, but still some material was removed. On the other hand, the pyrolytic graphite coatings applied by American Metal Products Company and High Temperature Materials, Inc., were completely adherent; no material was removed.

Oxidation Resistance of Coated Sleeves. The oxidation resistance of the coated graphite sleeves was determined by comparative oxidation tests on 1- and 5-in.-long specimens cut from coated and uncoated sleeves. The oxidation tests were conducted in the assembly shown in Fig. 4.9. In order to minimize the oxidation of the bare ends, the test specimen was held between the two stainless steel cover plates under a compressive load. The load, which provided a contact pressure of approximately 300 psi, was applied by set screws in the top of the muffle.

The gas flow system was designed to preheat the air by passing it down the length of the muffle and through a bed of alumina pebbles before it flowed over the specimen. The temperature was measured using a thermocouple capable of both translational and rotational movement, with the tip at a constant distance of approximately 1/8 in. from the inside surface of the specimen. In a typical run, the specimen was placed in the muffle, and then the muffle was alternately flushed with argon and evacuated several times. A steady flow of argon was then established, and the muffle was placed in the hot furnace. When the specimen reached the test temperature the load was applied to the cover plates and the air flow was started. After the test time of approximately 2 hr the argon flow was resumed and the muffle was removed from the furnace.

A summary of several tests run at 600°C on 5-in. specimens with an air flow of 20 cfh is presented in Table 4.4. Except for the sample of coated 901S graphite, the coatings provide only slight protection from oxidation. Small, completely coated samples of 901S were previously shown to be completely resistant to oxidation.[9] The weight loss on the 5-in.

[9]GCR Quar. Prog. Rep. Dec. 31, 1960, ORNL-3049, p. 210.

long coated 901S specimen was shown to be due primarily to oxidation of the uncoated ends under the cover plates.

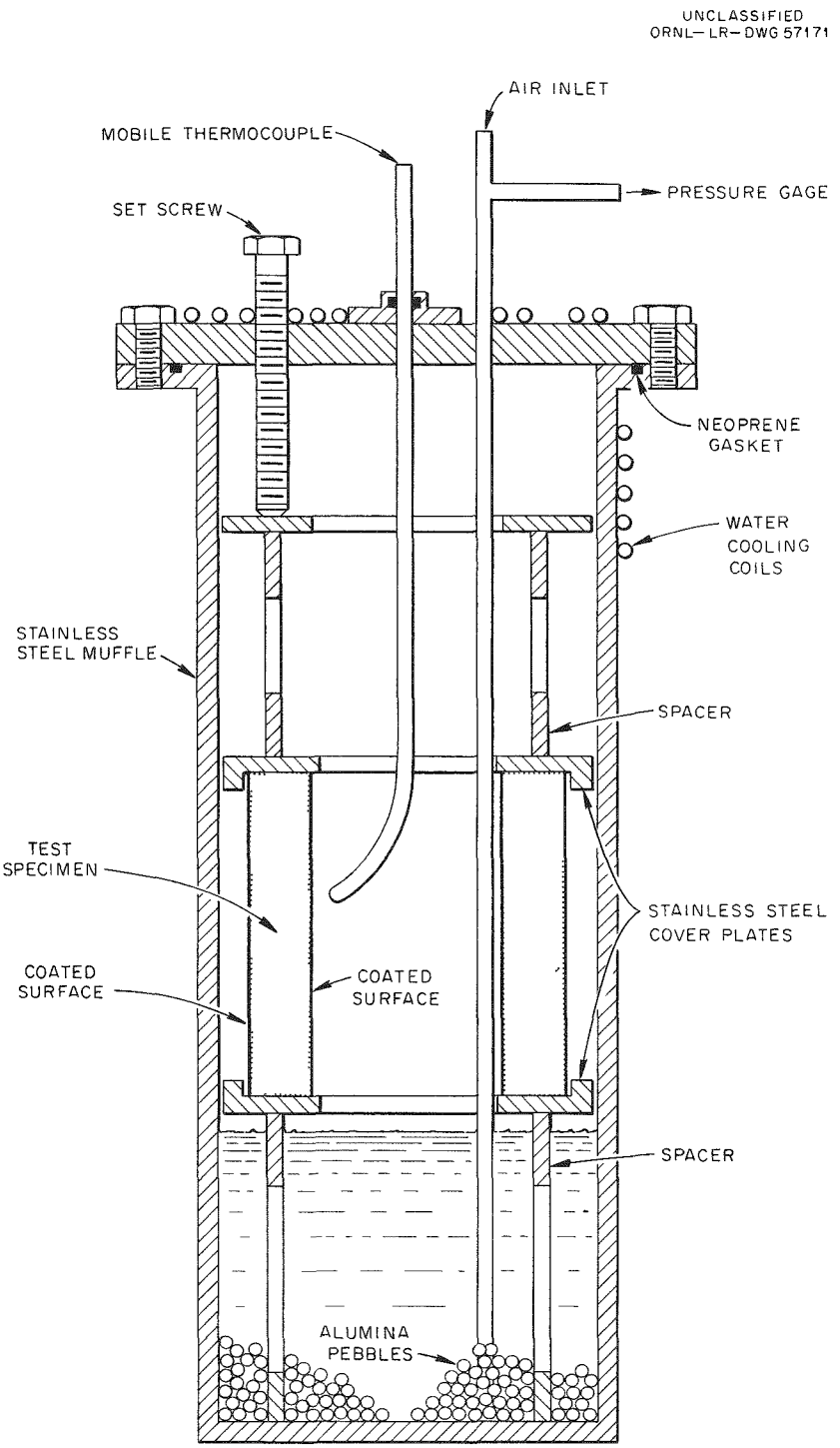

Fig. 4.9. Graphite Oxidation Test Assembly.

Table 4.4. Results of Oxidation Tests of Graphite at 600°C

Graphite Grade	Type of Coating	Coating Vendor	Test Time (hr)	Fractional Weight Loss
				$\times 10^{-3}$
NG-2	None		2	2.6
AGOT	None		2 1/2	12
R1-HLM	None		2	4.2
AHDG-1A	None		2	6.0
NG-2	SiC	National Carbon Company	2	1.7
NG-2	Si-SiC	American Lava Corporation	2	2.3
	SiC	Norton Company	2	5.2
901S	Si-SiC	American Lava Corporation	1 1/2	0.2
AHDG-1A	Pyrolytic graphite	American Metal Products Company	2	3.5

Several tests were made to determine the protection afforded by the coatings as a function of test temperature. The results of these tests are given in Table 4.5. The test conditions in all cases were identical for the coated and uncoated specimens. The uncoated specimens were cut from Speer nuclear grade 2 sleeves; the specimens coated by the National Carbon Company and the American Lava Corporation were of this same grade of graphite. The graphite used for the specimens coated by Norton was not identified.

The protection afforded by the coatings was observed to increase with temperature, but it is clear that the required twentyfold reduction in the

Table 4.5. Effect of Temperature on Protection Afforded by SiC Coatings

Temperature (°C)	Coating Vendor	Test Time (hr)	Air Flow (cfh)	Fractional Weight Loss per Hour		Ratio of Column 5 to Column 6 (approximate)
				Coated Specimen	Uncoated Specimen	
				$\times 10^{-3}$	$\times 10^{-3}$	
600	National Carbon Company	2	20	0.9	1.3	2/3
	American Lava Corporation	2	20	1.2	1.3	1
	Norton Company	2	20	2.6		
700	National Carbon Company	2	20	3.0	9.6	1/3
	American Lava Corporation	2	20	5.1	9.6	1/2
800	National Carbon Company	1	20	3.7	25	1/7
	American Lava Corporation	1	20	7.6	25	1/3
	Norton Company	1	20	20		
900	National Carbon Company	1	60	3.7	63	1/17

oxidation rate was not achieved below 900°C in these tests. It is important to note, however, that 901S graphite was not used as the base material in any of these tests.

Thickness Measurements. A tentative eddy-current technique has been developed for thickness measurement of SiC or siliconized SiC coatings on the EGCR graphite sleeve. One of the difficulties encountered has been the localized variation in conductivity over the surface of the sleeves. This has necessitated additional calibration curves for the extremes of conductivity, and has increased somewhat the uncertainty of the coating thickness measurement. Calibration accuracies seem to have a tolerance of ±0.001 in. or less.

Coating-thickness measurements have been made on representative sleeves from each of the three vendors (Speer, Great Lakes, and National Carbon) with coatings applied by National Carbon, American Lava, and Norton. The indicated coating thicknesses of the sleeves from National Carbon varied from about 25 to 60 mils, those from American Lava from about 2 to 6 mils, and those from Norton from about 9 to 17 mils. Representative sections of coatings from National Carbon Company have been prepared for metallographic examination. Several unsuccessful attempts have been made to use optical techniques for measuring the coating thickness on the sections. A technique has now been developed which seems to offer promise. Oblique lighting is used in making a magnified macrophotograph, which is then enlarged. The resultant print gives approximately a 12.5 magnification. A calibrated scale in the photograph permits direct measurement of the coating thickness. Because of the very irregular coating-graphite interface only an average rather than absolute measurement can be made.

A tentative eddy-current technique has been developed for the measurement of pyrolytic graphite coatings on EGCR sleeves. This technique has been applied to coatings prepared by High Temperature Materials, Inc., on sleeves from each of the three graphite vendors. Since it was not practical to obtain calibration samples to simulate different thicknesses of the pyrolytic graphite coating, no preliminary calibration curves were made. Calibration curves for converting eddy-current readings to thickness measurements must await metallographic and optical measurements. The identity of

each sleeve was lost during the coating process. Therefore, calibration curves will have to provide a scatter band to cover the entire range of conductivity variation found in the three types of sleeves. Obviously this will reduce the attainable accuracy.

Integrity of Coatings. Since samples of type 901S graphite were obtained previously[9] that had continuous and crack-free siliconized-SiC coatings, further studies of the electrode potential test were made. A galvanic cell was established using one of these samples as an electrode. The generated emf was measured with the coated graphite and with the coating removed to expose the bare graphite. A generated voltage of about 0.75 was found to be the maximum for a coated sample, but bare graphite gave a maximum voltage of 2.1. The potential generated by the exposed graphite was also found to vary with the area of contact. For an area 1/16 in. in diameter, an emf of 1.2 v was noted, while for areas with diameters of 5/32, 11/32, and 15/32 in., voltages of 1.6, 1.9, and 2.1 were noted. Hence, it appears that by monitoring the potential, it can be determined how much graphite is exposed through the coating.

Mechanical Properties of AGOT Graphite (C. R. Kennedy)

An examination of the mechanical properties of AGOT graphite is being made in order to predict its performance in the EGCR. The graphite columns in the reactor will initially be under a compressive loading. However, in operation the graphite will be subject to shrinkage induced by the fast-neutron flux. Because the neutron flux will vary from point to point in the reactor, bending strains will accumulate in the graphite columns. It is, therefore, desirable to investigate the mechanical properties, the effect of time and temperature on the properties, and the creep behavior of AGOT graphite in order to establish a failure criterion.

Specimens from three blocks of AGOT graphite have been examined using incrementally loaded and short-time tensile tests, short-time bending tests, and creep tests under compressive, tensile, and bending loads. The incrementally loaded tests are essentially very long-time tensile tests designed to investigate the time dependency in the tensile behavior of the graphite. The results of all short-time tests are summarized in Table 4.6. Specimens

from block 1 oriented parallel to the extrusion axis were tensile tested at room temperature and at 750°F, yielding fracture stresses of 2060 to 2370 psi, which are very consistent for graphite. The fracture strain, however, was not as consistent, varying from 0.152 to 0.206%. Incremental

Table 4.6. Tensile Properties of AGOT Graphite

Specimen No. and Orientation[a]	Block No.	Type Test[b]	Temperature[c] (°F)	Modulus of Elasticity (psi)	Fracture Stress (psi)	Fracture Strain (%)
				× 10^6		
8 P	1	Increment load	75	1.75	2050	0.154
1 P	1	Increment load	750	1.90	1900	0.165
12 P	1	Increment load	1100	1.50	1920	0.220
22 P	1	Increment load[d]	75	1.53	2220	0.200
14 P	1	Tensile	75	1.70	2635	0.205
17 P	1	Tensile	75	1.73	2315	0.206
18 P	1	Tensile	75	1.81	2310	0.175
19 P	1	Tensile	75	1.60	2300	0.200
23 P	1	Tensile	75	1.67	2370	0.205
24 P	1	Tensile	75	1.56	2290	0.206
26 P	1	Tensile	75	1.88	2270	0.178
42 P	1	Tensile	75	1.94	2072	0.163
43 P	1	Tensile	75	1.55	2141	0.176
44 P	1	Tensile	75	1.68	2208	0.189
45 P	1	Tensile	75	1.79	2063	0.152
46 P	1	Tensile	75	1.55	2101	0.193
30 N1	1	Tensile	75	0.55	674	0.142
33 N1	1	Tensile	75	0.54	814	0.208
35 N1	1	Tensile	75	0.55	618	0.124
37 N2	1	Tensile	75	0.58	1620	0.412
38 N2	1	Tensile	75	0.70	1363	0.298
39 N2	1	Tensile	75	0.56	1268	0.312
40 N2	1	Tensile	75	0.60	1250	0.300
10 P	1	Tensile	750	1.88	2270	0.178
1 N1	2	Tensile	75	0.78	1645	0.299
8 N1	2	Tensile	75	0.63	1865	0.405
23 N2	2	Tensile	75	0.53	1770	0.357
24 N2	2	Tensile	75	0.62	1895	0.342
25 P	2	Tensile	75	1.07	965	0.078
26 P	2	Tensile	75	1.14	1170	0.119
27 P	2	Tensile	75	0.94	1335	0.146

[a] P indicates specimens oriented parallel to extrusion axis; N1 indicates specimens oriented normal to extrusion axis; and N2 indicates specimens oriented normal to extrusion axis and N1 direction.

[b] Incremental tests loaded at approximately 2 psi/hr and tensile tests at approximately 600 000 psi/hr.

[c] All tests at 750 and 1100°F were run in argon.

[d] Creep tested under 1800 psi for 1323 hr and then incrementally loaded to failure at 0.267 psi/hr.

loading tests were also performed on the first block, on specimens oriented in the parallel direction, at 75, 750, and 1100°F, that yielded fracture stresses varying from 1900 to 2220 psi. These results are also quite consistent, although the values were lower than those obtained in the tensile tests. The fracture strains again demonstrated scatter, ranging from 0.154 to 0.22%. Results of these two series of tests demonstrate that the fracture stresses and strains are not temperature dependent from room temperature to 1100°F and are not time dependent over at least six orders of magnitude.[10]

Further verification that the deformation of graphite is not thermally activated over this temperature range is demonstrated by the results of creep tests. The results obtained at 78, 750, and 1100°F, presented in Fig. 4.10, illustrate that there is slight initial creep which saturates in a few hours and that no creep occurs thereafter. The strain-recording equipment is accurate to within 10^{-5} in./in., and thus the creep rate of these specimens must be less than 5×10^{-9} in./in.·hr.

The strength of graphite is normally assumed to be greatest in the direction parallel to the extrusion axis, and it demonstrates rotational

[10]GCR Quar. Prog. Rep. June 30, 1960, ORNL-2964, pp. 99–102.

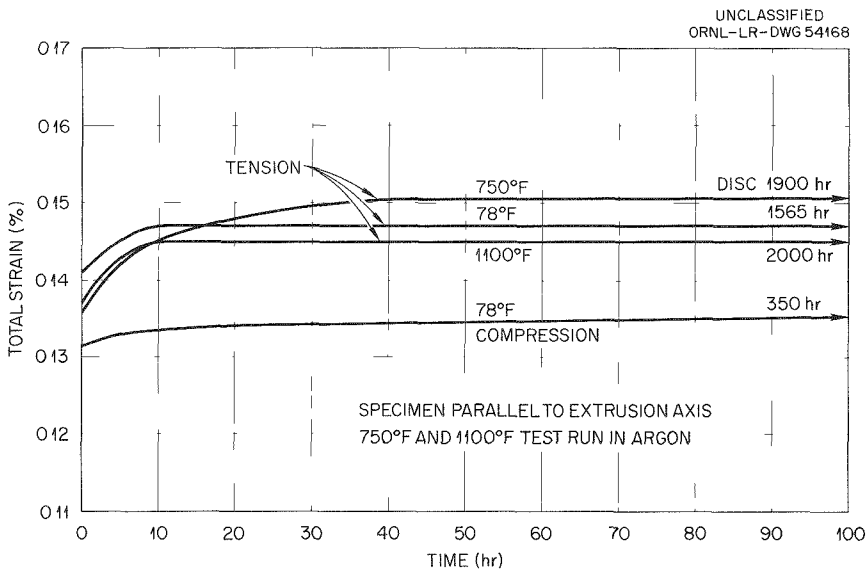

Fig. 4.10. Creep Tests of 4- by 4-in. Specimen (Block 1) of AGOT Graphite Under a Pressure of 1800 psi.

symmetry such that all transverse directions should have similar strength values. The results of tensile tests of specimens oriented in three directions in the first block do show that the parallel direction is strongest; however, the block does not have rotational symmetry, as may be seen in Fig. 4.11. The results of testing the second block demonstrated rotational symmetry; however, the transverse strength was greater than the parallel strength. These results are shown in Fig. 4.12. Radiography of the specimens from block 2 showed low-density zones oriented normal, or nearly normal, to the extrusion axis. The representative radiographs of these specimens shown in Fig. 4.13 serve to explain the loss of strength in the parallel direction. However, there were no indications in the radiographs of specimens from the first block that would explain the loss of rotational symmetry.

Tensile specimens from the third block, which is part of an actual EGCR column, have not been tested; however, radiographs of the specimens show gross low-density regions or cracks which will greatly limit the strength. These low-density regions in block 3 are preferentially oriented normal to a transverse direction.

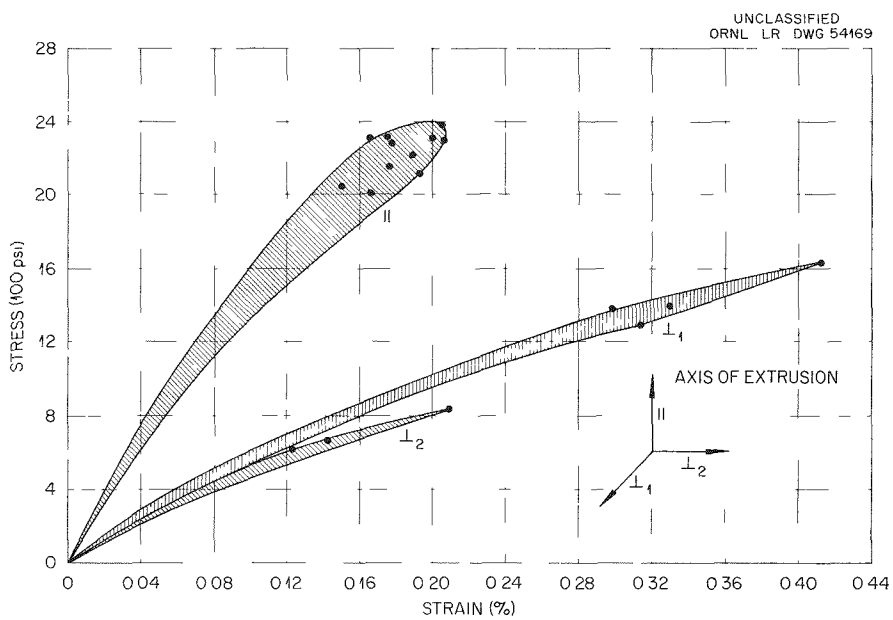

Fig. 4.11. Tensile Properties of AGOT Graphite, Block 1.

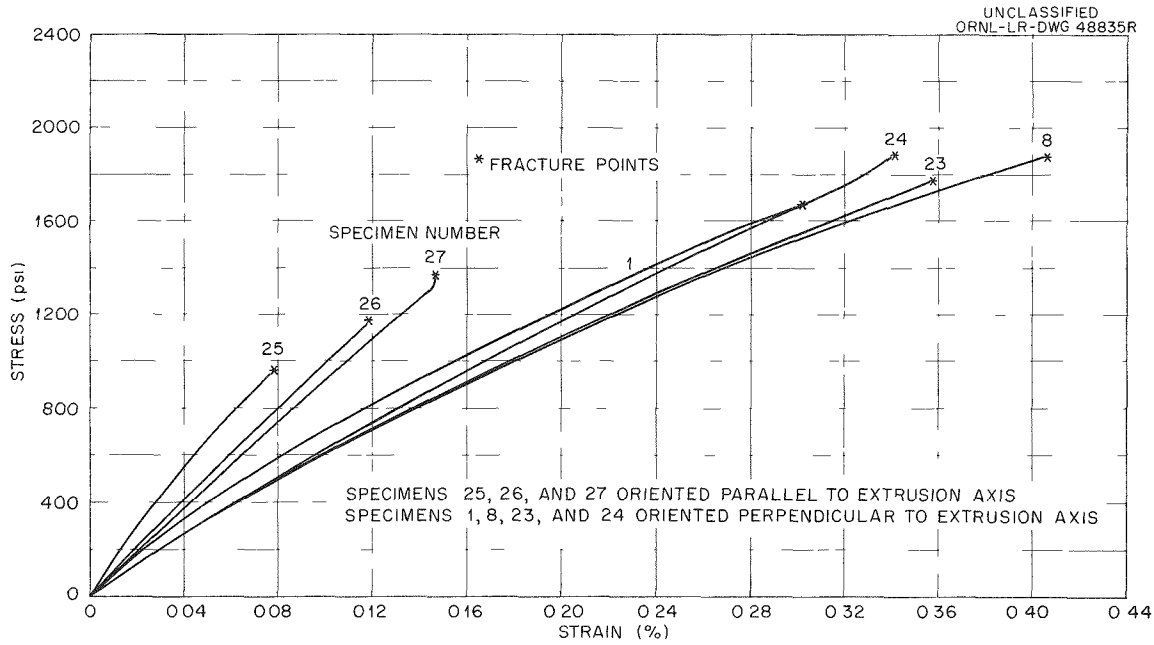

Fig. 4.12. Tensile Properties of Specimens from 16- by 16-in. AGOT Graphite Block 2.

One compressive creep test has been performed on a specimen from block 1. The results are also shown in Fig. 4.10 for comparison with the tensile creep results. The general form of the creep curve is similar to the form of the tensile creep curves.

Creep and short-time bending tests have been performed on specimens from blocks 1 and 3. The tensile test results are compared with the results of the short-time bending tests on block 1 in Fig. 4.14. The data show rather conclusively that the bending strength is greater than the tensile strength, but the strains at fracture are very similar. Actually, the bending stress values calculated elastically are in error, since some yielding does occur; however, this error is small. These tests were performed by measuring the deflection and by measuring the tensile and compressive fiber strain by means of strain gages. The error between an elastic calculation of the strains from the deflection and the actual strains, as measured, was in all cases less than 10%. Short-time bend test results for specimens from block 3 are compared in Fig. 4.15 with

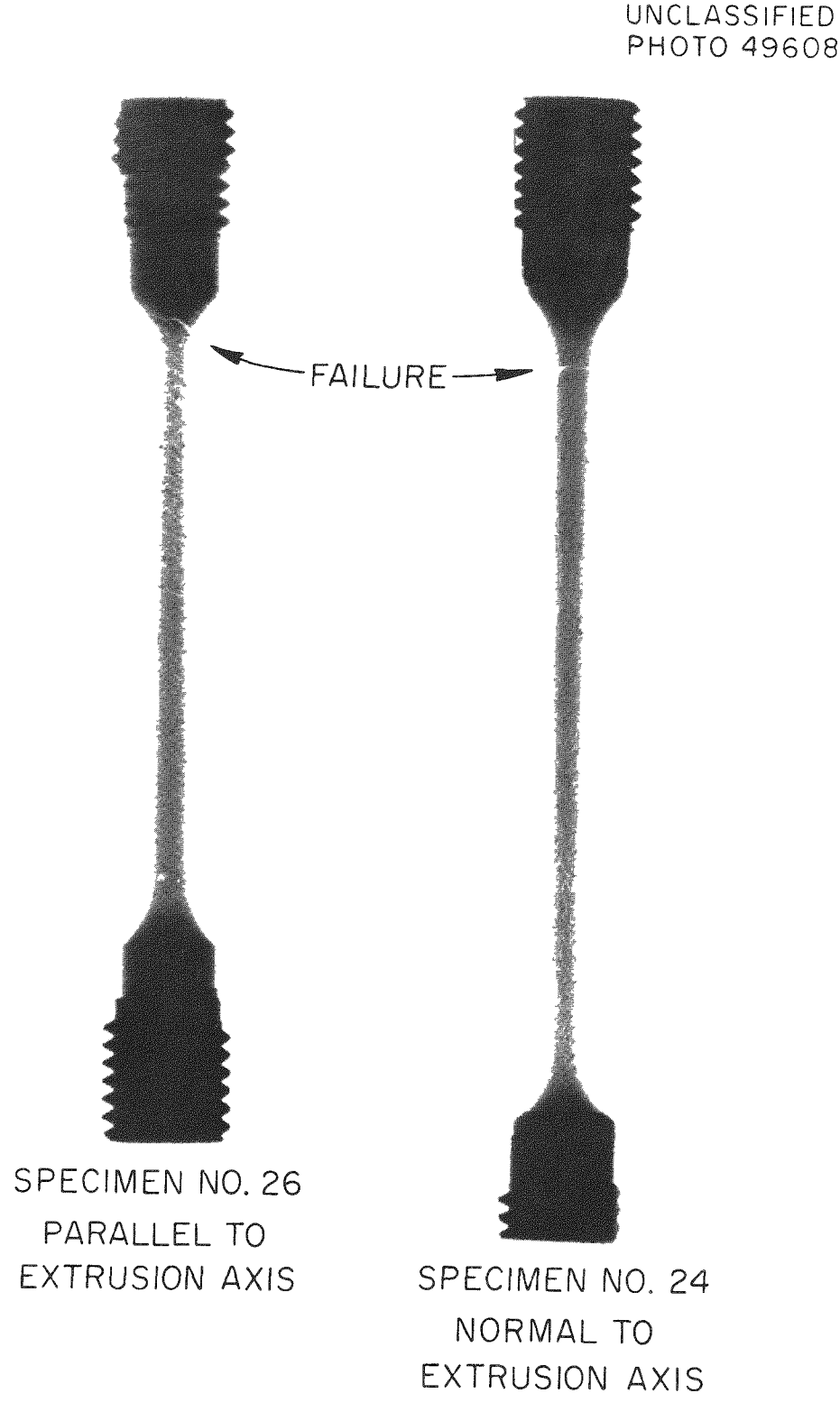

Fig. 4.13. Tensile Specimens from AGOT Graphite Block 2.

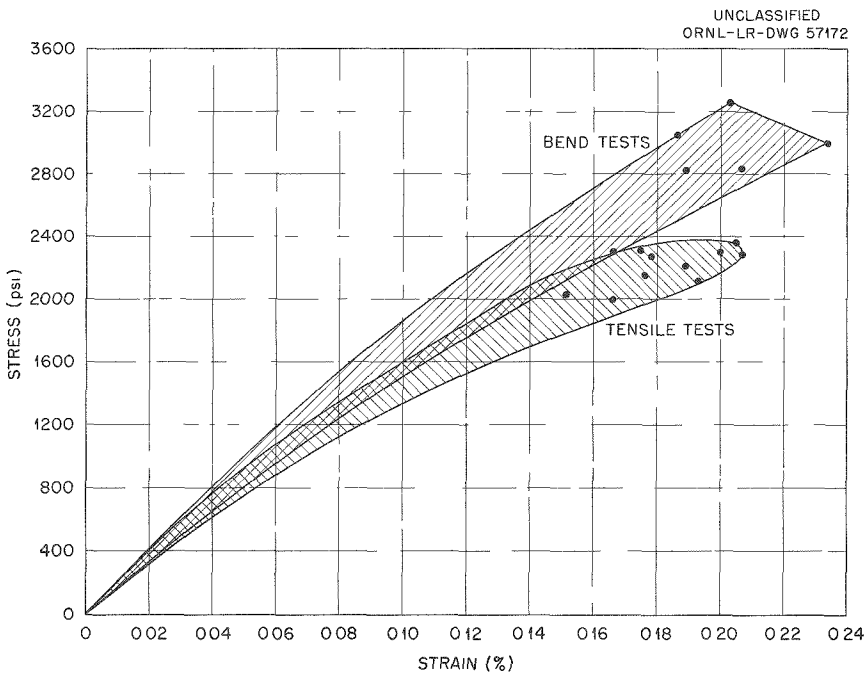

Fig. 4.14. Comparison of Tensile and Bending Properties of AGOT Graphite Short-Time Tested Under Third-Point Bending Loads at Room Temperature, Block 1.

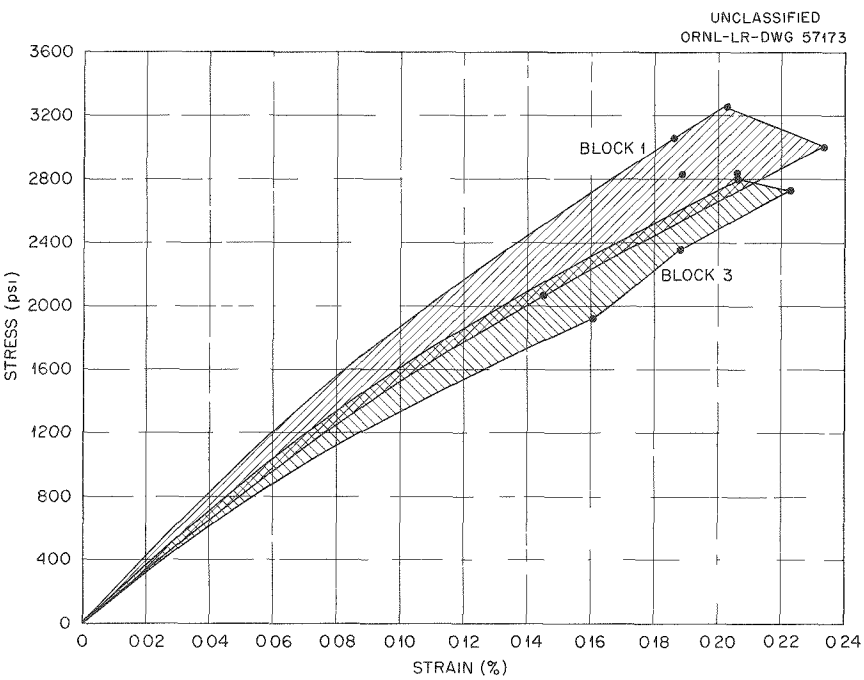

Fig. 4.15. Comparison of AGOT Graphite Blocks 1 and 3 Short-Time Tested Under Third-Point Bending Loads at Room Temperature.

the results obtained from testing block 1. The results show that the scatter of the results for block 3 is large and that the average strength is somewhat lower than for block 1. The results obtained in testing block 3 correlate closely with the distribution of low-density regions found in the specimens. These first five specimens are the first of 50 specimens taken from a single cross section for determining the strength gradient across the large column.

The results of creep testing of block 1 in bending are shown in Fig. 4.16. Again the shape of the creep curve is quite similar to the shapes of the tensile creep curves. It is interesting to note that the tensile and compressive strains eventually become similar, although they are different initially. This is caused by an initial shifting of the neutral axis as a result of the difference between the elastic modulus in tension and in compression. This induces the compressive stress to

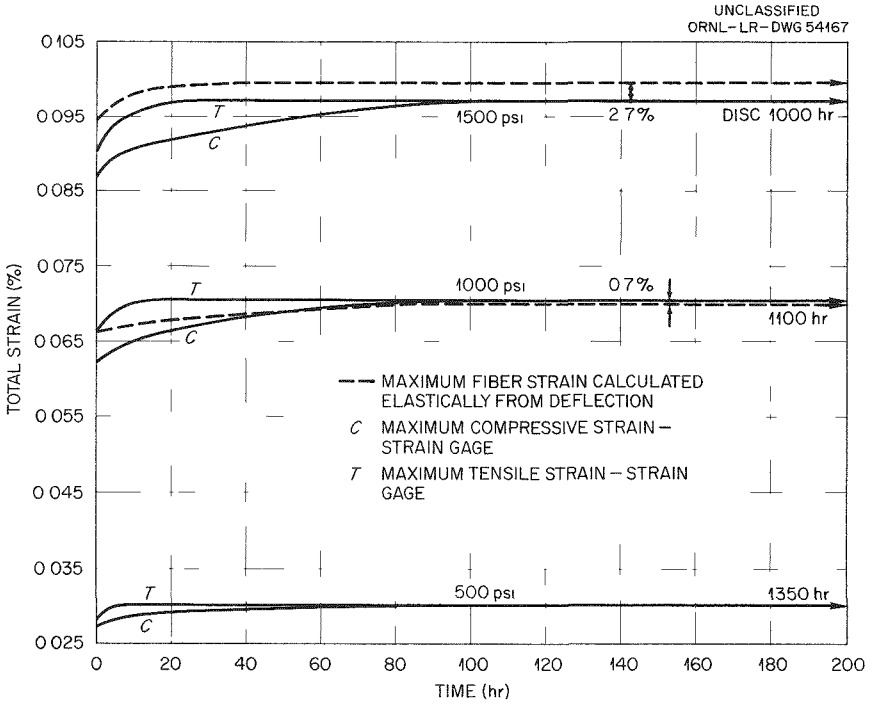

Fig. 4.16. Creep Data for AGOT Graphite Block 1 Tested Under Third-Point Bending Loads at Room Temperature.

become greater than the tensile stress, with the result that the neutral axis shifts back to the center again during creep.

The following conclusions can be stated on the basis of results from the test program:

1. The mechanical properties of graphite are not thermally activated in the temperature range from 78 to 1100°F; thus, the fracture stresses and strains are not dependent on time or temperature.

2. There exists wide variations in mechanical properties, and the mechanical anisotropy is difficult to predict.

3. The fracture stresses calculated elastically for bending are greater than the fracture stresses under tensile loads; however, the fracture strains are very similar.

4. There is a slight initial creep; however, the creep rate diminishes to less than 5×10^{-9} in./in.·hr in a short period of time.

5. The very low ductility of graphite indicates that it will not sustain tensile strains produced by variable shrinkage without fracturing unless the radiation-induced shrinkage is inhibited by stress or unless, under irradiation, graphite will sustain greater tensile strains without fracture.

Experimental Tube Collapse (J. T. Venard)

Three specimens having radius-to-thickness ratios of approximately 15 were collapsed under an external pressure of 600 psi at 1200°F. Their collapse times were 2783, 3615, and 4222 hr. Another similar specimen collapsed in 26 hr under an external pressure of 750 psi at 1200°F.

Material has been received for machining approximately 200 specimens of various sizes and radius-to-thickness ratios. This material is presently being inspected for flaws, and dimensional measurements are being made. Considerable difficulty has been experienced in maintaining leak-tight systems and good temperature control over the specimen length. The installation of new furnaces and test chambers is in progress.

Plastic Axial Elongation of Simulated EGCR Fuel Element During Thermal Cycling (W. R. Martin)

Axial elongation of a simulated EGCR fuel element during thermal cycling was observed previously[11] by using radiographic techniques to measure the

[11]GCR Quar. Prog. Rep. Dec. 31, 1960, ORNL-3049, pp. 213–6.

amount of plastic elongation. The experimental procedure and apparatus have been modified to permit measurement of the axial elongation by utilizing a variable differential transformer. The simulated element and extensometer are shown in Fig. 4.17.

The test results obtained with the revised technique show somewhat less elongation than reported previously, and they reveal the significance

UNCLASSIFIED
Y-38105

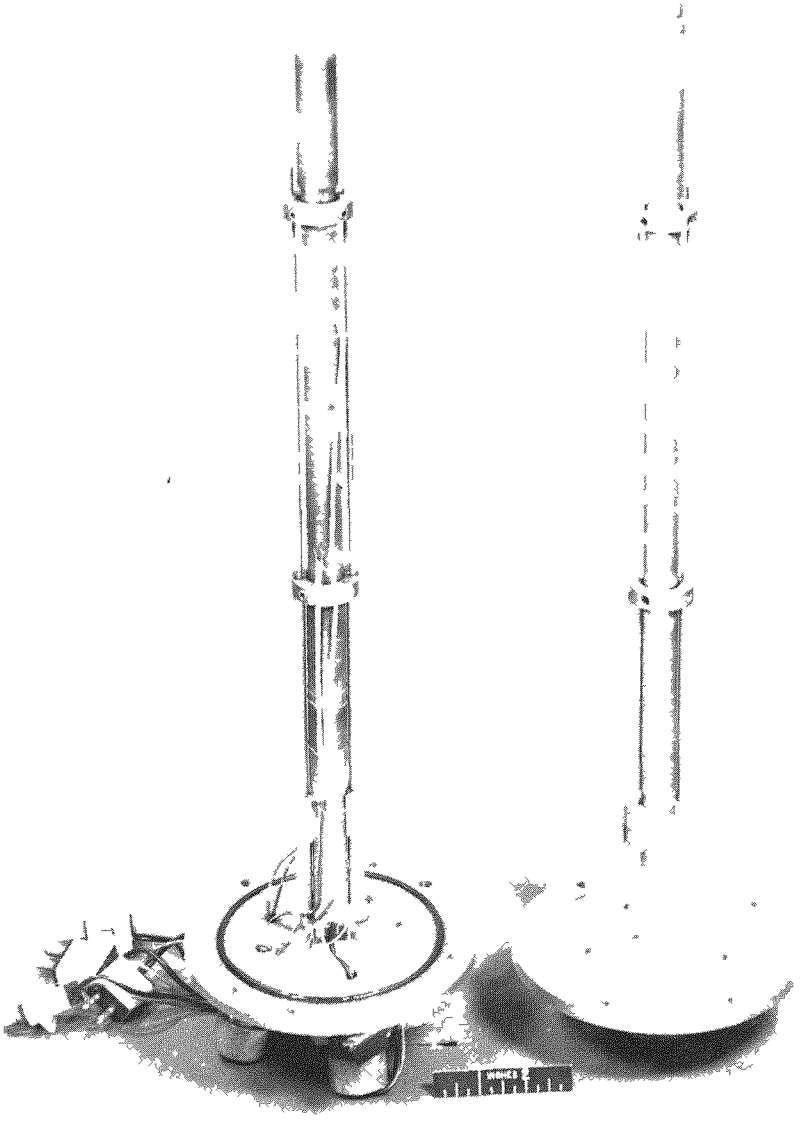

Fig. 4.17. Simulated EGCR Fuel Element with Extensometer Attached for Use in Thermal-Cycling Experiments.

of the lower temperature limit of the thermal cycle. The data, summarized in Table 4.7, show that axial elongation of the cladding did not occur after the lower temperature limit was raised to approximately 1000°F.

Table 4.7. Axial Elongation of Simulated EGCR Fuel Element During Thermal Cycling

Temperature Limits (°F)		Total Cycles	Rate of Elongation
Upper	Lower		
1500	1184	50	None
1500	1004	46	None
1500	950	10	Not measurable
1500	752	43	0.00015 in. per cycle
1500	700	46	0.00017 in. per cycle
1500	572	12	0.00025 in. per cycle

From this series of tests, the following conclusions were formulated:

1. The axial elongation rate or plastic strain per cycle is linear at a given temperature.

2. Heating and cooling rates during the thermal cycle affect the growth rate.

3. As the hold time during the elevated temperature portion of the thermal cycle is increased, the growth for that cycle also increases, asymptotically approaching a maximum with time.

4. The EGCR fuel elements will not deform plastically in the axial direction when cycled between temperature limits of 1000 and 1500°F.

Reactions of Type 304 Stainless Steel with CO-CO_2 Mixtures (H. Inouye)

Additional tests of type 304 stainless steel in mixtures of CO plus CO_2 in helium were completed in which 16 specimens were exposed for 1390 hr. The temperatures of these specimens ranged between 725 and 1850°F. The CO_2 was maintained at 0.117 vol % and the CO at 0.175 vol %, for a CO_2-to-CO ratio of 0.669 and a CO + CO_2 concentration of 0.292 vol % (based on helium at 315 psi pressure).

Oxidation of Type 304 Stainless Steel in CO-CO_2 Mixtures. The oxidation rate of the specimen at 1800°F followed a parabolic reaction rate for a period of about 500 hr, as in previous tests. However, after this time, an increasing oxidation rate was observed which persisted for the remaining test period. Based on the results of previous tests, an average weight gain of about 3 mg/cm^2 would be expected; however, in this case a weight gain of 4.3 mg/cm^2 was observed. Examination of the specimen after test showed that the reaction had resulted in the formation of large blisters. It was not possible to determine the temperature effects of this gas composition on the oxidation rates, because the oxide scale was not adherent after cooling the specimens to room temperature.

Previous tests[12] showed that the oxidation rates were independent of either the $CO + CO_2$ concentration up to 0.325 vol % or the CO_2-to-CO ratios up to 0.46. The results of this test show that a "break-away" phenomenon (accelerated oxidation) was encountered. The acceleration in the oxidation rate is thought to be due to the formation of $3Cr_2O_3 \cdot Fe_2O_3$, which has been identified as the solid reaction product in gases containing a high ratio of CO_2. The approximate reaction for its formation is

$$2Fe + 6Cr + 12CO_2 \rightarrow 3Cr_2O_3 \cdot Fe_2O_3 + 12CO \quad . \qquad (1)$$

The equilibrium constant, K, for the reaction is given by

$$K = \frac{A_{oxide} \, (P_{CO})^{12}}{(A_{Cr})^6 \, (P_{CO_2})^{12}} \quad ; \qquad (2)$$

that is, the activity of the oxide (A_{oxide}) is proportional to P_{CO_2}/P_{CO}. The above relationship leads to the conclusion that the formation of $3Cr_2O_3 \cdot Fe_2O_3$ is governed by P_{CO_2}/P_{CO} and is independent of the concentration of $CO + CO_2$. This is supported by the results of a previous test in which the $CO + CO_2$ was 0.325 vol % but no acceleration in the oxidation

[12]GCR Quar. Prog. Rep. Dec. 31, 1960, ORNL-3049, pp. 216–8.

rate was observed. If the oxidizing potential of the gases increases as P_{CO_2}/P_{CO} increases, it would be expected that still higher ratios of CO_2 to CO will cause the "break-away" reaction to occur at shorter times.

Carburization of Type 304 Stainless Steel in CO-CO_2 Mixtures. The factors governing the carburization of type 304 stainless steel in CO_2-CO mixtures were re-evaluated on the basis that the controlling reaction is

$$\text{Stainless steel} + 2CO \rightarrow \underline{C}\ (\text{in alloy}) + CO_2$$

or

$$K = \frac{(A_C)(P_{CO_2})}{(P_{CO})^2} \quad \text{and} \quad A_C = K\frac{(P_{CO})^2}{P_{CO_2}}$$

from which the activity of carbon (A_C) is found to be proportional to $(P_{CO})^2/P_{CO_2}$ instead of P_{CO_2}/P_{CO}, as reported previously.[13]

The gas compositions and the corresponding calculated values for the oxygen activities, P_{CO_2}/P_{CO}, and the carbon activities, $(P_{CO})^2/P_{CO_2}$, are presented in Table 4.8. The data show that the oxidizing tendencies of the gases depend only on the ratios of the gases, while the carburizing tendencies depend on the ratios of the gases and on their concentrations.

The effect of the carbon activity of the gas phase on the extent of carburization observed in the metal samples is shown in Table 4.9. Although a strict comparison is not possible because of the differences in the test time, it is apparent that the carbon content of the metal increased as the carbon activity increased. For the tests conducted at the lower values of the carbon activity or the short test time, maxima in the carbon contents were observed at about 1500°F. These phenomena indicate that the rate of the carburizing reaction is a variable, as well as the ratio of the gases.

[13]GCR Quar. Prog. Rep. Dec. 31, 1960, ORNL-3049, pp. 218–20.

Table 4.8. The Effect of the Concentration of CO and CO_2 on P_{CO_2}/P_{CO} and $(P_{CO})^2/P_{CO_2}$

CO[a] (vol %)	CO_2[a] (vol %)	(CO + CO_2)[a] (vol %)	P_{CO} (atm)	P_{CO_2} (atm)	P_{CO_2}/P_{CO}	$(P_{CO})^2/P_{CO_2}$
0.175	0.117	0.292	0.0372	0.0249	0.669	0.0557
0.014	0.0062	0.0202	0.0030	0.00134	0.462	0.0076
0.207	0.0248	0.2318	0.0444	0.00532	0.120	0.371
0.319	0.0057	0.3247	0.0684	0.00123	0.018	3.79

[a]Based on helium plus impurities at a pressure of 315 psi.

Table 4.9. Carburization of Type 304 Stainless Steel in CO-CO_2 Mixtures at Various Levels of $(P_{CO})^2/P_{CO_2}$

Test Temperature		Final Carbon Content (wt %)			
°C	°F	$(P_{CO})^2/P_{CO_2}$ = 0.0076, 700-hr Test	$(P_{CO})^2/P_{CO_2}$ = 0.0557, 1390-hr Test	$(P_{CO})^2/P_{CO_2}$ = 0.363, 840-hr Test	$(P_{CO})^2/P_{CO_2}$ = 3.79, 200-hr Test
400	750	0.065	0.065	0.070	0.068
500	930	0.065	0.066	0.070	0.068
600	1110	0.065	0.082	0.075	0.075
700	1290	0.093	0.121	0.100	0.120
800	1470	0.137	0.150	0.190	0.290
900	1650	0.115	0.142	0.407	0.177
1000	1830	0.027	0.055	0.732	0.095

Thermal Stability of Sb_2O_4 (A. T. Chapman, R. E. Meadows)

The formation and stability of Sb_2O_4, which has been proposed for use in an antimony-beryllium neutron source in the EGCR, was investigated. Preliminary ignition tests on 6- to 8-g samples of Sb_2O_3 for 30 min indicated that oxidation occurred at 600, 800, and 1000°C. However, the weight increase during ignition did not approach 5.49%, which would correspond to complete conversion of Sb_2O_3 to Sb_2O_4. The weight gain at 1000°C was less than that observed at 600 and 800°C, suggesting that Sb_2O_4 may dissociate at higher temperatures. Thermogravimetric measurements and differential thermal analysis (DTA) showed that at a heating rate of 10°C/min in air

the oxidation of Sb_2O_3 began at 525°C and was essentially complete at 650°C. During the latter stages of this experiment, a slight weight decrease was noted, indicating again the loss of oxygen at 950 to 1000°C. The ignition of another sample of Sb_2O_3 at a temperature below 525°C for a prolonged period, 60 hr at 400°C, indicated that oxidation was proceeding slowly. This ignition resulted in a weight gain of 5.36%; x-ray diffraction analysis of the product showed complete conversion to Sb_2O_4.

A calculation of the equilibrium oxygen pressures for the reaction $Sb_2O_4 \rightarrow Sb_2O_3 + 1/2\ O_2$, using existing thermodynamic data, gave the following results:

Temperature (°C)	Equilibrium Oxygen Pressure (atm)
600	1.1×10^{-5}
800	2.5×10^{-3}
1000	1.6×10^{-1}

These calculations indicate that the dissociation of Sb_2O_4 should not occur at 1000°C in air, where the oxygen partial pressure is approximately 0.2 atm. However, the ignition and thermal gravimetric analysis described above, as well as several literature references, indicated that Sb_2O_4 does lose oxygen at 1000°C. A temperature of 800°C, which is some 200°C above the anticipated service temperature, was selected for a long-term weight-change analysis. The ignition data for 6.75 g of Sb_2O_4 heated at 800°C for 72 hr are presented below:

Time (hr)	Weight Change Between Successive Measurements (mg)
4	−5.5
20	−3.3
28	−0.5
44	0.0
72	+0.2

This work indicated that the use of Sb_2O_4 may be feasible, since there is no indication of melting and the equilibrium oxygen pressure is less than 0.2 atm at 800°C. It should be noted, however, that the continuous

loss of oxygen from the capsule containing the Sb_2O_4 to a "getter" or through a leak would increase the concentration of Sb_2O_3 in the Sb_2O_4.

Manufacturing and Inspection Methods Development

Fabrication of Instrumented Capsules and Fuel Elements (E. A. Franco-Ferreira)

Work is proceeding on the fabrication of instrumented fuel capsules for in-pile irradiation tests in the ORR. The instrumentation and method of assembly of the capsules are similar to those of the fuel elements for the proposed instrumented fuel assembly for the EGCR. Each capsule contains two 0.040-in.-o.d. stainless steel-sheathed Chromel-Alumel thermocouples for cladding temperature measurements and a central thermocouple well for the measurement of the maximum fuel temperature. The capsule components are shown in Fig. 4.18. The cladding-temperature thermocouples

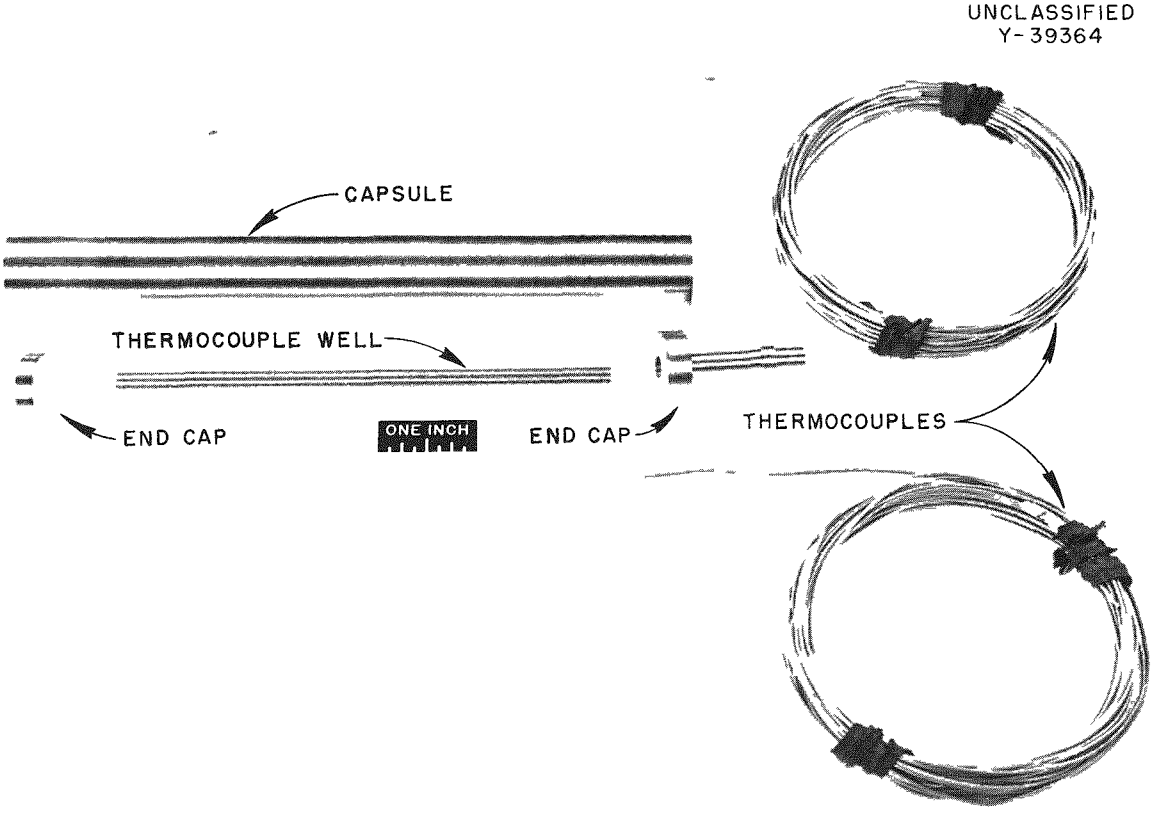

Fig. 4.18. Components of Instrumented Capsule.

are attached by the following procedure: (1) two holes are drilled diametrally opposite each other near the edge of the end cap; (2) the end cap is welded into the tube; (3) thermocouples are passed through the holes and the junctions are capacitor-discharge welded to the inside wall of the tube; and (4) the thermocouples are brazed with GE-81 alloy at the junction attachments and where they pass through the end cap.

Two subassemblies are illustrated in Fig. 4.19, and a typical attachment of a cladding thermocouple is shown. Metallographic sections taken through the end cap at the braze joint where the thermocouple is attached have revealed good fit-up and good flowability. Leaktight brazes can consistently be made.

The attachment of the thermocouple well to the top end cap is accomplished by brazing with gold, as previously reported.[14] The following

[14]GCR Quar. Prog. Rep. Dec. 31, 1960, ORNL-3049, pp. 221–2.

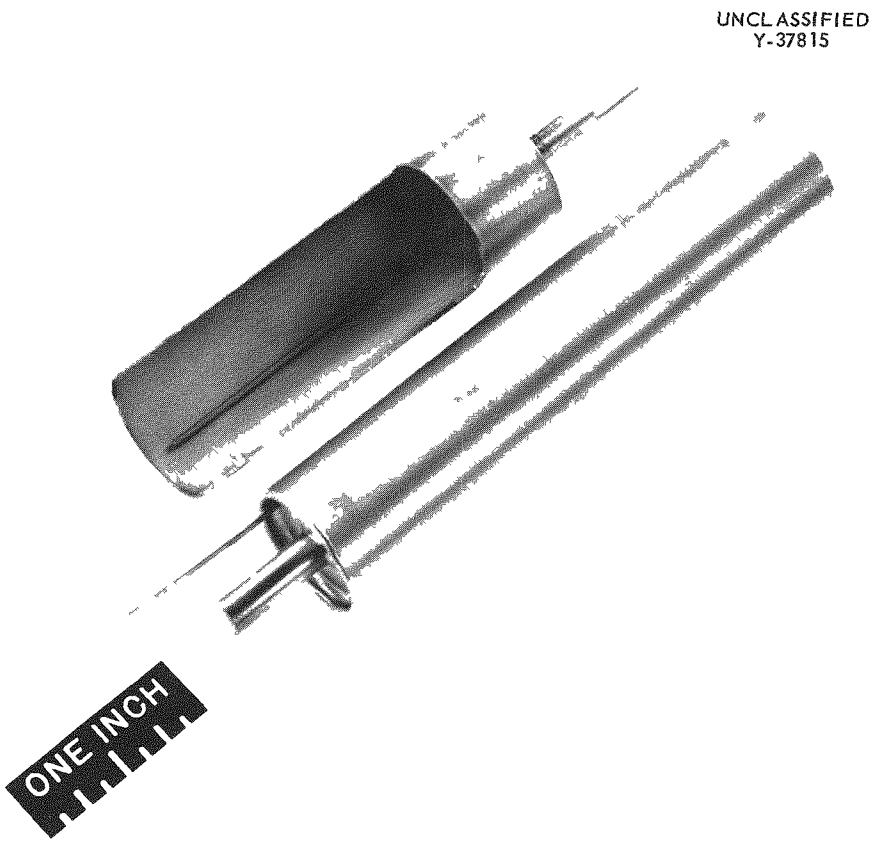

Fig. 4.19. Cladding Thermocouple Test Assembly Showing General Location of Attachment.

materials are under consideration for use as central thermocouple wells: tungsten, molybdenum, and Fansteel 82, a columbium-base alloy. Capsules have been built with all three of these thermocouple well materials, and it is expected that subsequent testing will enable a definite selection to be made for use in the EGCR instrumented fuel assemblies.

After the brazing operations are completed, the capsules are loaded with fuel pellets and the opposite end cap is welded. Those fuel pellets that pass over the cladding thermocouples are grooved to accept the thermocouples. A completed capsule is shown in Fig. 4.20.

Strength of EGCR Fuel Element End Closures (R. G. Gilliland)

As a result of the various studies and experiments on the dimensional stability of fuel elements, a decision was made to eliminate the head space

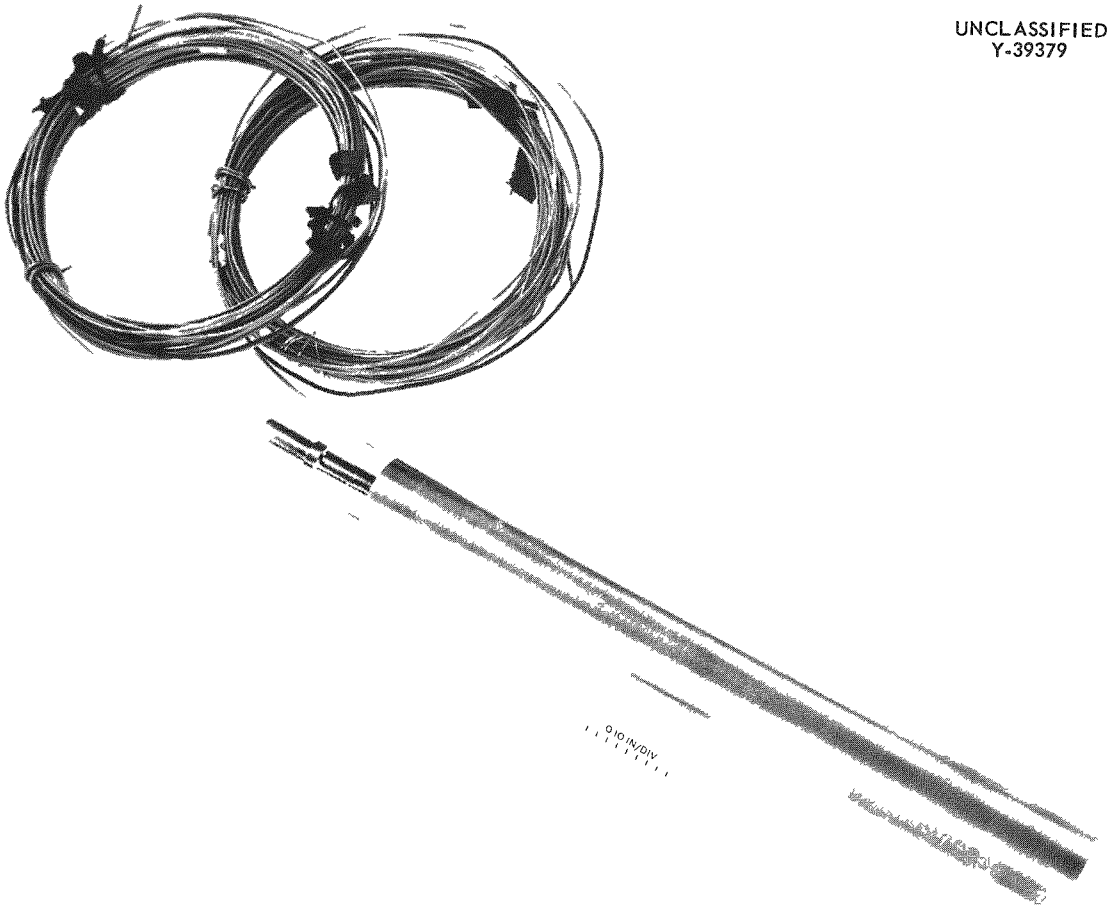

Fig. 4.20. Completed Instrumented In-Pile Capsule Assembly.

originally proposed between the end caps and the MgO wafer in the EGCR fuel elements. A question then arose concerning the strength of the end-cap welds in the case of slight expansion of the fuel column with respect to the cladding under certain conditions. Tests were initiated to determine the actual strength of weld joints of the EGCR design at room and elevated temperatures.

The specimens used in these tests were 6-in.-long type 304 stainless steel capsules fabricated with the EGCR end-cap design. Iron slugs were placed inside the capsules to simulate the fuel pellets. Rods, 3/8 in. in diameter, were attached to the end caps for testing the specimen in tension. These specimens were subjected to tensile tests at room temperature, 1300, and 1500°F. The results of these tests are presented in Table 4.10. Since the maximum extension of the UO_2 fuel length is predicted to be only 0.3% and the minimum extension before failure of the cladding was 2.7%, the strength and ductility of the end-closure welds appear to be adequate. All failures occurred in the heat-affected zones of the end-closure welds.

Table 4.10. Results of Tensile Tests on Mockup EGCR Fuel Elements

Sample No.	Test Temperature (°F)	Tensile Strength (psi)	Extension (%)	Yield Strength at 0.2% Offset (psi)
1	Room	57 400	3.0	37 200
2	Room	59 100	3.0	36 400
3	Room	58 700	3.0	38 100
4	1300	35 400	2.8	21 100
5	1300	31 000	2.7	17 600
6	1300	31 900	3.0	20 000
7	1500	20 000	11.6	13 000
8	1500	23 500	5.5	15 700
9	1500	23 000	6.2	15 100

Fabrication of Swaged Irradiation Test Capsules (J. T. Lamartine)

As a part of the program to study advanced fuels and fuel element concepts, capsules containing unsintered UO_2 were prepared for irradiation

to investigate the effects of surface area, density, and temperature on the rate of fission-gas release from such fuels. Four fuel capsules, approximately 6 1/4 in. long and 0.540 in. in diameter and clad with 0.020 in. of type 304 stainless steel, were fabricated for irradiation in the ORR poolside facility. Three of these capsules were produced by swaging UO_2 powder in stainless steel tubing at 800°C; these conditions were previously shown to reduce the surface area of the swaged UO_2.[15] The fourth capsule was fabricated by tamping the UO_2 fuel into a stainless steel tube. Pertinent characteristics of the four specimens are presented in Table 4.11.

Table 4.11. Fabrication Data on Swaged Irradiation Capsules Containing UO_2

Fuel Capsule	Type of UO_2	Method of Fabrication	UO_2 Density (% of theoretical)	Expected Irradiation Conditions	
				Linear Heat Rating (Btu/hr·ft)	Central Temperature (°F)
ORNL 1-S	Fused and ground	Swaged at 800°C	93.2	15 000	4420
ORNL 2-S	Fused and ground	Swaged at 800°C	93.2	8 000	2980
ORNL 3-S	High fired	Swaged at 800°C	86.6	15 000	4680
ORNL 5-S	Fused and ground	Tamp packed	58.3	8 000	3980

Nondestructive Inspection of EGCR Loop Through-Tube Welds (K. V. Cook, R. W. McClung)

Both V-groove and fillet welds have been proposed for use in the welding of the EGCR experimental loop through-tubes. The feasibility of using isotope radiography for inspecting these welds was studied on sample weldments of both types. An Ir^{192} source was placed in the center of the tube and the radiographic film was wrapped around the outside. Under optimum conditions, a 2% sensitivity was obtained by this method in portions of the radiograph. Slightly poorer sensitivities were observed in most of the film. Thus under the best conditions this procedure offers only marginal results.

[15] J. T. Lamartine and W. C. Thurber, Development of Swaged Stainless Steel Fuel Rods Containing UO_2, ORNL CF-59-10-8, Oct. 12, 1959.

Some discontinuities were detected in the welds by this method. However, when conventional x-ray techniques were used to determine the actual weld quality under more optimum conditions, many more discontinuities were found that had not been detected by the isotope examination. These discontinuities are being evaluated by comparing them with commercial standards of quality, such as the ASME Boiler Code.

Beryllium Investigations

Compatibility of Beryllium with Gases (W. J. Werner)

This report summarizes the status of the studies concerned with determining the factors that affect the accelerated oxidation, or "break-away" phenomenon, which is observed when beryllium is exposed to wet CO_2. At the time these studies were initiated there was considerable disagreement as to the effect of time, temperature, water vapor content of the CO_2, and fabrication history on the "break-away" phenomenon. As a result, the problem was approached from the standpoint of first understanding the reactions of beryllium with the individual gases in question (CO_2, H_2, and H_2O) and then correlating this information with the observed rates of oxidation in wet CO_2.

Reaction with CO_2. The reactions of beryllium with dry CO_2 were studied in the temperature range 550 to 720°C for periods up to 1000 hr at reduced and atmospheric pressure. Representative reaction rates at 550, 600, 650, and 720°C are shown in Fig. 4.21. The sample material for these tests was QMV beryllium powder (−200 +230 mesh), the analysis of which is presented in Table 4.12. In all cases the reaction with dry CO_2 was found to be independent of pressure; moreover, the rate of weight gain continuously decreased with time, indicating the formation of a protective oxide. The equations describing the reaction rates are of the form

$$\Delta w = Kt^{1/n} \quad ,$$

where Δw is the weight gain in $\mu g/cm^2$, K is a constant, t is the time in hours, and n is a constant. In this series of tests, n was approximately 2.

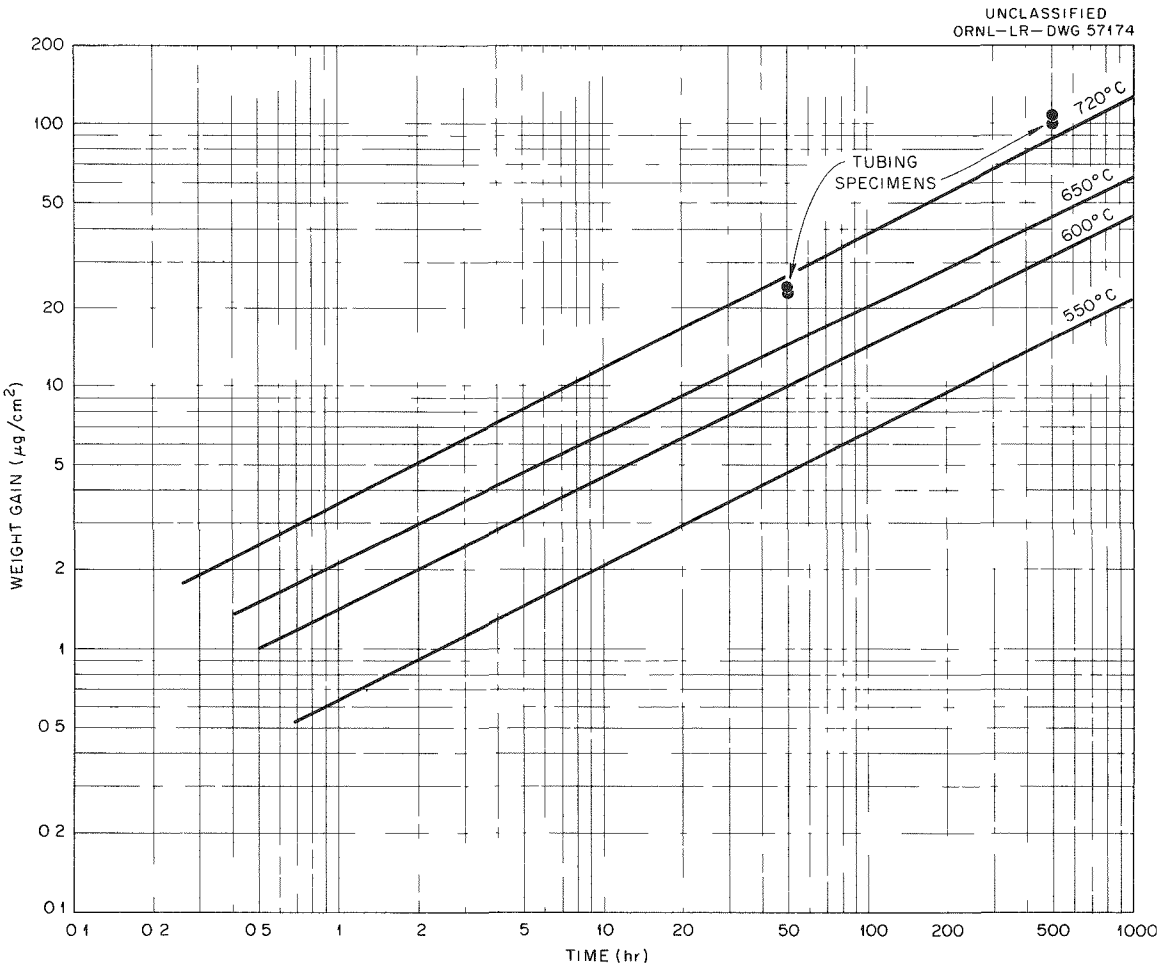

Fig. 4.21. Representative Rate Curves for the Oxidation of Brush QMV Beryllium Powder Compared with Data for Beryllium Tubing.

The values of K for the various test conditions are tabulated below:

Test Temperature (°C)	K ($\mu g/cm^2 \cdot hr$)
500	0.48
600	2.025
650	3.844
720	15.21

In addition to the tests run on powder samples, four samples of tubing (two machined from Brush hot-pressed block and two machined from

Table 4.12. Chemical Analyses of Various Types of Beryllium Used for Compatibility Tests

Impurity	Pechiney Flake (ppm)	Brush QMV Powder (ppm)	Brush HP Tubing (ppm)
Fe	≤80	1 400	1 300
Si	6	400	450
Mn	1		
Mg	≤1	460	100
Al	≤20	500	650
Cu	≤1		110
Ni	<2		160
Ag	<0.2		2
Ca	<10		100
C	<90	1 100	~1200–1300
BeO	200	17 400	15 400
Cl	~80		

Brush hot-extruded rod) were exposed to dry CO_2 for 50 and 500 hr at 700°C for comparison with the powder samples. The results of these tests are also plotted in Fig. 4.21 and, in Table 4.13, are compared directly with the data from powder. It may be seen that the data obtained with tubular specimens generally verifies the data for powder samples.

Chemical and x-ray analyses of the specimens after testing showed that BeO and Be_2C are the products of the reaction of beryllium with CO_2. The results of the chemical analyses are presented in Table 4.14. Although these data exhibit some scatter, it appears that carbon pickup increases with increasing temperature and time, as expected.

Table 4.13. Comparison of Data Obtained on Beryllium Powder and Tubing in Dry CO_2

Specimen	Weight Gain ($\mu g/cm^2$)	
	50-hr Test	500-hr Test
Hot-pressed tubing at 700°C	24.6	104
Hot-extruded tubing at 700°C	23.5	131
Powder (−200 +230) at 720°C	27	88

Table 4.14. Analyses of Beryllium Powder Samples After Testing

Test Temperature (°C)	Time at Temperature (hr)	CO_2 Pressure	Carbon Content (wt %)
600	334	~1 μ	0.57
	477	~1 μ	0.14
	528	~760 mm	0.64
650	431	~760 mm	0.7
	433	~1 μ	1.3
720	222	~1 μ	0.13
	409	~760 mm	2.0
	1006	~1 μ	2.64
838[a]	335	~1 μ	0.63
	1014	~1 μ	1.82

[a]Samples sintered during tests.

Reaction with Water Vapor. The reactions of various types of beryllium with approximately 4% H_2O vapor in flowing helium are being studied in the temperature range 550 to 650°C. Samples of Brush QMV powder, Brush tubing machined from hot-pressed block, and high-purity Pechiney flake are being tested. Chemical analyses of these materials are presented in Table 4.12. Rate curves for the reaction of Brush powder at 550 and 600°C, Pechiney flake at 550°C, and Brush tubing at 650°C are shown in Fig. 4.22. The rate curves for the Brush powder differ from those for the Pechiney flake and Brush tubing in that the initial reaction consists of a period of nonprotective oxidation during which the weight gain is proportional to the elapsed time. The later stages of the test showed that a protective oxide was subsequently formed and the reaction proceeded at a rate comparable to that observed in dry CO_2. The possibility exists that one or more of the impurities present in the Brush powder is responsible for the initial nonprotective reaction. X-ray analysis of the powder after testing showed a decrease in Be_2C content; therefore, it is conceivable that surface decarburization occurs during the early stages of the test and is manifested by that portion of the curve with a slope of approximately 1.

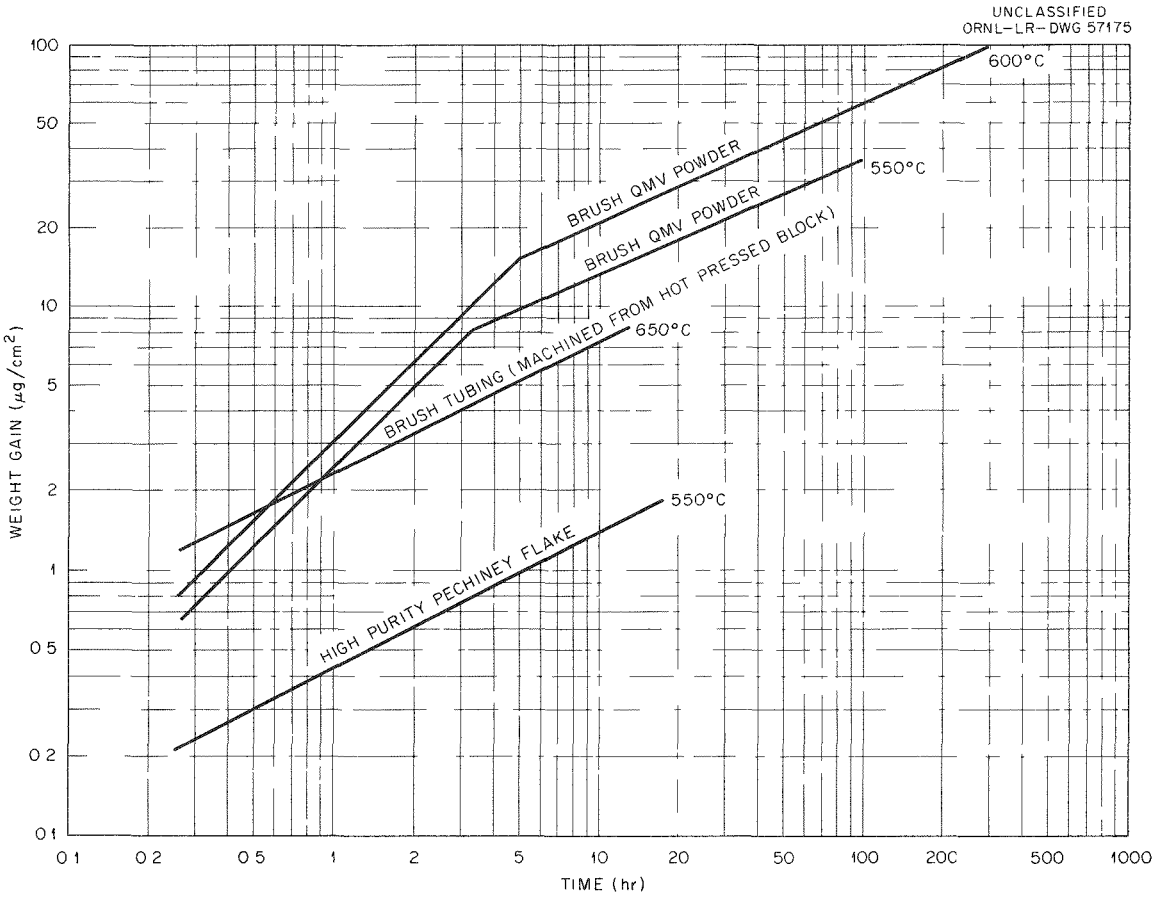

Fig. 4.22. Rate Curves for the Reactions of Various Types of Beryllium with ~4% H_2O Vapor in Flowing Helium.

In addition to the dynamic tests for determining the reaction rates, four static tests were conducted to determine the products of the reaction of Brush QMV powder with H_2O vapor. These tests were run at 600, 650, and 700°C for approximately 100 hr. The results of mass-spectrometer determinations of the gaseous reaction products are presented in Table 4.15.

Reaction of Be_2C with H_2O Vapor and H_2. A test has been started for determining the rate of reaction of Be_2C powder with approximately 4% H_2O vapor in flowing helium. It is thought that the rate curve for this reaction will have a slope of approximately 1, which is characteristic of a nonprotective oxidation reaction.

In addition to this test, a series of static tests for determining the products of the reactions of Be_2C with H_2O vapor and with H_2 have been started. The results of mass-spectrometer analyses of the gaseous products of the reactions of Be_2C with H_2O at 500 and 550°C are given in Table 4.16.

Table 4.15. Results of Mass-Spectrometer Analysis of Gas Present After Reacting Brush QMV Powder with H_2O Vapor

Gas	Composition of Gaseous Reaction Products After Test (%)		
	Tested at 600°C	Tested at 650°C	Tested at 700°C
H_2	99.52	99.78	99.80
CH_4	0.04	0.04	0.03
H_2O	0.10	0.06	0.06
N_2 + CO	0.21	0.11	0.09
O_2			
Ar	0.09		
CO_2	0.02	0.01	0.01

Table 4.16. Results of Mass-Spectrometer Analysis of the Gaseous Products of the Reaction of Be_2C with H_2O at 500 and 550°C

Gas	Composition of Gas (%)				
	Reacted at 500°C		Reacted at 550°C		
	Test No. 1	Test No. 2	Test No. 1	Test No. 2	Test No. 3
H_2	61.4	69.6	41.6	40.8	49.6
CH_4	27.0	21.0	48.2	48.0	44.2
H_2O	0.5	0.3	0.2	0.3	0.2
HC	1.4	1.3	2.1	2.3	1.5
N_2 + CO	9.4	7.6	7.8	8.5	4.3
CO_2	0.2	0.2	0.1	0.1	0.5

Beryllium Joining (R. G. Gilliland)

The usefulness of beryllium as a cladding material for gas-cooled reactor fuel depends to a large extent on the development of suitable joining techniques. The evaluation of various joining procedures for beryllium currently includes the development of high-temperature brazing alloys and the continuation of electron-beam welding studies. A quantity of beryllium tube-burst specimens was also fabricated for use in studies of stress-rupture properties and radiation effects.

Fusion Welding. Initial experiments with the electron-beam fusion welding process have indicated it to be very promising for the sealing of beryllium fuel element tubes. A typical joint is shown in Fig. 4.23. This weld was made using a beryllium tube that had been warm extruded to size by the Brush Beryllium Company. Welded samples for studies of mechanical properties and grain-size measurements are being prepared using tubing obtained from several vendors in order to compare the results for electron-beam welded specimens with those for tungsten-arc welded samples.

Tube-Burst Specimen Fabrication. The beryllium end-closure techniques previously developed[16] are being applied to the fabrication of

[16]GCR Quar. Prog. Rep. Dec. 31, 1960, ORNL-3049, pp. 231–5.

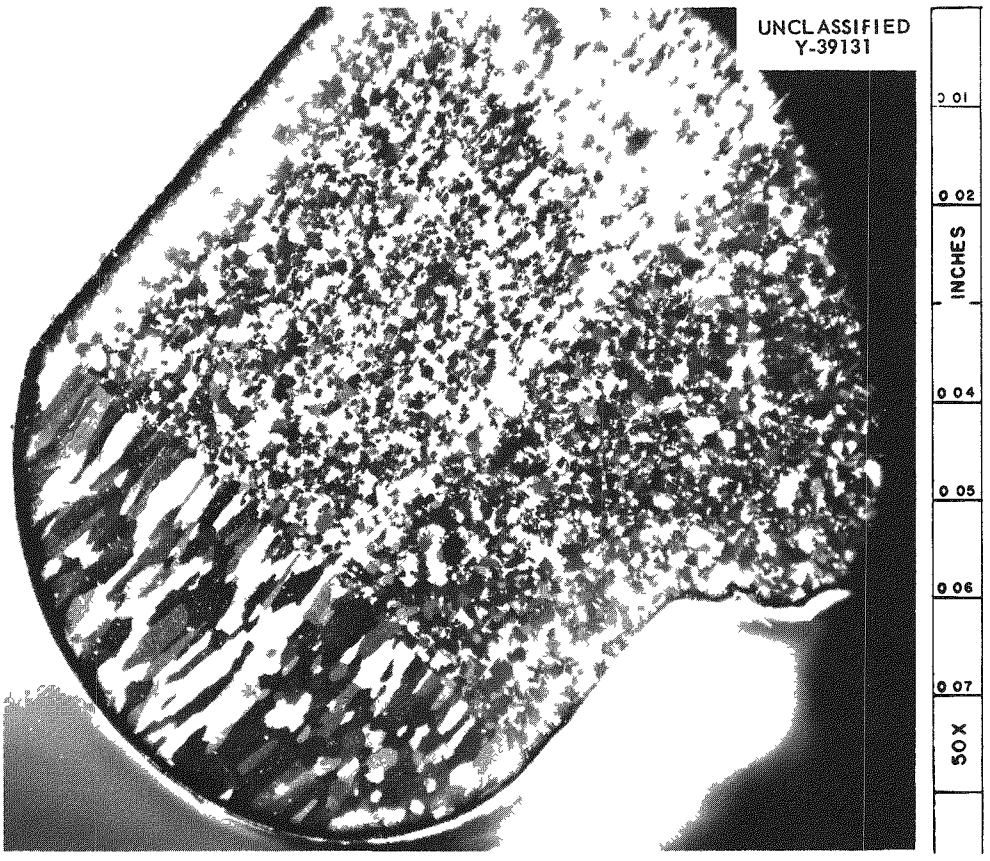

Fig. 4.23. Typical Electron-Beam Welded Beryllium Tube-to-End Cap Joint. Joint soundness is evident. Polarized light. Unetched. 50X.

a quantity of beryllium tube-burst specimens for in- and out-of-pile mechanical property testing. The latest group of specimens was fabricated by the Y-12 Development Group using the methods and procedures prescribed by ORNL. These samples were helium leaktight, but slight porosity in the fusion end-cap welds was revealed by radiography. A number of these specimens are available for mechanical testing as follows:

Specimen Identification	Number of Specimens
Brush A	12
Brush D	19
Pechiney	18
ICI	10

Joining by Pressure Bonding (ORNL Subcontract 2029 at Battelle Memorial Institute, reported by J. T. Lamartine). An investigation is being conducted at Battelle on the gas-pressure bonding of beryllium and beryllium-UO_2 platelet compartmented fuel plates. The effort in this program has included (1) the bonding of beryllium-to-beryllium specimens to develop optimum bonding parameters, (2) the bonding of beryllium-to-UO_2 to investigate compatibility of the cladding with the fuel, and (3) an investigation of various prebonding surface treatments on beryllium.

A number of pickling procedures were evaluated in the interest of obtaining beryllium specimens free from surface oxide and contamination. The most promising solution found was 450 ml H_3PO_4, 26.5 ml H_2SO_4, 53 g CrO_3, which produced a bright, shiny surface finish after the removal of about 0.0005 in. of metal from the beryllium sample. Beryllium-to-beryllium specimens pickled in this solution were bonded at 1550 and 1650°F for 1 hr at 10 000 psi and examined metallographically. Grain growth across the bond interface, which Battelle considers as one of the criteria of good metallurgical bonding, was not evident. Encouraging results were obtained, however, with specimens in which the mating surfaces were pickled and then abraded prior to bonding. Grain growth across the bond interface was observed in a small I-beam specimen, which simulated the bonding of ribs to a cover sheet, that was bonded at 1600°F for 2 hr at 10 000 psi and in

two 2- by 5-in. sheet specimens bonded at 1525 and 1650°F for 4 hr at 10 000 psi. Grain growth was greatest in the specimen bonded at the highest temperature, as expected. Metallographic examination of beryllium-to-UO_2 specimens bonded at 1650 and 1750°F for 4 hr at 10 000 psi has revealed reaction zones at the interfaces on the order of 0.0001 in. or less.

Examination of Beryllium-Clad UO_2 Pellets (C. K. H. DuBose)

A quantity of beryllium-clad UO_2 cylinders was obtained from Sylvania-Corning Nuclear Corporation for use in irradiation experiments. These were prepared by a process, developed by Sylcor, that involves hot isostatic pressing of a preformed assembly. Beryllium powder was hydrostatically pressed into a tubular preform, and the tubes were filled with UO_2 pellets and capped with cold-compacted beryllium end plugs. The assembly was then sealed in a steel can and pressed isostatically at 1950°F at a pressure of 5000 psi for 1/2 hr in argon. The clad assemblies were then finished by pickling and machining.

A single-pellet assembly was prepared for examination by mounting in an epoxy resin and machining it to remove somewhat less than one-half the diameter of the cylinder. This left the UO_2 pellet supported by the undercut beryllium sleeve, but it exaggerated the thickness of the beryllium sleeve. Macroscopic examination of the polished section revealed cracking of the UO_2 pellet. The geometric pattern of the cracks, as shown in Fig. 4.24, suggests that the cracks resulted from stresses generated during the pressing operation. Large inclusions may be observed in the interface between the beryllium sleeve and the end plug. This layer of inclusions was tentatively identified as MgO, which was used to coat the UO_2 pellets before assembly to inhibit the reaction between UO_2 and beryllium.

The end plug-to-sleeve interface at the other end of the pellet was examined microscopically. As indicated in Fig. 4.25, bright-field and polarized-light photomicrographs of this area show very little grain growth across the interface. Most of the interface between the UO_2 and beryllium revealed a translucent material, presumably the MgO previously identified. In addition to this, a phase lighter than the beryllium was observed along much of the interface that extended into the grain boundaries of the

UNCLASSIFIED
Y-36415

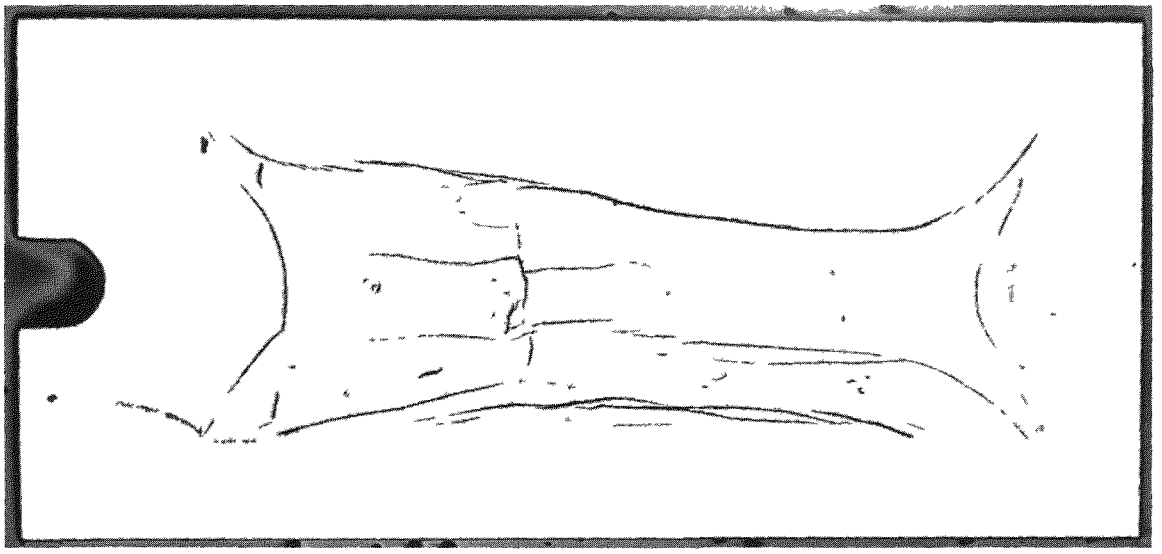

Fig. 4.24. Macroscopic Longitudinal Section of Beryllium-Clad UO_2 Cylinder. As polished. 7X.

beryllium for approximately 0.002 in. This lighter phase, which is anisotropic, is shown in Fig. 4.26. It has not been definitely identified.

Beryllium Tubing Inspection Development (R. W. McClung)

Studies are being made on improved eddy-current techniques for the evaluation of beryllium tubing, with particular reference to finned tubing. The attainable sensitivity of an eddy-current examination is determined, in part, by the proximity of the coil to the area being inspected. The principal concern for integrity in a finned tube is the tube wall. The inspection of finned tubing from the inside should be more satisfactory; therefore, an internal bobbin-type coil was constructed. The test coils of the bobbin were produced similarly to those which are being used for encircling-coil techniques. The bobbin coil was made to fit the bore of a 1/2-in.-o.d., 0.035-in.-wall tube.

Tests were conducted with a reference standard consisting of a type 304 stainless steel tube containing 1/32- and 1/64-in.-diam holes drilled through one wall and 0.003- and 0.005-in.-deep longitudinal notches in the inner and outer surfaces. Much larger responses were recorded from the drilled holes than from the longitudinal notches. The difference is

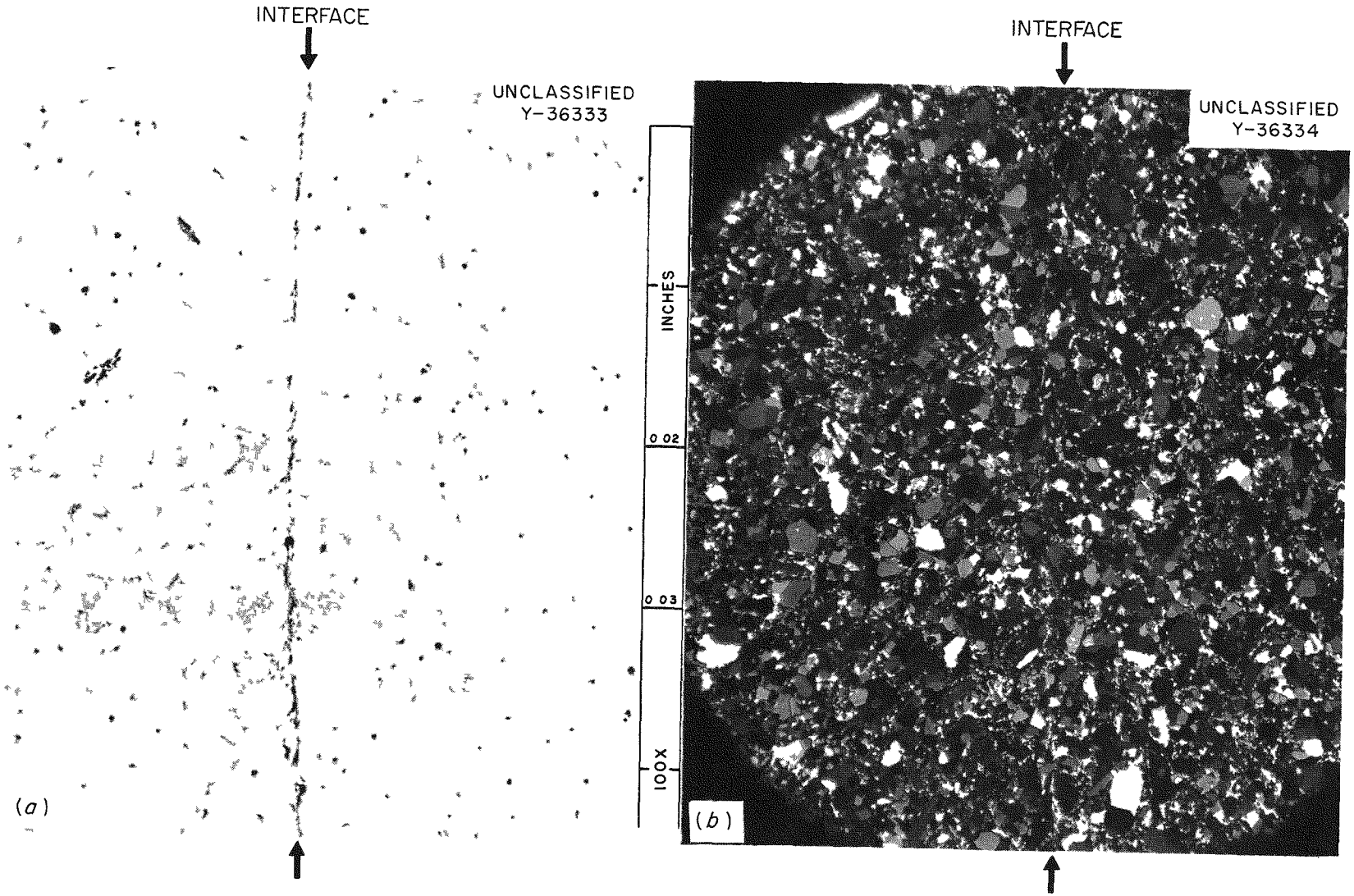

Fig. 4.25. End Plug-to-Sleeve Interface at End of Beryllium-Clad UO_2 Cylinder. (a) Bright field. (b) Polarized light. As polished. 100X.

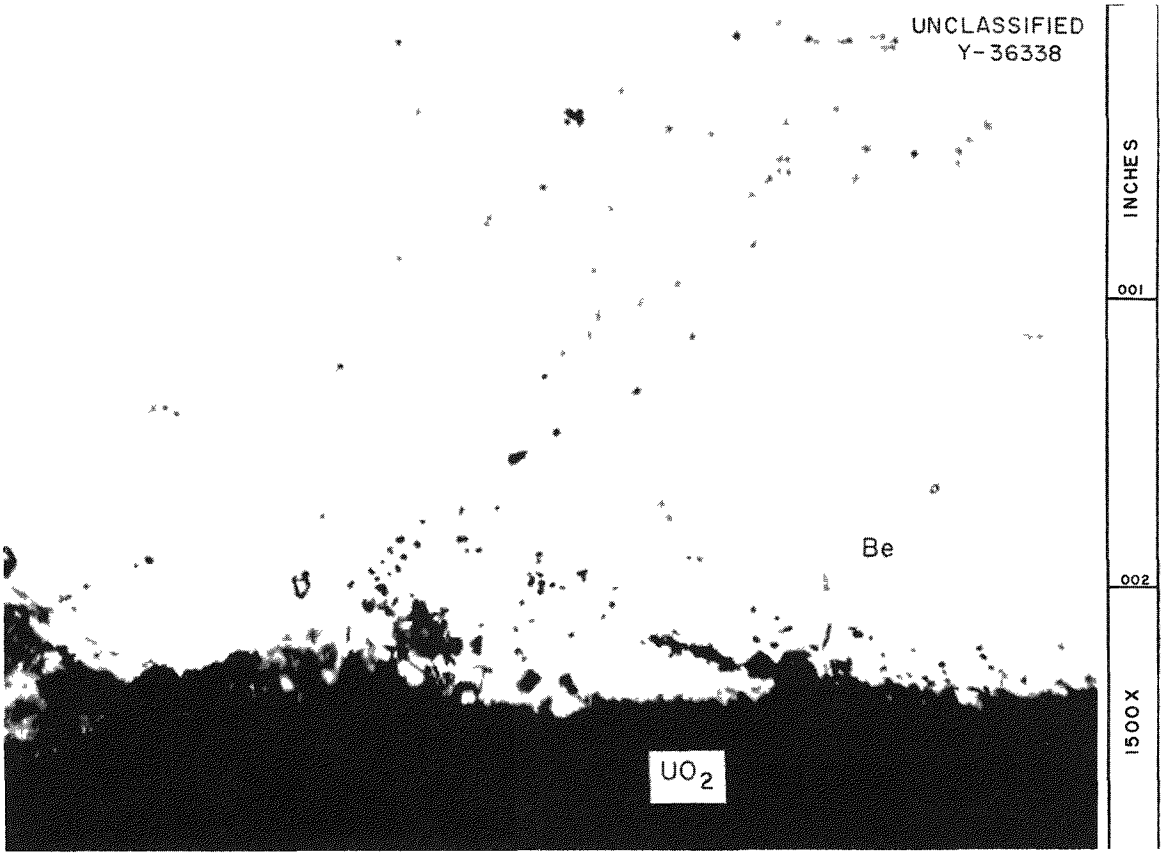

Fig. 4.26. Interface Between UO_2 and Beryllium, Showing Third Phase Lighter than Beryllium. As polished. 1500X.

so great that a common-sensitivity setting cannot be used to display both types of defect with "on-scale" recordings. The machined notches are much more comparable to naturally occurring cracks, although drilled holes are used as reference standards by many inspection groups in this country and abroad. The notches on the inner surface were readily detectable, but some difficulty has been encountered in obtaining a reasonable response from notches on the outer surface.

Stress-Rupture Properties of Beryllium Tubing (J. R. Weir)

Investigation of the stress-rupture properties of beryllium tubes at 600°C is essentially complete. Tests have begun at 700°C on tubing manufactured by Pechiney, ICI, and the Brush Beryllium Company, using warm-extruded tubing and tubes machined from hot-pressed block and hot-extruded rod from the latter company. Insufficient data have been obtained to

construct stress-rupture curves; however, a few trends are apparent. It has been observed that the ductility of the tubes and the rank in terms of strength are similar at 700°C to those observed at 600°C.

5. IN-PILE TESTING OF COMPONENTS AND MATERIALS

Fuel Element Irradiation Program

D. B. Trauger

Full-Diameter Prototype EGCR Fuel Capsules (F. R. McQuilkin)

Beryllium Cladding and UO_2 Grain-Size Studies (V. A. DeCarlo, A. A. Abbatiello, R. L. Senn, A. W. Longest). Irradiation of the eight group III capsules described previously[1] is continuing. A summary of temperatures recorded February 7 and the estimated total burnup through March 3 is given in Table 5.1.

Table 5.1. Temperature and Burnup Data for the Group III Capsules Being Irradiated in the ORR

Capsule No.	Number of Chromel-Alumel Thermocouples Remaining Operative	Cladding Surface Temperature (°F)[a]				Estimated Total Burnup[b] (Mwd/MT)
		Design	High	Low	Average	
01A-3[c]	6	1600 (max)	1520	1332	1444	1700
02-3	4	1112 (av)	1100	970	1041	2300
03-3	1	1112 (av)			1065[d]	2000
04-3	5	1112 (av)	1160	1000	1076	1900
05-3	1	1112 (av)	1150	1085	1117	2700
06-3	4	1112 (av)	1080	1030	1050	2100
07-3	1	1112 (av)	1020	1009	1014	1900
08-3[e]	6	1600 (max)	1450	1125	1297	1100

[a] Readings taken February 7, 1961.

[b] Estimates of total UO_2 burnup are based on 200 Mev/fission and were calculated as of March 3.

[c] The tungsten-rhenium central thermocouple indication is 1865°F.

[d] High and low thermocouples have failed.

[e] The tungsten-rhenium central thermocouple is sealed off as a result of a failure during a late stage of assembly.

The blanket pressure of the helium has been maintained at 300 psig for all eight capsules since December 18, 1960. On this date the second incremental stepwise pressure increase of 75 psi was made on capsule 03-3. The history through February 12 of all blanket gas pressure increases,

[1] GCR Quar. Prog. Rep. Sept. 30, 1960, ORNL-3015, p. 107.

applied thermal cycles, and periodic leak checks of the beryllium-clad capsules (02-3 through 07-3) is summarized in Figs. 5.1, 5.2, and 5.3. Capsules 01-3 and 08-3 consisted of prototype-diameter stainless steel-clad UO_2 specimens for grain-size studies. These capsules contain tungsten-rhenium central thermocouples, are not thermally cycled, and have been maintained with the blanket gas at a pressure of 300 psig.

The gas circulators installed in November to reduce temperature fluctuations in the control gas circuits of capsules 05-3, 06-3, and 07-3 were effective, as described in the previous report,[2] but have been removed because of their high failure rate. New circulators have been procured, modified for capsule use, and tested for installation during reactor cycle 33 shutdown.

[2]GCR Quar. Prog. Rep. Dec. 31, 1960, ORNL-3049, p. 242.

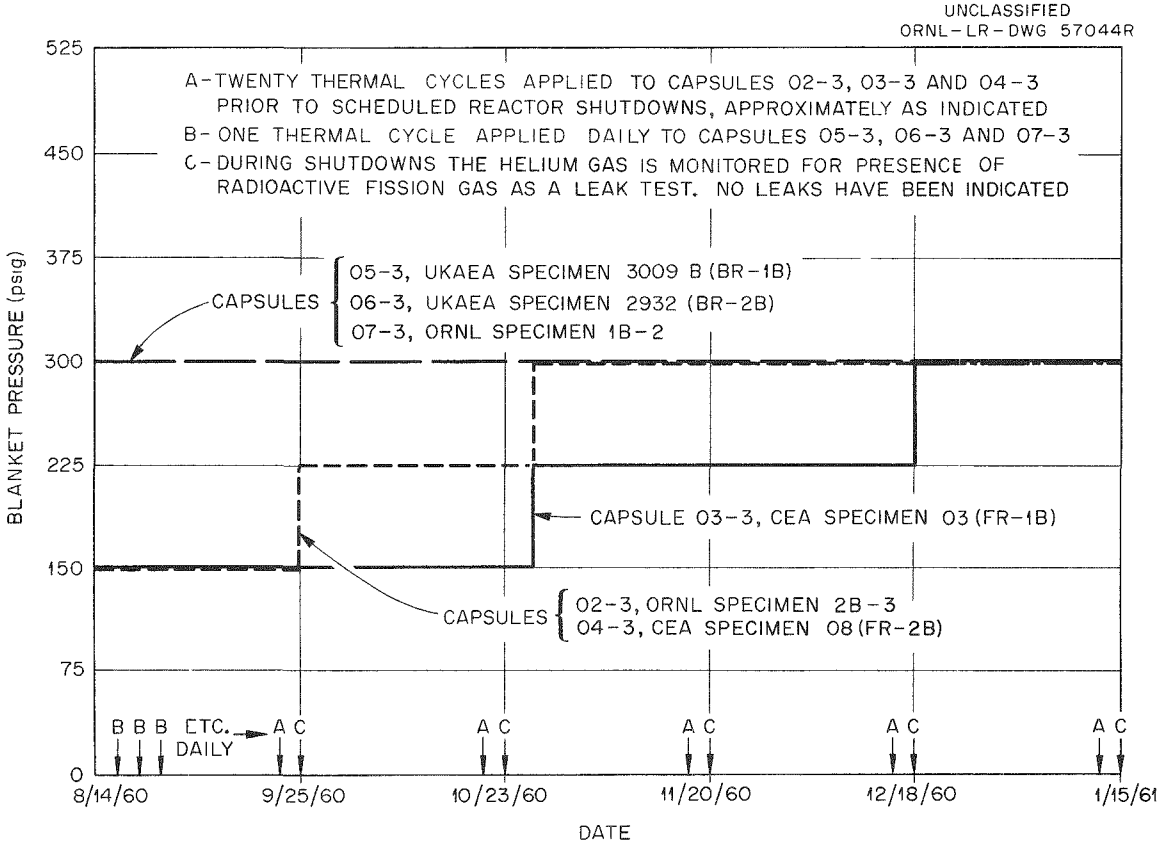

Fig. 5.1. Operating History of Beryllium-Clad Group III Capsules in the ORR.

During cycle 32 shutdown a neutron thermopile for continuously monitoring the thermal-neutron flux was installed in the irradiation facility

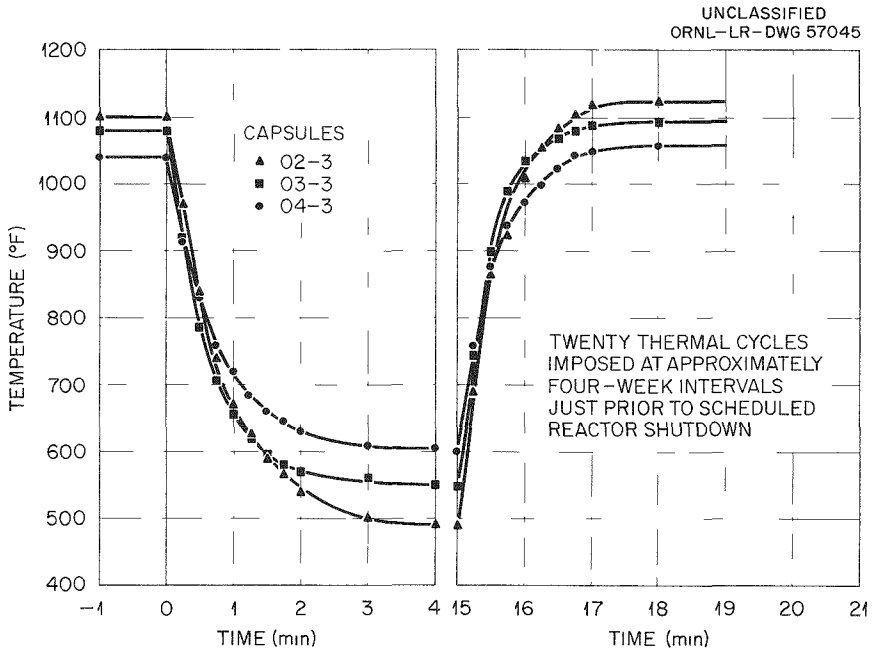

Fig. 5.2. Thermal Cycles Imposed by Cadmium Shutter on Capsules 02-3, 03-3, and 04-3.

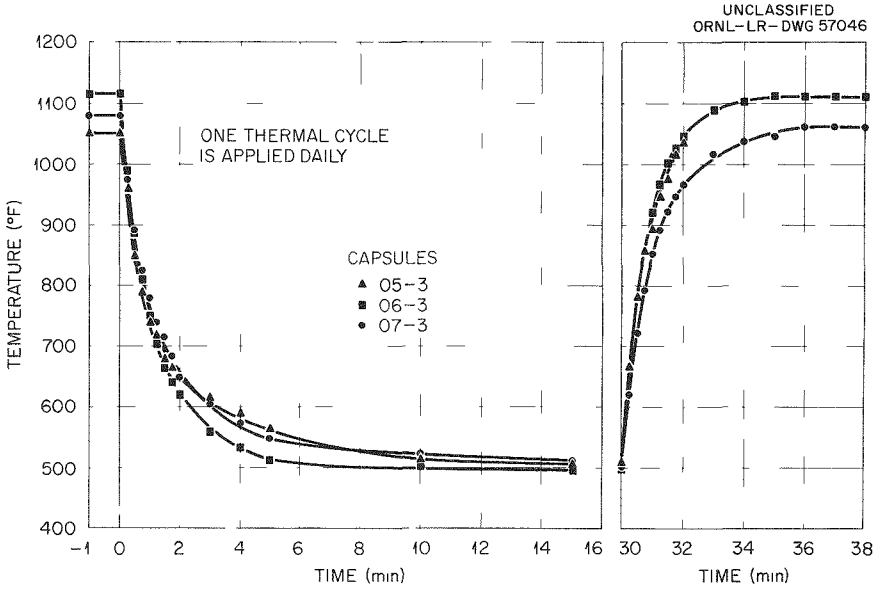

Fig. 5.3. Thermal Cycles Imposed by Cadmium Shutters on Capsules 05-3 and 07-3.

at a distance of 19 1/2 in. from the reactor face. It has operated very satisfactorily thus far and is currently being calibrated.

Planning and design work were completed and fabrication work is nearing completion for replacement of group III capsules with group IV units during ORR cycle 34 shutdown. During this shutdown the capsule-mounting plates which do not permit location adjustment during operation will be replaced with remotely operated screw-driven positioners. Except for capsules equipped with thermal-cycling shutters, the new "flux modulator" will provide each individual capsule with 10 in. of travel. Movement of the capsules with shutters is restricted because the clearance between shutters is not adequate to permit adjacent assemblies to pass.

Since in the positioner travel zone, 1 to 5 in. from the reactor tank face, the unperturbed flux gradient drops by a factor of 4 on the north half (capsule positions 1-4) and a factor of 3 on the south half (positions 5-8), the positioning mechanism is equipped for rather fine adjustment. As an aid in neutron-flux monitoring during capsule irradiation, all nonshuttered capsules are being equipped with tubes for flux-monitoring-wire. Data from these wires will supplement data from the continuously operated thermopile.

Fabrication of the eight group IV capsules is nearing completion. These units include two EGCR prototype full-diameter (0.759-in.-o.d.) stainless steel capsules containing UO_2 of different grain sizes. Each is equipped with (1) a tungsten-rhenium central thermocouple (one in a molybdenum well and the other in a Fansteel 82 well), (2) two grounded-junction, Chromel-Alumel thermocouples in 0.040-in.-o.d. stainless steel sheaths brazed to the cladding inner surface, and (3) two 1/16-in.-o.d. thermocouples banded to the cladding outer surface as for previous experiments. All five thermocouples are located on a common diameter at the mid-plane of the specimen to provide the most direct comparison possible. Two French CEA beryllium-clad UO_2 capsules similar[1] to those irradiated in group III are included in group IV. Provisions are being made to increase the blanket gas pressure to 850 psig for these two capsules. The remaining capsules in this group are four specially prepared stainless

steel-clad UO_2 fuel assemblies, three of which are swaged to 0.540 in. o.d. One has tamp-packed fuel in a 0.528-in.-o.d. cladding.

ETR Experiments (F. R. McQuilkin). Irradiation of 14 EGCR-prototype full-diameter capsules designed to attain various values of UO_2 fuel burnup is continuing in the ETR. As a result of various changes in the reactor core, the neutron-flux pattern shifts were such that capsules E-2 and E-11 were receiving approximately 28 and 35% of design flux. These capsules are to be relocated during cycle 36 shutdown. Since other capsules have been affected similarly, but to a lesser extent, decisions for their possible relocations are being delayed until after another anticipated flux shift.

Capsule E-12 has a plugged gas line. Since this capsule has achieved only a small fraction of its scheduled 13 000-Mwd/MT burnup, another capsule (designated as E-12R) is being prepared as a replacement. NaK blanket gas lines are partially plugged on capsules E-1A and E-5, but since these capsules will have completed their design irradiation to 3000-Mwd/MT burnup by the end of cycle 37, they will remain in the reactor as scheduled.

Miniature-Capsule Fission-Gas-Release Experiments (F. R. McQuilkin, W. E. Thomas)

Operating data for miniature capsules in the LITR are given in Table 5.2. Assembly L-M1 containing BeO-UO_2 fuel was designed for low-temperature irradiation to a high burnup (10 000 to 13 000 Mwd/MT) and subsequent postirradiation tests for determining the fission-gas-release rate

Table 5.2. Operating Data for Miniature Capsules in LITR

Experimental Assembly No.	Fuel Composition	U^{235} Enrichment (%)	Central Fuel Temperature (°F)		Date Installed	Date Removed	Estimated Burnup
			"a" Capsule	"b" Capsule			
L-M1	BeO-UO_2	20	1150	1550	10-20-60	In-pile	
L-M2	BeO-UO_2	50	1990	2490	9-14-60	2-7-61	5 at. %
L-M3	BeO-UO_2-ThO_2	93	1800[a]	2080	11-22-60	In-pile	
L-M4	BeO-UO_2	50	2040	2480	2-8-61	In-pile	
L-C1	UC	10	2150	2300	11-3-60	12-13-60	3500 Mwd/MT
L-C2	UC	10	2050	2550	12-14-60	In-pile	
L-C3	UC	10	2300	2500	12-14-60	In-pile	
L-T1	UO_2	10	1300	1475	12-19-60	In-pile	

[a]Thermocouple failed on startup; value is calculated.

parameter, D′. Assemblies L-M2 and L-M4 containing BeO-UO_2 fuel are designed for irradiation at temperatures ranging from 2000 to 2500°F and are scheduled for burnups from 2 to 5 at. % of the total uranium. Upon completion of the irradiation period, the capsules will be pierced in a hot cell and the fission gas and helium evolution will be measured. Likewise, capsules containing BeO-UO_2-ThO_2 fuel will be operated under similar conditions and analyzed for fission-product retention.

Assembly L-C1 containing UC fuel was removed at low burnup, after approximately one month of irradiation; it served as a means of testing the design, as well as a specimen for use in perfecting techniques for post-irradiation examination of the fuel material. Assemblies L-C2 and L-C3, both containing UC fuel, are now in-pile and are to be irradiated to a minimum burnup of 15 000 Mwd/MT.

Thermocouple test L-T1ab is being conducted as an in-pile evaluation of reduced-diameter (0.020 in. o.d. and 0.040 in. o.d.) stainless steel-sheathed Chromel-Alumel thermocouples designed for service in irradiation capsules and in-pile loops. The test assembly contains four 0.040-in.-o.d. thermocouples and three 0.020-in.-o.d. thermocouples operating at temperatures ranging from 150 to 1475°F. Two thermocouples are in contact with UO_2, one 0.020 in. in diameter operating at 1300°F and the other 0.040 in. in diameter operating at 1475°F. Only one failure (a 0.020-in.-o.d. thermocouple) has occurred in 73 days of operation.

In order to provide for simultaneous screening tests of pyrolytic-carbon-coated uranium dicarbide particles without interfering with other GCR experiments, an additional instrumented facility is being constructed. All work on this facility is scheduled to be completed on or before May 2, 1961. Design and construction of the first test assembly containing particles manufactured by High Temperature Materials, Inc., was completed. This assembly was inserted in an existing LITR facility on March 8, 1961.

Advanced Fuel Element Testing (C. W. Cunningham, J. A. Conlin)

The third graphite-encapsulated test fuel element with a UC_2-graphite matrix (ORNL-MTR-48-3) was irradiated for only one of four scheduled MTR reactor cycles beginning January 3, 1961, and ending January 16, 1961.

The activity of the helium purge gas increased at a rapid rate while the MTR was at a 40-Mw power level, even though the capsule was fully retracted. During the irradiation period, the MTR operated 425 Mwd. A comparison of the operating data for the second and third tests, presented in Table 5.3, showed the gas activity to be excessive and the test was terminated. The graphite capsule apparently failed. The third test element is being shipped to the GE Vallecitos hot-cell facilities for inspection of the encapsulating graphite and the silicon seal.

During irradiation the gas activity was too high to permit normal collection of samples for gamma-ray spectrographic analysis. However, a gas sample was trapped in the shielded purge gas line where it passes an ion chamber, and the activity decay was followed for 26 hr. The successive

Table 5.3. Comparison of ORNL-MTR-48-2 and ORNL-MTR-48-3

	ORNL MTR-48-2	ORNL MTR-48-3
Encapsulating graphite body		
Outside length, in.	2.505	6.02
Outside diameter, in.	1.875	1.882
Inside length, in.	1.5	5
Inside diameter, in.	1.000	1.000
Minimum wall thickness at thermocouple well, in.	3/16	1/4
Permeability to helium at 25°C, cm^2/sec	1.5×10^{-8}	5.9×10^{-9}
Fueled graphite matrix		
Outside diameter, in.	0.996	0.996
Total length, in.	1.47	4.94
Fission power density, w/cm^3	140	170
Total fission power, kw	2.75	11.0
Operating conditions after four days in-pile		
Helium flow rate, cm^3/hr	200	200
Graphite wall average temperature, °F	1500	1050
Purge gas activity, counts/min	500	120 000

half-life periods were 3.1, 3.0, 3.0, 3.3, 3.7, 5.7, and 7.2 hr. The principal radioactivity appeared to come from 2.8-h Kr^{88}. The nuclides that were later identified in a sample of this gas were 2.8-hr Kr^{88}, 4.4-h Kr^{85m}, 5.27-d Xe^{133}, and 9.20-h Xe^{135}.

Examination of Irradiated Capsules

ORR- and ETR-Irradiated Prototype Capsules (J. G. Morgan, M. T. Morgan, M. F. Osborne, H. E. Robertson)

The postirradiation examinations of five group I and eight group II ORR-irradiated capsules are essentially completed, except for metallographic examination of the group II capsules. Gas-removal and high-temperature pressure measurements have been made on the remaining three group I capsules, and one ETR capsule (E-9) was examined.

During slitting and opening of the group II capsules, the fuel pellets generally remained in the as-assembled position, as may be seen in Figs. 5.4, 5.5, and 5.6. All pellets had visible cracks, and most pellets fell apart when removed. Fourteen pellets were removed intact and measured; all dimensions agreed with preirradiation values to within 0.5%.

All eight group II capsules and the E-9 capsule were pierced, and the gas was removed and analyzed. The fraction of fission gas released from the fuel, based on the total production calculated from burnup measurements, is given in Table 5.4. Since the gas removed from capsule 04-2 was mostly air, the capsule was assumed to have leaked prior to sampling. Mass-spectrometer analyses of the gases showed about 80% nitrogen, but not much oxygen, in capsules 07-2 and 08-2, as indicated in Table 5.5. The inference is that the capsules contained air when sealed and that most of the oxygen reacted during irradiation. The effect of this atmosphere on the fuel has not yet been determined. The sample of gas from capsule 06-2 was lost during analysis.

The void volumes measured for six group II capsules and the E-9 capsule are listed in Table 5.6. Agreement with the calculated geometric void volume was fair, except for capsules 04-2 and 06-2, in which the open porosity of the BeO center rod contributed about 4.5 cm^3. Subsequent

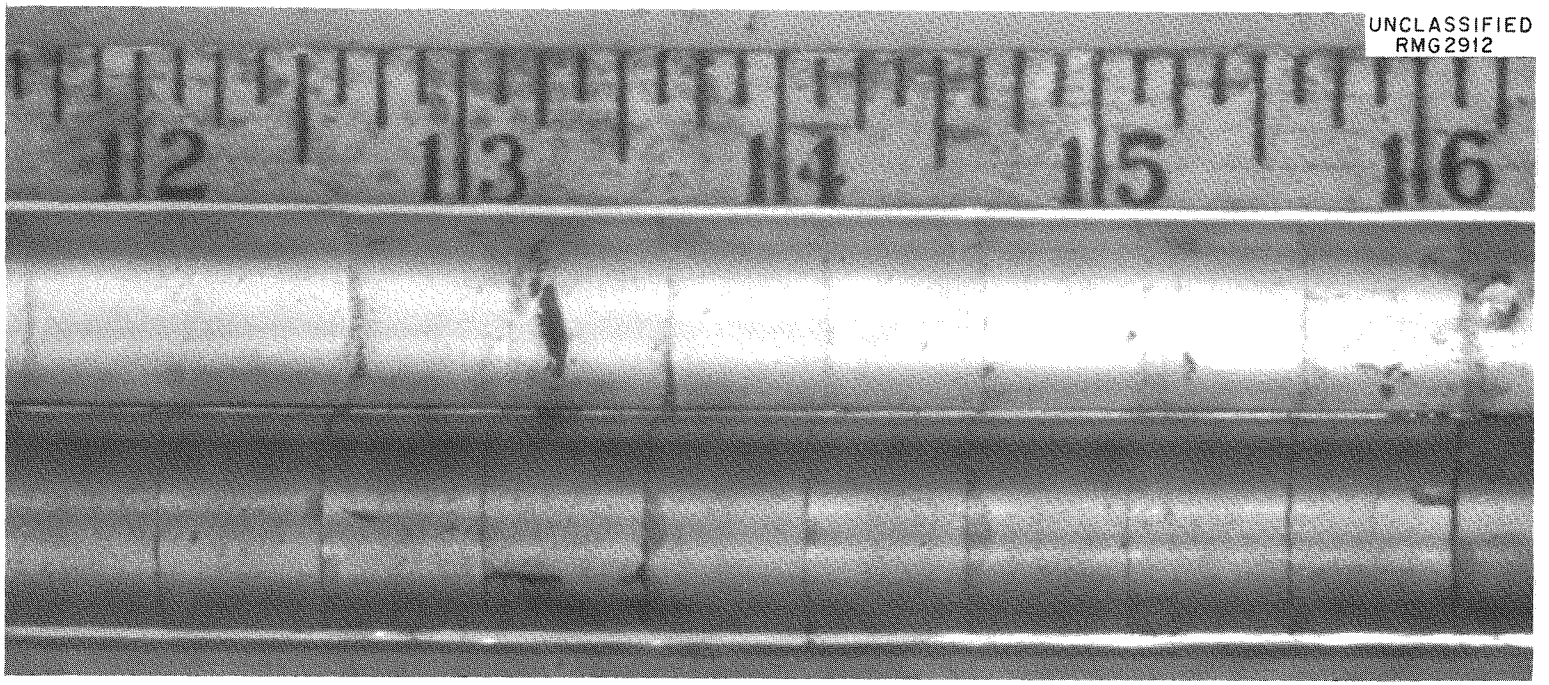

Fig. 5.4. ORR-Irradiated Capsule 02-2 Showing Inner Surface of Stainless Steel Capsule and Outer Surfaces of Hollow UO_2 Pellets.

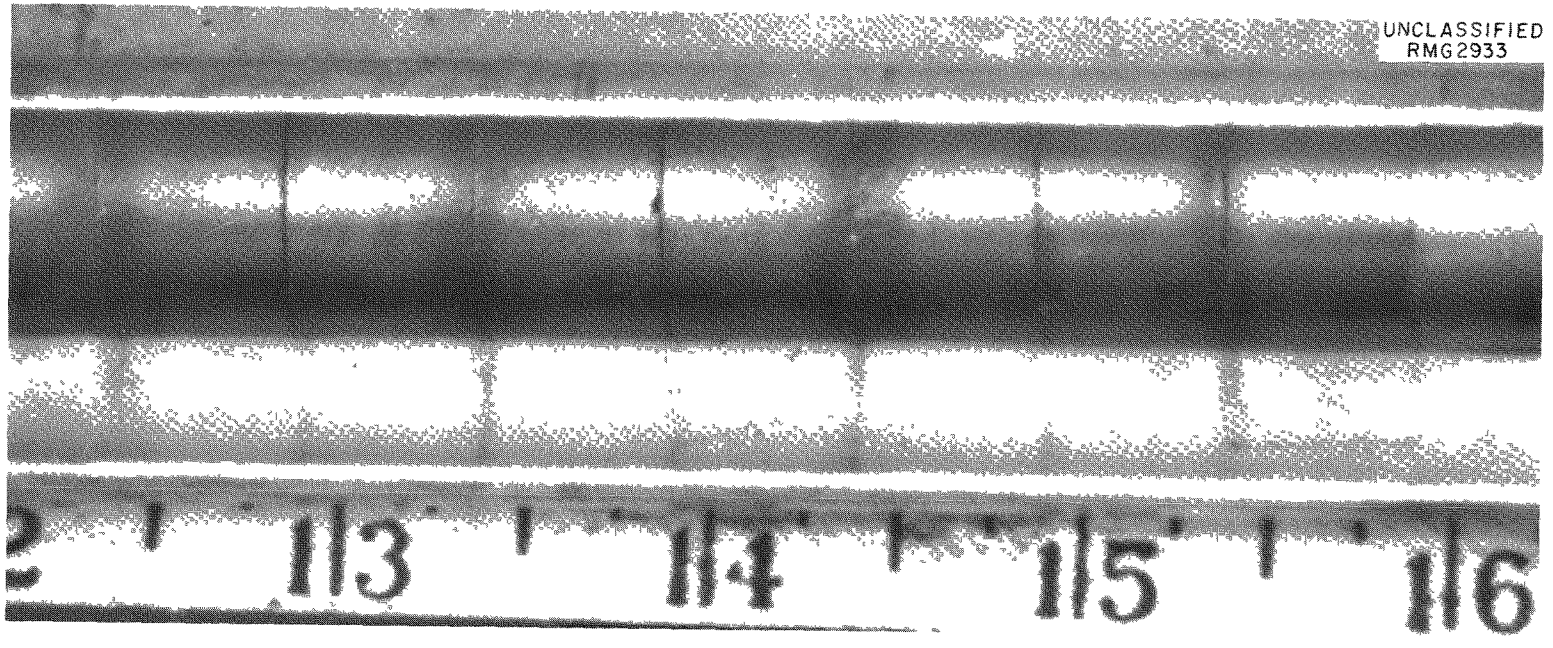

Fig. 5.5. ORR-Irradiated Capsule 04-2 Showing Inner Surface of Stainless Steel Capsule and Outer Surfaces of Hollow UO_2 Pellets. Central space filled with BeO rod.

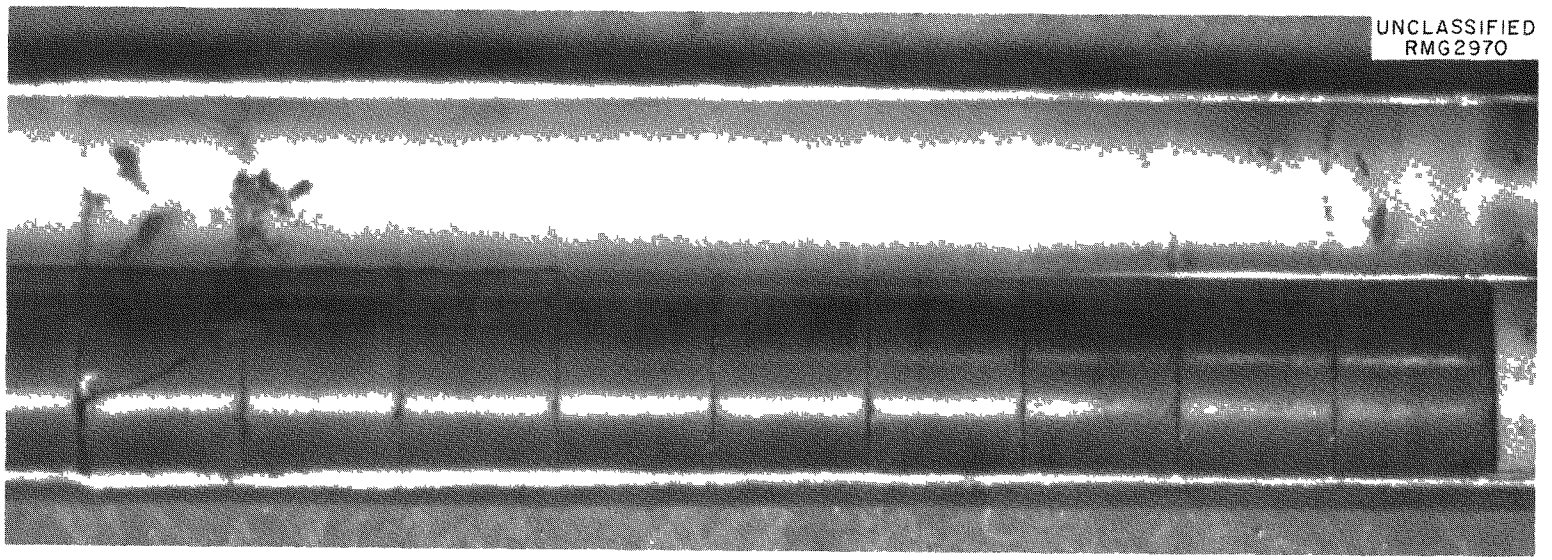

Fig. 5.6. ORR-Irradiated Capsule 08-2 Showing Inner Surface of Stainless Steel Capsule and Outer Surfaces of Solid UO_2 Pellets.

density measurements verified this contribution, giving a bulk density of 1.49 g/cm^3 and an immersion density of 3.00 g/cm^3 for the BeO rod in capsule 04-2. Diameter measurements of the BeO rod showed a decrease of about 0.001 in.

The results obtained with three methods of burnup analysis are compared in Table 5.7. The most reliable data for these enrichments are considered to be those from measurement of the Ce^{144}-to-uranium ratio.

Table 5.4. Release of Kr^{85} Fission Gas from ORR-Irradiated Group II Prototype Capsules

Capsule No.	Burnup from Ce^{144} Analysis (Mwd/MT)	Average Irradiation Temperature (°F)		Average Oxygen-to-Uranium Ratio	Fuel Pellet Geometry	Kr^{85} Release (%)
		Cladding Surface (measured)	Central UO_2 (calculated)			
01-2	1670	1322	2500	2.01	Hollow	0.53
02-2	1400	1427	2800	2.01	Hollow	0.55
03-2	1460	1369	2700	2.02	Hollow	0.76
04-2	1680	1291	2850	2.008	Hollow with BeO rod in center	0.07[a]
05-2	2500	1491	3100	2.005	Hollow	1.5
06-2	1690	1513	2850	2.005	Hollow with BeO rod in center	1.1
07-2	1310	1303	3400	2.03	Solid	0.51
08-2	1110	1496	3400	2.03	Solid	0.31
E-9	3200[b]	1300	2700	2.03		3

[a]Capsule apparently leaked.

[b]Estimated from flux measurement.

Table 5.5. Results of Mass-Spectrometer Analyses of Gas Samples from ORR-Irradiated Group II Capsules

	Capsule 01-2	Capsule 02-2	Capsule 03-2	Capsule 04-2	Capsule 05-2	Capsule 07-2	Capsule 08-2
Aliquot size, cm^3 at 30°C and 760 mm Hg	1.11	1.08	1.06	1.07	1.01	1.00	1.15
Gas constituents, vol %							
CO_2	0.07	0.04	0.02	0.09	0.07	0.08	0.15
Ar	0.56	0.45	1.97	1.07	0.95	4.08	2.58
O_2	0.27	0.13	0.23	19.14	0.40	0.26	3.99
N_2	0.98	0.50	2.18	78.28	20.65	82.12	81.35
He	97.19	98.33	93.44		74.09	12.37	11.30
H_2O			0.44	1.22	1.96		
Xe	0.79	0.45	1.47	0.20	1.58	0.93	0.47
Kr	0.13	0.10	0.24	Trace	0.31	0.15	0.16
Total	99.99	100.00	99.99	100.00	100.01	99.99	100.00
Ratio of krypton to xenon in gas sample[a]	0.16	0.22	0.16		0.20	0.16	0.34

[a]Ratio of krypton to xenon in gas produced by fission is 0.157.

The immersion density of one fuel pellet from each of five group I and seven group II capsules was measured by the CCl_4 vacuum-impregnation technique. The results are presented in Table 5.8. A small increase was

Table 5.6. Internal Void Volumes of ORR-Irradiated Group II Capsules Measured at 31°C

Capsule No.	Fuel Pellet Geometry	Void Volume (cm^3)	
		Calculated	Measured
01-2	Hollow	9.8	
02-2	Hollow	9.8	9.6
03-2	Hollow	9.8	10.2
04-2	Hollow with BeO rod in center[a]	2.1	6.7
05-2	Hollow	9.8	10.0
06-2	Hollow with BeO rod in center[a]	2.1	6.7
07-2	Solid	3.1	
08-2	Solid	3.1	3.6
E-9	Hollow with BeO rod in center[a]		5.8

[a]BeO rods contain approximately 4 cm^3 open porosity.

Table 5.7. Comparison of Burnup Data for ORR-Irradiated Group I and Group II Capsules

Capsule No.	Burnup (Mwd/MT)		
	Based on Co^{60}	Based on Ce^{144}-to-U Ratio	Based on U^{235}-to-U^{236} Ratio
01-1	1100	1710	1880
02-1	1200	1820	1770
03-1	1000	1530	2200
05-1	2100	2610	2650
06-1	1300		1970
01-2	1530	1670	
02-2	1550	1400	
03-2	1510	1460	
04-2	1840	1680	
05-2	2430	2500	
06-2	1610	1690	
07-2	1060	1310	
08-2	1070	1110	

observed for all pellets except the pellet from capsule 05-1; the maximum change was about 2.5%.

Upon longitudinal slitting of capsule E-9, the cladding spread open appreciably at the center, as shown in Fig. 5.7, even though the ends were

Table 5.8. Immersion Densities of Fuel Pellets from Group I and Group II Capsules and Capsule E-9

Capsule No.	Immersion Density (g/cm^3)		Change in Density (g/cm^3)
	Preirradiation (±0.01 g/cm^3)	Postirradiation (±0.02 g/cm^3)	
01-1	10.68	10.75	+0.07
02-1	10.75	10.77	+0.02
03-1	10.68	10.76	+0.08
05-1	10.76	10.65	−0.11
06-1	10.77	10.80	+0.03
01-2	10.74	10.78	+0.04
02-2	10.72	10.78	+0.06
03-2	10.71	10.76	+0.05
04-2	10.73	10.78	+0.05
05-2	10.57	10.82	+0.25
07-2	10.63	10.83	+0.20
08-2	10.76	10.82	+0.06
E-9	10.65	10.75	+0.10

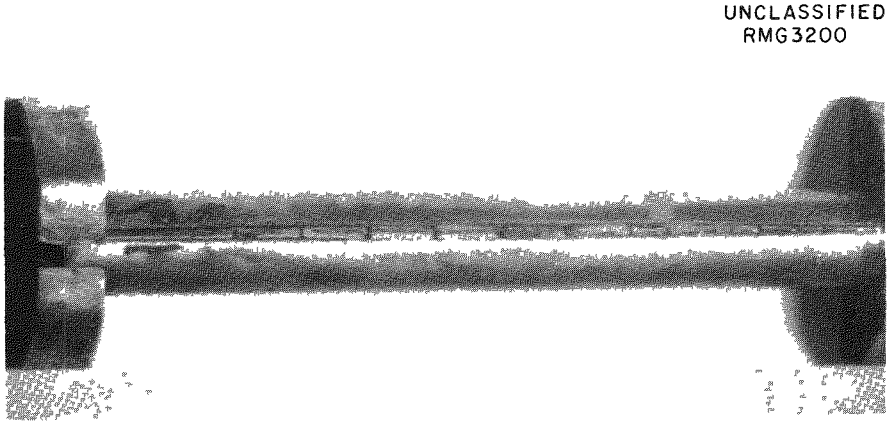

Fig. 5.7. Capsule E-9 After Longitudinal Slitting, Showing Spreading of Cladding. 0.75X.

clamped together, indicating a considerable tensile stress. This behavior has not been observed in any other capsule. Dimensional measurements of the E-9 capsule showed a maximum bow of 0.008 in. A bulge in the upper half of the cladding showed an increase of 0.002 in. in diameter at that point.

Metallographic Examination of ORR-Irradiated Group I Capsules (E. L. Long, Jr.)

The metallographic examinations of the ORR-irradiated group I capsules, except capsules 04-1, 07-1, and 08-1, have been completed. Control samples representative of the UO_2 pellets in the group I capsules are shown in Figs. 5.8 and 5.9 in both the as-polished and etched conditions. Figure 5.8 shows the UO_2 sample that is representative of the fuel pellets in capsules 01-1 and 03-1, and Fig. 5.9 shows the sample representative of the fuel pellets in capsules 02-1, 05-1, and 06-1. A considerable amount of a second phase material (estimated to be approximately 10% of the volume) was observed and was identified in other samples as UN_2. A grain-boundary phase that is also present has not been identified. In both control samples, the microstructure was made up of equiaxed grains; however, the 02-1, 05-1, and 06-1 control samples showed slightly larger and more uniform grains. Even though the density of the group I UO_2 pellets is 95% of theoretical, a considerable amount of porosity is indicated in Figs. 5.8 and 5.9. It does not appear that the porosity is a result of the polishing operation.

Capsule 01-1. A transverse section of irradiated pellet 40-9, which was located near the center of capsule 01-1, was prepared. An increase in the porosity is apparent across the entire cross section, as shown in Fig. 5.10. This increase in porosity does not seem to have been dependent on the thermal gradient that existed in-pile. The cladding temperature was maintained at 1300 to 1500°F in all the group I capsule irradiations, and the temperature of the inner surfaces of the UO_2 pellets in capsule 01-1 was calculated to be approximately 2500°F. The etched sample revealed a fairly uniform grain size, as well as a slight increase in grain size throughout the fuel pellet when compared with the control sample. The light second phase observed in the control sample was not present. An

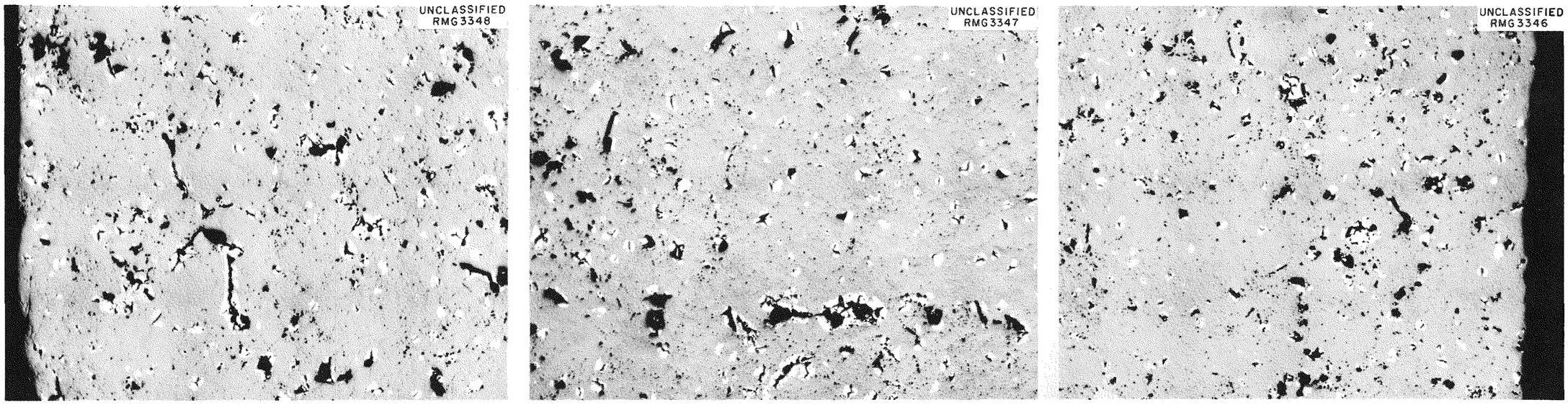

Fig. 5.8. Metallographic Sections of Unirradiated UO_2 Control Sample Representative of Fuel Pellets in Group I Capsules O1-1 and O3-1. (a), (b), and (c) show outer, central, and inner areas, respectively, of hollow pellet as polished (250X). (d), (e), and (f) show same sections after etching. The light, second phase distributed throughout the microstructure has been identified as UN_2. The grain-boundary phase has not been identified. Note porosity and equiaxed grains. Original reduced 12%.

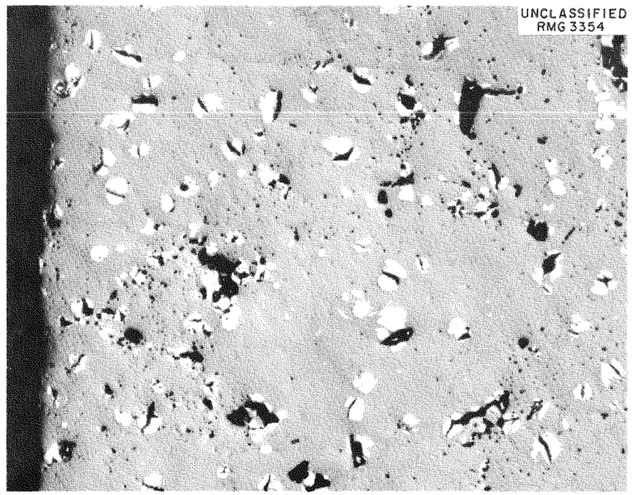

(a)

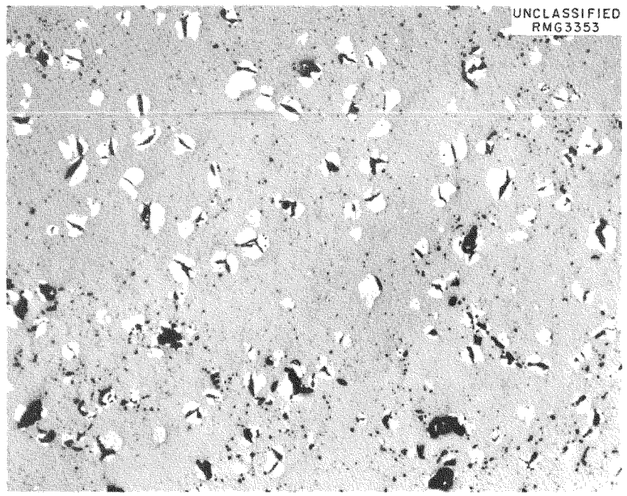

(b)

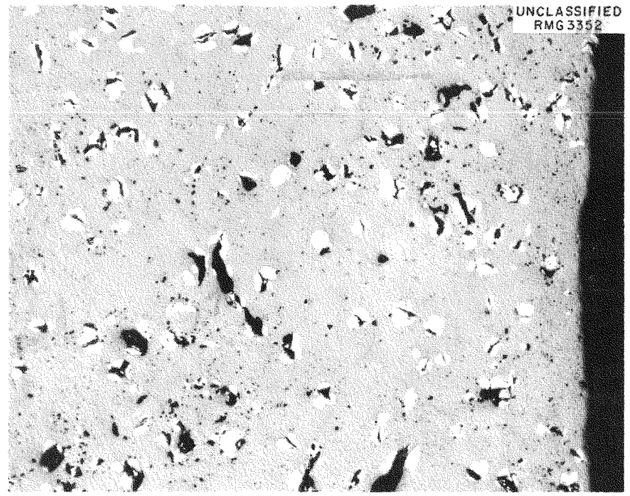

(c)

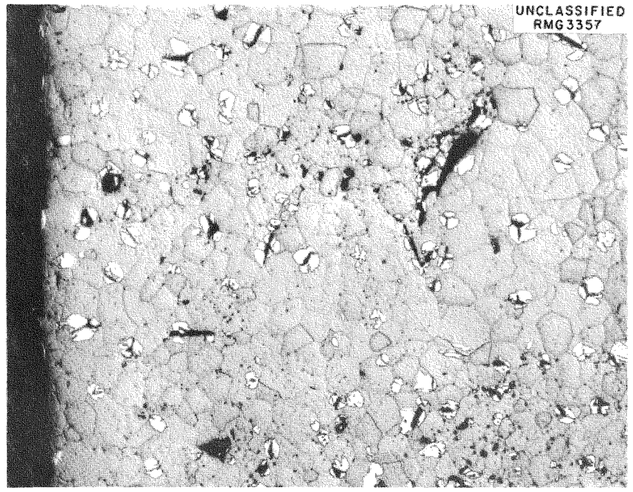

(d)

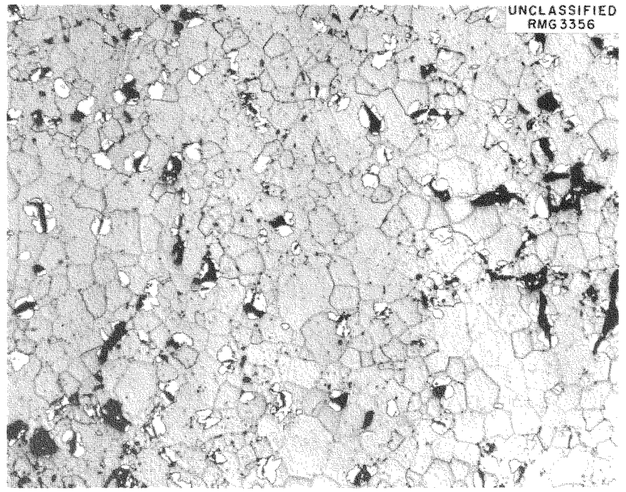

(e)

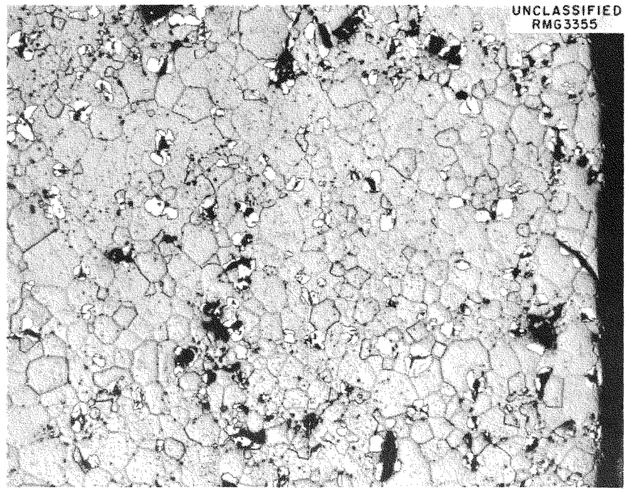

(f)

Fig. 5.9. Metallographic Sections of Unirradiated UO_2 Control Sample Representative of Fuel Pellets in Group I Capsules 02-1, 05-1, and 06-1. (a), (b), and (c) show outer, central, and inner areas, respectively, of hollow pellet as polished (250X). (d), (e), and (f) show same sections after etching. The light second phase distributed throughout microstructure has been identified as UN_2. The grain-boundary phase has not been identified. Note porosity and uniform, equiaxed grains. Original reduced 12%.

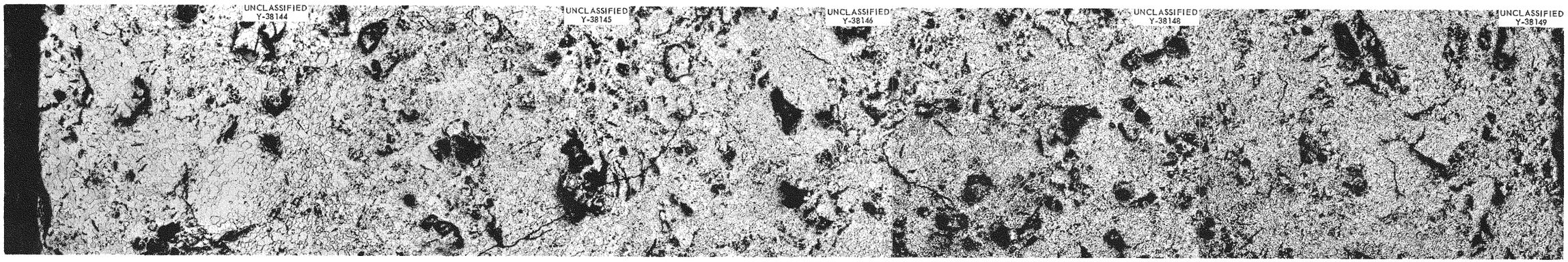

Fig. 5.10. Transverse Section of UO_2 Pellet 40-9 Which Was Located Near the Center of ORR-Irradiated Capsule 01-1. Outer surface of hollow pellet at left; inner surface at right. Note porosity across entire cross section and absence of second phase that was present prior to irradiation (see Fig. 5.8). Etched. 100X. Original reduced 24%.

acicular structure may be seen dispersed throughout the inner half of the fuel pellet. This structure, shown at the inner surface in Fig. 5.11, is apparently temperature dependent, since an increase in the size and frequency of the needles occurs as the inner surface is approached.

Capsule 03-1. Pellet 40-23 was selected as the representative sample for the metallographic examination of capsule 03-1. The pellet was prepared in the same manner as pellet 40-9 from capsule 01-1. An apparent increase in porosity was again noted when the pellet was compared with the control sample. Even though the calculated internal temperature was higher in this capsule than in capsule 01-1, 2700 versus 2500°F, there is no observable difference in the average grain size of the two pellets. The grain size decreases as the inner surface is approached. The acicular structure is not as well developed as in the case of pellet 40-9 from capsule 01-1, but it was apparently a major factor in inhibiting the grain growth.

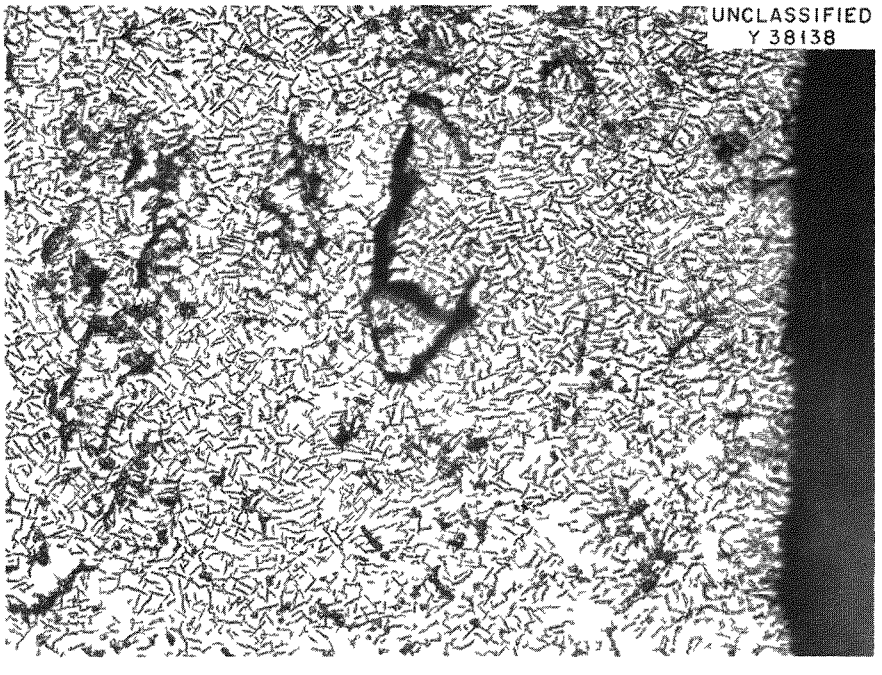

Fig. 5.11. Transverse Section at Inner Surface of UO_2 Pellet 40-9 from Capsule 01-1. This needle-like structure was dispersed throughout the inner half of the fuel pellet. An increase in size and frequency occurred as the inner surface was approached. Etched. 250X.

Capsule 02-1. Two UO_2 pellets were selected from capsule 02-1 for postirradiation metallographic examination: pellet 220-5, which was at the bottom of the capsule, and pellet 220-9, which was located near the center of the capsule. The calculated internal temperature of this capsule was 2800°F. A large amount of the apparent porosity present in both these pellets, as shown in Fig. 5.12, is believed to have been introduced during polishing. Practically all the fractures in these pellets were intergranular, and thus the conditions were ideal for "pull-outs" to occur during polishing.

The light second phase, UN_2, found in the control sample was not present in either of the pellets from capsule 02-1. The grain size in both irradiated pellets was fairly uniform and only slightly greater than in the control sample. However, there were differences between the pellets. The bottom pellet (220-5) had more fractures than the pellet from the center of the capsule (220-9). Also, the acicular structure seen in UO_2 pellets from other capsules was present in only the pellet from the center (220-9). A heavy concentration of the needles extended into the pellet from the inner surface for approximately 0.002 in., as shown in Fig. 5.13, which indicates the possibility that an atmospheric reaction occurred during irradiation. Such a leak was not evident, however, during the in-pile period. The center pellet had more intergranular fractures, especially in the outer surface regions, than the pellet from the bottom of the capsule.

Capsule 05-1. Two samples were selected from capsule 05-1 for postirradiation metallographic examinations: pellet 217-7, from the bottom of the capsule, and pellet 219-6, which was located near the center of the capsule. The calculated internal temperature during irradiation was 3100°F. As in the case of the samples from capsule 02-1, much of the apparent porosity is believed to be a result of polishing. An examination at a magnification of 250 revealed a larger amount of intergranular cracking than was evident in the capsule 02-1 pellets. The outer surface of the pellet from near the middle of the stack (219-6) was more severely fractured than the outer surface of the bottom pellet.

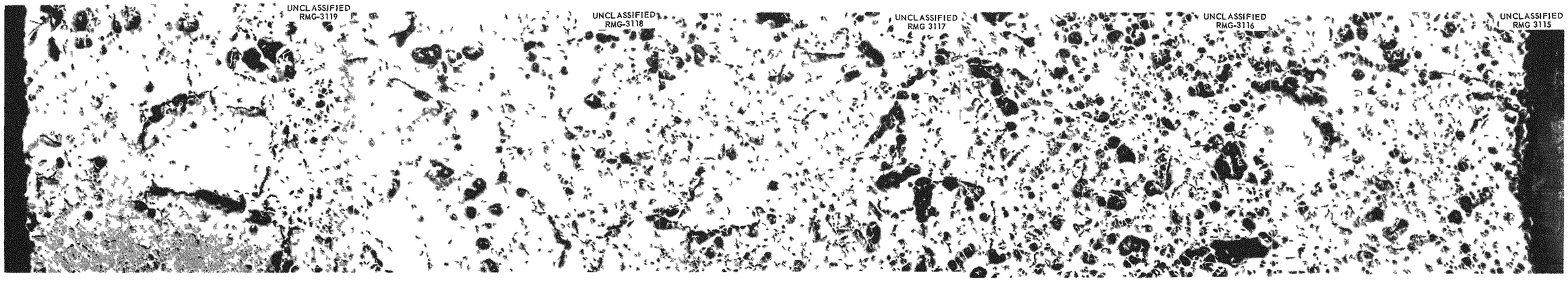

(a)

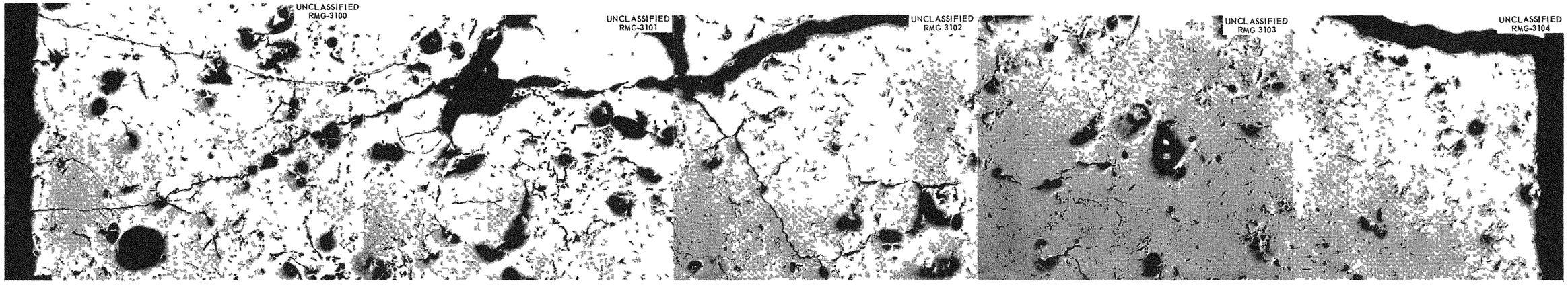

(b)

Fig. 5.12. Transverse Sections of UO_2 Pellets from Capsule 02-1. Pellet 220-9 from near the center of the stack is shown in (a), pellet 220-5 from the bottom of the stack is shown in (b). A large amount of the apparent porosity is believed to have been introduced during polishing. Intergranular fracturing occurred in both pellets. As polished. 100X. Original reduced 24%.

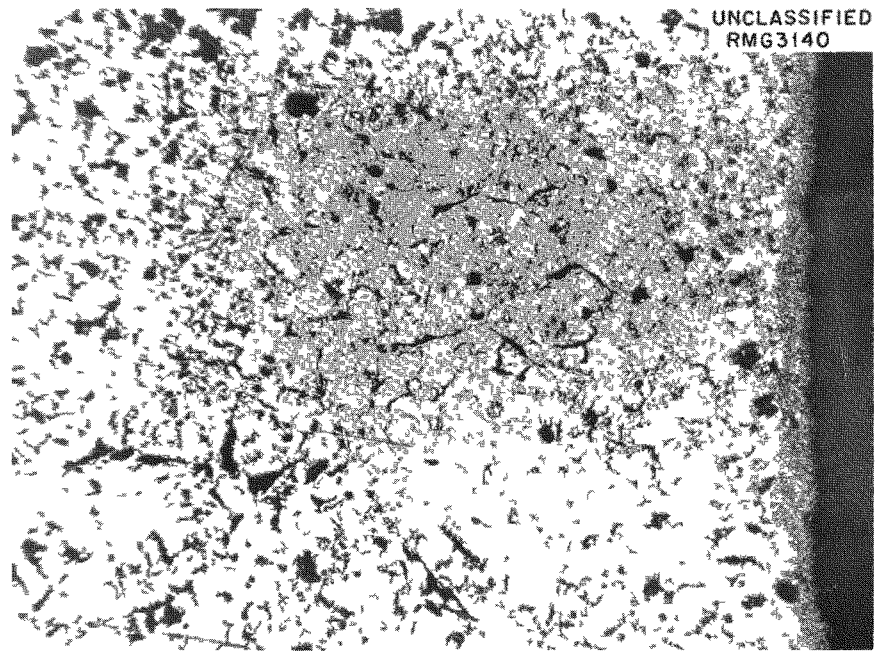

Fig. 5.13. Transverse Section at Inner Surface of UO_2 Pellet 220-9 from Center of Capsule 02-1. Note heavy concentration of "needles" that extend into the pellet for approximately 0.002 in. from inner surface (at right), indicating the possibility that an atmospheric reaction occurred during irradiation. Etched. 100X.

Again the UN_2 found in the control sample was not observed. The typical acicular structure was evident in both pellets. In the bottom pellet (217-7) this structure was present from approximately mid-radius to the inner surface, and in the pellet from near the center of the stack (219-6) the needles covered the inner two-thirds of the cross section. A continuous grain-boundary phase was found near the inner surface of the bottom pellet, whereas there was a continuous grain-boundary phase across the entire cross section of pellet 219-6. Three areas representing the outer, central, and inner regions of pellet 219-6 are shown in Fig. 5.14. No appreciable increase in grain size as compared with that of the control was noted.

Capsule 06-1. A BeO bushing was included in the center of the stack of hollow UO_2 pellets in capsule 06-1. The pellet selected for post-irradiation metallographic examination was 226-7, which was located near the center of the capsule. The calculated internal temperature of the capsule during irradiation was 2850°F.

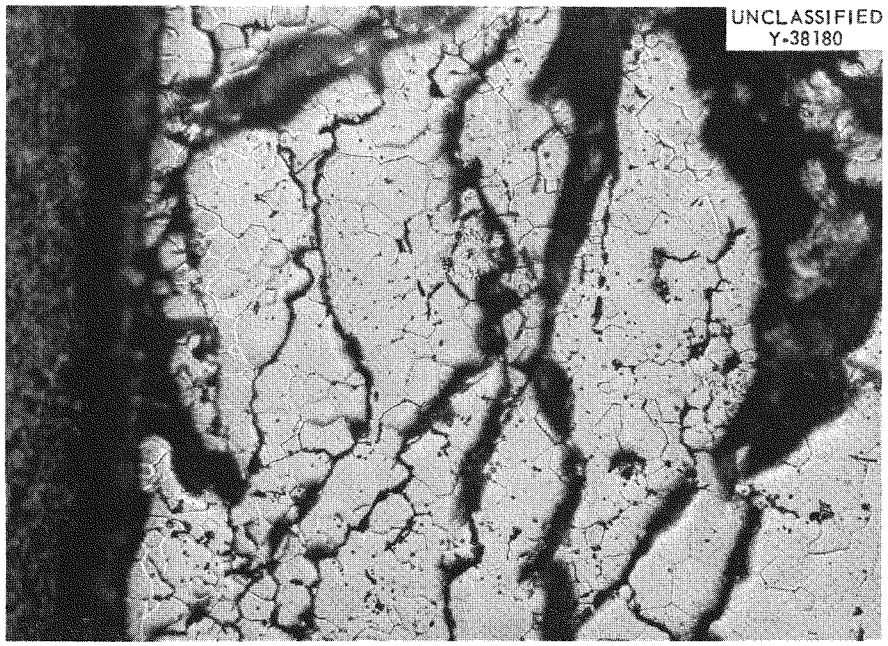

(a)

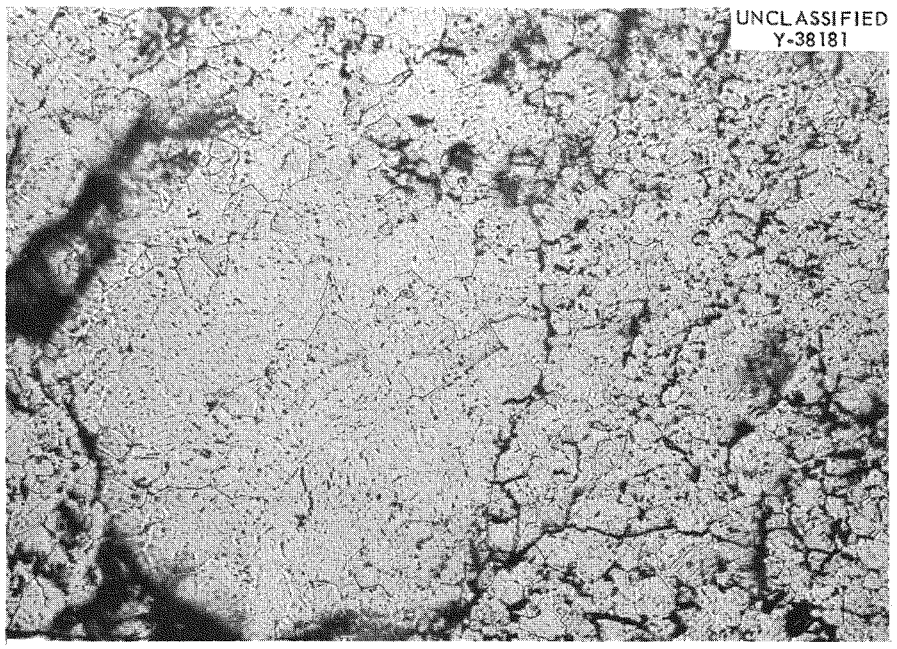

(b)

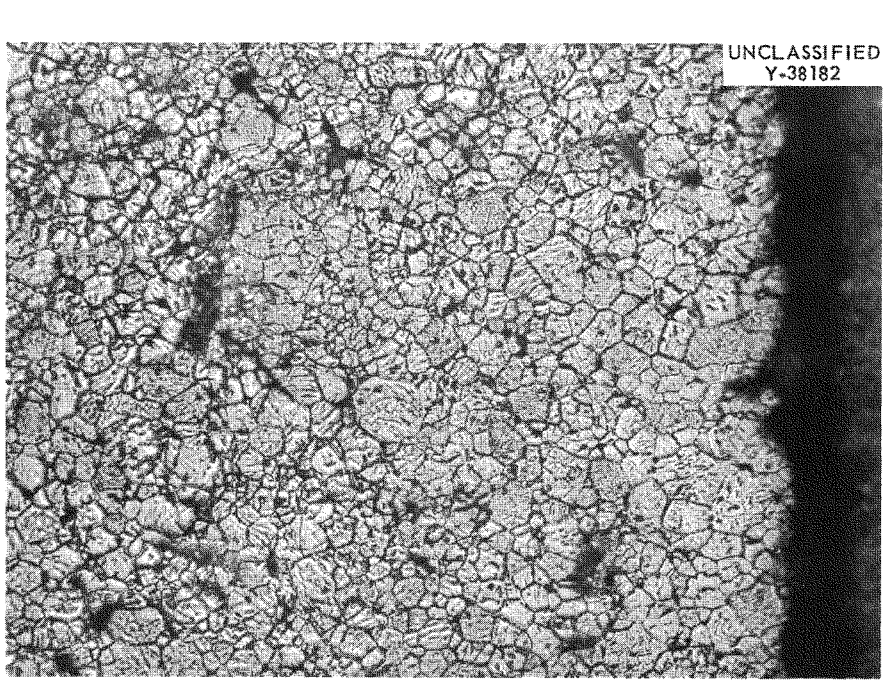

(c)

Fig. 5.14. Representative Areas from Pellet 219-6, Which Was Located Near the Center of Capsule 05-1. Severe intergranular fractures are shown in (a), the outer region. Note also the grain-boundary phase. The acicular structure is shown to extend beyond the center of the pellet (b), and it becomes fully developed at the inner surface (c). The UN_2 found in the control sample is not present.

The results of the metallographic examination are shown in Figs. 5.15 and 5.16. The majority of the porosity shown is believed to be real. Except for the radial crack and a few fractures at the outer surface, the general appearance of this sample is not unlike that of the control sample. Specifically, the grain size appears unchanged, as well as the size and distribution of the UN_2 phase. Only a few needles can be seen near the inner surface. There is a decrease in the amount of the UN_2 phase near the outer surface, compared with the control. The distribution of the UN_2 and the structure are shown in Fig. 5.16, which presents areas at the outer surface, center, and inner surface of the pellet, respectively.

Conclusions. The formation of the acicular structure in all the UO_2 pellets, except pellet 220-5 from the capsule 02-1, seems to be dependent upon temperature (which may only be estimated). Attempts are being made to identify the needle-like precipitate by x-ray diffraction. Dependence of the formation of the acicular structure on the presence of UN_2 should be revealed by the examination of capsules 07-1 and 08-1, which were fired only in hydrogen. Examinations of these capsules are under way.

The presence of the acicular structure is apparently deleterious with respect to the mechanical strength of UO_2 at elevated temperatures, as was evidenced by the increase in intergranular fracturing with the associated increase in internal temperatures and higher burnup. This was shown in capsule 06-1 in which a marked reduction in intergranular fracturing was evident, as was the absence of the acicular structure, even though the calculated internal temperature was 2850°F. The function of the BeO rod in retarding the formation of the needles is not clear. The needle-like structure, which apparently forms on the slip planes of UO_2, is also a factor in inhibiting grain growth.

The UO_2 pellets near the center of the stack suffer a greater amount of intergranular cracking, especially at the outer surface, than the pellets located at the bottom. This was seen in the examination of pellets from capsules 02-1 and 05-1.

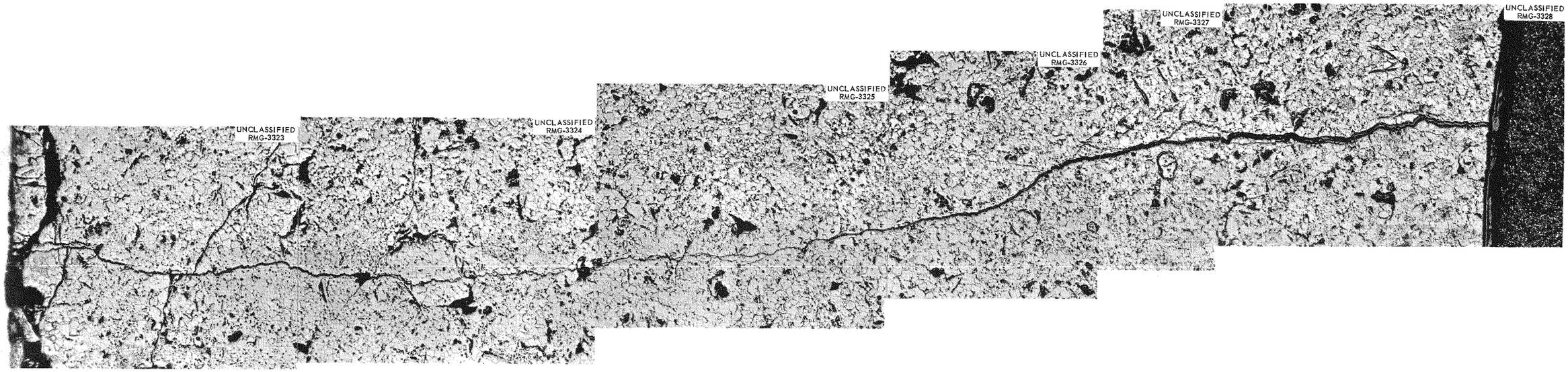

Fig. 5.15. Transverse Section of UO_2 Pellet 226-7 from Near the Center of Capsule 06-1. A BeO bushing was placed down the center of the stack of hollow UO_2 pellets. The outer surface of the pellet is at the left. Etched. 100X. Original reduced 26%.

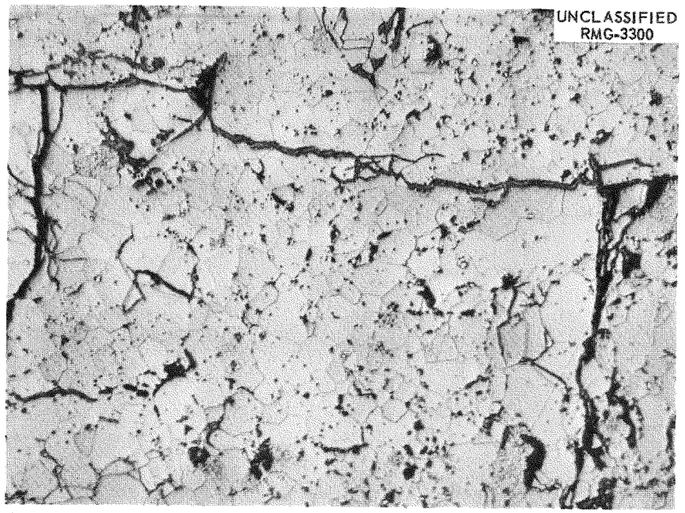

(a)

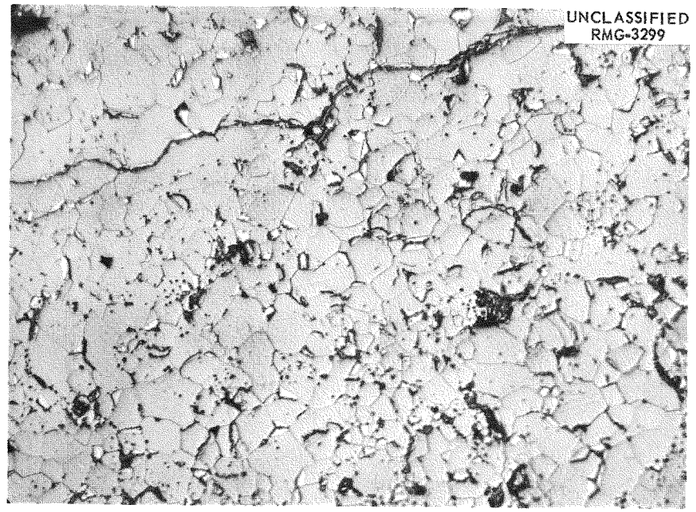

(b)

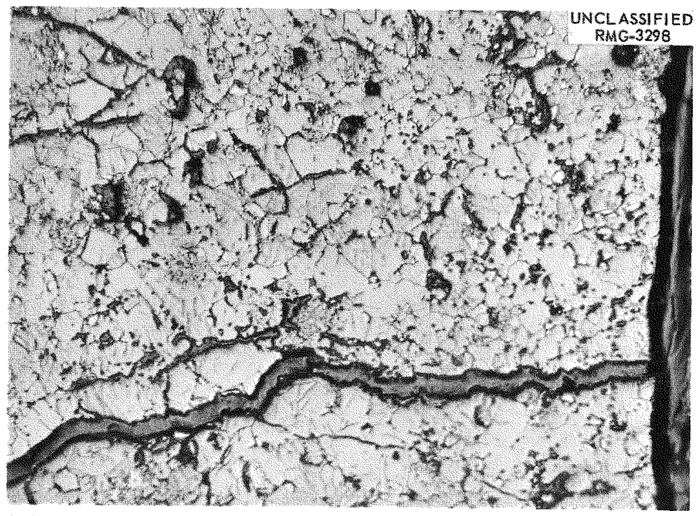

(c)

Fig. 5.16. Representative Areas from Pellet 226-7 Which Was Located Near the Center of Capsule 06-1. Only a small amount of UN_2 remains in the outer region (a), while an amount approximately equal to that seen in the control sample remains in the central region (b) and in the inner region (c). Only a few needles are present at the inner surface, as compared with other group I capsules examined to date. Etched. 250X.

LITR-Irradiated Miniature Capsules (J. G. Morgan, M. T. Morgan, M. F. Osborne, H. E. Robertson)

Examinations of UO_2 pellets irradiated in the LITR are under way, and techniques are being established, by examination of control material, for examining a capsule containing UC and one containing UO_2 dispersed in BeO. Fission-gas-release measurements were made for four capsules, and the data are presented in Table 5.9. No gas samples were obtained from capsules L-24b and L-27a, apparently because of in-pile leakage. The unusually high release for capsule L-24a may be related to the 30 000-Mwd/MT burnup, which is the highest experienced in this program. It should be noted that in the next highest burnup case,[3] 22 000 Mwd/MT for capsule L-11b, a similar, unusually high gas release occurred. The high gas release for capsule L-32b may be attributed to the very high operating temperature; an average temperature of at least 3400°F, with a maximum of 3800°F, was indicated.

The thermocouple from capsule L-32b, which remained operative throughout the 84-day test at the highest temperatures experienced by a miniature capsule, exhibited no damage other than the usual darkening and a slight bulging of the tantalum cladding in the fuel region, as shown in Fig. 5.17.

A slight decrease in the immersion density of the UO_2 from the four capsules was indicated by measurements in CCl_4, as shown in Table 5.10. However, these changes are generally within experimental error. Density

[3]GCR Quar. Prog. Rep. June 30, 1960, ORNL-2964, p. 156.

Table 5.9. Release of Kr^{85} Fission Gas from UO_2 as a Function of Burnup and Temperature

LITR-Irradiated Capsule No.	Burnup Based on Co^{60} Activity (Mwd/MT)	Effective UO_2 Central Temperature (°F)	Oxygen-to-Uranium Ratio	Bulk Density (% of theoretical)	Kr^{85} Release (% of Kr^{85} formed)
L-24a	30 000	2450	2.02	94.80	36
L-27b	16 000	3000	2.005	94.07	1.6
L-32a	8 500	3000[a]	2.004	94.26	8.0
L-32b	8 500	3400	2.004	93.71	67

[a]Estimated from capsule L-32b data; thermocouple failed at startup.

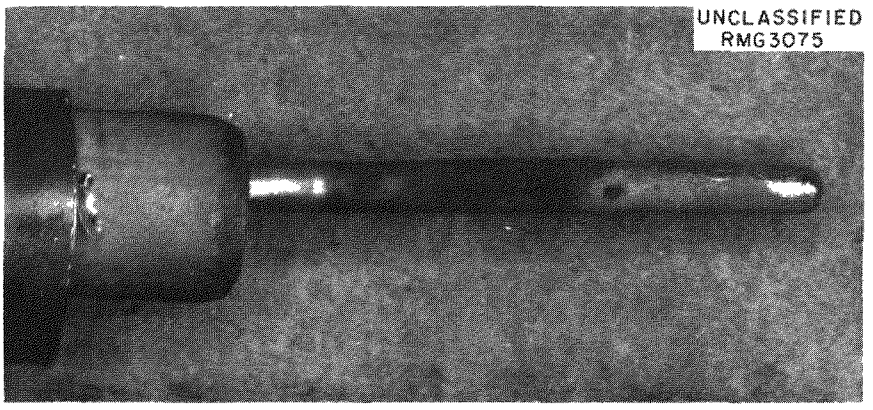

Fig. 5.17. Tantalum-Clad Thermocouple Which Experienced Temperatures as High as 3800°F During Irradiation in Capsule L-32b.

Table 5.10. Effect of Irradiation on Density of UO_2

Capsule No.	Burnup Based on Co^{60} Activity (Mwd/MT)	Effective UO_2 Central Temperature (°F)	Bulk UO_2 Density (% of theoretical)	Pellet Density Before Irradiation		Pellet Immersion Density After Irradiation (g/cm^3, ±0.2)
				Bulk Density (g/cm^3)	Immersion Density (g/cm^3)	
L-24a	30 000	2450	94.80	10.40	10.78	10.5
L-27b	16 000	3000	94.07	10.32	10.40	10.4
L-32a	8 500	3000[a]	94.26	10.34	10.43	10.5
L-32b	8 500	3400	93.71	10.28	10.63	10.5

[a]Estimated from capsule L-32b; thermocouple failed at startup.

measurements of fuel from capsules L-23a, L-23b, and L-24b were impossible because of fusion of the fuel with the depleted UO_2 insulators.

MTR-Irradiated UC_2-Graphite Dispersions (J. G. Morgan, M. F. Osborne)

Two MTR-irradiated experimental assemblies have been examined that contained UC_2-graphite dispersion fuel pellets canned in graphite. The test operating conditions are shown in Table 5.11.

Dimensional data for the two elements from assembly MTR-48-1 is shown in Table 5.12. A significant decrease in diameter and an increase in length were observed in both cases. The longitudinal growth was apparently restricted by the graphite can, since there was a slight extrusion of the fuel pellet into the relief space at the solid end of the can. The bulk

densities of the two fuel pellets were calculated from the weights and dimensions, and a small increase during irradiation was found, as shown in Table 5.13.

Table 5.11. Operating Conditions for UC_2-Graphite Experiments Irradiated in the MTR

Test Conditions	Assembly MTR-48-1		Assembly MTR-48-2	
	Element A	Element B	Element A	Element B
Time at power, hr	1440	1440	2700	2700
Average temperature, °F				
In graphite can wall	1570	1310	1500	1500
In center of fuel (calculated)	3350	3600	2500	2500
Estimated burnup, % of uranium atoms	13	6	20	20
Average fission power density, w/cm^3	270	300	140	140
Fuel concentration, wt % UC_2	10.52	19.33	5.59	8.00
Uranium enrichment, % U^{235}	93.12	93.12	93.12	93.12

Table 5.12. Effect of Irradiation on the Dimensional Stability of the UC_2-Graphite Elements Tested in Assembly MTR-48-1

	Preirradiation	Postirradiation	Change (%)
Element A diameter, in.			
Average	0.997		
Top		0.966	−3.1
Middle		0.962	−3.4
Bottom		0.954	−4.2
Element A length, in.			
Average	1.469		
Edge		1.508	+2.7
Center		1.544	+5.2
Element B diameter, in.			
Average	0.997		
Top		0.973	−2.4
Bottom		0.946	−5.1
Element B average length, in.	1.468	1.521	+3.5

Table 5.13. Effect of Irradiation on Density of UC_2-Graphite Fuel

	Bulk Density (g/cm^3)		Change (%)
	Preirradiation	Postirradiation	
Element A	1.887	1.930	+2.5
Element B	2.017	2.120	+5.1

The fuel elements of assembly MTR-48-2 were gamma scanned, the dimensions of the graphite can were measured, and the graphite can was examined for evidence of the leak indicated by high sweep-gas radioactivity during irradiation. No unusual radioactivity was disclosed by the gamma scan, no dimensional changes in the graphite can were detectable, and the leak in the graphite can was not apparent during initial examination. However, upon immersion in hot silicone oil, a thin stream of bubbles was observed to be escaping from one of the thermocouple holes. After exposure of the thermocouple hole by cutting away a section of the graphite, the small leak was located about 1/2 in. from the rear of the element opposite the bottom of the threaded seal plug.

Measurements of Fission-Gas Pressure at Operating Temperatures (M. T. Morgan)

The postirradiation internal pressure measurements of four EGCR prototype capsules at temperatures up to 1740°F have been successfully concluded. As reported previously,[4] this experiment was prompted by concern that because of high yield and mobility the cesium and rubidium fission products, which have boiling points under 1500°F, might contribute significantly to the internal fuel element pressure at operating temperatures. The experimental apparatus for these measurements has been described in detail.[5]

No pressure contribution from the vaporization of cesium and rubidium metals or their compounds was found within the accuracy of the equipment.

[4]GCR Quar. Prog. Rep. March 31, 1960, ORNL-2929, pp. 159–62.

[5]Proceedings of the Eighth Conference on Hot Laboratories and Equipment, TID-7599, Book 2, Dec. 1960.

This may be seen by the linear relationship of pressure and temperature shown in Figs. 5.18 through 5.21. Bench tests showed the pressure transducer to have a maximum deviation of ±15 mm Hg at 1700°F. The pressures for capsule 06-1 were reported earlier[6] as internal capsule pressures in psia. The capsule void volume used in calculating these pressures has now been measured and found to differ greatly from the previously calculated value because of the porosity of the BeO central rod. This difference reduces the previously reported pressures by a factor of 2.4. The fission-gas pressure data reported in Figs. 5.18 through 5.21 differ from internal capsule pressure data because of the added volume of

[6]GCR Quar. Prog. Rep. Dec. 31, 1960, ORNL-3015, p. 119.

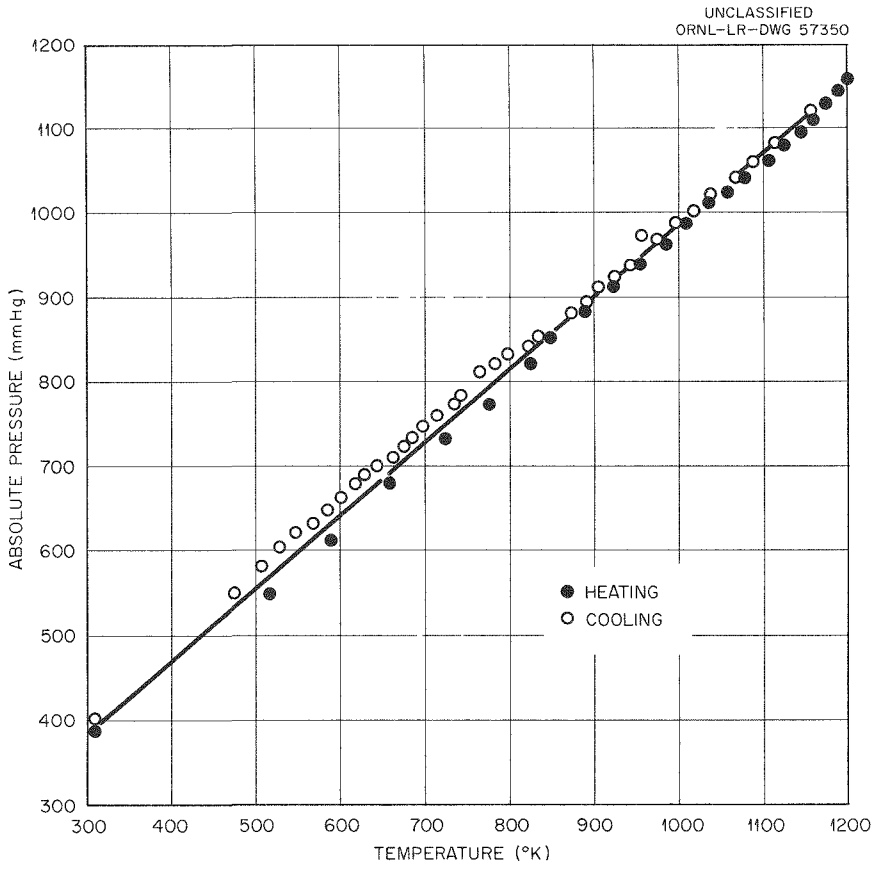

Fig. 5.18. Postirradiation Measurement of Fission-Gas Pressure in ORR-Irradiated Capsule 04-1.

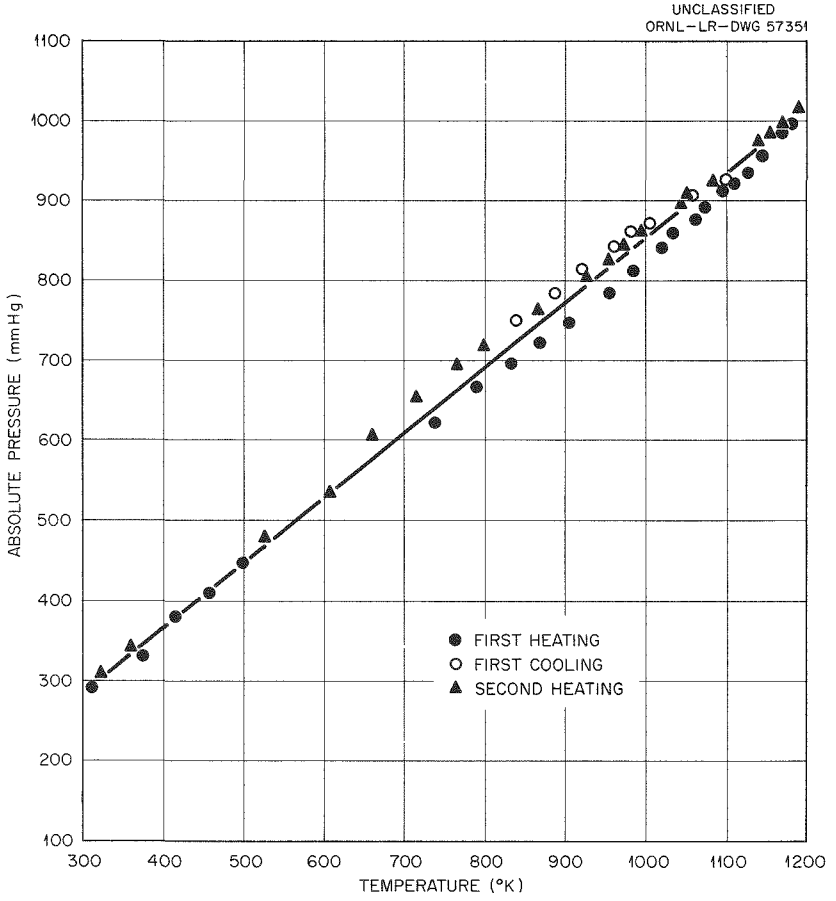

Fig. 5.19. Postirradiation Measurement of Fission-Gas Pressure in ORR-Irradiated Capsule 06-1.

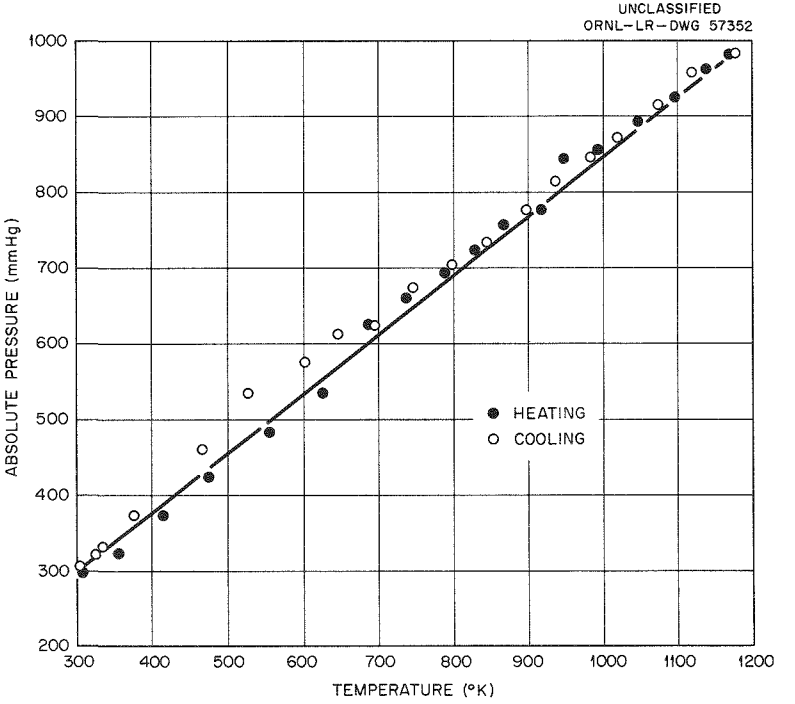

Fig. 5.20. Postirradiation Measurement of Fission-Gas Pressure in ORR-Irradiated Capsule 07-1.

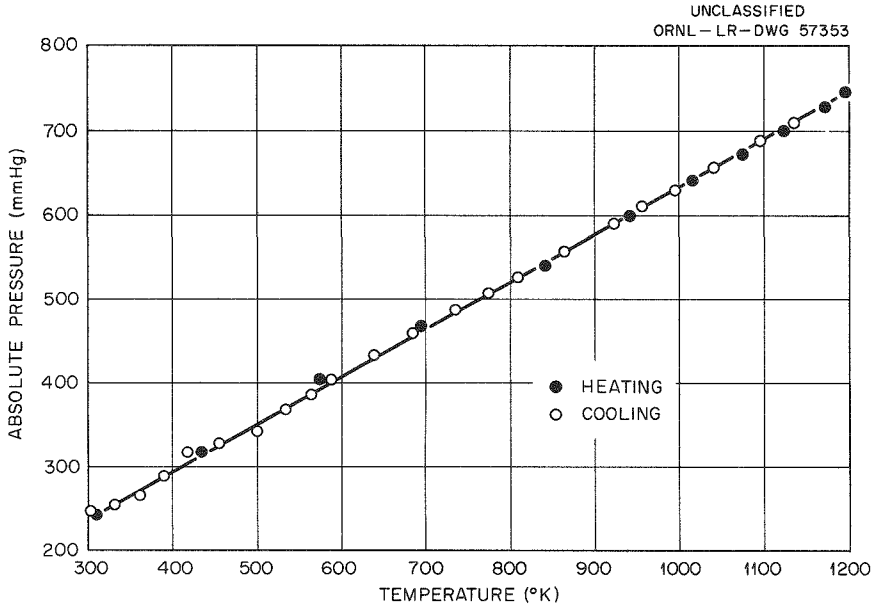

Fig. 5.21. Postirradiation Measurement of Fission-Gas Pressure in ORR-Irradiated Capsule 08-1.

the apparatus. These data will be converted to internal capsule pressures later when volumetric measurements have been completed. The fission gas has been collected and will be analyzed.

Advanced Materials Irradiated in ORR Closed-Cycle Loop (P. E. Reagan, M. T. Morgan, C. D. Baumann)

The capsule designated B9-2, containing two ThO_2-UO_2 pellets, has been opened for examination. Each pellet was sealed in a graphite can coated on the outside with siliconized SiC. The capsule was withdrawn from the reactor flux zone after only 7 hr at a graphite temperature of 1800°F because of coating failure. The siliconized-SiC coating had crumbled and was carried by the coolant gas to the loop filter. The graphite had completely oxidized. The two ThO_2-UO_2 pellets had broken into seven pieces, which retained their general cylindrical contour, but the edges were rounded off, possibly because of being tumbled by the coolant gas. The two clad pellets and their thermocouple wells are shown before irradiation in Fig. 5.22, and the seven broken pieces removed from the capsule after irradiation are shown in Fig. 5.23.

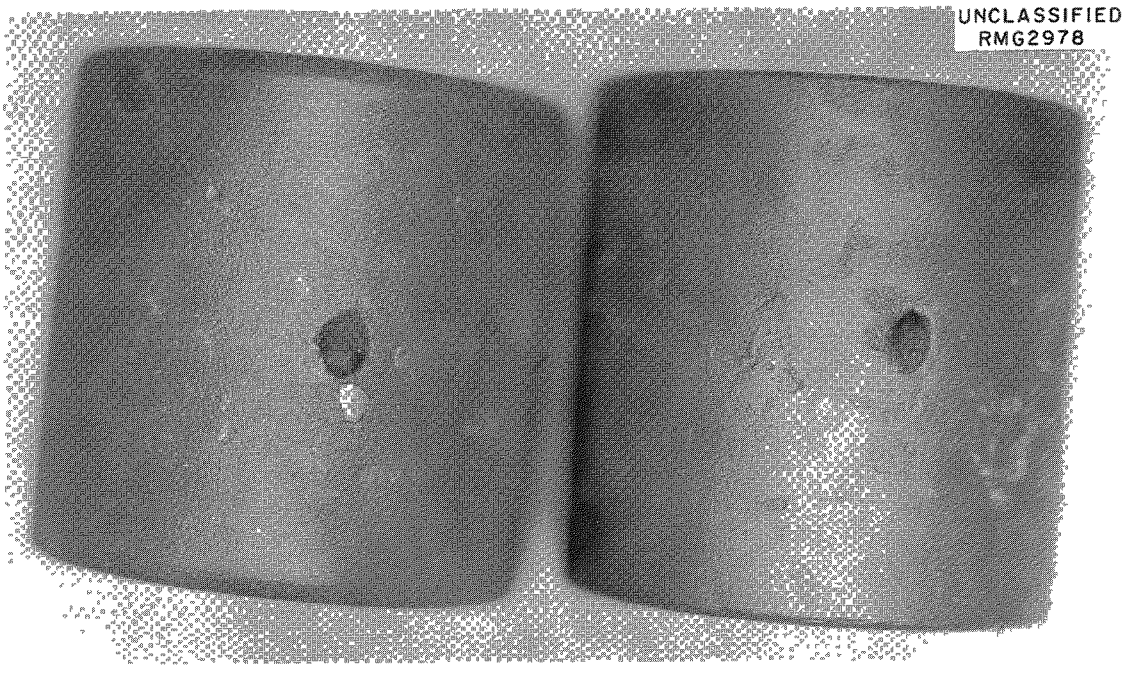

Fig. 5.22. ThO_2-UO_2 Pellets Clad in Graphite and Coated with Siliconized Silicon Carbide. The indentations are thermocouple wells. 4X.

Capsule B9-3, which contained two UO_2 cylinders clad in graphite and coated with siliconized SiC was irradiated in the ORR closed-cycle loop facility B9 at 1500°F to a thermal-neutron dose of 2.2×10^{20} neutrons/cm^2. Both samples failed but in different ways. Holes developed in the graphite can of the top sample and in the siliconized-SiC coating along the thermocouple trench, as shown in Fig. 5.24. The hole was readily located by the emission of bubbles when the sample was submerged in hot silicone oil. The bottom sample failed by complete graphite separation at the bottom of the UO_2 cylinder. This was probably due to a difference in longitudinal thermal expansion between the graphite can and the UO_2 pellet. The samples were constructed with a 0.006-in. end clearance between the UO_2 and the graphite. Calculations showed that this end gap would be filled by thermal expansion at a UO_2 temperature of about 2500°F if the graphite can were held at 1500°F. Although metallographic examination of the samples has not been completed, results indicate that the UO_2 cylinder walls reached 3400°F during irradiation. The two pieces of the broken graphite can are shown in Fig. 5.25. The UO_2 cylinder was easily

removed from the graphite can. A few cracks were noted along the cylinder wall, as shown in Fig. 5.26. It was observed that both ends of the 0.250-in. hole through the cylinder became filled with UO_2 during irradiation.

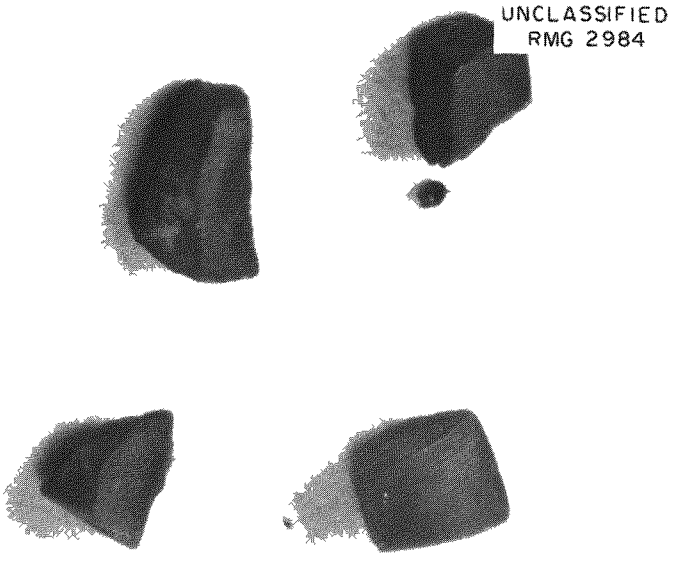

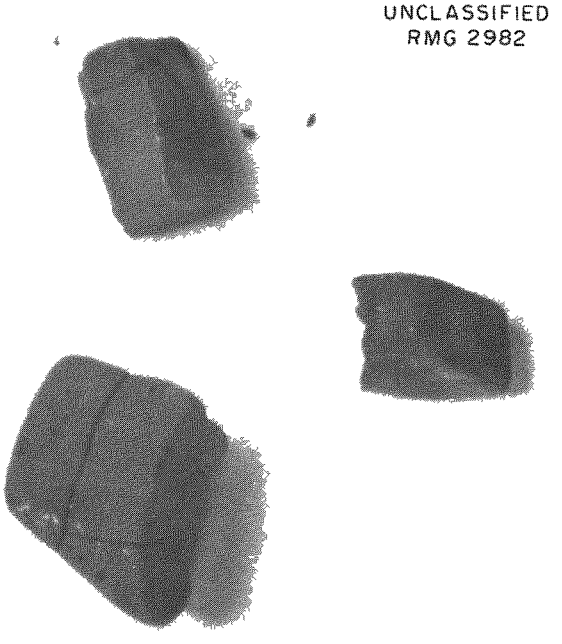

Fig. 5.23. Broken Pieces of ThO_2-UO_2 from Capsule B9-2. 2X

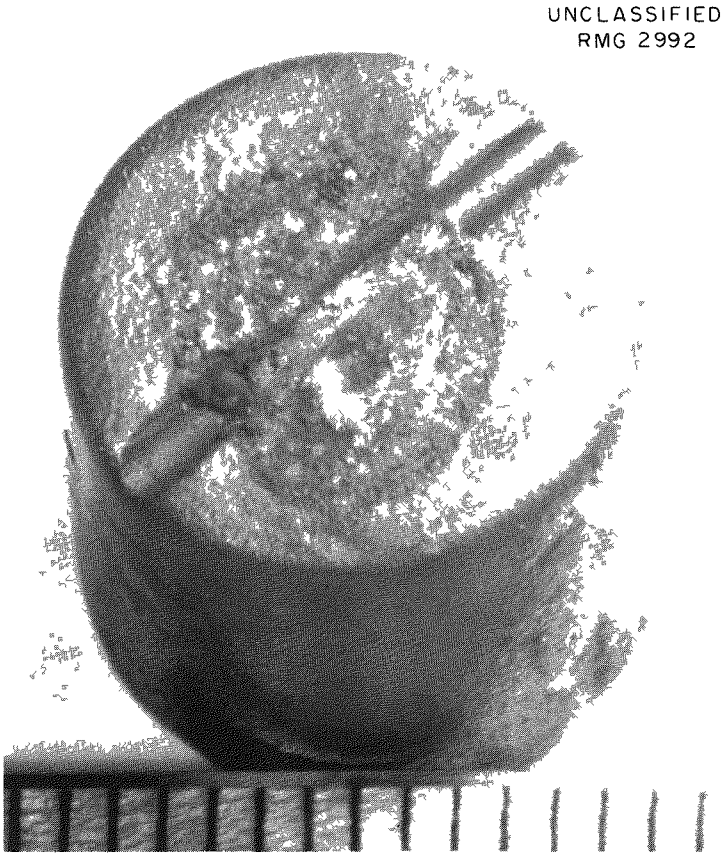

Fig. 5.24. Graphite-Clad UO_2 Pellet from Capsule B9-3 Showing Failure of Siliconized SiC Coating Along Thermocouple Trench. 4X

Both samples were impregnated with plastic and sectioned. In both cases, UO_2 was found to have moved, probably by sublimation, from the inside walls and deposited to fill both ends of each cylinder. The UO_2 wall thickness decreased from 0.125 to about 0.090 in. A section of the bottom end of the top sample is shown in Fig. 5.27.

Capsule B9-4, containing two UO_2 cylinders, has also been disassembled. These UO_2 cylinders were encased in low-permeability uncoated graphite and then sealed in an Inconel capsule in helium. The capsule was irradiated for 1000 hr at 1800°F. There was no reaction between the inside wall of the Inconel capsule and the graphite can. Visual inspection showed no graphite cracking or deformation and no diameter changes were noted, but both samples increased in length approximately 0.0001 in./in., that is, 1%. The samples are shown before and after irradiation in Fig. 5.28. The

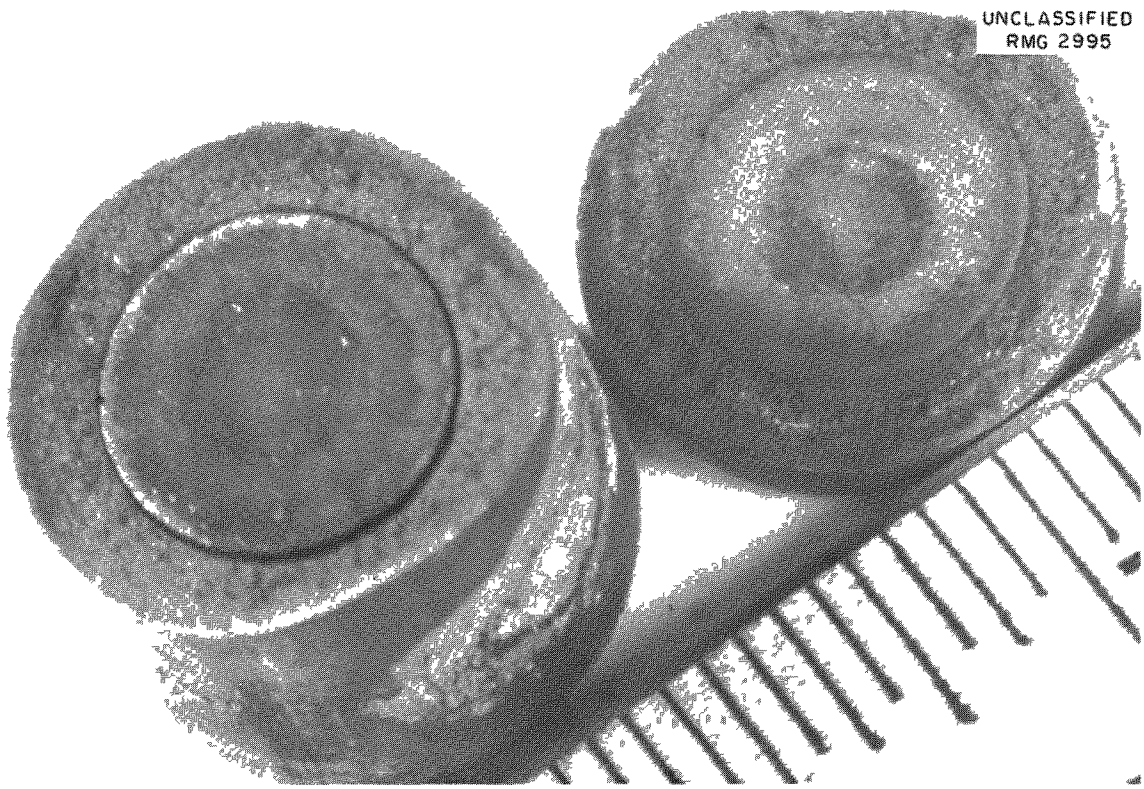

Fig. 5.25. Broken Graphite Can on UO_2 Pellet from Capsule B9-3. 4X

hot-silicone-oil bubble test, which indicated no leakage before irradiation, showed many holes along both graphite can walls after irradiation. Escaping bubbles may be seen as several white streams rising from the graphite in Fig. 5.29. Both samples have been sectioned, and metallographic examinations of the component materials are in progress.

Two UC_2-graphite pellets canned in graphite have been irradiated. These pellets, irradiated in capsule B9-5, differ in construction from previous samples in that the UC_2 was dispersed in a graphite matrix, a graphite shell was formed around the dispersion, and the shell was coated with siliconized SiC. Before irradiation the samples were oxidation tested for 138 hr at 1800°F and hot-oil-bubble tested for evaluation of the continuity of the cladding. The two specimens were then enclosed in a helium-filled Inconel can through which Inconel-sheathed thermocouples were inserted. The samples were irradiated at 1800°F in a flux of 1×10^{14} thermal neutrons/$cm^2 \cdot sec$. After 170 hr of irradiation, as increase in

UNCLASSIFIED
RMG 2991

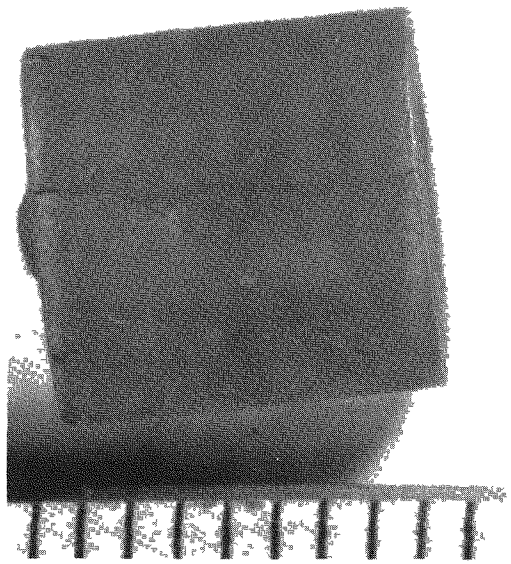

Fig. 5.26. Cracked UO_2 Cylinder from Graphite Can Shown in Fig. 5.25. 4X

UNCLASSIFIED
RMG 3126

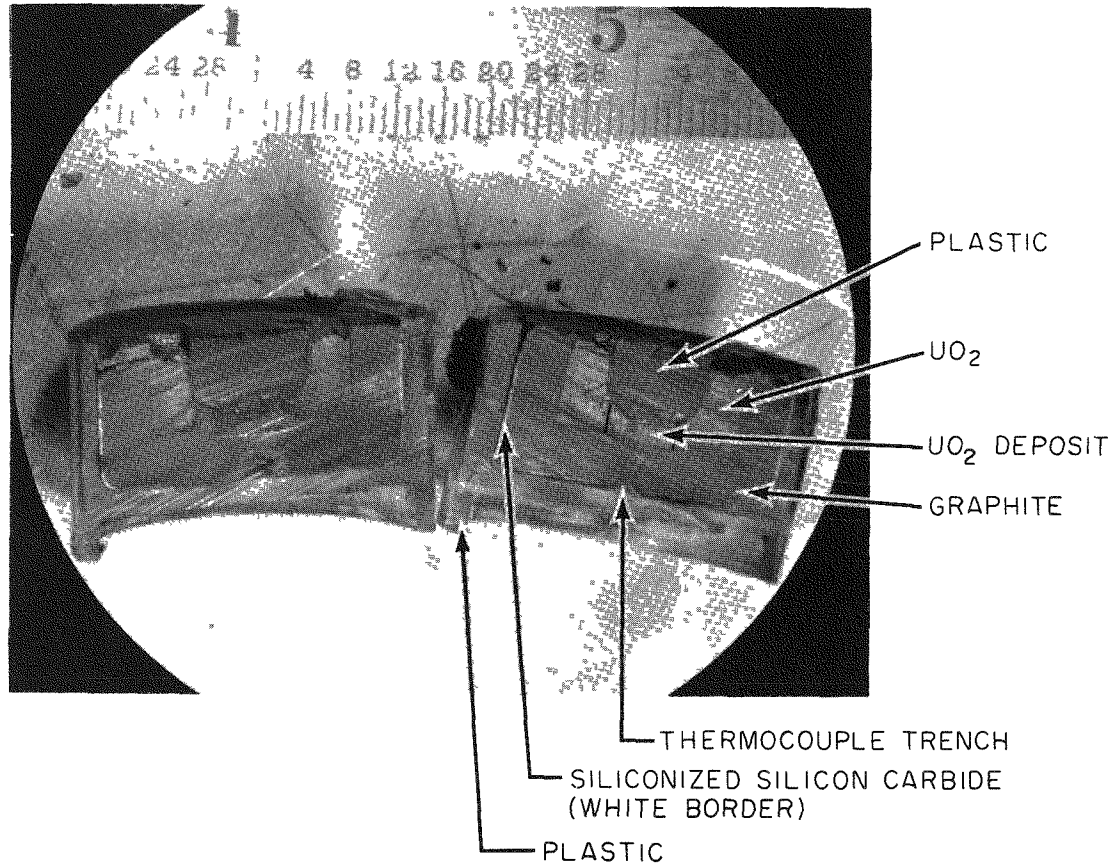

Fig. 5.27. Cross Section of Sample from Capsule B9-3 Showing UO_2 Deposit at End of UO_2 Cylinder. 2X

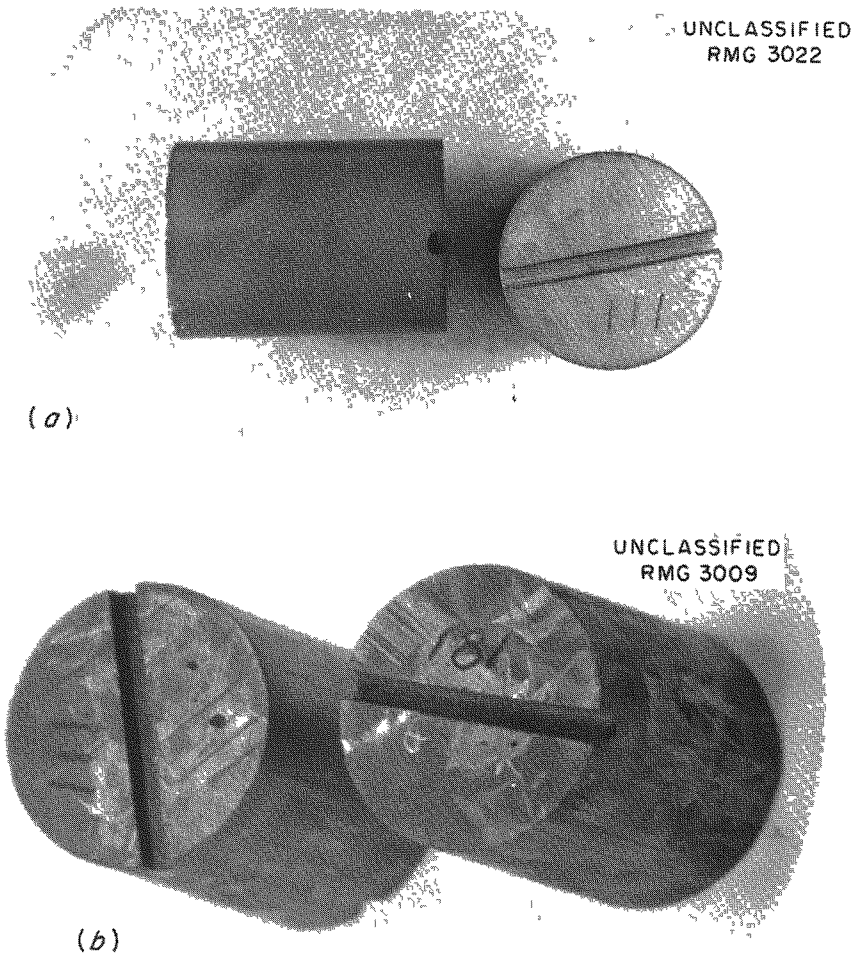

Fig. 5.28. UO_2 Cylinders Encased in Low-Permeability Graphite (a) Before and (b) After Irradiation in Capsule B9-4. 2X

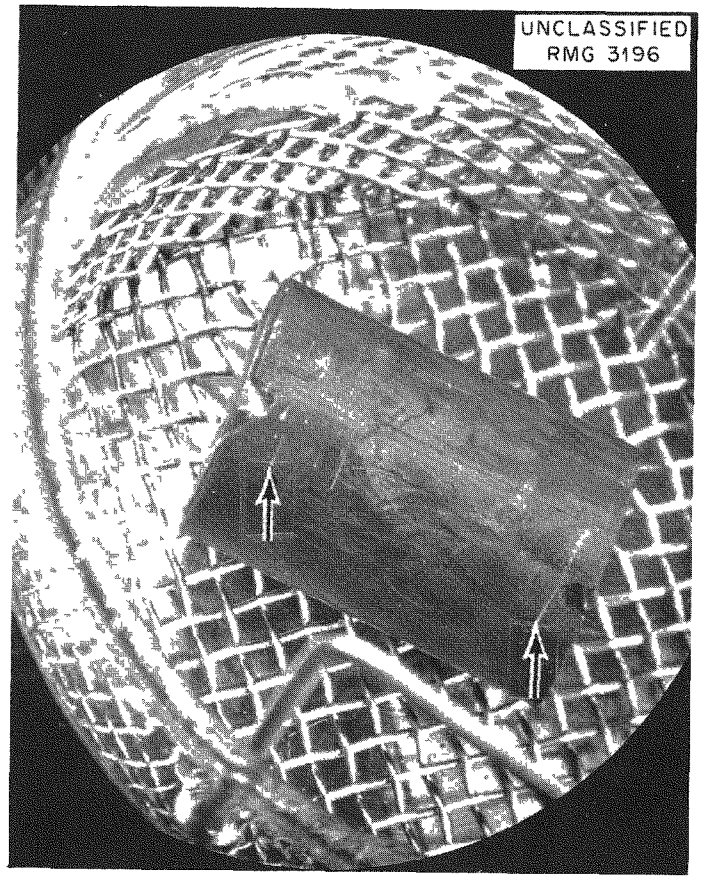

Fig. 5.29. Irradiated Sample from Capsule B9-4 Showing Bubbles Escaping at Holes in Graphite Can. 2X

coolant gas activity was noted, and the test was terminated. From the presence of fission gas in the coolant, it can be concluded that one, if not both, samples failed. The leak in the Inconel capsule probably developed at a weld where the thin thermocouple sheath passed through the capsule wall.

Designs have been completed for modifying the B9 loop to consist of a single-pass air-cooled system. The modification includes the addition of helium flow lines to sweep fission gases from the in-pile sample to a gamma-ray spectrometer and a trap located in the reactor pool to collect solid daughters of short-lived fission gases.

Instantaneous Fission-Gas-Release Experiment

R. M. Carroll, M. D. Karkhanavala

Examination of Graphite-Clad UO_2 Sample

The sample of UO_2 clad in low-permeability graphite with an outer 0.001-in. coating of pyrolytic carbon was removed from the C-1 facility in the ORR and examined in a hot cell. The manner of gas release during irradiation had established that the cladding was ineffective in retaining fission gas.[7] Postirradiation examination has revealed that the graphite cladding had not failed grossly; there were no obvious cracks, but the pyrolytic carbon coating had blistered and flaked away in several places, as may be seen in Fig. 5.30. A hot-oil leak test revealed the pin hole shown in Fig. 5.31. This opening through the graphite was enough to allow free interchange of gases between the inside and outside of the graphite container and cause the in-pile behavior previously reported.[7]

Tests of Thin-Plate UO_2 Sample

The sample now being irradiated in the ORR C-1 facility is in the form of two thin plates of UO_2 (1 × 0.5 × 0.040 in.) sandwiched together. The two slabs are held between two ThO_2 plates to insure that there will be no fission recoils embedded in the metal walls of the capsule which

[7]GCR Quar. Prog. Rep. Dec. 31, 1960, ORNL-3049, p. 261–3.

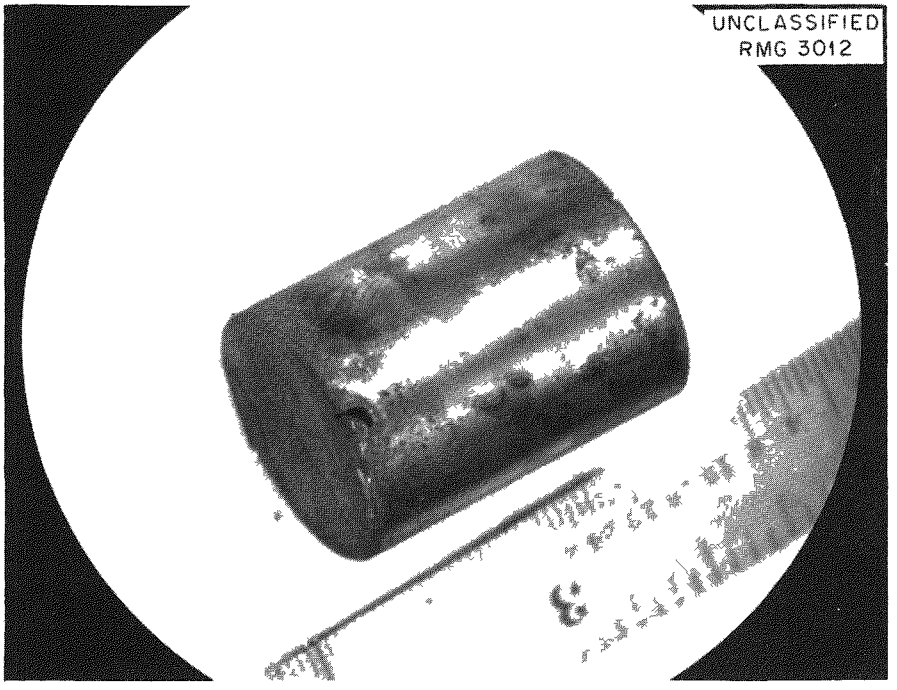

Fig. 5.30. Pyrolytic Carbon Coating After Irradiation. 2X

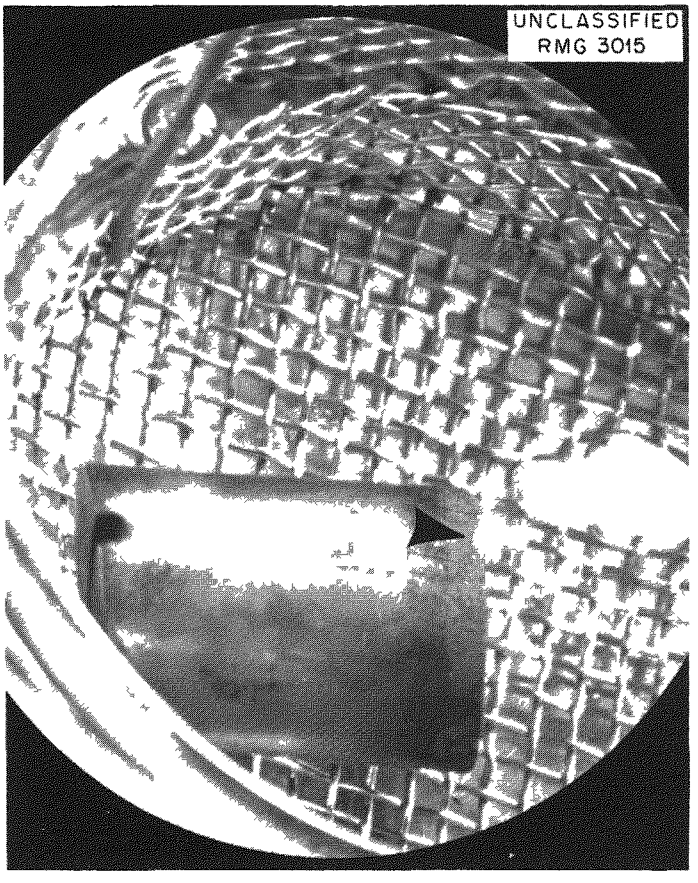

Fig. 5.31. Sample of Fig. 5.30 Immersed in Hot Oil. Gas bubbles emerged at point indicated by arrow. 2X

could subsequently diffuse out and contribute to the temperature-dependent gas release. These plates are inserted in an Inconel holder which fits into an Inconel capsule. Thermocouples are sandwiched between the plates and pressed tightly against the UO_2 surface by means of tungsten springs which act on the ThO_2 plates and through these on the thermocouples. The experimental apparatus is described in Figs. 5.32 and 5.33.

The fission-gas release from this ThO_2-shielded sample is essentially the same as from the previous unshielded sample. This demonstrates that back diffusion of fission products from the metal capsule is not a significant contribution to the fission-gas release. The fission-gas release from the UO_2 is highly temperature dependent down to a temperature of 700°C. This temperature dependence was observed for the three previously[8] irradiated samples.

During irradiation, when the flux is constant, the production rate of a given isotope is also constant. The total amount of the isotope within the fuel continues to increase until the loss rate is equal to the production rate. The loss of the fission product from the system may be by radioactive decay, leakage, or both. In any event, the total amount of isotope within the fuel will reach equilibrium within the time required for the radioactive decay rate to equal the production rate (~5 half lives of the isotope). In the case of the xenon isotopes Xe^{133} and Xe^{135}, there are iodine precursors which add to the time required for equilibrium. Normally, the loss by leakage (diffusion) from the UO_2 is much less than the radioactive decay loss, and the equilibrium amount of isotope within the UO_2 is not greatly disturbed by changing the temperature, which changes the diffusion loss. Therefore the flux is maintained as constant as possible, and the temperatures are controlled by varying the cooling-air flow rate.

In addition to the steady-state losses, there are losses by bursts which occur during a temperature change. These must be allowed to subside before a steady-state production versus loss relation can be attained.

---

[8]R. M. Carroll and C. D. Baumann, Experiment on Continuous Release of Fission Gas During Irradiation, ORNL-3050, Feb. 1961.

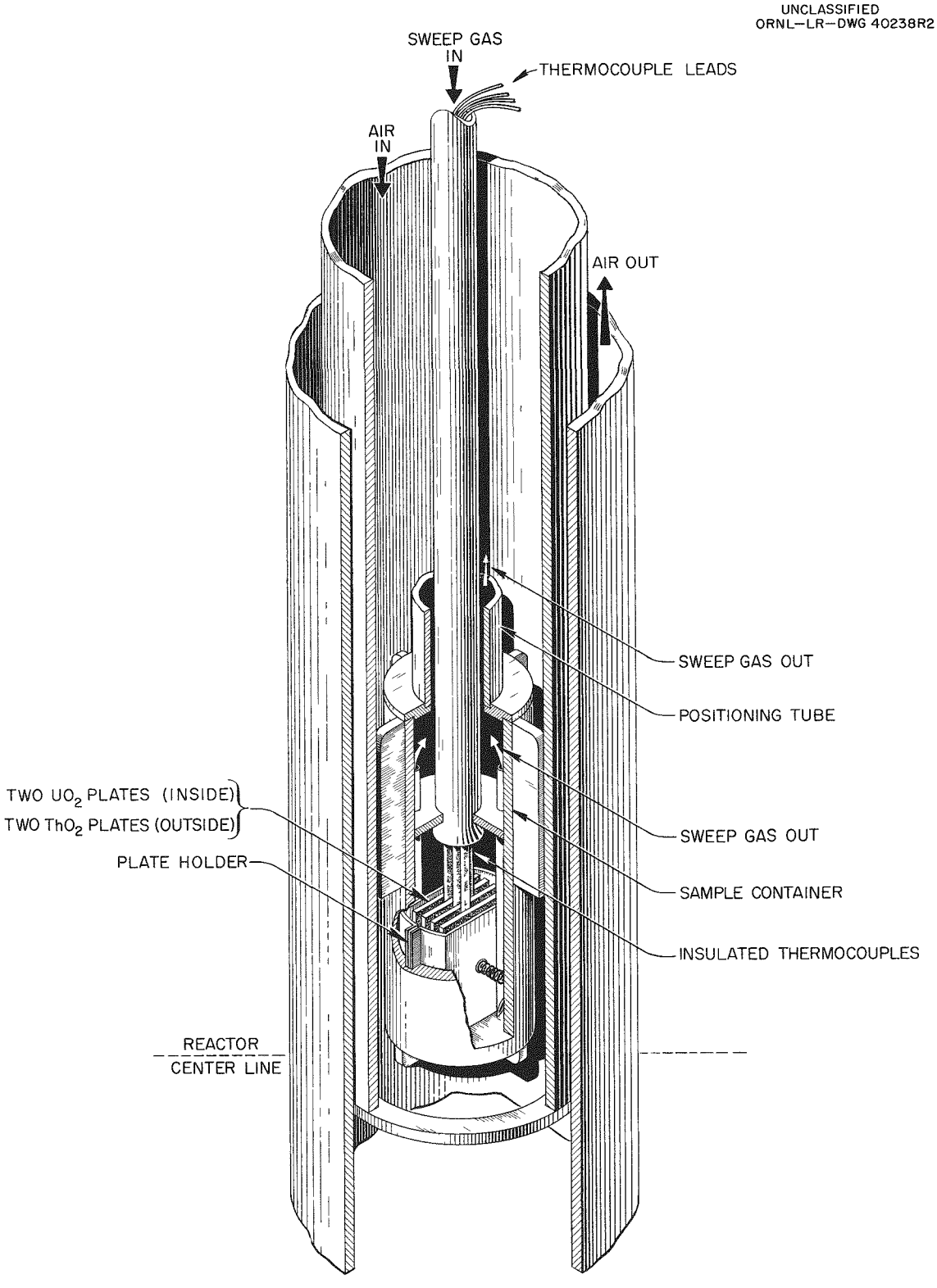

Fig. 5.32. Experimental Apparatus for Instantaneous Fission-Gas-Release Tests.

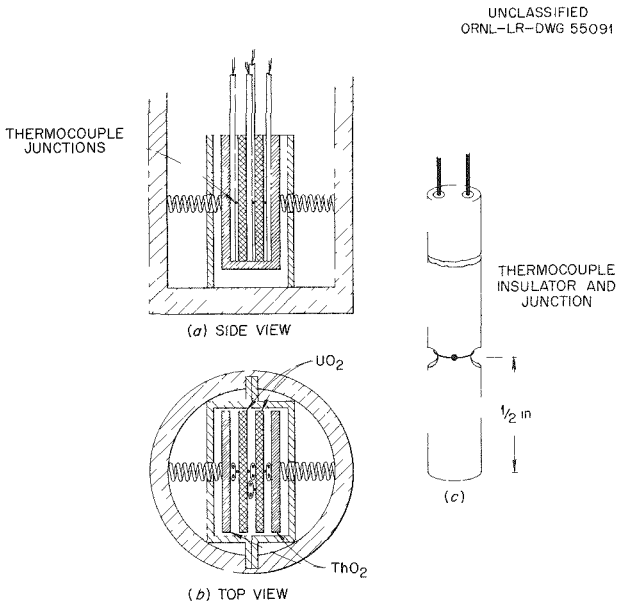

Fig. 5.33. Construction of Fuel Assembly for Instantaneous Fission-Gas-Release Experiments.

Iodine is also released from the UO_2 in a temperature-dependent manner, and it must be allowed to reach an equilibrium so that the total amount deposited on the walls of the system is no longer time dependent. The times for equilibrium are dependent then upon the isotopes observed and the previous irradiation history of the UO_2. Starting with an unirradiated sample, 30 days would be required for Xe^{133} equilibrium, but only 4 days for Xe^{135}, one day for Kr^{85m} and Kr^{88}, and 2 hr for Xe^{138}. With a sample which already contains a store of isotopes, the equilibrium is obtained more rapidly. A typical run is depicted in Fig. 5.34, which shows the time the sample was inserted into the reactor, the resulting heating burst, the gradual attainment of equilibrium in the gas release, and the cooling burst when the sample was withdrawn. The continued release of xenon from the plated iodine was measured to obtain the emission rate of iodine from the UO_2.

Fission-gas release runs were made at 720, 890, 1010, and 1100°C. The first three runs gave results similar to those of Fig. 5.34, which illustrates the run at 890°C, but the run at 1100°C was unusual in that equilibrium was not established within the usual 3 to 5 days. Moreover, the short-lived isotopes Kr^{88}, Kr^{85m}, and Xe^{138} showed release rates that increased with time at the same rate as the release of Xe^{133} and Xe^{135}. This led to the conclusion that some change in the release mechanism, such as slow grain growth or a phase change, was occurring. The run was terminated after 7 days when the reactor was shutdown for refueling. The fuel is now being tested at a lower temperature to see whether a permanent change occurred during the high-temperature run.

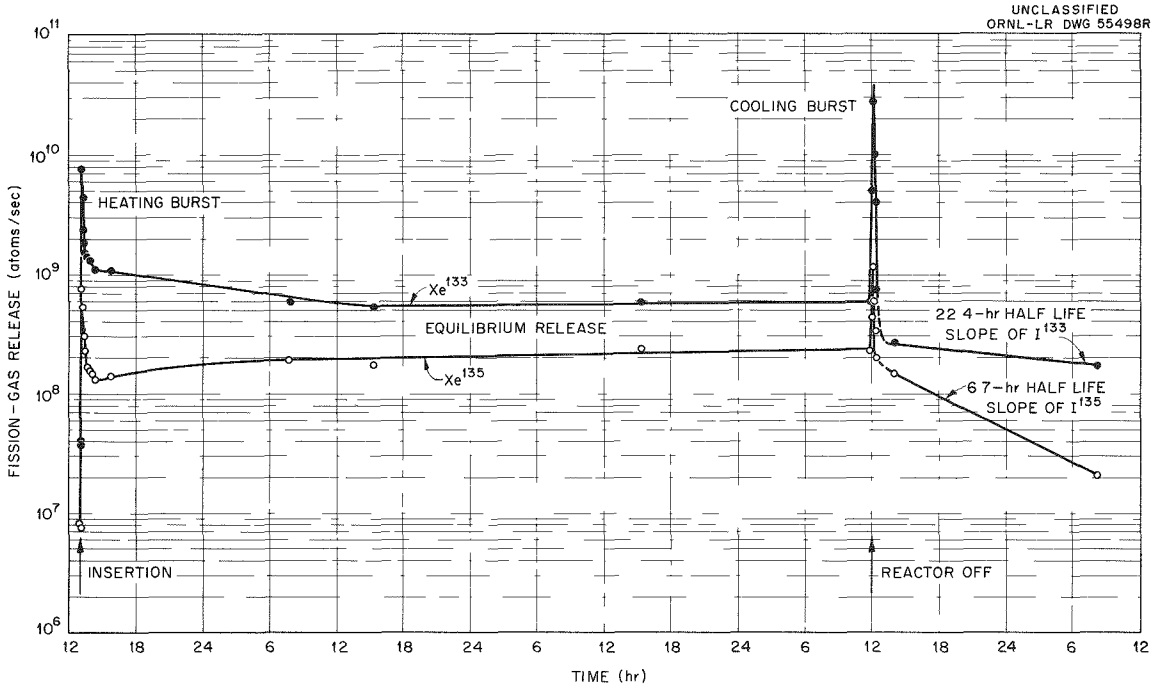

Fig. 5.34. Xe^{133} and Xe^{135} Release from UO_2 During Irradiation at 890°C in a Thermal-Neutron Flux of 3.7×10^{12} Neutrons/cm^2·sec.

The quantity of an isotope released in the cooling burst was proportional to the amount of isotope within the fuel and to the temperature. Table 5.14 gives data from three runs in which the sample was cooled to the same temperature within the same time (about 1 min) but the initial temperatures were different.

The isotopic diffusion coefficients were calculated, using an infinite-slab model, based on steady-state production and release of a radioactive

Table 5.14. Gas Release During Cooling Bursts

Initial Temperature (°C)	Total Atoms in UO_2		Quantity Released in Cooling Burst (%)	
	Xe^{133}	Xe^{135}	Xe^{133}	Xe^{135}
890	6.0×10^{16}	2.6×10^{15}	0.023	0.022
1010	6.6×10^{16}	2.7×10^{15}	0.048	0.065
1100	4.4×10^{16}	2.4×10^{15}	0.57	0.53

isotope.[8] Since the 133-135 isobars diffuse first as iodine and then as xenon, with a different decay constant for each form, the isotopic diffusion coefficients are difficult to calculate. Moreover, the I-Xe^{135} diffusion coefficient should be corrected for neutron capture by Xe^{135}, and this cannot be done until the I^{135} diffusion coefficient is known. The diffusion coefficients (Table 5.15) were therefore calculated by neglecting the diffusion of iodine and using the decay constant of xenon. This is more nearly justified in the case of Xe^{133} than for Xe^{135}, so the diffusion coefficients for both I-Xe^{135} and I-Xe^{133} are presented only for comparison. The diffusion coefficients obtained for Kr^{88} are not subject to the above errors because of the short (15-sec) half life of Br^{88}, and the Kr^{85m} coefficients probably have a very slight error introduced because of the 3-min Br^{85} precursor.

The measurements of Kr^{88} and Kr^{85m} given in Table 5.16 were taken between December 9 (when the sample was first installed in the reactor) and February 11. They show that there was no apparent change in release rates during this period of irradiation.

The activation energy for release of I-$Xe^{133,135}$ and $Kr^{88,85m}$ at temperatures up to 1010°C is 40 kcal/mole. It is not surprising that krypton and xenon have the same activation energy, and it seems likely that the activation energy for iodine release is also 40 kcal/mole. This agrees with the conclusion obtained from the study of the first thin-plate specimens[8] that the iodine was released with the same temperature dependence as xenon and krypton. The activation energy of the Kr^{88} from that

Table 5.15. Diffusion Coefficients for Iodine-Xenon Chain

Temperature (°C)	Release Relative to Production (%)		Release Rate Relative to Total (%/sec)		Diffusion Coefficient (cm^2/sec)	
	I-Xe^{133}	I-Xe^{135}	I-Xe^{133}	I-Xe^{135}	I-Xe^{133}	I-Xe^{135}
720	0.17	0.05	3.6×10^{-7}	2.4×10^{-6}	1.3×10^{-14}	1.45×10^{-14}
890	0.66	0.26	1.0×10^{-6}	8.8×10^{-6}	1.8×10^{-13}	4.1×10^{-13}
1010	1.47	0.68	2.3×10^{-6}	2.5×10^{-5}	9.25×10^{-13}	2.7×10^{-12}
1100	36.2	10.1	8.4×10^{-5}	4.1×10^{-4}	5.5×10^{-10}	5.8×10^{-10}

Table 5.16. Diffusion Coefficients for the Krypton Isotopes

Temperature (°C)	Atoms in Fuel		Production Rate (atoms/sec)		Release Rate (atoms/sec)		Diffusion Coefficient (cm^2/sec)		Order of Measurement
	Kr^{88}	Kr^{85m}	Kr^{88}	Kr^{85m}	Kr^{88}	Kr^{85m}	Kr^{88}	Kr^{85m}	
710	1.1×10^{15}	5.4×10^{14}	7.7×10^{10}	2.4×10^{10}	5.2×10^{6}	5.6×10^{6}	8.7×10^{-16}	7.1×10^{-15}	5
750	8.3×10^{14}	4×10^{14}	5.7×10^{10}	1.8×10^{10}	6.1×10^{6}	4.0×10^{6}	2.3×10^{-15}	6.5×10^{-15}	3
800	8.3×10^{14}	4×10^{14}	5.7×10^{10}	1.8×10^{10}	7.8×10^{6}	3.5×10^{6}	3.8×10^{-15}	4.9×10^{-15}	4
938	6.8×10^{14}		4.7×10^{10}	1.4×10^{10}	3.2×10^{7}		9.0×10^{-14}		1
1005	7.0×10^{14}	3.4×10^{14}	4.8×10^{10}	1.5×10^{10}	2.4×10^{7}	7.63×10^{6}	4.5×10^{-14}	3.4×10^{-14}	2
1010	8.0×10^{14}	3.9×10^{14}	5.5×10^{10}	1.7×10^{10}	4.0×10^{7}	4.8×10^{7}	1.0×10^{-13}	9.5×10^{-13}	6
1100	8.0×10^{14}	3.9×10^{14}	5.5×10^{10}	1.7×10^{10}	4.3×10^{8}	3.5×10^{8}	1.2×10^{-11}	5.4×10^{-11}	7

sample of UO_2 was 30 kcal/mole; however, the sample was found to have been oxidized during irradiation.

Xe^{138} Measurements

Xenon-138 is formed directly by fission and by decay of 5.9-s I^{138}, and thus iodine diffusion can be neglected for this isobar. Xenon-138 has a 17-m half life, but unfortunately its gamma emission is not well known. Its daughter, Cs^{138}, however, has a 32-m half life and a well-known gamma emission scheme. The sweep gas is passed through filters to remove cesium entrained in the gas before it enters the counting tube. Cesium-138 is formed in the counting tube by the decay of Xe^{138}, and it adheres to the walls of the counting tube. The decay of the Cs^{138} plated on the walls of the counting tube is measured by diverting the fission gas from the counting tube and purging the counting tube with an inert gas to remove all gaseous products (the Cs^{138} plated upon the walls of the counting tube is not removed by this treatment). Since at equilibrium the decay rate of Cs^{138} is equal to the decay rate of Xe^{138}, the amount of Xe^{138} emerging from the fuel can be calculated.

The Xe^{138}-Cs^{138} equilibrium for a given fuel temperature and flux is attained within 4 hr, and the diffusion coefficient obtained from the Xe^{138} is not complicated by its iodine precursor. This method was used to establish that the increasing fission-gas release in the 1100°C run was the result of a change in release mechanism, rather than an approach to equilibrium. Equilibrium was not reached in 3 1/2 days, even for the Xe^{138}. During the last 3 1/2 days of the 1100°C run (at constant flux and temperature), the Xe^{138} release increased by a factor of 2.1, Xe^{135} release increased by a factor of 2.4, and Xe^{133} release increased by a factor of 2.6. Unfortunately, this method of measuring Xe^{138} was developed during the 1100°C run, and no lower temperature measurements have yet been obtained.

Thermal-Neutron Flux Measurements by Argon Activation

The perturbed thermal-neutron flux within the capsule has been determined by using argon as the sweep gas and then measuring the activation

of the argon. Argon has very suitable properties for use as a continuous flux monitor. It is inert and can be used as a protective atmosphere. The only isotope of significance is Ar^{40} (99.6%) which has a 0.53-barn thermal-neutron absorption cross section with no resonance peaks. The other isotopes, Ar^{36} (0.34%) and Ar^{38} (0.06%), do not decay with gamma-ray emission upon neutron capture. With neutron capture, $Ar^{40} + n \rightarrow Ar^{41}$, which decays with a 1.83-h half life, emitting a single 1.29-Mev gamma ray for 99% of the disintegrations.

Since the fuel capsule is in the highest flux position and the volume of the sweep gas lines in the flux is small compared with the volume of the capsule, the argon is assumed to be activated entirely within the capsule. The flux, ϕ, is determined by the relation:

$$\phi = \frac{Ar^{41}}{Ar^{40}\sigma t} ,$$

where

Ar^{40} = number of atoms of Ar^{40} entering and leaving the fuel capsule each second, determined by flow rate,

Ar^{41} = formation rate of Ar^{41}, determined by gamma-ray spectrometry,

σ = microscopic absorption cross section of Ar^{40},

t = average time (sec) the Ar^{40} atoms are exposed to flux.

The time of exposure, t, is affected by the temperature within the fuel capsule, since the argon density decreases when the gas is heated by the fuel. The fuel capsule has a fixed volume, and the gas pressure cannot change, so the flow velocity of the argon increases in the high-temperature zone. The gas cools before it leaves the reactor, and because of the wide range of temperatures within the fuel capsule (typically, 1000°C at fuel, 500°C at capsule wall), the gas temperature cannot be calculated. An empirical graphical solution was obtained by varying the temperature of the fuel capsule with air cooling while at a constant flux level. A clear linear relation of activation to temperature was established for each power level, and this relation was extrapolated to the temperatures

at which the gas flow was measured. This extrapolated measurement gave the activation which would occur if the fuel capsule did not heat the argon.

When the extrapolated values for the flux are plotted as a function of distance from the reactor, the flux decreases exponentially with increasing distance from the reactor (Fig. 5.35). This is to be expected, since the fuel capsule is above the reactor lattice and neutrons are being absorbed by an increasing thickness of water. The variation of flux during a reactor cycle as the control rods are withdrawn to compensate for loss of reactivity is also given in Fig. 5.35. During a refueling of the reactor, the fuel elements were shifted so that the element adjacent to the experimental assembly was replaced by one with lower enrichment. This caused the flux at the test position to decrease by about 20%. All these measurements were taken within a two-month period. They demonstrate the variation of flux that may be expected at an experiment location and therefore the need of continuous monitoring.

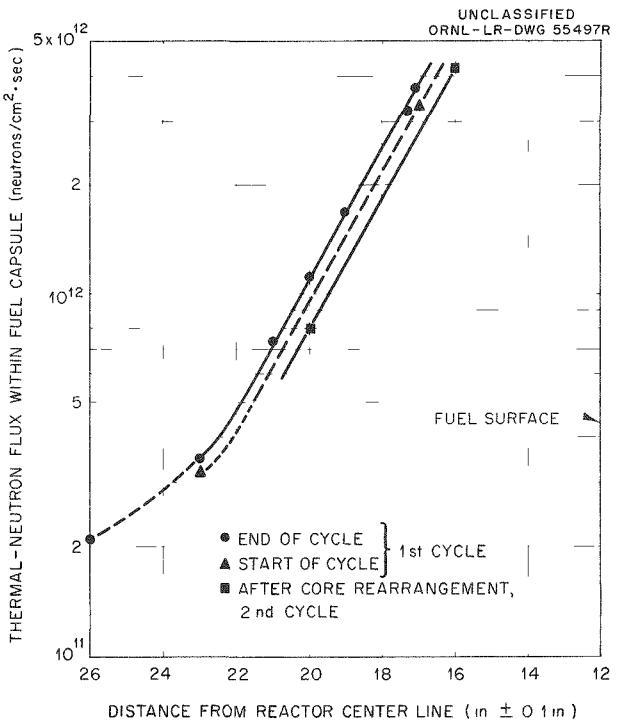

Fig. 5.35. Thermal-Neutron Flux in ORR Reactor Position C-1.

Measurements of Electrical Conductivity and Thermoelectric Power

Electrical conductivity measurements were made on the UO_2 thin plates by using the spring-loaded thermocouples as electrical contacts (Fig. 5.33). Good contact was obtained and yet the contacts yielded to the thermal expansion of the UO_2. The potential-drop method of measurement was chosen because it would eliminate the need to know the variation of the resistivity of the lead wires. The corresponding arms of the thermocouples were used as the current lead-in wires and potential probes. The same thermocouples were used to measure the temperature of the UO_2.

The electrical resistivity of the sample was measured prior to installation in the reactor. After assembling and leak testing the entire apparatus, a small Nichrome-wound furnace was placed around the capsule to obtain elevated temperatures. The temperature between the two plates was always higher than the outside temperature during irradiation, and this temperature gradient generated a thermoelectric emf between the UO_2 and the platinum thermocouples. It was found during in-pile testing that superposition of the thermoelectric emf on the potential drop across the UO_2 plate made measurements more difficult, particularly at higher temperatures. This thermoelectric emf was used to measure the resistance of the UO_2 plates, using the classical method for measuring the internal resistance of a battery.

The thermoelectric emf was erratic for some unknown cause, and yet the measurements have shown that the UO_2 behaved like an n-type conductor. This erratic behavior may be due in part to contact difficulties, which have also affected the electrical conductivity measurements. The formation of fission products, especially iodine, between the platinum contacts and the UO_2 may be responsible for the contact troubles. A detailed study was made of these fluctuations.[9]

The in-pile measurements of resistivity fall into two, more of less distinct, groups. Measurements made up to an irradiation dose of about 10^{18} neutrons/cm^2 fall very close to the values obtained for the unirradiated material (Fig. 5.36). Measurements made during irradiation to doses greater than 10^{18} neutrons/cm^2 fall on an almost parallel line of lower resistivity.[9] The curves obey the general expression for electrical resistivity. The activation energies calculated for the unirradiated and irradiated material are:

	Activation Energy (ev)
Unirradiated (room temperature to 200°C)	0.83
Unirradiated (400 to 750°C)	0.65
Irradiated up to 10^{18} neutrons/cm^2 (150 to 700°C)	0.5
Irradiated beyond 10^{18} neutrons/cm^2 (150 to 800°C)	0.5

[9]M. D. Karkhanavala and R. M. Carroll, In-Pile Measurement of the Electrical Conductivity and Thermoelectric Power of Sintered UO_2, ORNL-3093 (in press).

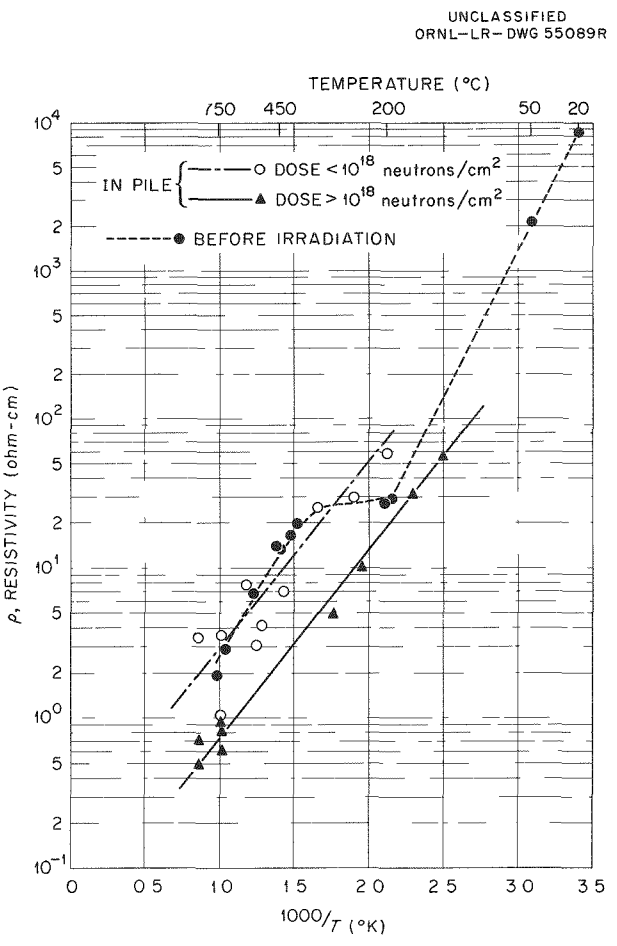

Fig. 5.36. Effect of Irradiation on Electrical Resistivity of UO_2.

Radiation Effects on Structural Metals

Pressure Vessel Steels (R. G. Berggren, T. J. Humphreys)

Experiment ORR-8 in which tensile and impact specimens of a carbon steel weld metal and a high-strength, low-alloy steel are being irradiated at 150°F and 400 to 1800°F, respectively, was started January 23, 1961. The experimental assembly was installed in the "piggyback" position of the ORR poolside facility. The furnace section containing the tensile specimens being irradiated at 800°F failed early in the experiment, and exposure is continuing at about 350°F. This temperature is also of interest and will provide useful data even though the furnace heater has failed. Neutron-flux monitoring experiments were also started but were

interrupted for irradiation-aging experiments on a zirconium-niobium alloy. Considerable difficulty was experienced in maintaining the desired temperature distribution because of changes in gamma heat distribution and shortcomings of the control instrumentation. Only three instruments were used to control the 13 furnace sections.

A new control panel has been designed for use with future experiments in the ORR. This panel will contain 36 controllers for 68 furnace sections and will make possible improved control of exposure conditions. It is expected that the new control panel will be ready for use in the next elevated-temperature experiment. Designs of the apparatus for the improved experiments, including a neutron-flux monitoring experiment, have been completed, except for tube-bending experiments, which have required revision because of changes in neighboring equipment.

The exposure of ASTM A-212, grade B, steel specimens in the GCR-ORR loop No. 1 is continuing. A set of E-7016 weld metal tensile and impact specimens has been assembled but will probably not be installed until GCR-ORR loop No. 1 has been rebuilt.

Experimental assembly ORR-30 containing impact specimens of ASTM A-212, grade B, steel plate and simulated heat-affected zones is being prepared for irradiation at about 140°F in the ORR.

Inconel and Stainless Steel (N. E. Hinkle, J. W. Woods, J. C. Zukas)

Preparations for disassembly of irradiated experimental assemblies have been completed. The assemblies scheduled for examination include both Inconel and type 304 stainless steel specimens. The initial post-irradiation examination will include diameter measurements and macrophotography. These procedures will be followed by metallographic examinations of selected specimens.

Six special "boron-controlled" heats of Inconel are being prepared for testing to determine the effect of B^{10} impurities on the in-pile time to rupture. The materials to be tested are described in Table 5.17.

Type 304 stainless steel tests are in progress. The stainless steel in-pile stress-rupture experiments are alternated with the Inconel experiments. A summary of the stainless steel and Inconel results to date is

given in Figs. 5.37, 5.38, and 5.39. Points with arrows are for specimens which did not rupture during irradiation, indicating rupture times beyond the value given.

Table 5.17. Special Heats of Inconel for Study of Effect of Boron on In-Pile Time to Rupture

Material	Heat No.	Form of Boron	Boron Concentration[a] (ppm)		
			Soluble	Insoluble	Total
MTR Inconel[b]	NX 8962		30	1	31
CX-900 Inconel[b]	NX 5757		41	1	42
Special Inconels					
1	0B	Natural boron			<10
2	2B	Natural boron			20
3	10B	Natural boron			100
4	4B11	B^{11} enriched to 98.5%			40
5	6B11	B^{11} enriched to 98.5%			60
6	6B10	B^{10} enriched to 95%			60

[a]The soluble and insoluble analyses were supplied by C. Feldman of ORNL. Where only total concentration is listed, the value was supplied by the manufacturer and is nominal.

[b]The MTR and CX-900 Inconel heats have already been tested.

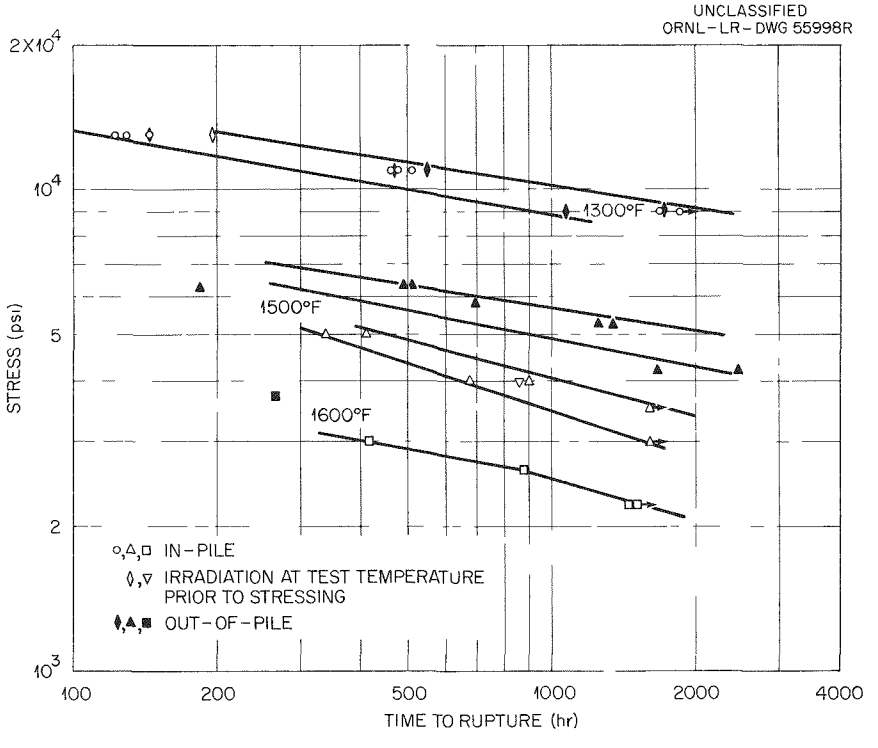

Fig. 5.37. Results of Stress-Rupture Tests in Air on Type 304 Stainless Steel (Superior Tube Co. Heat No. 23999X).

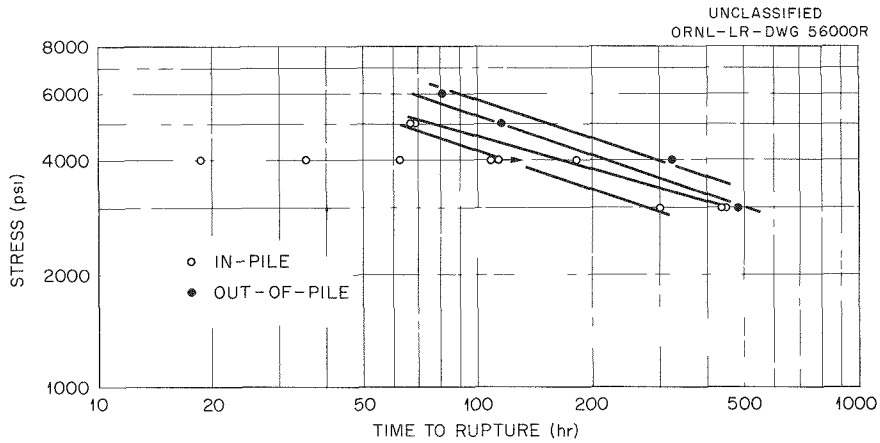

Fig. 5.38. Results of Stress-Rupture Tests at 1500°F in Air on Inconel CX-900 (INCO Heat No. NX5757).

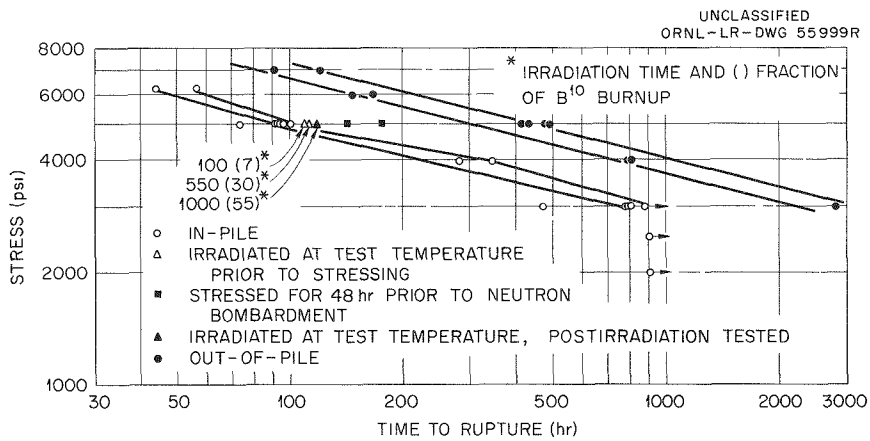

Fig. 5.39. Results of Stress-Rupture Tests at 1500°F in Air on Inconel (INCO Heat No. NX8962).

Radiation Effects on Beryllium (J. R. Weir, W. W. Davis)

Irradiation of the third high-temperature beryllium-swelling specimens was completed, and postirradiation examinations were initiated. The specimens were held at 600, 700, 740, and 780°C during an exposure of approximately 3.6×10^{20} neutrons/cm^2 (>1 Mev). This experiment differed from previous swelling experiments in that the exposure was greater (by about 3 times) and the specimens were 2-in.-long sections of tubes manufactured by various techniques rather than sheet coupons.

The swelling data obtained from pre- and postirradiation density measurements are given in Table 5.18. The fabrication history is also given in Table 5.18, if known. In other cases the fabricator is listed. It appears that for the exposure in this experiment, swelling became significant at temperatures above 700°C. The density changes of specimens 4 and 6 are unexpectedly high. Specimen 6 was impossible to clean after the irradiation, indicating that corrosion may have occurred during the experiment. This could have caused the change in density to be greater than that due to the irradiation-induced swelling alone. Metallographic examinations of these specimens are under way and should provide a more accurate appraisal of the results.

Postirradiation experiments on specimens subjected to cold irradiation are continuing. Some results of bend tests on specimens given postirradiation annealing treatments at various temperatures for 1 hr are shown in Fig. 5.40; the bend ductility as a percentage of the preirradiation

Table 5.18. Swelling of Beryllium During Irradiation at Elevated Temperatures

Specimen No.	Fabricator or Fabrication History	Irradiation Temperature (°C)	Density Change (%)
1	Pechiney	600	−0.27
4	Pechiney	700	−3.5
7	Pechiney	740	−1.3
2	Machined warm-extruded rod	600	+0.05
5	Machined warm-extruded rod	600	+0.05
3	Chesterfield	600	+0.33
6	Chesterfield	700	−5.5
9	Warm-extruded rod	600	+0.16
10	Warm-extruded rod	600–700[a]	−0.22
8	Warm-extruded rod	780[b]	−1.0
11	Machined hot-pressed block	600	+0.22
12	Machined hot-pressed block	600	+0.05

[a]The temperature decreased linearly with time from 700 to 600°C during the irradiation.

[b]The temperature was 780°C during the first half of the irradiation. The furnace then burned out, and the temperature was 425°C for the remainder of experiment.

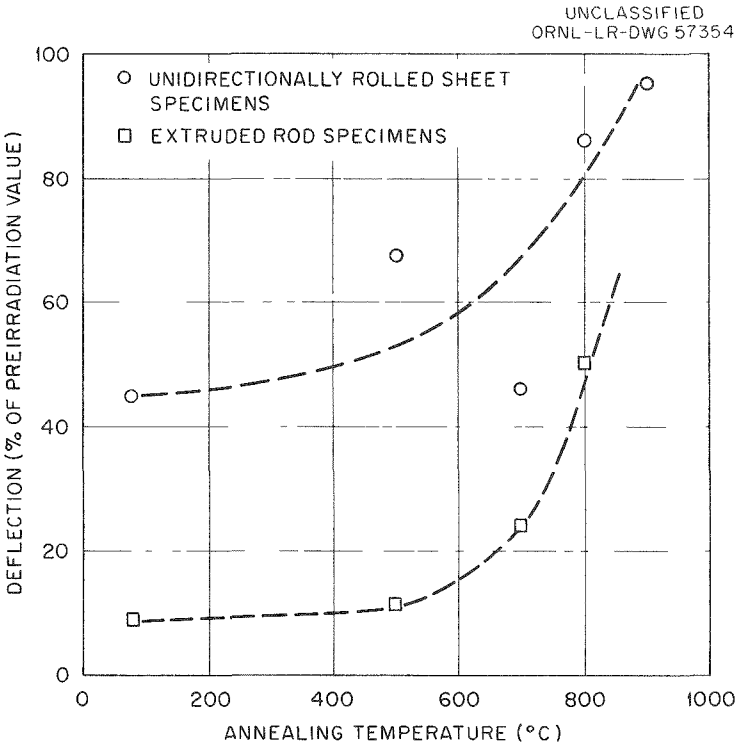

Fig. 5.40. Effect of Irradiation and Postirradiation Annealing for 1 hr on the Bend Ductility of Beryllium.

value is plotted versus the annealing temperature for unidirectionally rolled sheet specimens and specimens obtained from extruded rod. Recovery of ductility occurred rapidly at annealing temperatures above 700°C. The strength values follow a similar tendency although the scatter is rather large.

The two in-pile beryllium tube-burst experiments were completed in which internally pressurized beryllium tubes were held at 600°C. The intent of these experiments was to investigate the effect of exposure to different fluxes in the ORR poolside position [flux (>1 Mev) $\sim 3 \times 10^{13}$ neutrons/cm^2·sec] and the B-8 core position [flux (>1 Mev) $\sim 9 \times 10^{13}$ neutrons/cm^2·sec] and to study the effect of the integrated flux. Some specimens were stressed immediately and others were held at temperature for a period of time prior to stressing so that the exposure would build up. A photograph of one of the two experimental assemblies is shown in Fig. 5.41.

UNCLASSIFIED
PHOTO 52248

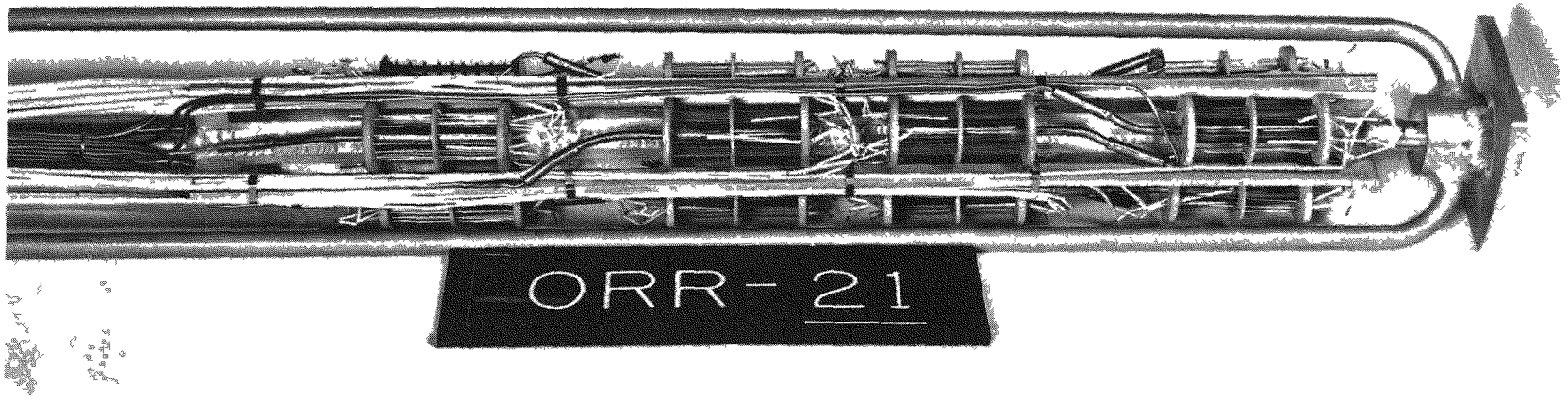

Fig. 5.41. Partially Assembled Beryllium Tube-Burst Apparatus for Irradiation in ORR Core Position B-8.

A comparison of in-pile and out-of-pile stress-rupture data for beryllium tubing machined from hot-pressed block is presented in Fig. 5.42. It may be seen that the high-exposure in-pile specimens exhibit lower strength than the lower exposure and out-of-pile specimens. The stress to produce rupture in times between 5 and 100 hr appears to be decreased by a constant stress value of approximately 2000 psi for the higher exposure [3×10^{20} neutrons/cm^2 (>1 Mev)].

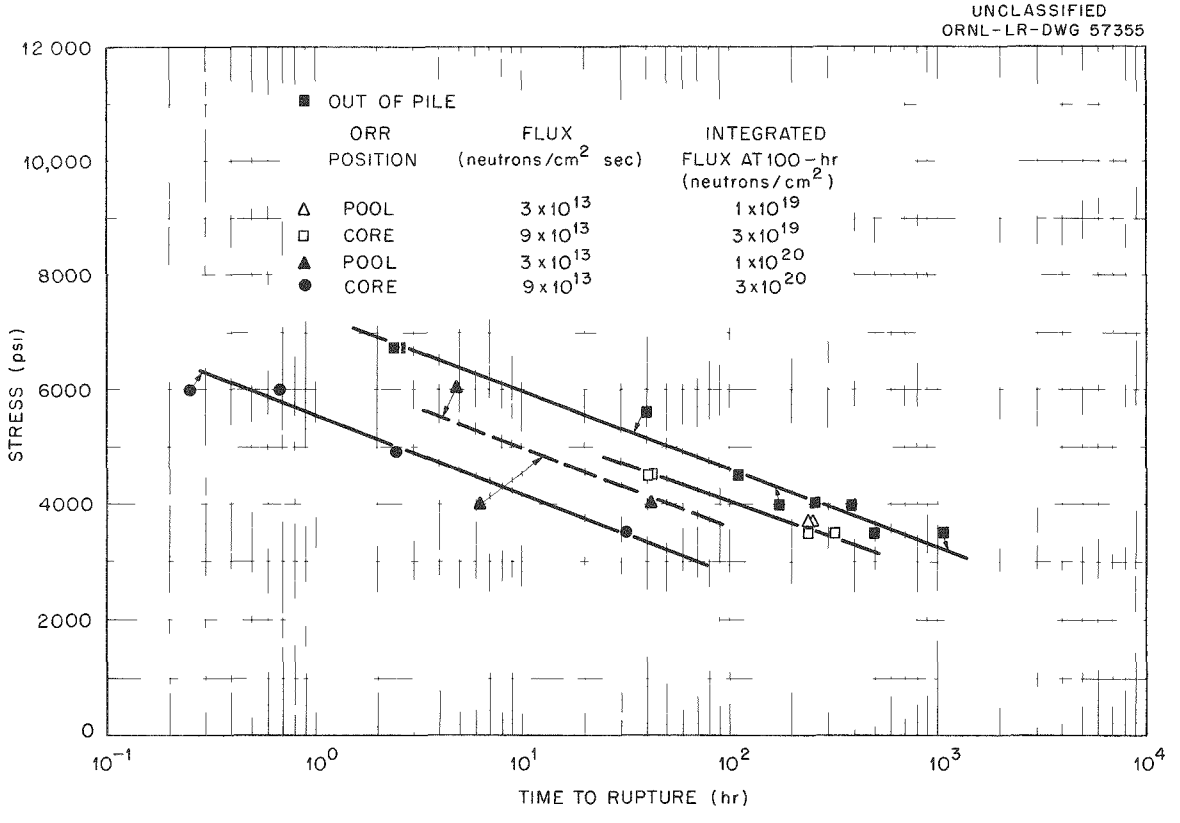

Fig. 5.42. Comparison of Stress-Rupture Results for Beryllium Tubes Tested Out-of-Pile and In-Pile at 600°C.

6. OUT-OF-PILE TESTING OF MATERIALS AND COMPONENTS

Compatibility Tests of Graphite, Structural Materials, and Gaseous Coolants

J. H. DeVan, B. Fleischer, A. M. Smith

Isothermal Tests with Static Helium

Following completion of the scheduled static pot tests,[1] a single test facility was charged with AGOT graphite and was operated at the maximum temperature attainable with the existing heater, that is, 1700°F. Reactions between impurities desorbed by the graphite at that temperature and various iron-base alloys were studied by means of test specimens located above the graphite. The test system was operated for 240 hr, at which time a leak occurred in the type 316 stainless steel test vessel.

The results of this elevated temperature test (STP 23) are compared in Table 6.1 with the results of similar tests conducted at 1400°F (STP 9) and at 1100°F (STP 21). It may be noted that the austenitic stainless steel specimens exhibited consistent weight gains, which increased as a function of the test temperature. The weight gains of ferritic materials, on the other hand, decreased as a function of test temperature, and in some cases a weight loss occurred.

Specimens of the austenitic and type 410 stainless steels were covered by a grey or black oxide film, the thickness of which increased with temperature. Metallographic examinations of stainless steel specimens tested at 1400 and 1700°F, in addition, revealed evidence of surface decarburization. Diffraction studies of the oxide films formed on all stainless steel specimens indicated the oxidation products to be spinels of the type $Fe(Fe,Cr)_2O_4$ and $MnFe_2O_4$. Low-alloy steels exposed in these tests showed no visible evidence of oxide films. Decarburization was apparent at the surfaces of the low-alloy steel specimens tested at 1400 and 1700°F.

---

[1] D. B. Trauger, Materials Compatiblity and Fuel Element Test Program, in Proceedings of Information Meeting on Gas-Cooled Power Reactors, TID-7564, p. 165 (Dec. 1958).

Table 6.1. Weight Changes of Steel Specimens After Reaction with Impurities Desorbed from AGOT Graphite

Test Specimen	Weight Change (mg/cm^2)[a]		
	Tested at 593°C	Tested at 760°C	Tested at 926°C
Type 316 stainless steel, 18% Cr–10% Ni–2.5% Mo–bal Fe	+0.062	+0.17	+0.33
Type 304 stainless steel, 18% Cr–10% Ni–bal Fe	+0.046	+0.17	+0.19
Type 310 stainless steel, 25% Cr–20% Ni–bal Fe	+0.055	+0.15	+1.36
Type 410 stainless steel, 12% Cr–bal Fe	+0.10	+0.08	−0.056
Low-alloy steel, 2.25% Cr–1% Mo	+0.47		+0.014
Low-alloy steel, 3% Cr–0.9% Mo	+0.43	+0.04	+0.009
Mild steel, 0.15% C	+0.03	−0.12	−0.16

[a]Values shown represent average weight changes of four test specimens.

The events leading to decarburization were discussed in a previous report[2] in conjunction with the 1400°F test. It was suggested that metal-gas reactions involving stainless steels begin to out-weigh graphite-gas reactions at test temperatures above 1100°F and that CO and CO_2 impurities are consumed through metal-gas reactions at such a rate that the ratio P^2_{CO}/P_{CO_2} favors decarburization. The test recently completed at 1700°F affords further evidence that CO-CO_2 concentrations in a closed stainless steel system containing graphite can become decarburizing as a result of gas-metal reactions. The vapor-phase thermodynamic activities of carbon based on the CO-CO_2 concentrations for the 1700°F test, as well as for the 1400 and 1100°F tests, are listed in Table 6.2. It is apparent that the tendency for the carbon activity to decrease between 1100 and 1400°F, as cited previously,[2] continues in the range from 1400 to 1700°F and that extremely low carbon activities are attained at 1700°F.

[2]GCR Quar. Prog. Rep. March 31, 1960, ORNL-2929, pp. 187–90.

Table 6.2. Carbon Activities in Static Pot Environments Based on $CO-CO_2$ Concentrations at Various Test Times

Time at Temperature (hr)	Thermodynamic Activity[a] of Carbon		
	Tested at 593°C	Tested at 760°C	Tested at 926°C[b]
0	0.53	30.0×10^{-3}	5.6×10^{-5}
10	0.58	8.0×10^{-3}	1.0×10^{-5}
100	0.44	1.7×10^{-3}	7.4×10^{-5}
240			5.5×10^{-5}
900	1.0	0.27×10^{-3}	

[a]Based on the reaction $2\ CO \rightleftharpoons C + CO_2$, for which $a_c = k_T P_{CO}^2/P_{CO_2}$, taking graphite as the standard state; data from L. S. Darken and R. W. Gurry, Physical Chemistry of Metals, McGraw-Hill, New York, 1953.

[b]Test terminated after 240 hr.

Low-Pressure Thermal-Convection Loop Tests with Helium Containing Controlled Amounts of Impurities

Additional tests have been run to investigate gas-metal reactions between various structural steels and $CO-CO_2$ impurities in helium at 1100°F. A type 316 stainless steel thermal-convection loop, described previously,[1] has been utilized for these experiments. Impure helium is circulated by natural convection at 45 psia through a heated test section maintained at 1100°F and a cold leg section at 500°F. In addition to various steel specimens and graphite, the test section contains an independently heated type 304 stainless steel simulated fuel element maintained at 1500°F. Results of four experiments completed in this facility were reported previously.[2-5]

The fifth controlled impurity experiment (TCL 14) was intended to operate with impurity levels of CO and CO_2 of less than 500 ppm, respectively. However, despite the fact that the graphite within the test section had been outgassed in a previous test, desorption of contaminants by

[3]GCR Quar. Prog. Rep. June 30, 1960, ORNL-2964, p. 186.

[4]GCR Quar. Prog. Rep. Sept. 30, 1960, ORNL-3015, p. 123.

[5]GCR Quar. Prog. Rep. Dec. 31, 1960, ORNL-3049, pp. 273–6.

the graphite resulted in a concentration of 1000 ppm CO_2 for a short period of time at the start of the test. Continued purging of the test loop with pure helium quickly lowered the CO_2 and CO concentrations to 500 ppm, respectively, and a gradual reduction of CO and CO_2 occurred over the next 200 hr until concentrations of 100 ppm, respectively, were reached. This impurity concentration was then maintained for the duration of the 900-hr test.

Immediately following this test, a sixth experiment (TCL 15) was run with helium containing a relatively high-impurity concentration (10 000 ppm CO_2 and 2500 ppm CO). This test was designed to provide a CO_2 partial pressure equivalent to the maximum impurity concentration specified for the EGCR primary coolant. The present EGCR specification provides for a CO_2 level of 1600 ppm (by volume) in helium at 300 psia.

The graphite used in experiment TCL 15 had been previously degassed in tests TCL 13 and 14; however, as the loop temperature approached operating conditions, the concentrations of H_2, H_2O, CO, and CO_2 were of the order of 2000 ppm for H_2 and 150 to 500 ppm for the other constituents. Within 100 hr after reaching the operating temperature, essentially all impurities except CO and CO_2 had disappeared from the system, and these were of the order of 400 and 200 ppm, respectively.

Sufficient CO_2 was then added to the loop to raise the level of this impurity to the specified range of 0.9 to 1.0 vol %. Considerable difficulty was encountered in obtaining the desired level, since the CO_2 added to the loop disappeared as a consequence of gas-metal reactions within a matter of hours. Approximately 400 hr after the loop was brought to temperature, the desired CO_2 level was established, and the 900-hr test period started. The desired 0.9 to 1.0 vol % CO_2 and the resultant 0.2 to 0.3 vol % CO were then maintained by making daily injections of CO_2 into the loop.

Weight increases recorded for the test specimens utilized in experiments TCL 14 and TCL 15 are compared in Table 6.3. Specimens exposed in experiment TCL No. 14, despite the relatively low impurity concentration (~100 ppm CO_2 and CO), exhibited weight gains similar to those reported for previous loop tests,[5] in which the CO and CO_2 impurities ranged from

Table 6.3. Results of Thermal-Convection Loop Tests TCL 14 and 15 in Which Steel Specimens Were Exposed to Helium Containing CO and CO_2

Helium pressure: 45 psia
Specimen temperature: 1100°F
Test duration: 900 hr

Steel Specimens	Weight Increase (mg/cm^2)	
	Test TCL 14 (0.01% CO_2 + 0.01% CO)	Test TCL 15 (1.0% CO_2 + 0.25% CO)
Mild steel, 0.15% C	3.14	6.05
Low-alloy steel, 2 1/4% Cr–1% Mo	(a)	5.57
Low-alloy steel, 5% Cr–0.5% Mo	1.82	5.04
Low-alloy steel, 7% Cr–0.5% Mo	1.20	1.60
Type 430 stainless steel, 17% Cr	0.30	0.32
Type 304 stainless steel, 18% Cr–8% Ni	0.14	0.30

[a]Specimens underwent a weight loss as a consequence of film spalling.

450 to 1800 ppm. In loop TCL 15, which contained a much higher concentration of impurities (10 000 ppm CO_2 and 2500 ppm CO), low- and medium-alloy steels exhibited significantly higher weight gains, but steels containing 7% or more chromium had only slightly higher weight gains than in previous tests.

In both tests, specimens containing 7% or more chromium became covered with a relatively light, adherent oxide film, while lower alloy specimens developed relatively heavy, poorly adherent oxide films. In the case of the latter specimens, the oxidation product was composed of a metallic-appearing outer layer and a black substrate, the nature of which was discussed previously.[6] Considering the poor adherence of this film, it is not surprising that the rate of oxidation of the lower alloy specimens was more sensitive to an increase in gas impurity concentration than specimens having a less pervious oxide product.

The poor adherence of the oxidation films produced on the low-alloy materials made it possible to remove the oxidation products from these materials to obtain measurements of the total weight of oxide and of the

[6]GCR Quar. Prog. Rep. March 31, 1960, ORNL-2929, p. 193.

metal which was oxidized. Results of these measurements are compared in Table 6.4 with oxidation data reported for plain carbon and chromium steels tested at 1100°F in air. It may be seen that the addition of 5% Cr reduces the rate of oxidation of steels in the various CO_2-CO mixtures by no more than a factor of 2 within the 900-hr test period. It is interesting that the rate of oxidation of the 5% Cr alloy in test TCL 15, in which the highest concentration of CO and CO_2 was used, was nearly as great as that reported for air at 1100°F. The variations in the total concentration of CO_2 and CO, as would be expected, appear to have less of an effect on the rate of oxidation than variations in the ratio of these contaminants. Reducing the concentrations of CO_2 and CO to 100 ppm, respectively, in test TCL 14 did not measurably reduce the rate of oxidation compared with that in test TCL 13 in which the CO_2 and CO concentrations were 500 and 450 ppm, respectively.

Table 6.4. Oxidation of Low-Alloy Steels in Air and in Helium Contaminated by CO and CO_2

Helium pressure: 45 psia
Test temperature: 1100°F
Test duration: 900 hr

Loop No.	Impurity Concentration (vol %)		Ratio of Partial Pressures, CO_2 to CO	Steel Specimen	Weight of Oxide Film (mg/cm^2)	Weight of Metal That Reacted (mg/cm^2)
	CO_2	CO				
10	0.13	0.18	0.72	Plain carbon, 0.15% C	14.1	10.2
				Low alloy, 2.25% Cr–1% Mo	7.9	5.7
12	0.15	0.18	0.83	Plain carbon, 0.15% C	7.3	5.3
				Low alloy, 2.25% Cr–1% Mo	5.5	4.0
				Low alloy, 5% Cr–0.5% Mo	5.7	4.1
13	0.05	0.045	1.1	Plain carbon, 0.15% C	12.8	9.3
				Low alloy, 2.25% Cr–1% Mo	10.5	7.6
				Low alloy, 5% Cr–0.5% Mo	5.9	4.3
14	0.01	0.01	1.0	Plain carbon, 0.15% C	10.5	8.3
				Low alloy, 5% Cr–0.5% Mo	6.6	4.8
15	1.0	0.25	4.0	Plain carbon, 0.15% C	21.3	15.0
				Low alloy, 2.25% Cr–1% Mo	20.2	14.6
				Low alloy, 5% Cr–0.5% Mo	14.4	9.2
	Air[a,b]			Plain carbon, 0.15% C	98	71
				Low alloy, 2.25% Cr–1% Mo	54	39
				Low Alloy, 5% Cr–0.5% Mo	18	13

[a] H. H. Uhlig, The Corrosion Handbook, pp. 644–7, Wiley and Sons, Inc., New York, 1948.

[b] Steels for Elevated Temperature Service, pp. 21–25, United States Steel Co., 1949.

Forced-Circulation Loop Tests

Evaluations of the small-scale gas purification system[7] installed on the forced-circulation loop have been completed, and the loop is again being utilized for materials compatibility experiments. The first of these experiments, designated FCL 5, is designed to provide data for a study of the oxidation of graphite and structural metals as a consequence of controlled H_2O additions to high-temperature helium. The H_2O addition, which will be made in the form of water-saturated helium, is intended to mock up the maximum allowable rate of H_2O inleakage specified for the EGCR (0.8 lb/day) and, making allowance for the difference in system volume, will be established at a rate of 5.8×10^{-3} lb/day. It is proposed to control the level of other impurities produced as a consequence of water injection by continuous flow of a side stream through the gas purification system.

The loop is currently operating with a test section temperature of 1400°F, a helium pressure of 45 psia, and a flow rate of 230 lb/hr. The flow rate through the purification train is established at 0.774 lb/hr.

Continuous operation of the CO_2 and H_2O adsorber and periodic use of the catalytic oxidizer effectively maintained the impurity concentrations below the maximum levels specified for the EGCR as the loop was brought to operating temperature. After reaching operating conditions, CO and CO_2 continued to be degassed from the AGOT graphite test section at such a rate that water injection could not be started immediately. It has been necessary to operate the CO_2 adsorber continuously and the catalytic oxidizer intermittently to maintain impurity levels within desired limits. Water injection will be initiated as soon as other impurity concentrations have stabilized.

Graphite-Metal Diffusion Studies

Contradictory data exist concerning the effect of temperature and pressure on the rate of carburization of stainless steels in intimate contact with graphite. Much of the disparity in test results appears to

---

[7]GCR Quar. Prog. Rep. June 30, 1960, ORNL-2964, p. 189.

have stemmed from differences in the purity of the gaseous atmospheres surrounding the test specimens. Accordingly, an investigation has been initiated to systematically study the effects of temperature, contact pressure, atmosphere, and surface treatments on the rate of carburization of type 304L stainless steel in contact with graphite. The equipment being utilized for these experiments is illustrated in Fig. 6.1. Metal test specimens in the form of flat disks are sandwiched between circular graphite disks and are compressed by a pneumatically loaded push rod. An outer type 316 stainless steel container (not shown in Fig. 6.1) surrounds the test specimens to provide for the establishment of various gaseous atmospheres. A Conoseal flange joins the outer container to the upper shaft assembly.

An initial test to evaluate the performance of the equipment was operated at 1300°F under a vaccum of 5×10^{-5} mm Hg. Contact pressures on the diffusion couples ranged from 500 to 2000 psi. After 90 hr a leak

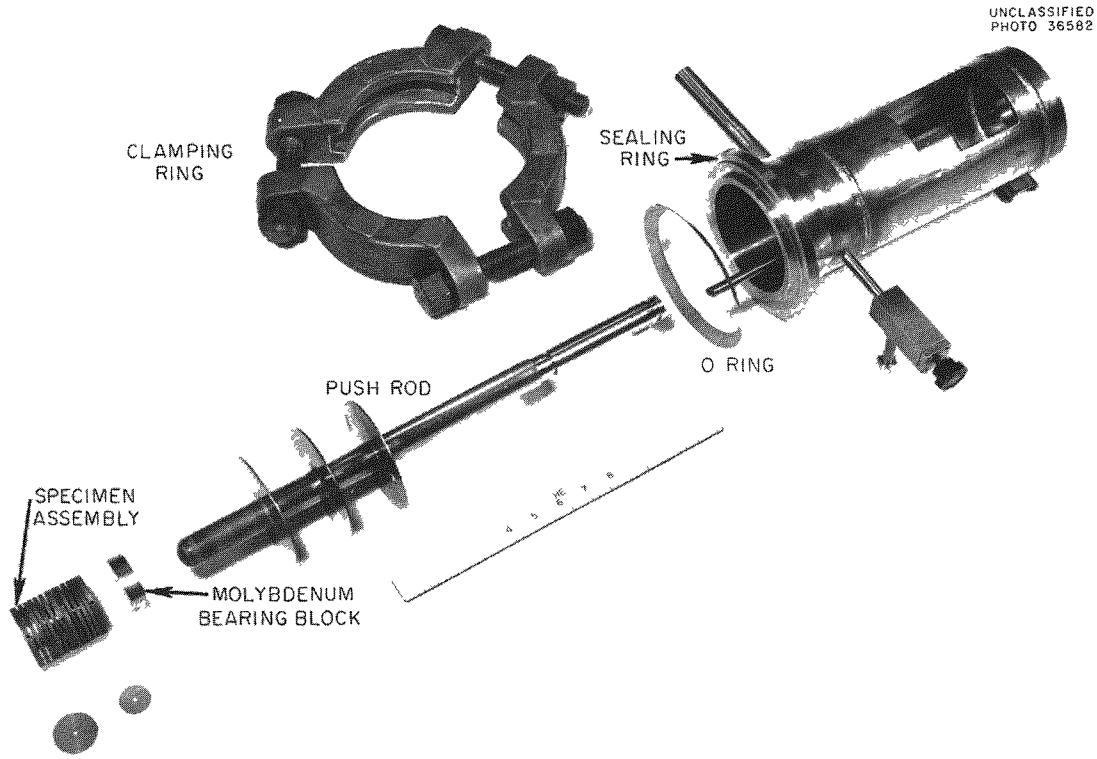

Fig. 6.1. Test Apparatus Employed for Graphite—Stainless Steel Diffusion Studies.

developed at the O-ring seal through which the shaft enters the test chamber. The failure was attributed to overheating of the Neoprene O-ring, and an O-ring adapted to higher temperature service has been substituted. Preparations are currently being made for a second test under vacuum at 1300°F.

Hydrogen-Graphite Compatibility Studies

The use of hydrogen as a coolant for high-temperature reactor systems presents two potential corrosion problems. First, if used in combination with a graphite moderator, the reaction of hydrogen with graphite should tend to establish a highly carburizing gas mixture through the formation of methane. If used in systems which do not contain appreciable carbon, an opposite effect will be promoted, namely, decarburization. Materials compatibility studies of high-pressure hydrogen systems have accordingly been programed.

Although the nature of the test program will be similar to that carried out for impure helium, system pressure becomes an important parameter in the case of pure hydrogen, and pressure ranges intended for reactor applications must be exactly simulated in the test equipment. Three high-temperature autoclaves are now on order and are scheduled to be received by June 1, 1961. The autoclaves provide an open test volume approximately 3 in. in diameter and 17 in. in length and will accommodate gas pressures of 10 000 psi at 1200°F and 1000 psi at 1500°F.

Evolution of Gas from Graphite

L. G. Overholser, J. P. Blakely

Experimental studies of the degassing behavior of commercial reactor-grade graphite have been continued utilizing the methods described previously.[8] Two specimens of graphite prepared from needle coke by the National Carbon Company for use in the EGCR at Oak Ridge and the NPR at Hanford have been investigated. The rate of release of gas by these

[8]GCR Semiann. Prog. Rep. June 30, 1959, ORNL-2767, p. 190.

specimens at 300, 600, and 1000°C and the composition of the evolved gas have been determined. High-temperature degassing studies have also been carried out at temperatures up to a maximum of 1800°C.

The EGCR material was prepared as a 16-in. × 16-in. × 20-ft extruded bar from Continental Lake Charles No. 1 needle coke using a 2800°C graphitization temperature. A 6-in. slab was cut perpendicular to the extrusion axis from section No. 2 of a bar from the furnace load identified as file No. 16. This section No. 2 had been cut 36 in. from one end of the original bar. Two series of specimens were machined from the slab for examination. Series A came from a region 1 to 4 in. from the surface, and series B came from the central part of the slab. The total ash content was found to be ~120 ppm for samples from series A and ~300 ppm in the case of series B. The ash consists mainly of iron, but significant amounts of calcium and vanadium are also present.

The graphite for the NPR, designated TSX, has a 6- × 6-in. cross section and was prepared from a No. 50 flour mix of Continental Lake Charles No. 1 needle coke. A graphitization temperature of 3000°C was used, followed by gas purification. This material supposedly is of higher purity than the AGOT-LS graphite examined earlier.[9] The particular sample received at ORNL from Hanford has an ash content of ~500 ppm and is not representative of this grade of graphite. The ash contained ~50% calcium.

Data obtained by degassing the specimens at a maximum temperature of 1000°C using external radiant heating are presented in Table 6.5. The results given for the EGCR graphite show that the material from the central region (series B) evolved somewhat more gas than did that cut from nearer the surface. Also, a larger volume of CO was found for the series B samples. A comparison of the results for the EGCR graphite with those given previously[9,10] for other needle-coke graphite samples (NCN, 560 ppm ash; AGOT-VCB, 350 ppm ash; AGOT-LS, 400 ppm ash) prepared by National Carbon Company shows some striking differences. The gas collected between 300 and 600°C from the EGCR graphite contained ~20 vol % CO_2, as compared

---

[9]GCR Quar. Prog. Rep. Sept. 30, 1960, ORNL-3015, p. 125.

[10]GCR Quar. Prog. Rep. June 30, 1960, ORNL-2964, p. 190.

Table 6.5. Volume and Composition of Gas Evolved by 1 1/2-in.-diam, 2-in.-Long Graphite Specimens at 300, 600, and 1000°C

Graphite Sample	Temperature (°C)	Time (hr)	Gas Volume (cm^3/100 cm^3 of graphite)	Gas Constituents												Other
				H_2		Hydrocarbons		H_2O		CO_2		N_2		CO		
				vol %	cm^3	vol %	cm^3	vol %	cm^3	vol %	cm^3	vol %	cm^3	vol %	cm^3	
EGCR A-121-B	300	36	0.9	2		26	0.2	51	0.5	9	0.1	5		7	0.1	
	600	19	2.7	10	0.3	20	0.6	16	0.4	20	0.5	2	0.1	31	0.8	
	1000	22	11.3	48	5.4	2	0.2	1	0.1	1	0.1	3	0.3	44	5.0	
	Total		14.9		5.7		1.0		1.0		0.7		0.4		5.9	
A-131-B	300	18	0.6	2		15	0.1	56	0.3	7		9	0.1	7		
	600	22	2.9	10	0.3	19	0.6	16	0.5	20	0.6	2	0.1	31	0.9	
	1000	21	8.7	54	4.7	1	0.1	0.6	0.1	2	0.1	0.5		42	3.7	
	1000	32	1.7	64	1.1	1		0.7				1		33	0.6	
	Total		13.9		6.1		0.8		0.9		0.7		0.2		5.2	
B-223-B	300	16	0.6	2		8		67	0.4	3		16	0.1	1		
	600	22	3.1	6	0.2	16	0.5	17	0.5	15	0.5	5	0.2	14	0.4	28% SO_2
	1000	21	11.9	28	3.3	2	0.3	0.7	0.1	5	0.6	1	0.1	63	7.5	
	1000	50	2.5	66	1.7	6	0.1	0.5		0.4		4	0.1	23	0.6	
	Total		18.1		5.2		0.9		1.0		1.1		0.5		8.5	
B-213-B	300	23	0.7	2		10	0.1	59	0.4	5		17	0.1	3		
	600	46	2.9	5	0.2	17	0.5	16	0.5	19	0.6	4	0.1	17	0.5	22% SO_2
	1000	21	13.7	24	3.2	0.7	0.1	0.7	0.1	7	1.0	2	0.2	66	9.0	
	1000	76	2.8	67	1.9	2		0.9		0.4		7	0.2	22	0.6	
	1000	66	1.5	66	1.0	1				0.8		9	0.1	23	0.4	
	Total		21.6		6.3		0.7		1.0		1.6		0.7		10.5	
TSX NPR-1-B	300	19	0.3	0.7		1		92	0.3	2		2		0.6		
	600	43	3.6	4	0.1	10	0.3	13	0.5	60	2.2	2	0.1	10	0.3	
	1000	19	10.9	36	4.0	1	0.1	2	0.2	9	0.9	0.6	0.1	51	5.5	
	1000	48	2.7	57	1.5	1		0.9		0.1		0.4		41	1.1	
	Total		17.5		5.6		0.4		1.0		3.1		0.2		6.9	
NPR-5-B	300	10	0.3	0.8		2		89	0.3	3		3		0.6		
	600	7	22.0	0.8	0.2	3	0.7	6	1.3	83	18.3	2	0.4	5	1.1	
	600	63	2.5	21	0.5	36	0.9	7	0.2	26	0.5	4	0.1	7	0.2	
	1000	19	9.4	52	4.9	3	0.3	0.7	0.1	2	0.2	0.6	0.1	41	3.8	
	1000	24	2.6	67	1.7	4	0.1	1		0.1		1		26	0.7	
	Total		36.8		7.3		2.0		1.9		19.0		0.6		5.8	

with 40 to 70% for the other needle coke specimens. Also, the volume of gas collected in this temperature range was much less in the case of the EGCR graphite. In fact, the degassing behavior of the EGCR graphite at 600°C resembles that of the GLC graphite.[9] The GLC graphite prepared by the Great Lakes Corporation under specifications similar to those for the AGOT-LS graphite has an ash content of ~300 ppm (low calcium). The release of large quantities of CO_2 appears to be associated with the presence of calcium as an impurity in the graphite. Thus, NCN, AGOT-VCB, and AGOT-LS graphite specimens, which have higher calcium contents than EGCR and GLC graphite, evolved much larger volumes of CO_2. It may be noted that the EGCR series B specimens evolved a large amount of SO_2 at 300 to 600°C.

The results given for TSX will not be discussed in detail, because the samples examined were not representative. The results obtained for the two samples are very dissimilar. The high calcium content of this graphite correlates with the large CO_2 evolution in the case of sample NRP-5B.

Data obtained by degassing the specimens to a maximum temperature of 1800°C by induction heating are given in Table 6.6. There is some evidence that the total gas content of the EGCR graphite specimens from near the surface (series A) was less than that found for specimens from the central region. The values for the two series of specimens overlap, however, and it is believed that the bulk of the graphite in the cross section sampled has a total gas content of 40 to 50 $cm^3/100\ cm^3$ of graphite. This volume may be compared with ~100 cm^3 for NCN, ~55 cm^3 for both AGOT-VCB and AGOT-LS, and ~45 cm^3 for GLC graphite.[9-11] The volume of CO evolved by GLC graphite, however, is only ~15 cm^3, which is to be compared with ~25 cm^3 for EGCR graphite. The volume of CO evolved by NCN, AGOT-VCB, and AGOT-LS specimens approximates that evolved by EGCR graphite. All the needle coke graphite specimens prepared by the National Carbon Company, including the EGCR graphite, have evolved during heating from 30 to 1000°C about two-thirds of the total amount released during heating from room temperature to 1800°C. The corresponding fractional release was less than

[11]GCR Quar. Prog. Rep. Dec. 31, 1960, ORNL-3049, pp. 287-97.

Table 6.6. Volume and Composition of Gas Evolved by 1 1/4-in.-diam, 1-in.-Long Graphite Specimens at 1000, 1400, and 1800°C

Graphite Sample	Temperature (°C)	Time (hr)	Gas Volume (cm^3/100 cm^3 of graphite)	Gas Constituents											
				H_2		Hydrocarbons		H_2O		CO_2		N_2		CO	
				vol %	cm^3	vol %	cm^3	vol %	cm^3	vol %	cm^3	vol %	cm^3	vol %	cm^3
EGCR A-131-A	1000	7	22.4	35	7.9	3	0.7	4	0.9	5	1.1	0.9	0.2	51	11.4
	1400	6	7.7	41	3.2	0.7	0.1	0.6	0.1	0.3		2	0.2	53	4.1
	1800	12	7.2	37	2.6			0.4				3	0.2	60	4.3
	Total		37.3		13.7		0.8		1.0		1.1		0.6		19.8
A-111-A	1800	7	14.1	12	1.7	0.3		0.2		1	0.2	0.7	0.1	86	12.1
A-121-A	1800	4	23	38	8.8	1	0.2	1	0.2	1	0.2	2	0.4	57	13
A-112-A	1800	7	44	41	18	0.4	0.2	0.1		0.6	0.3	1	0.4	57	25
A-122-A	1800	6	48	42	20	0.5	0.2	0.3	0.1	0.3	0.1	0.9	0.4	56	27
A-132-A	1800	5	48	41	20	0.4	0.1	0.2	0.1	0.8	0.4	0.8	0.4	57	28
B-213-A	1000	5	29.2	37	10.9	1	0.3	0.3	0.1	0.2	0.1	1	0.4	60	17.4
	1400	6	10.3	69	7.1	1	0.1	0.5	0.1	0.3		3	0.3	26	2.7
	1800	6	6.2	45	2.8	0.6		0.5		0.1		5	0.3	30	3.0
	Total		45.7		20.8		0.4		0.2		0.1		1.0		23.1
B-223-A	1800	8	44	37	16	0.5	0.2	0.7	0.3	0.6	0.3	2	1.0	59	26
B-211-A	1800	11	49	41	20	0.6	0.3	0.5	0.2	0.6	0.3	2	1.0	55	27
B-222-A	1800	7	47	37	17	0.4	0.2	0.4	0.2	0.8	0.4	2	1.0	59	27
B-212-A	1800	7	55	33	18	0.4	0.3	0.2	0.1	0.5	0.3	2	1.3	64	35
TSX NPR-5A	1000	5	78	14	11	0.2	0.2	0.5	0.4	2	1.7	0.2	0.2	83	64
	1400	9	23	18	4	0.3		0.5	0.1	0.2		3	0.7	79	18
	1800	8	12	3	0.4			0.1		0.1		4	0.5	92	11
	Total		113		15.4		0.2		0.5		1.7		1.4		93
NPR-1A	1700	<1	124	16	20	0.1	0.1	2	2.4	1	1.2	0.7	1	80	99
	1800	4	12	4	0.5	0.2		0.7	0.1	1	0.1	0.8	0.1	93	11
	Total		136		20.5		0.1		2.5		1.3		1.1		110

one-half for GLC graphite and for several needle coke specimens prepared by Speer Carbon Company.[11] In some cases, this difference can be accounted for by the difference in the volume of CO released, but in others it cannot.

The gas released by the TSX graphite is characterized by an extremely high CO concentration. The total volume is only slightly greater than that reported[9] for NCN graphite, but the volume of CO is approximately three times as large. In this case, some factor such as the graphitization temperature or the atmosphere during letdown must be responsible, in part, for this behavior rather than just the impurities present.

The results of studies of the volume of gas released as a function of time at 300, 600, and 1000°C are given in Figs. 6.2 and 6.3 and in Table 6.7. Plots of the log of time versus the volume of gas released

Table 6.7. Volume-Time Relationships for EGCR and TSX Graphite Specimens Degassed at 300, 600, and 1000°C

Graphite Sample	Temperature (°C)	Time Interval (min)	Volume-Time Relationship[a]
EGCR A-131-B	300	30–1000	V = 0.13 log t + 0.19
B-213-B	300	100–1400	V = 0.10 log t + 0.34
TSX NPR-1-B	300	30–1200	V = 0.17 log t − 0.19
EGCR A-121-B	600	90–1100	V = 0.53 log t + 0.9
B-213-B	600	30–2800	V = 0.44 log t + 1.3
B-223-B	600	100–1300	V = 0.35 log t + 1.9
TSX NPR-1-B	600	450–2600	V = 1.6 log t + 0.06
NPR-5-B	600	100–300	V = 17 log t − 20
		600–4200	V = 2.3 log t + 16
EGCR B-213-B	1000	150–3000	V = 3.1 log t + 4.1
		4000–10000	V = 5.2 log t − 2.8
B-223-B	1000	200–1200	V = 2.7 log t + 3.1
TSX NPR-1-B	1000	75–450	V = 2.6 log t + 1.9
		1200–4000	V = 8 log t − 14
NPR-5-B	1000	80–220	V = 2.6 log t + 0.17
		1100–2500	V = 7 log t − 12

[a]Volume expressed as cm^3 (STP) of evolved gas per 100 cm^3 of graphite; time in minutes. Samples were degassed at 300°C prior to degassing at 600°C and degassed at 300 and 600°C before degassing at 1000°C. The intercepts do not include the gas removed at the lower temperatures.

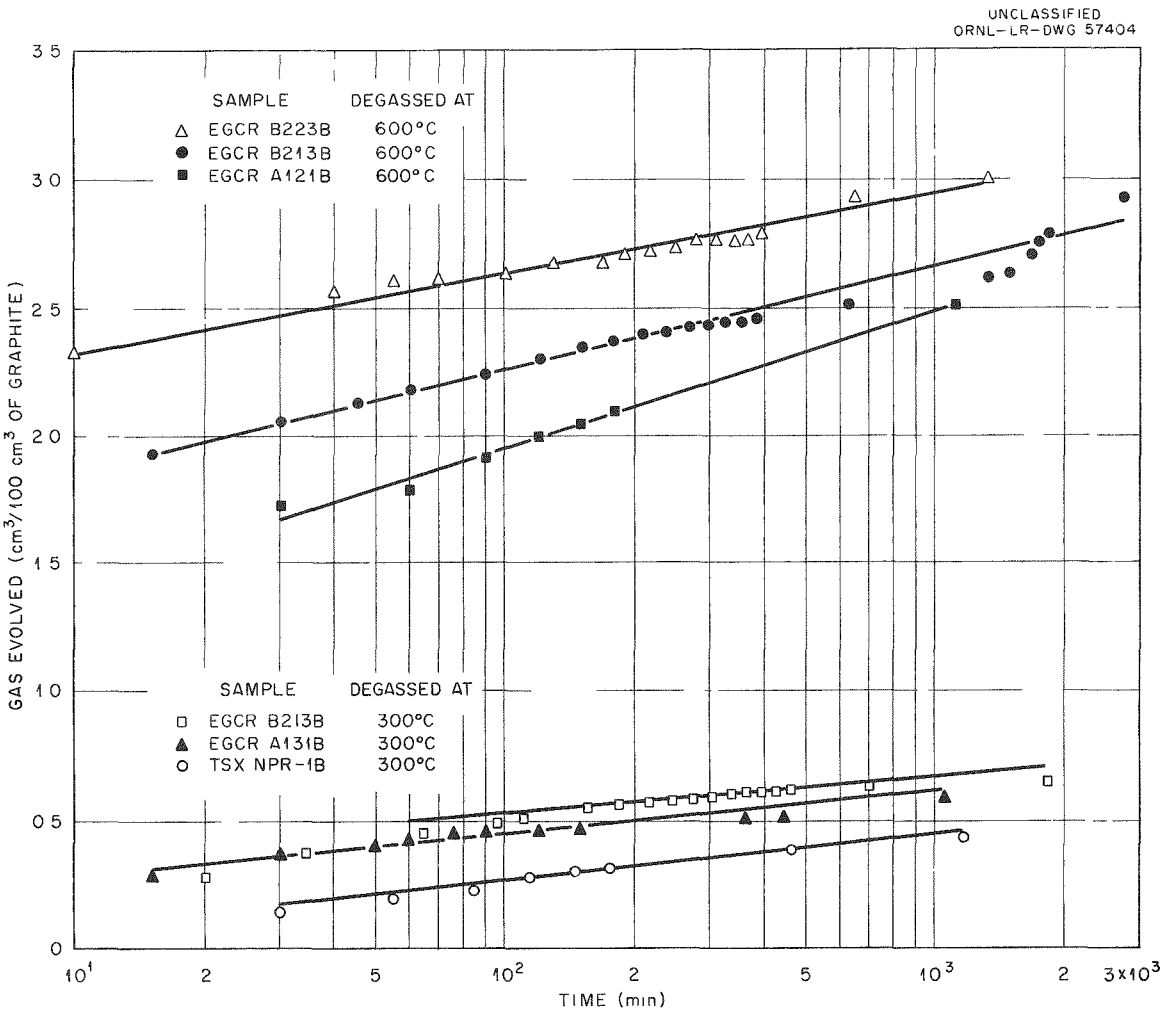

Fig. 6.2. Volume of Gas Evolved by EGCR and TSX Graphite Specimens at 300 and 600°C Plotted Against Log Time.

give essentially linear relationships at 300°C. The gas evolved at this temperature consists primarily of water, hydrocarbons, and nitrogen.

Similar treatment of the data obtained at 600°C reveals some differences in the degassing behavior of the samples. The EGCR graphite and one sample of the TSX graphite gave linear relationships over the time intervals studied. Similar results were reported previously[9-11] for a number of other specimens. Values for the slope at 600°C range from 0.35 to 1.0 for a considerable number of specimens, including the EGCR samples. In general, these samples released a relatively small volume of gas containing less than 25 vol % CO_2 between 300 and 600°C. The other type of degassing behavior at 600°C is exemplified by TSX sample NPR-5-B. A plot of

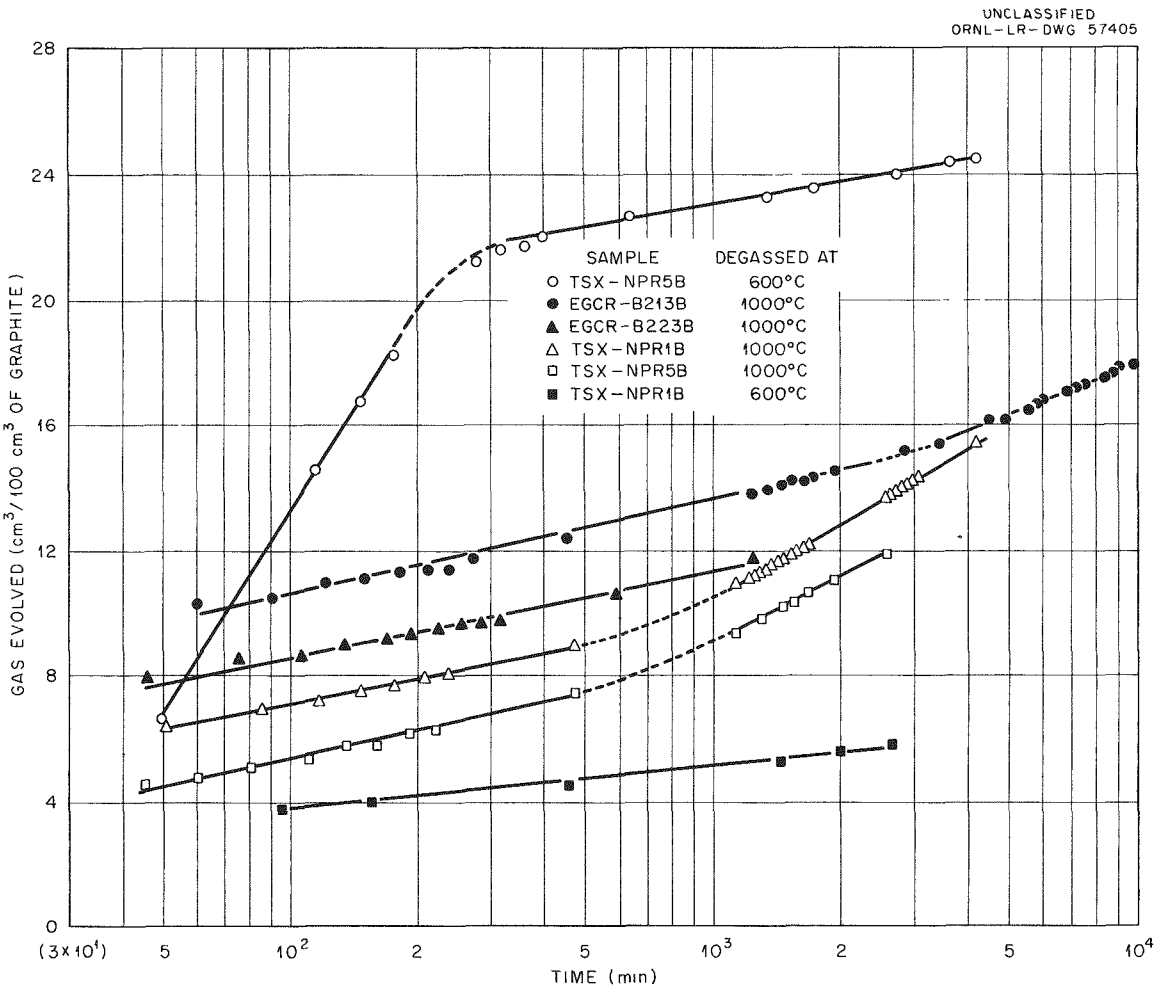

Fig. 6.3. Volume of Gas Evolved by EGCR and TSX Graphite Specimens at 600 and 1000°C Plotted Against Log Time.

volume versus log of time in this case results in a curve having a large slope during the early part of the degassing followed by a rather abrupt decrease in slope. A linear relationship then follows with a slope more nearly comparable to that reported for the EGCR graphite at 600°C. Similar behavior was reported previously[9] for NCN and AGOT-LS graphite. These specimens, as well as the TSX sample NPR-5-B evolved large volumes of gas between 300 and 600°C that contained 40 to 80 vol % CO_2. As mentioned previously, large evolution of CO_2 appears to be associated with the presence of calcium as an impurity. The initial large slope must arise from the release of CO_2, and the subsequent smaller one corresponds to

the evolution of other constituents. Data given in Table 6.5 for TSX sample NPR-5-B at 600°C show that the sample collected during the time interval corresponding to the smaller slope contains less CO_2 and more H_2 and hydrocarbons.

Plots of the volumes evolved at 1000°C versus the log of time result in essentially straight lines with slopes of ~3 during the earlier stages of the degassing. Although not reported here, slopes in the range of 2 to 3 have been found for a large number of specimens, including some with an ash content of <50 ppm. The data given in Table 6.7 and Fig. 6.3 show that an increase in the slope occurs, followed by another time interval during which the slope is essentially constant but approximately double that found for the earlier stage of the degassing. Data presented in Table 6.5 suggest that the concentration of H_2 in the gas evolved at 1000°C increases with time, accompanied by a decrease in the CO concentration. It appears probable that the final slope represents primarily the desorption behavior of hydrogen and that the earlier slopes correspond to release of mixtures of CO and H_2 in which the concentration of CO is higher than that present in the later stages of degassing.

Interdiffusion of Noble Gases in a Low-Permeability Graphite

R. B. Evans, III

Considerable attention has been given to techniques of determining the permeability coefficients of graphite samples that exhibit low values of porosity and forced-flow rates.[12] In line with this work, the techniques for studying the interdiffusion of noble gases in porous media have been modified so that very low interdiffusion rates can be measured under steady-state conditions. The results of several uniform total pressure experiments are presented in Fig. 6.4 for interdiffusion within the helium-argon-CEY graphite system. (CEY graphite is a coated pipe material manufactured by the National Carbon Company.)

---

[12]GCR Quar. Prog. Rep. Dec. 31, 1960, ORNL-3049, pp. 297–302.

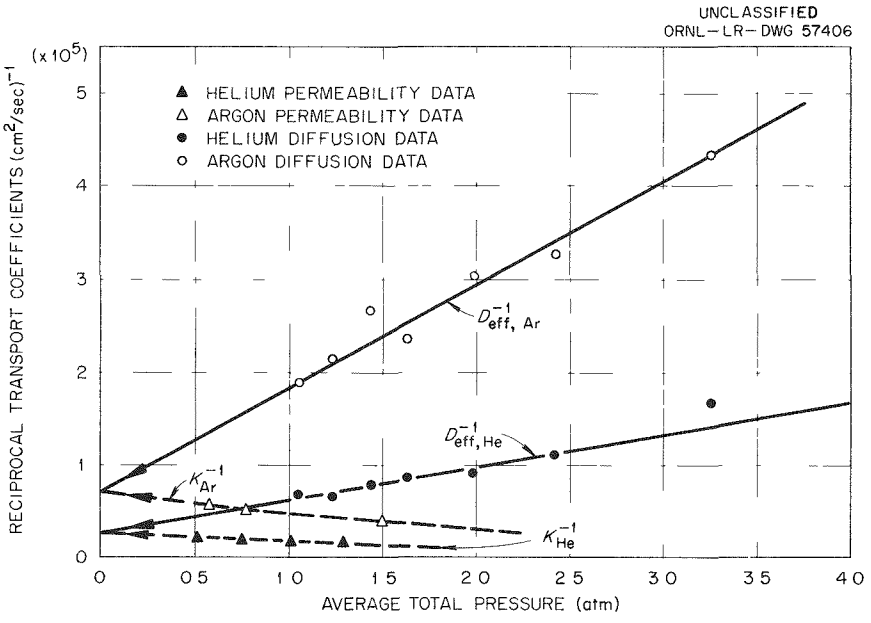

Fig. 6.4. Reciprocal Transport Coefficients for Helium and Argon in Coated CEY Graphite Pipe.

Based on the initial permeability data, it was tentatively concluded that the diffusion would follow a Knudsen mechanism over a wide pressure range, since the permeability coefficients did not show a strong pressure dependence. An applicable equation for the diffusion described above is[13]

$$(D_{eff})^{-1} = bP_m + \left(K_{P_m \rightarrow 0}\right)^{-1} ,$$

where P_m is the mean pressure of the flowing gas, b is related to the mutual diffusion coefficient, and K is the permeability coefficient. This is an approximate relationship that is valid when the partial pressure profiles of the gases involved are linear and/or b is small.

The curves show that the theory is applicable as $P \rightarrow 0$; within this region K and $D_{eff,i}$ become identical. However, the mutual diffusion term b plays an increasingly important role as the pressure is increased. At reactor pressures, Knudsen effects would not be of Knudsen classification;

[13]R. B. Evans, III, J. Truitt, and G. M. Watson, Superposition of Forced and Diffusive Flow in a Large-Pore Graphite, p. 43, ORNL-3067, Feb. 24, 1961.

rather, the mechanism would be essentially the same as that observed with AGOT[13] graphite (with lower rates).

The average $(K/D)_{He}$ ratio for AGOT graphite is 400 at 1 atm total pressure; whereas that for CEY graphite is 6. It was hoped that materials with permeability coefficients as low as that of CEY graphite (10^{-6} to 10^{-5} cm^2/sec) would have a K/D ratio of unity, since, if this were true, the determination of K or the determination of D could be obviated. However, the data indicate the necessity of performing both determinations to characterize flow behavior within materials such as CEY graphite.

Porosity of Type CEY Graphite Pipe

N. V. Smith, W. T. Ward

Permeability coefficients and porosity values for graphite are important in reactor design calculations because the total amount of fission-product buildup within the graphite depends on the porosity, and the permeability coefficient gives a measure of the steady rate of transport of gases (including fission products) through the graphite.

Porosity may be determined by two methods: first, by direct measurement of the amount of gas absorbed in the pores of the specimen and, second, by calculating the porosity from transient flow data, including the time required for steady-state flow conditions to be reached.

The direct method is applicable to relatively high-porosity, high-permeability graphite in which the amount of absorbed gas is sufficient for a reasonably accurate measurement. The second method would be impractical for this type of graphite because the time required to reach steady state is too short to be measured accurately unless a very thick specimen is used. For very low-permeability, low-porosity graphite the reverse would be true.

Type CEY graphite pipe (permeability constant K = $\sim 10^{-5}$ cm^2/sec) falls somewhere between these extremes. Its porosity (pores accessible to gas) was calculated from permeability data to be 11.6%. This value was distrusted because the time required to reach steady-state flow was very short (approximately 20 sec). Therefore porosity measurements were

made using the direct method in an apparatus similar to one described in a Bureau of Mines bulletin[14] and porosity values were calculated from density measurements. The section of pipe was sliced parallel to the pipe axis into a number of pieces in order to expose more surface to the helium and reduce the time required for the helium to permeate the pores. The pipe was found to consist of 11.1 vol % open voids, that is, voids accessible to helium; 9.3 vol % closed voids, that is, voids inaccessible to helium; and 79.6 vol % solid material. The agreement between the calculated and measured values is surprisingly good considering the uncertainty in measuring the equilibrium time in the permeability experiments.

Development of Instruments for Analyzing Helium

J. C. White, A. S. Meyer, Jr.

Extensive studies[15] of the Greenbrier process chromatographs during the past six months have demonstrated that, while the instruments offer reproducible and dependable analyses of contaminant concentrations in helium in excess of 1000 ppm, application to the determination of lower concentrations requires frequent adjustment and calibrations. Since at lower concentrations reproducibility is primarily limited by fluctuations in the base line, the ultimate sensitivity is best expressed in terms of absolute reproducibility. For concentrations below 100 ppm the optimum reproducibility of measurement of all components except hydrogen is of the order of 2 to 5 ppm. Variations in the measurement of the concentration of hydrogen usually range from 25 to 75 ppm. The poorer reproducibility of the hydrogen measurements is caused principally by the similarity of the thermal conductivity of hydrogen to that of helium; however, additional uncertainties are sometimes introduced by small quantities of neon

[14] C. G. Rall, H. C. Hamontre, and D. B. Taliaferro, Determination of Porosity by a Bureau of Mines Method, Report of Investigations 5025, February 1954.

[15] GCR Quar. Prog. Rep. Dec. 31, 1959, ORNL-2888, p. 178.

in the sample. Neon is not adequately resolved from hydrogen when 25-cm^3 samples are used to obtain increased sensitivity. Detectors that have been tested for improvement of hydrogen sensitivity include a catalytic-combustion detector and a gas-density balance. Neither detector offers significant improvements over the thermistor bridge. Recently, the stability of the instrument has been improved by shielding the thermistors with closely spaced screens following a technique similar to that recommended by Kieselbach.[16] Although the improvement effected by this modification has not been thoroughly evaluated, it does not appear sufficient to permit satisfactory measurement of concentrations in the ppm range, particularly for future operations in a radioactive environment that will limit access to the analyzer section of the instrument.

In view of the above-mentioned problems, current investigations are directed toward the application of more sensitive detectors based on ionization measurements. The most promising detector appears to be a thermionic ionization gage[17] in which a portion of the eluted gases from the chromatographic column is passed at a pressure of about 500 μ through an ionization gage tube that is operated at an ionization potential between that of the ionization energy of helium, 24.5 ev, and that of the contaminants, 12.5 to 15.6 ev. When an eluted peak passes through the tube, the molecules of the contaminant are ionized by collision with the electrons to yield positive ions which are collected at a negatively charged plate and produce a current proportional to the concentration of the contaminants.

In initial tests with conventional ionization gages, excessive background currents were obtained when accelerating potentials above 19 v were used. At this potential the ionization gage offered little advantage over the thermistor detectors. The background results from the ionization of helium by the small fraction of electrons whose energy exceeds the ionization potential of helium. The excess energy of these electrons is the result of variations in potential over the length of the directly heated

---

[16]R. Kieselbach, Anal. Chem., 32: 1749 (1960).

[17]S. A. Ryce and W. A. Bryce, Can. J. Chem., 35: 1293 (1957).

filament and of the energy distribution of thermionic electrons from a high-temperature source. In order to reduce the spread in the energy of the ionizing electrons, a modified tube with a unipotential cathode that is coated with oxide has been assembled by installing the three inner elements of a 6F6 receiving tube in the envelope of a VG1A ionization gage. By operating the modified tube at an accelerating potential of 21 v and measuring the positive ion current with the electrometer circuit of an ionization gage power supply, sensitivities for the measurement of hydrogen and oxygen several hundredfold that obtained with thermistor detectors have been observed.

The modified tube is subject to limitation in that the cathode can be temporarily poisoned by oxidizing gases, some background apparently results from positive ions emitted by the cathode and some materials, such as CO_2, are apparently gettered by the cathode. A second ionization gage tube is being fabricated with a demountable cathode in order to test other cathode coatings, such as lanthanum boride, LaB_6.[18] In a third tube, which is now being designed, electrons will be injected into the collision space from an electron gun. High-energy electrons and positive ions will be excluded from the collision space by magnetic analysis of the electron beam, and contact between the eluted gases and the cathode will be limited.

In addition to providing improved sensitivity, a successful thermionic ionization detector would permit the simplification of other chromatograph components, because it is relatively insensitive to environmental factors such as temperature, pressure, and flow rate. Thus, the higher cost of the detector would be partly offset, and chromatographs of a more convenient size for shielding and location in limited space could be designed.

Investigation of Adsorbers for Removing Fission-Product Gases from Helium

W. E. Browning, R. D. Ackley, R. E. Adams

Removal of Iodine Vapor

Studies of means for the removal of radioactive iodine vapor from high-temperature helium streams have been continued. Iodine retention

tests are performed using adsorber beds approximately 0.25 in. in depth to give a rapid indication of the relative value of the adsorber material for application to full-scale iodine adsorbers with much larger depths of adsorbent material. This method of investigation provides a screening test of various materials for iodine retention and data for more detailed studies of the mechanism of iodine release from various materials. Pertinent test conditions and results for the materials studied during the period of this report are listed in Table 6.8.

Table 6.8. Results of Tests of Various Materials as Adsorbers for Removal of Iodine Vapor from High-Temperature Helium

Adsorbent Material	Test Temperature (°C)	Bed Depth (in.)	Gas Velocity (ft/min)	Duration of Test (hr)	Iodine Retention (%)
Pittsburgh BPL charcoal, 8/14 mesh	320	0.375	13.6–110.8	144	16.0
Columbia G charcoal, 8/14 mesh	320	0.25	13.6–110.8	166	94.7
Pittsburgh PCB charcoal, 6/16 mesh	325	0.25	14.9–117.4	168	97.6
Pittsburgh BPL charcoal, 12/30 mesh	325	0.25	13.6–75.6	168	30.2
Whetlerite ASC charcoal,[a] 12/30 mesh	325	0.25	13.4–44.1	216	99.99+

[a]This material is made by impregnating Pittsburgh BPL charcoal with salts of silver, copper, and chromium.

One type of charcoal, Whetlerite ASC, exhibits iodine adsorption and retention capabilities vastly superior to those of the other materials tested. This charcoal, designed for use in gas masks for protection against war gases, is manufactured by impregnating Pittsburgh BPL charcoal with salts of silver, copper, and chromium. The apparent value of these metal salts for iodine retention may be assessed by comparing the 30.2% iodine retention of Pittsburgh BPL, 12/30 mesh, with the 99.99+% iodine retention of Whetlerite ASC, 12/30 mesh. Workers at General Atomic recently reported similar iodine adsorption and retention capabilities for activated charcoal impregnated with silver metal.[19] A more detailed study

[18]J. M. Lafferty, J. Appl. Phys., 22: 299 (1951).

[19]HTGR Quarterly Report, Oct.–Dec. 1960, General Atomic, San Diego, Cal.

of Whetlerite charcoal and other impregnated charcoals over a wider temperature range is in progress.

While a quantitative definition of the mechanism of iodine release from charcoal and silver surfaces has not as yet been obtained, it may be observed that the manner in which iodine is eluted from silver surfaces and the rate of elution are significantly different from the manner and rate of release from charcoal surfaces and, further, that differences in iodine release characteristics exist between the various types of charcoal. Efforts are being made to elucidate the mechanisms involved.

It was previously observed, based upon rather limited data, that silver was probably a more promising iodine-removal material than charcoal for application at high temperatures under EGCR conditions.[20] In light of the more recent data, however, iodine-removal materials for EGCR conditions would be rated, in order of decreasing efficiency, as Whetlerite charcoal, virgin charcoal (coconut type, such as Pittsburgh PCB), and silver metal.

Removal of Radioactive Noble Gases from Carrier Gases

Studies of means for the removal of krypton and xenon from gaseous coolants were also continued. Dynamic krypton adsorption measurements were made on two previously untested types of charcoal; additional evaluations of krypton diffusion in charcoal were undertaken; a statistical analysis of equilibrium krypton and xenon adsorption isotherms was conducted; the retention of fission gases by type 4A Linde molecular sieves was investigated; and measurements were made of apparent thermal conductivities for a group of charcoals with helium, nitrogen, and carbon dioxide, separately, in the voids. Certain grades of charcoal are employed in reducing the concentration of radioactive krypton and xenon in coolants and other carrier gases by the method based on holdup, resulting from physical adsorption, and subsequent radioactive decay in the charcoal. Consequently, as promising adsorbents become available and time permits, they are tested for applicability in fission-gas adsorbers. Dynamic

[20]GCR Quar. Prog. Rep. Dec. 31, 1960, ORNL-3049, pp. 302–8.

krypton retention measurements have been made for Pittsburgh PCA charcoal, 12/30 mesh, and copper-impregnated Pittsburgh BPL charcoal, 12/30 mesh, at 25°C with helium carrier gas at a superficial gas velocity of 1.8 ft/min. The results of these measurements may be summarized in terms of the k value, which is a direct measure of holdup time, and the N value, which gives the number of theoretical plates. The PCA charcoal gave a k of 55 cm^3/g and an N of 64 plates per foot; the corresponding values for the BPL copper-impregnated charcoal were 22 cm^3/g and 70 plates per foot.

Further calculations were made of effective or apparent diffusion coefficients for krypton in charcoal adsorbers, using experimental data in conjunction with the appropriate solution of the diffusion equation. These coefficients are needed for predicting the performance of adsorbers operating at low carrier gas velocities where transport by longitudinal diffusion may be important. Previously, values were given for krypton in Pittsburgh PCB (12/30 mesh) activated carbon with stagnant helium at 1 atm as the predominant component of the gas phase at 0, 25, and 60°C.[20] Less extensive measurements made on Pittsburgh PCB (6/16 mesh) and Columbia HCC (12/28X mesh) charcoal indicated no significant difference in extent of krypton diffusion in the three adsorbents, but this is probably due to lack of resolution, since the effective diffusion coefficient is expected to increase with charcoal grain size, other factors being constant.

The usefulness of equilibrium or static krypton and xenon adsorption data has been mentioned before and a fair quantity of such data for certain samples of charcoal and type 5A sieves has been presented in a semiquantitative manner.[20] The data provide a check on dynamic measurements and theory and are a convenient source of information regarding xenon adsorption, since the Xe^{133} tracer used in dynamic measurements is not always readily available. The aforementioned data have been statistically analyzed by means of an Oracle linear regression code. The various data, which were isotherms, were fitted to the Freundlich equation; and the temperature dependence was calculated according to $k = Ae^{B/T}$, where k is a defined adsorption coefficient, A and B are evaluated constants, and T is absolute temperature. The detailed results of the calculations have been reported.[21]

Linde molecular sieves, types 4A and 5A, are being considered for use in removing traces of water vapor and carbon dioxide from reactor coolants. If regeneration gases are to be vented to the atmosphere, the quantity of radioactive fission-product gases associated with the sieves must be low. Previously, dynamic krypton adsorption results for type 4A sieves indicated that krypton adsorption was negligible, and, presumably, xenon adsorption would also be negligible, since pores inaccessible to krypton would be inaccessible to xenon. To further investigate type 4A sieve behavior, static adsorption data were obtained at 25°C for krypton and at 25 and 60°C for xenon. Krypton adsorption was found to be surprisingly large. Equilibration times were relatively long, however, and this is probably the explanation for the dynamic observations. For krypton pressures less than 1 mm Hg, the indicated volume adsorbed per gram of type 4A material is approximately 0.011 cm^3 (STP)/mm Hg. The extent of indicated xenon adsorption per gram of type 4A material was negligible at 25°C, but at 60°C appeared to be ~0.0005 cm^3 (STP)/mm Hg. An increase in physical adsorption with temperature is contrary to theory, so these results are evidently affected by some rate process. Also, since the amounts adsorbed depend on a void space determination using helium, the indicated extents of adsorption would tend to be low, as should be recognized in estimating possible atmospheric contamination during regeneration. In a related earlier study, performed by members of the MIT Practice School, dynamic retention of krypton by type 5A sieves was measured at 25°C as a function of the amount of loading with carbon dioxide and with water.[22] They found that undesirably high loadings were required to reduce krypton retention to negligible values. In view of these results for both type 4A and 5A sieves, provision for radioactive decay may be required prior to regeneration.

---

[21]R. D. Ackley and W. E. Browning, Adsorption of Krypton and Xenon on Activated Carbon and Linde Molecular Sieves, ORNL CF-61-2-32, Feb. 14, 1961.

[22]E. E. Wright, Jr. and A. R. McLain, Krypton Holdup in Molecular Sieves, KT-548, Nov. 8, 1960.

In the design of adsorbers for use where the heat of radioactive decay is appreciable, the thermal conductivity of the charcoal-carrier gas system is an important parameter, since the design must provide for dissipation of the heat thus produced. Fairly precise measurements of thermal conductivity for Columbia G charcoal with various gases in the voids have been reported.[23] In order to expand this type of information, measurements have been made on Columbia G and four other types of charcoal by members of the MIT Practice School using the Northrup method. This method, while perhaps not highly precise, permits collection of a relatively large quantity of data in a short time. The preliminary results, which are for charcoal temperatures of approximately 45°C, are summarized in Table 6.9, together with earlier data for Columbia G charcoal. Where a comparison is possible, good agreement is observed, and, in general, the results appear to be consistent. Details of experimental procedures and results have been reported.[24]

---

[23]GCR Quar. Prog. Rep. Sept. 30, 1959, ORNL-2835, pp. 143, 145–7.

[24]P. M. Roth and C. R. Wunderlich, Determination of Effective Thermal Conductivities of Charcoal Beds, KT-564, Feb. 23, 1961.

Table 6.9. Apparent Thermal Conductivities of Charcoal-Gas Systems

Type of Charcoal	Mesh Size	Thermal Conductivity [Btu/hr·ft^2 (°F/ft)]		
		Charcoal-He	Charcoal-N_2	Charcoal-CO_2
Columbia G	8/14	0.226[a]	0.113[a]	0.092[a]
Columbia G	8/14	0.202[b]	0.115[b]	0.097[b]
Columbia ACC	6/14X	0.133	0.090	0.090
Columbia HCC	12/28X	0.181	0.091	0.088
Pittsburgh PCB	6/16	0.166	0.103	0.092
Pittsburgh PCB	12/30	0.183	0.113	0.112

[a]Data obtained previously.

[b]New data.

Measurement of High Temperatures

W. T. Rainey, R. L. Bennett

Drift Studies in a Stagnant Helium Atmosphere

Previous studies showed that Chromel-P undergoes severe intergranular attack in the region of the high-temperature gradient when placed in a furnace at 1000°C with a stagnant helium atmosphere. The attack is apparently a selective oxidation of chromium which results in a reduction of the emf output.

Tests have been started on a group of nickel-chromium alloys to determine whether they are more resistant than Chromel-P to deterioration. Series of the following couples were prepared from 24-gage bright wire: (1) Chromel-A vs alloy 875, (2) Chromel-AA vs alloy 875, (3) special Chromel-P vs special Alumel, and (4) regular Chromel-P vs regular Alumel. After eight days of exposure at 1000°C in stagnant helium, the emf outputs of the regular Chromel-P vs Alumel couples had drifted an average of −1.66 mv (a temperature error of −41.5°C), while the emf outputs of the special Chromel-P vs Alumel couples had drifted −1.53 mv (a temperature error of −39.5°C). No significant changes have been observed thus far in the outputs of the other alloys.

These tests are being carried out in protection tubes which were not purged of air before testing. Under such conditions it would be expected that alloys of the 90% nickel, 10% chromium type would show selective oxidation of chromium in the gradient region. Therefore, it is not surprising that regular and special Chromel-P have shown negative emf drifts. Alloys of the 80% nickel, 20% chromium type, such as Geminol-P, Chromel-A, and Chromel-AA, do not show emf drift under these conditions. Alloy 875 is an aluminum-chromium-iron alloy which is recommended as the negative element for use with Chromel-A and Chromel-AA under reducing atmospheric conditions.

Drift Studies in a Graphite-Helium Environment

Long-term drift studies on stainless steel-sheathed Chromel-P vs Alumel thermocouples in a graphite-helium environment have been continued.

The thermocouples were inserted into an AGOT graphite cylinder contained in a stainless steel can. A stagnant helium pressure of 3 psig was applied, and the temperature of the hot end of the block was maintained at 870°C. Control couples of each type of material were exposed to the same temperature profile by inserting them into stainless steel wells which extended into the graphite cylinder. Three series of thermocouples have been placed in the block.

The first series of couples consisted of type 304 and type 310 stainless steel-sheathed wires. The drifts of these materials over a 12-week period are shown in Fig. 6.5. The emf outputs of the type 304 stainless steel-sheathed couples drifted −1.2 mv (−30°C temperature error) after 83 days, while the type 310 stainless steel-sheathed couples showed essentially no deviation in emf output. The outputs of the control couples, which were exposed to air in stainless steel tubes, drifted slightly positive (+0.17 mv, +4.2°C) during the same period. These couples were placed in the cold graphite block, and then the block was brought up to test temperature.

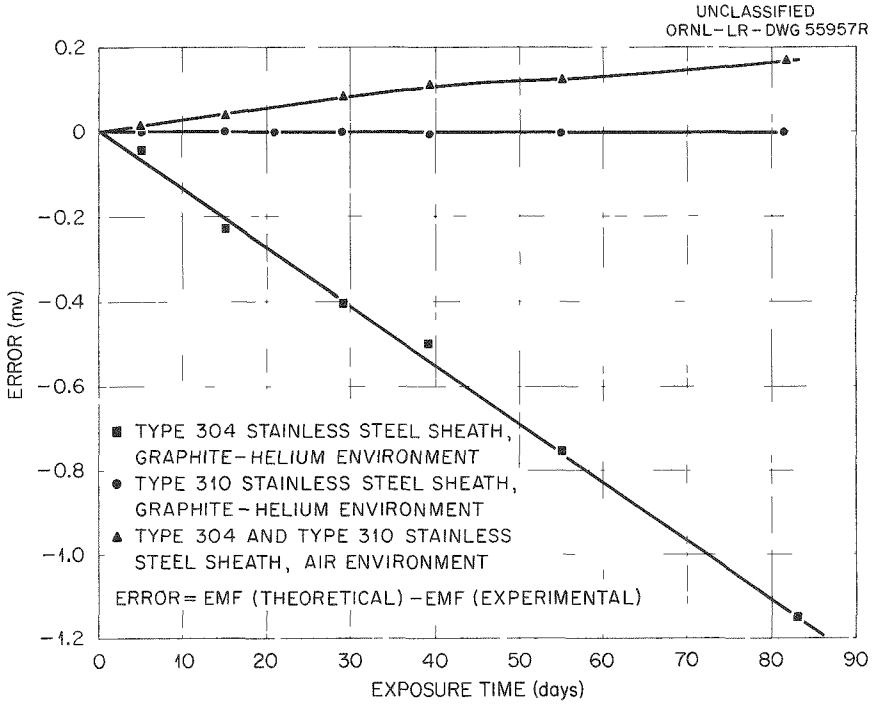

Fig. 6.5. Drift Data for Chromel-P vs Alumel Sheathed Thermocouples in a Graphite-Helium Environment.

The second series of thermocouples consisted entirely of type 304 stainless steel-sheathed material from the same source as the first set. These were placed in the block while it was hot and after the original pressure had been released. Instead of reproducing the large negative drifts of the first set, the emf outputs of these couples drifted slightly positive. After 23 days, the outputs indicated a +0.15-mv drift (+3.8°C temperature error) compared with the −0.38-mv change (−9.5°C temperature error) in the output of the same material in the first series of tests. The difference was apparently due to the gases which were evolved from the graphite upon heating. Some of the gaseous atmosphere escaped when the pressure was released before the second series of tests was started. For this reason a third series of couples was tested in a fresh graphite cylinder.

The third series of couples was exposed to the same conditions as the first by placing the couples in a fresh graphite block before heating. The materials tested were: (1) type 304 stainless steel-sheathed couples from the first series of tests which had been exposed to the graphite-helium environment for 83 days and which had shown large negative drifts in emf output, (2) type 304 stainless steel-sheathed couples from the second series which had been exposed to an outgassed graphite-helium environment and which had shown slight positive drifts in emf output, (3) new 0.125-in. type 347 stainless steel-sheathed couples, and (4) new type 304 stainless steel-sheathed couples from another manufacturer.

After 30 days of exposure, the emf outputs of the type 304 stainless steel-sheathed couples from previous runs had drifted −0.48 mv (−12°C temperature error), while the outputs of the new type 304 stainless steel-sheathed couples from another source had drifted only −0.09 mv (−2.2°C temperature error). The emf outputs of the type 347 stainless steel-sheathed couples showed practically no change.

Error profiles were obtained for couples of the first series by comparing their emf outputs with the output of a standard couple as they were withdrawn from an isothermal tube furnace. The data are shown in Fig. 6.6. The results indicate that the maximum attack occurred at 10 in. from the hot junction, which was at 746°C in the graphite block. Essentially all

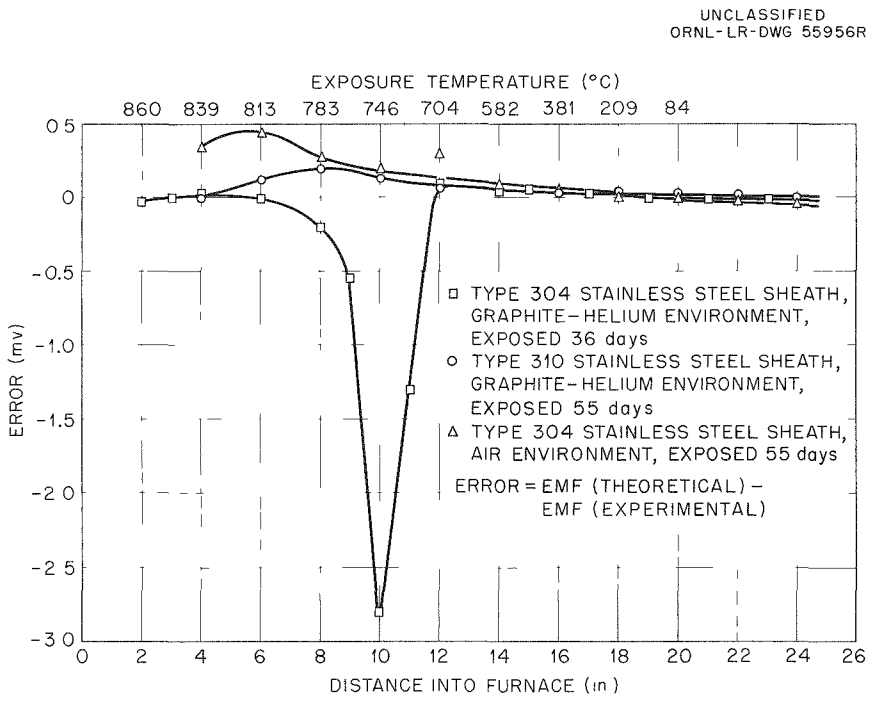

Fig. 6.6. Thermal-Gradient Profiles for Chromel-P vs Alumel Sheathed Thermocouples After Exposure in a Graphite-Helium Environment.

the negative error was shown to be due to the Chromel-P leg of the couple by spot welding a platinum wire to the hot junction of the sheath and determining error profiles of the individual leads. The thermocouples were cut at 1-in. intervals, and a metallurgical examination was made of the cross sections of the couple. These examinations revealed that intergranular attack, as shown in Fig. 6.7, had occurred at 10.5 in. from the hot junction in the graphite-helium environment. The Chromel-P wire was found to be magnetic in this region, indicating a loss of chromium metal.

It is not clear why the type 310 and type 347 stainless steel-sheathed couples have shown practically no drift or why the type 304 stainless steel-sheathed couples from one manufacturer drifted more rapidly than those from another. It does appear that the gases evolved from the graphite play an important part in the drift. Differences in manufacturing techniques may result in varying properties such as density, or the magnesia insulation or imperfections in the sheath could cause different rates of diffusion of gases to the wire.

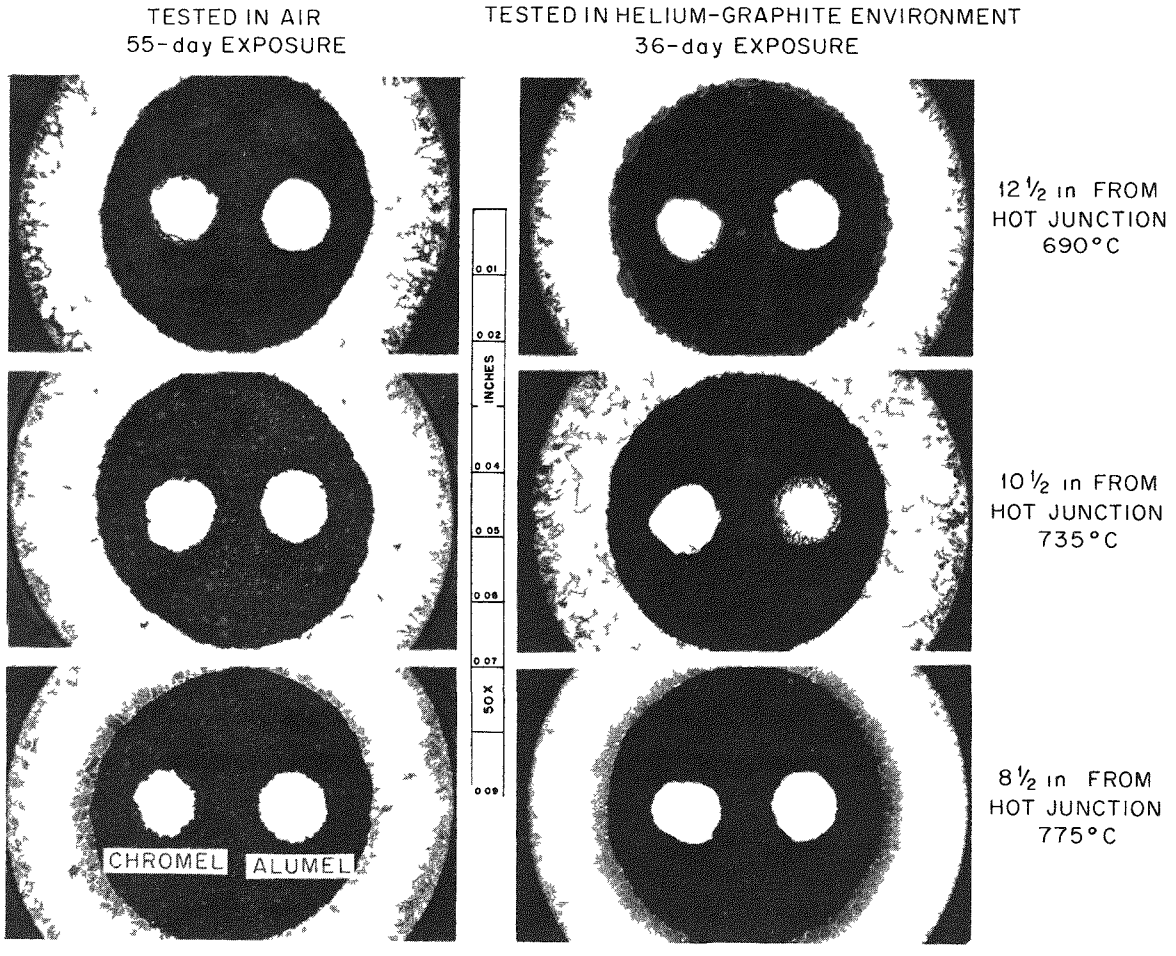

Fig. 6.7. Metallographic Sections of Type 304 Stainless Steel-Sheathed Thermocouples After Exposure in a Graphite-Helium Environment.

High-Temperature Furnace

H. L. Hemphill, W. T. Rainey, R. L. Bennett

A high-temperature furnace with a helical graphite resistance heater has been constructed and partially tested. It has a heated zone 1 in. in diameter and 2.5 in. in length, and it is designed for inert-atmosphere operation. Test assemblies will be isolated from the furnace atmosphere by a tantalum tube through which clean helium will be passed. The furnace has been operated continuously for several days at 2000°C. Temperatures in excess of 2500°C have been attained for brief periods at a power input

of 9.3 kw. Changes in the power supply design and graphite element are being made that will allow maximum transfer of power to the heater element.

Pneumatic Temperature Probe

H. M. Hochreiter

A research and test program has been initiated for determining the practicability of using gas thermodynamics for measuring elevated temperatures. Present work is centered on a specific configuration which has been named the pneumatic temperature probe. The pneumatic temperature probe consists of two flow nozzles in series, both operating at critical flow velocity. The temperature of the flowing gas at the upstream nozzle can be obtained when the pressure at each nozzle and the downstream temperature are known.

Development of the device is aimed at (1) immediate application to measurements in the EGCR and (2) high-temperature measurements for many EGCR and ORNL applications. The limitations of present thermocouple materials for long term use at elevated temperatures makes resort to this device attractive for many applications. A preliminary study made by the Marquardt Corporation for ORNL showed that such a device would be practical for the EGCR. Subsequent extensive theoretical studies and limited tests at ORNL have been generally encouraging. Information now indicates that errors in the desired (remote) temperature measurement will be:

1. proportional to the errors in the measured downstream (local) temperature,
2. a function of the error of the measured pressure ratio,
3. equal to 1/2% per 100°F for nozzle expansion (if uncorrected),
4. equal to 0.5% per 100°F for specific heat changes in diatomic and polyatomic gases (if uncorrected),
5. equal to 4 to 6% for nozzle flow coefficient variations with Reynolds' number unless nozzle pairs are carefully matched in performance,
6. equal to an undetermined value for corrosion and erosion of the nozzle, which will cause changes in area and the flow coefficient.

In order to determine the practical limits of these variables and also to demonstrate working models and complete systems, a test loop has been set up and preliminary runs have been made using bottled gases. A compressor is currently being installed which will permit constant recirculation of any gas for long-term evaluation. Temperatures up to 2000°F and pressures to 1000 psi can be used in circulating helium or any other suitable noncorrosive gas.

Practical nozzle design and construction, up to the present, has been narrowed to the use of sapphire throats (venturi sections) mounted in stainless steel or Inconel housings. It was felt that sapphire, because of its hardness, chemical resistance, low thermal expansion, and radiation resistance, was the most practical material available for the critical throat sections. Prior to the availability of the sapphire throat sections fabricated by an outside vendor, stainless steel and Inconel sections were fabricated at ORNL and tested. Subsequently, the sapphire throat sections have been received, mounted in suitable metallic housings, and also tested. A number of nozzle pairs between 0.014 and 0.062 in. in diameter have been fabricated. Results on the limited testing so far indicate that flow coefficients for given pairs of nozzles are better than anticipated. This will simplify matching the nozzles. Coefficient variations over a 5:1 pressure range proved to be in the order of less than 1%. The effectiveness of divergent discharge sections for nozzle design proves that such sections affected considerable recovery of the temporary drop. While this is widely known to be true in large nozzles, there was some question as to the effectiveness in diameter sizes of 0.014 to 0.062 in.

Theoretical work on the response time of the probes and typical probe systems has been done and compared with the Marquardt test, with good general agreement. It appears from the present design parameters that a response time in the order of 8 sec per point will be realistic for each point in the EGCR.

7. DEVELOPMENT OF TEST LOOPS AND COMPONENTS

EGCR In-Pile Loops

F. H. Neill

Through-Tube Design (R. E. Helms, W. S. Chmielewski, E. R. Schmidt)

The reduction in the number of loops from eight to four has not changed the design requirements on the tee sections. Title II drawings for the bottom-nozzle tee sections for all four loops and Title I designs for the four top-nozzle tee sections have been completed and approved. Title II detail design drawings for the four top-nozzle tee sections are approximately 90% complete.

The requirement for INOR-8 in the steam loop has been eliminated with the substitution of an Inconel overlay in those regions that will be exposed to two-phase fluids as a result of axial thermal gradients along the nozzle tee section. The axial temperature profile of the 5 1/2-in.-o.d. through-tube for 335-kw loop operation has been calculated. (Temperature profiles for full power operation at 1500 kw were presented previously.[1]) The tube surface temperature versus axial position on the tube is shown on Fig. 7.1, and the temperature difference across the tube versus axial position on the tube is indicated on Fig. 7.2.

The effects of the vertical force, torque, and bending moments at the junction of the reactor vessel and the lower nozzles of the four loops resulting from reactor pressure, component weight, and loop thermal expansion were studied. The data are summarized in Table 7.1. The allowable nozzle loadings, based on primary-plus-secondary stress intensity of 90% of yield strength, are 260 000 in.-lb for the 5 1/2-in.-o.d. lower nozzles and 330 000 in.-lb for the 9 1/2-in.-o.d. lower nozzles. The calculations were made, however, for a conservative differential expansion of 5.75 in. at the lower tee; the expected differential expansion at the lower tee is 3.84 in. Further, final design calculations indicate that hanger loads will considerably reduce the nozzle loadings.

---

[1]GCR Quar. Prog. Rep. Dec. 31, 1960, ORNL 3049, p. 314.

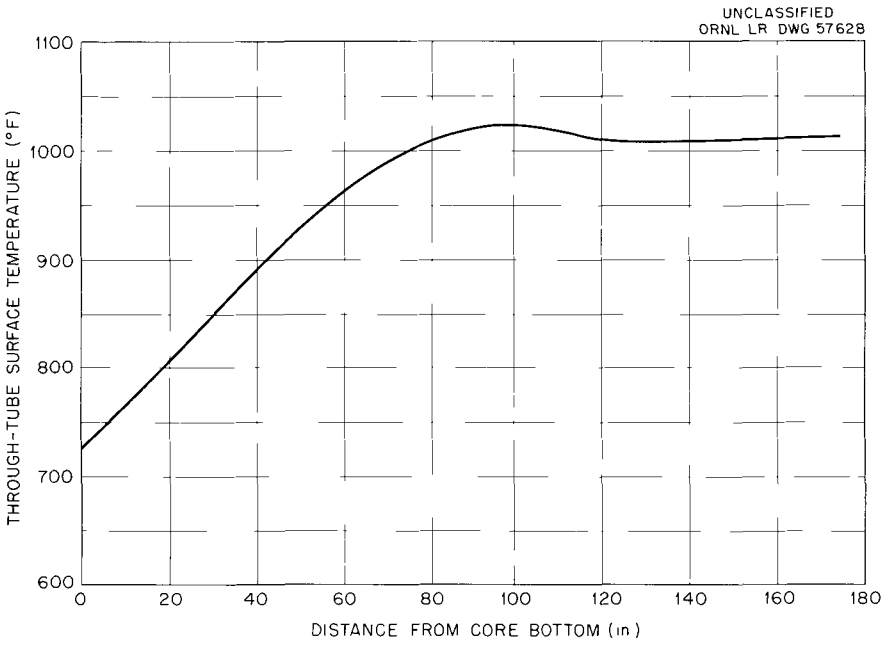

Fig. 7.1. Through-Tube Surface Temperature During Loop Operation with an Unattemperated Fuel Assembly at 335 kw (950°F Inlet Gas Temperature) for the Case of the Central Control Rod Fully Inserted and Bank Insertion of the Remaining Control Rods to 62 in. ($\delta k = 0.025$).

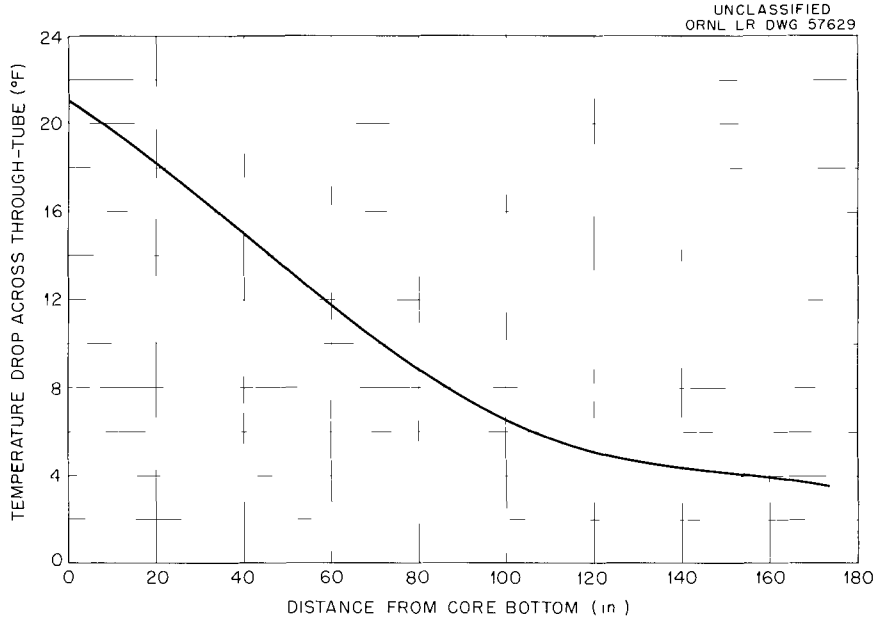

Fig. 7.2. Temperature Drop Across Through-Tube During Loop Operation at 335 kw.

Table 7.1. Vertical Force, Torque, and Bending Moments on Junction of Reactor Vessel and Lower Nozzles of Experimental Loops

Loop No.	Loop Coolant	Downward Vertical Force (lb)	Torque (in.-lb)	Bending Moment (in.-lb)
TL-1	Steam	38 820	646 030	351 200
TS-2	He or CO_2	16 800	62 560	385 600
TS-3	He or CO_2	16 840	63 820	330 900
TL-4	Hydrogen	39 170	152 030	341 700

The results of preliminary calculations of reactions at the junction of the reactor vessel and the upper nozzles of the four loops are presented in Table 7.2.

The calculations were made for two conditions: (1) the reactor hot and the loop hot and (2) the reactor hot and the loop cold. The data of Table 7.2 are for condition 2, which gives the greater loadings. A vertical (upward) growth at the upper nozzle tee of 3.25 in. was used in the pipe-stress analysis.

The bending moments at the upper nozzles are considerably below the allowable loadings based on a primary-plus-secondary stress intensity of 90% of yield strength, which are 270 000 in.-lb for the 5 1/2-in.-o.d. nozzles and 330 000 in.-lb for the 9 1/2-in.-o.d. nozzles.

Table 7.2. Vertical Force, Torque, and Bending Moments on Junction of Reactor Vessel and Upper Nozzles of Experimental Loops

Loop No.	Upward Vertical Force (lb)	Torque (in.-lb)	Bending Moment (in.-lb)
TL-1	30 600	49 440	298 180
TS-2	14 000	10 820	199 310
TS-3	14 020	10 570	202 300
TL-4	22 490	66 550	242 700

Additional work is being done in conjunction with Tennessee Valley Authority personnel to improve and expand pipe stress calculational program SHARE No. GS 3812. This work consists of changing the input format, increasing the problem size capability, and making the program compatible with the IBM 7090.

Component Design

Mainstream Filter. (E. R. Schmidt) A test program for evaluating the efficiency, the pressure drop that would cause failure, and the resistance to thermal cycling of two types of commercially available absolute filters has been initiated. The results of these tests will be used to select the filter element to be used in the helium and carbon dioxide loops.

Cooler. (A. W. Culp) The mainstream gas cooler has been modified in order to facilitate fabrication of the unit. The number of re-entrant boiler tubes has been decreased from 60 to 38, with a corresponding increase in heat transfer length from 7 to 11 ft. Two-phase pressure drop and driving-head calculations indicated that the exit steam quality from the tubes operating at full power conditions will be of the order of 5 to 10% with natural-convection flow. The gas-side pressure drop in the cooler is less than 1.1 psi at full cooling and increases to 1.8 psi with no cooling.

Auxiliary Gas System. (W. S. Delicate, L. C. Fuller) Final design criteria for the helium supply system and the sniffer gas system were prepared. Preliminary design criteria for the cooling system for use during removal of an experimental assembly are being prepared. Basically the proposed system consists of a small cooler (helium-to-demineralized water) and a small blower supported by the service machine. All equipment supported by the service machine is readily removable, and no internal changes to the service machine are required. The necessary pipe and valves are included to provide forced circulation of coolant upward through the through-tube and into the service machine (to provide cooling while the experimental assembly is being lifted) and, by means of a bypass line, return of the coolant to the main loop circuit or, in a

loop, through the cooler, the blower, and the service machine (to provide cooling of the experimental assembly while in the service machine). Lines and equipment are being sized to provide cooling at pressures ranging from atmospheric to 300 psig. In order to simplify equipment requirements and to eliminate the need for metal hoses trailing the service machine, it is planned to replace the CO_2 with helium in any loop operating with CO_2 prior to removal of an experimental assembly.

The final criteria and the Title I flowsheet for the gas transfer and storage system were completed. Title II drawings for the gas storage tanks have been prepared. A design analysis of the system was made.

Title I assembly drawings of the purification system heat exchanger and charcoal bed have been completed. The heat exchanger is a counterflow, concentric-tube cooler with loop gas in a 1-in. sched.-40 pipe cooled by water in a 1 1/2-in. sched.-40 pipe. The charcoal bed contains a silver screen, a 14-in.-deep charcoal bed, and a high-temperature absolute filter in a 14-in.-i.d., 29 3/4-in.-long pressure vessel.

Final criteria for the loop offgas system were prepared. The system is designed to discharge all waste gases of the loops to the atmosphere via the cell ventilation system. The maximum radiation dose at the surface of the ventilation ducts in the utility tunnel, which will occur during loop blowdown, will be about 3.8 mr/hr.

The decontamination system has been redesigned and final criteria were prepared. The decontaminating solutions are made up by pumping, with positive displacement pumps, saturated solutions of reagents into a heated header. The header, which is common to all loops, heats the solutions to about 200°F before they reach a loop.

Loop Cooling Water System. (A. W. Culp) Title I criteria have been completed for the cooling water system. The system is similar to that proposed in the preliminary criteria, except that the two large booster pumps originally incorporated in the service-water system have been eliminated. Since the service water flows for cooling the loops have been significantly reduced, with a corresponding decrease in the pressure drop of the system, the service water pumps now have sufficient head requirements to maintain the necessary flow to the condensers on the sixth floor.

Cell Ventilating and Washdown System. (A. W. Culp, W. S. Delicate) Title I criteria have been completed for the cell ventilation system, the cell washdown system, and the cell temperature control system. The cell ventilation system will be used only when the experimental loop is shut down for maintenance and inspection and there is no radioactive gas in the cell, although provision is made for venting the cell during operation of the loop. The cell washdown system employs a portable hot-water jet spray which is positioned in the ceiling for remotely spraying the contaminated cell. The cell temperature control system maintains the cell temperature below 110°F by transferring the heat to two 50-kw air-to-water coolers in the cell. When operating the loop with CO_2, the cell temperature will be maintained above 90°F by throttling the water flow to each cooler and using electrical heating elements in each unit.

Storage Holes (E. R. Schmidt)

The design criteria, process flow diagram, and the Title I assembly and piping drawings for the storage holes for experimental assemblies were prepared, and the required changes to existing plant drawings were made. The design analysis has been completed except for the detailed stress analyses.

Design and Hazards Report (C. Michelson)

A preliminary hazards and design summary report for the EGCR experimental loops is being prepared. This report will include a complete design description of the Title I loop design proposed by ORNL and an evaluation of the hazards associated with the operation of these loops.

At such time as construction of the experimental loops is authorized, this design proposal will be used as the starting point for a detailed (Title II) design. A final hazards summary report will be issued upon completion of the Title II design. The final report will treat the design, operation, and hazards in much greater detail but will follow the same outline as the preliminary report.

EGCR Component Tests

R. E. MacPherson

Microswitch Electrical Breakdown Tests (A. S. Olson)

A description of the switch being tested, the test conditions, and the preliminary results were presented previously.[2] The results of additional tests are reported in Tables 7.3 and 7.4. The switch was examined

[2]GCR Quar. Prog. Rep. Dec. 31, 1960, ORNL-3049, pp. 331–33.

Table 7.3. Voltage Breakdown in Helium of the V3-1301 Microswitch in Tests with Potential Applied Across Normally Closed and Common Contacts

Helium Test Pressure (psig)	Test Temperature (°F)	Breakdown Potential (v, ac)
300	70	>500[a]
300	530	>500[a]
1	530	269
10	530	416
20	530	448
1	530	289

[a]Highest potential applied; no breakdown evident.

Table 7.4. Voltage Breakdown in Helium of the V3-1301 Microswitch After Periods of Mechanical Cycling with Electrical Loading Across the Switch Contacts

Conditions During Mechanical Cycling			Electrical Test Conditions		
Number of Cycles Completed	Helium Pressure (psig)	Temperature (°F)	Helium Pressure (psig)	Temperature (°F)	Breakdown Potential (v, ac)
1250	300	530–540	300	540	>500[a]
			1	530	245
2450	300	530	300	530	>500[a]
			1	530	240
3300	125	100	300	535	>500[a]
			1	530	240
			1	70	305
			125	75	>500[a]

[a]Highest potential applied; no breakdown evident.

visually after completion of these tests, and it showed no damage. The switch and test assembly are shown in Figs. 7.3 and 7.4. It is anticipated that the microswitch will normally operate under a helium pressure

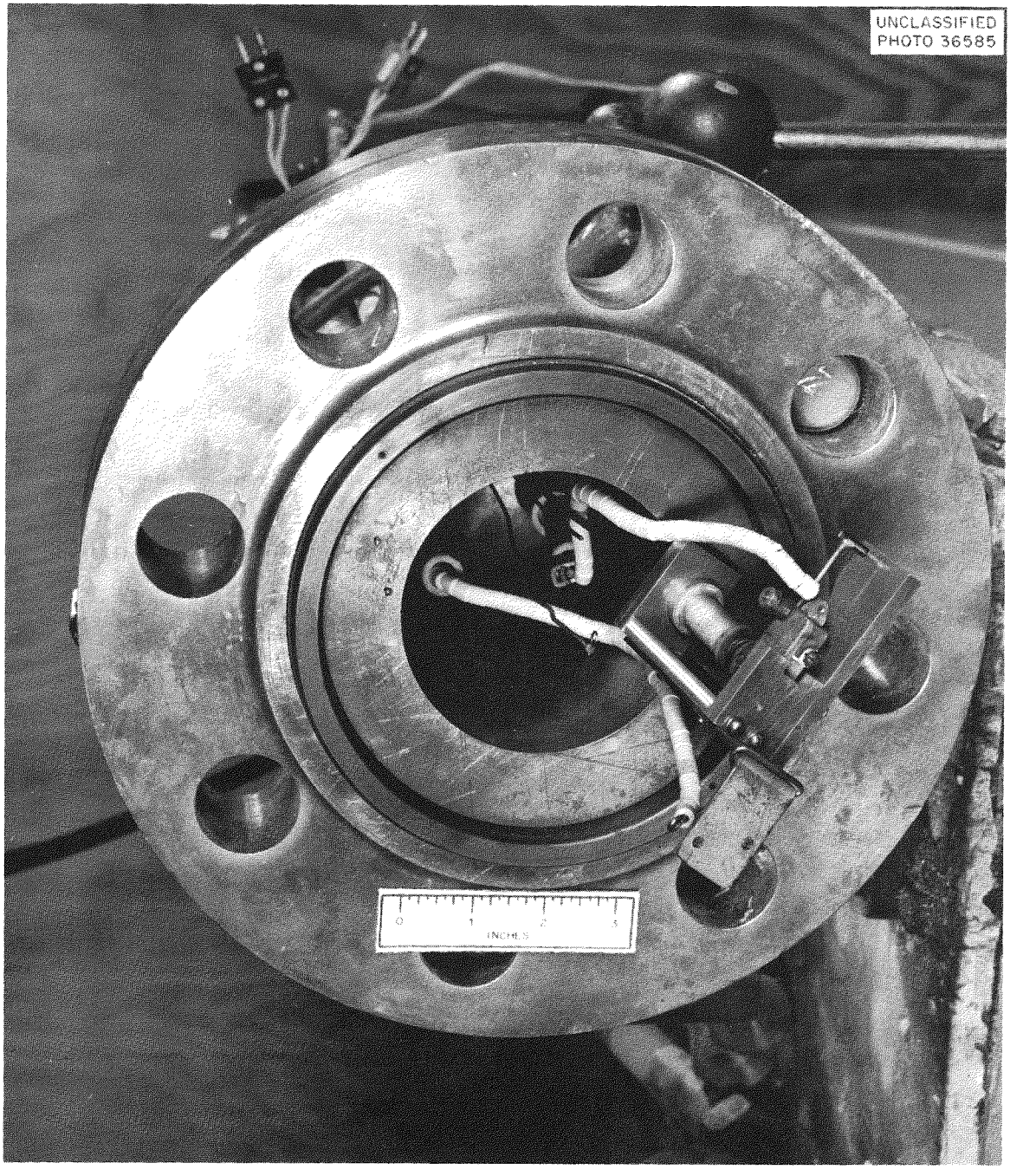

Fig. 7.3. EGCR Microswitch and Test Assembly.

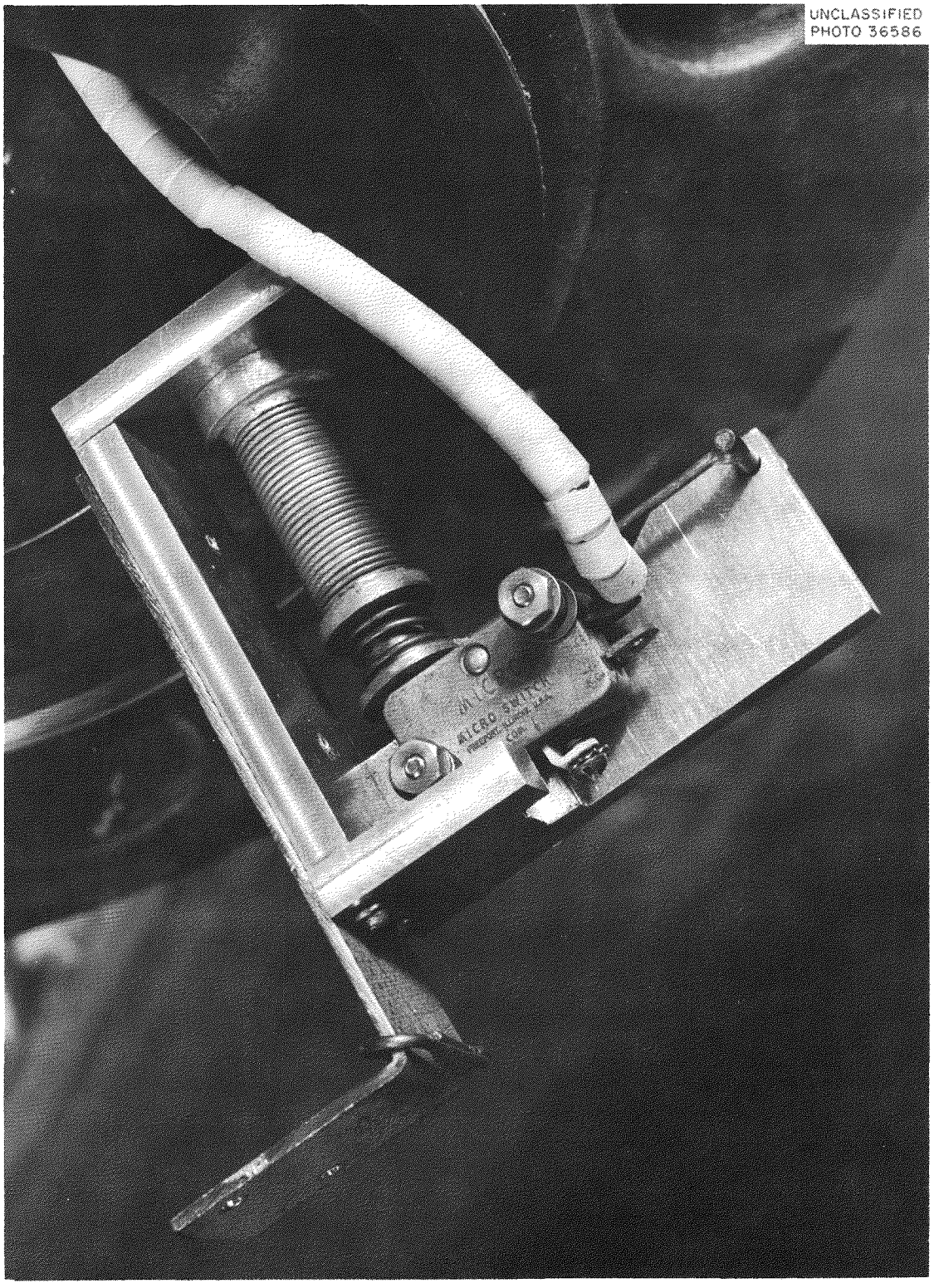

Fig. 7.4. EGCR Microswitch and Cycling Mechanism Shown After Completion of Tests.

in the range 125 to 300 psig at temperatures from 70 to 530°F. From the results presented in Tables 7.3 and 7.4 and those previously reported,[2] it can be concluded that this switch will be satisfactory for use under the normal conditions of operation.

Tests of Valves for EGCR Buffer-Gas System (A. S. Olson)

All-stainless-steel, bellows-sealed, 1/4-in. globe valves (type TY445, manufactured by Hoke, Inc.) have been proposed for use in the buffer-gas and leak-detection system[3,4] of the EGCR experimental loops. Helium leakage of 10^{-8} cm^3 (STP)/sec has been established as acceptable for valves used in the buffer-gas system.

Three Hoke valves have been tested to date. The bellows of each valve was leak tested at room temperature and atmospheric pressure. No leak was indicated by a helium mass spectrometer leak detector with a sensitivity of 1×10^{-10} cm^3 (STP)/sec. The valve seat on each valve was leak tested with the same equipment at room temperature with a helium pressure differential of 1000 psig. Again no leak was indicated. One of the valves was mechanically cycled 300 times between opened and closed positions, and it subsequently showed no leakage with a pressure difference of 400 psig of helium. The same valve was checked at room temperature to determine the minimum torque required to close it and to obtain a leakage rate less than that detectable by the helium mass spectrometer. On the initial tightening of the valve seat, a torque of 20 in.-lb was required to obtain no leak. However, when the valve was reopened and then closed, a torque of 50 in.-lb was required. Repetition of this operation yielded the latter value as the minimum torque required to obtain leaktightness.

Tests of 6-in. "Y" Globe Valve for EGCR Loops (A. S. Olson)

The 6-in. "Y" globe valve ordered from the Wm. Powell Company was received and is currently being tested. Grease and dirt were found inside the valve body, but visual examination of the valve seat and plug indicated no scoring of these surfaces.

---

[3]GCR Quar. Prog. Rep. Sept. 30, 1960, ORNL-3015, p. 160.

[4]GCR Quar. Prog. Rep. June 30, 1960, ORNL-2964, pp. 239–40.

Both the inlet and outlet ends of the valve body casting were given a dye-check examination. The outlet end gave porosity indications of approximately 10 to 30 dots per square inch over one-quarter of the inside edge, as well as some porosity indication on the outer surface. During welding of the pipe caps to the valve body, the weld joint on the valve inlet end showed indications of porosity after three weld passes and after completion of the welded joint. The dye-penetrant method was used for this check. X-ray photographs taken after three weld passes on each end between 6-in. pipe caps and the valve body gave no indication of cracks.

The seal weld was made between the valve body and bonnet. There was no indication of leakage when checked with a helium mass spectrometer leak detector, although a few dye penetrant indications were obtained. A torque of approximately 450 ft-lb was applied to each bolt of the flange joint between the body and bonnet to complete the reassembly of the valve.

The valve was installed in the test facility as shown in Figs. 7.5, 7.6, and 7.7. An insulating pad consisting of several layers of corrugated stainless steel sheet was placed between the lower end of the valve and the furnace heaters to prevent excessive temperature at this end of the valve.

A diagram of the helium piping for the test system is shown in Fig. 7.8. This system permits leak checks to be made on the valve seat and on the buffer zone between the valve stem packings at any desired pressure conditions. A high-pressure manometer has been used to measure the leakage rates at valve pressures up to 300 psig. At higher values, pressure decay rates have been obtained using precision pressure gages.

The initial helium leak rate of the valve seat at room temperature was 0.38 cm^3 (STP)/hr with a pressure difference across the valve seat of 300 psig. The helium leak rate at room temperature from the buffer zone with its pressure at 1100 psig and with the valve pressure at 1000 psig was 3800 cm^3 (STP)/hr or 0.13 scf/hr. Essentially all this leakage was from the buffer zone into the valve.

After raising the valve body temperature to 1000°F at a rate not exceeding 50°/hr, a leak check of the valve seat indicated helium leakage of 15.6 cm^3 (STP)/hr with a pressure difference of 300 psig. The leak rate from the buffer zone was 4.7 scf/hr, with the buffer zone and valve

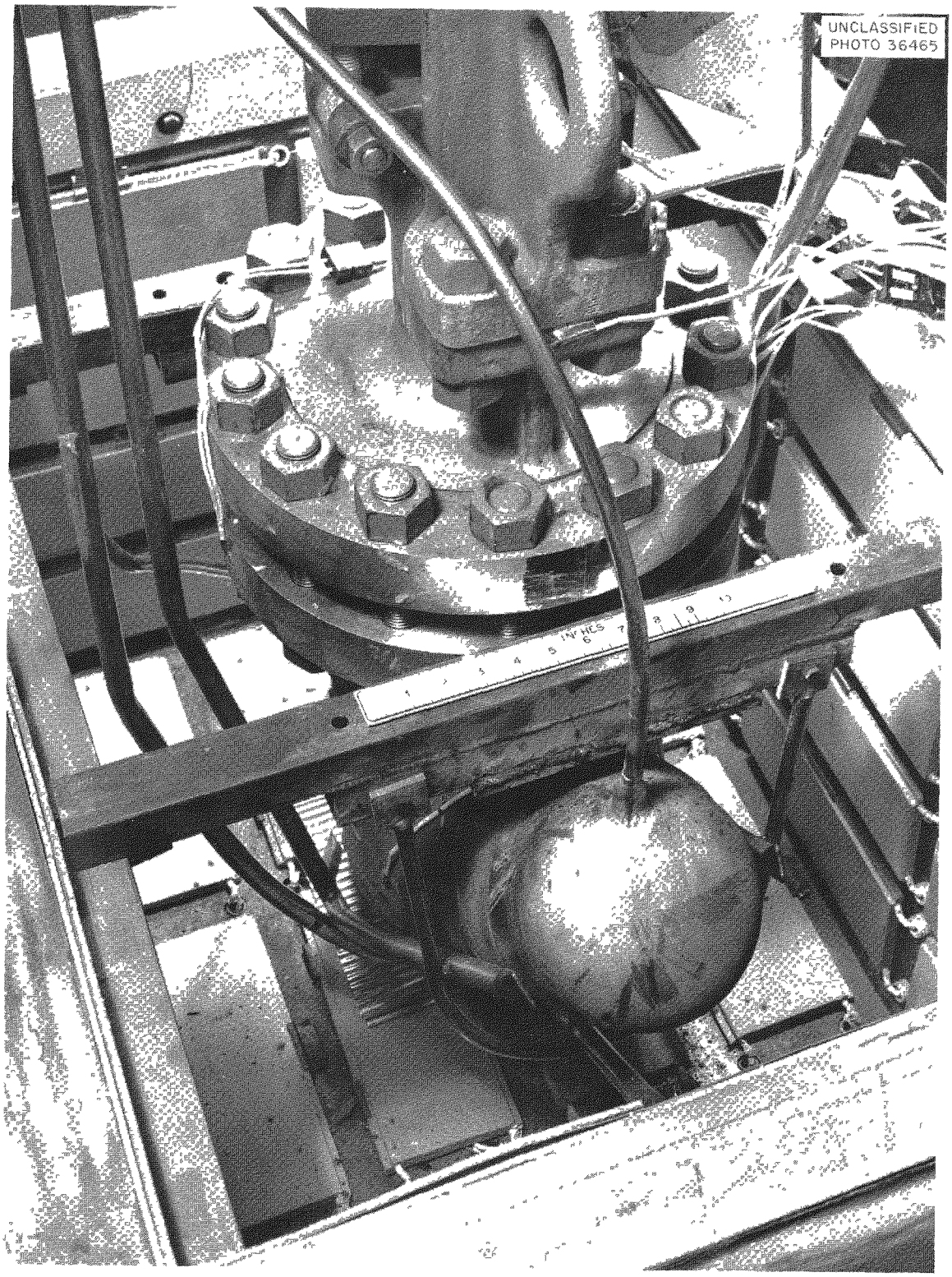

Fig. 7.5. View from North End of Powell Globe Valve Installed in Test Furnace.

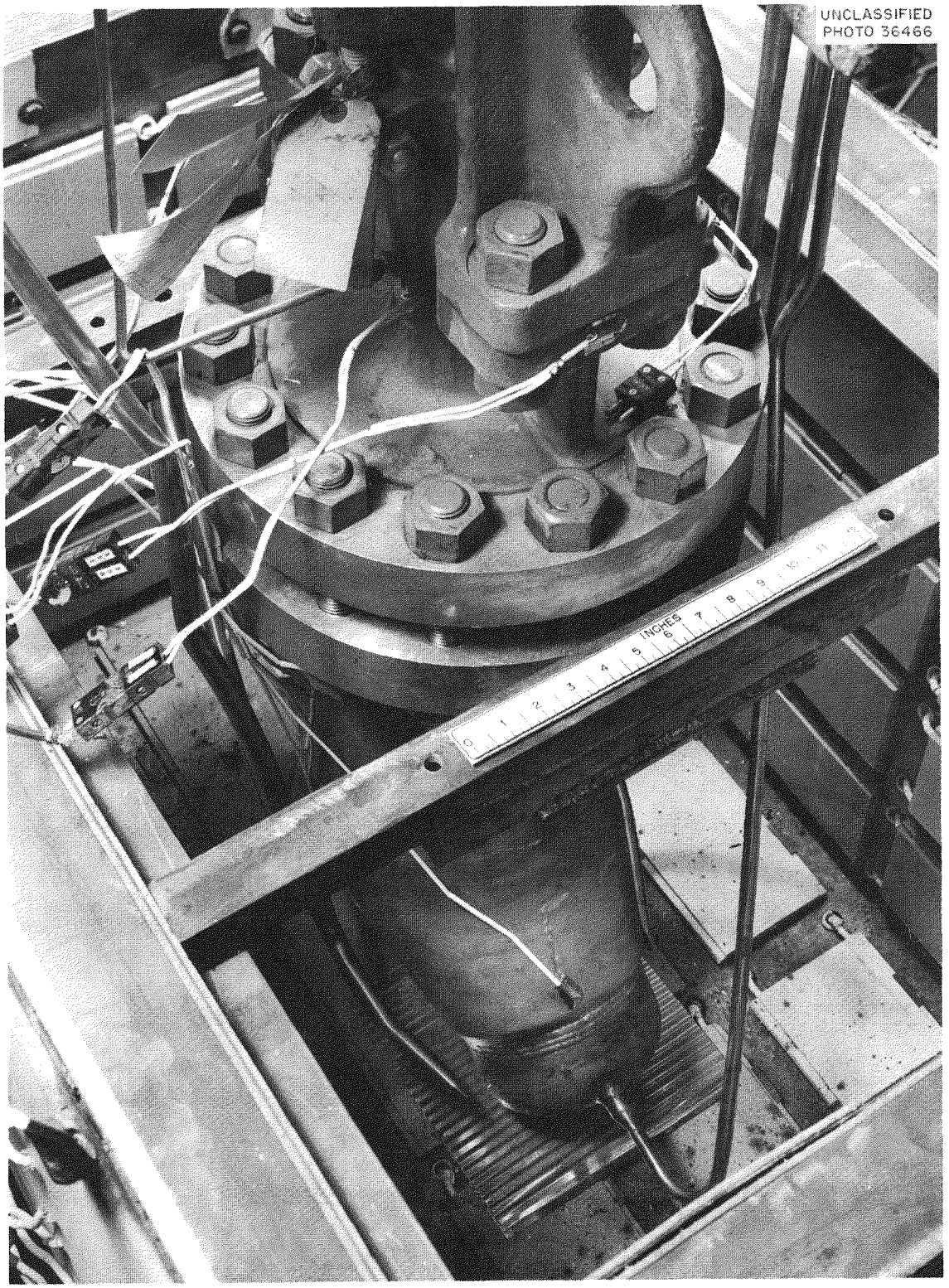

Fig. 7.6. View from South End of Powell Globe Valve Installed in Test Furnace.

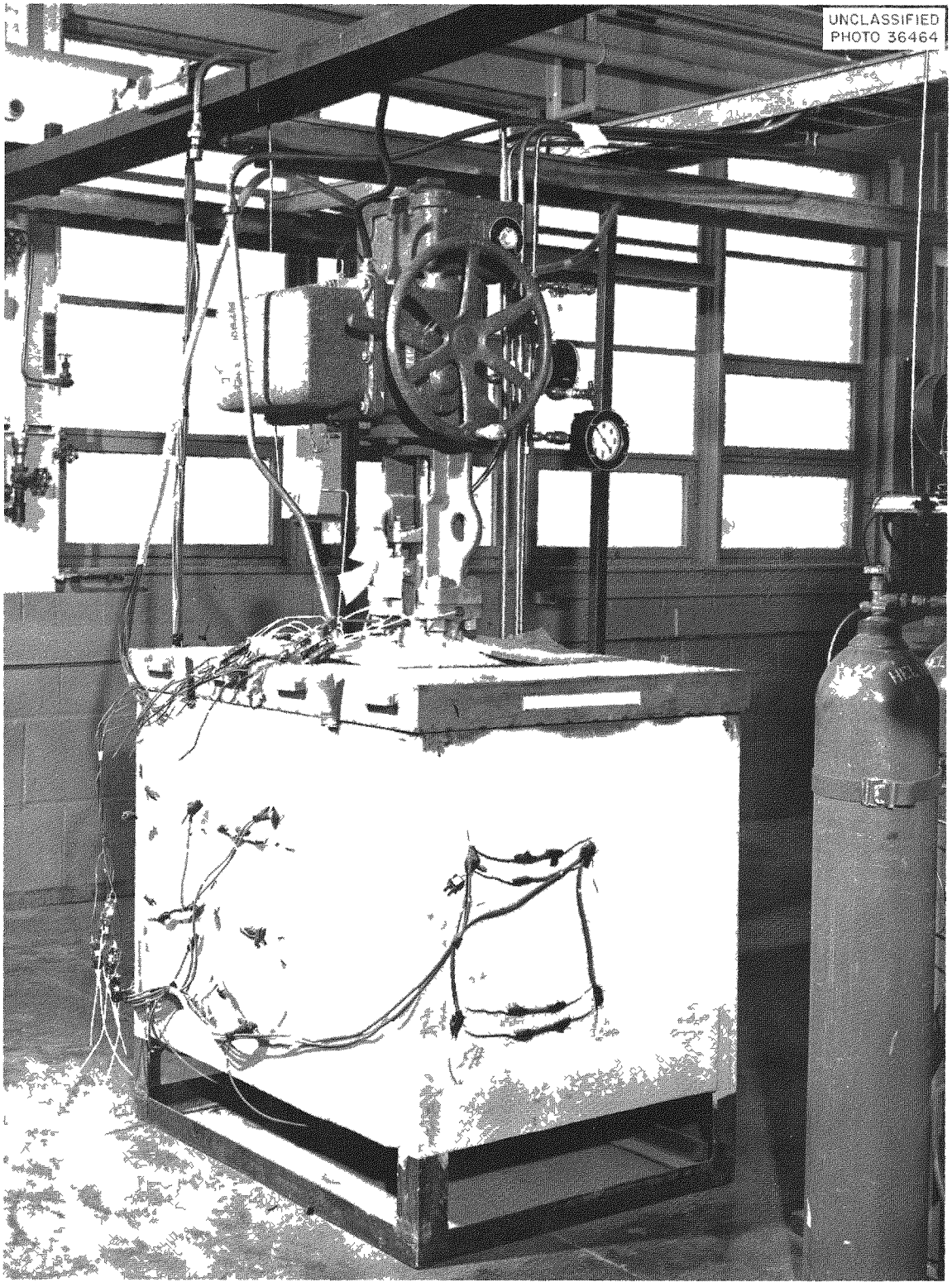

Fig. 7.7. Completed Installation of Powell Globe Valve in Test Furnace Showing Limitorque Drive Above the Furnace.

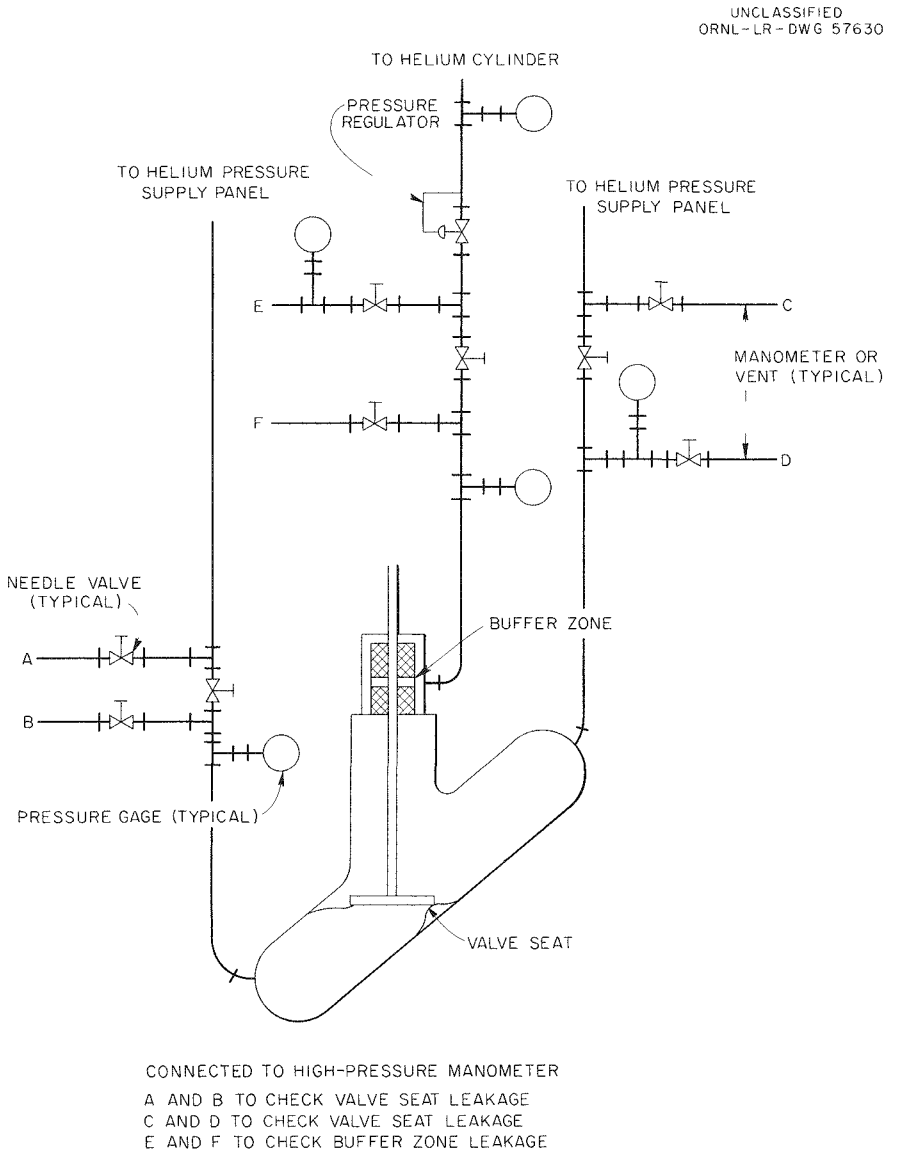

Fig. 7.8. Diagram of Helium Piping System for Leak Tests of Powell Globe Valve.

body pressures at the previous levels. Again essentially all this leakage was from the buffer zone into the valve. Subsequent tightening of the packing gland bolts to a torque level of 120 ft-lb reduced this leak rate to approximately 1.9 scf/hr, which is considered excessive. Communication with the valve manufacturer indicated that further tightening of the valve stem packing is not desirable. Thermal cycling of the valve between 200 and 1000°F in 8-hr cycles has been started. About 25 of the proposed 100 cycles have been completed.

Mockup Test of Experimental Through-Tube Bearing Surface (A. M. Smith)

A test facility to simulate the bearing surface in the lower tee sections of the experimental loops and to check the amount of galling which might be expected between the lower tee section and the through-tube has been designed and is presently being constructed. Tests are to be conducted at 950°F on two types of plating, Stellite No. 6 and Linde Flame plate LW-IN30. Mechanical loading during the test will simulate the thrust and bending moment loads to which the bearing will be exposed in the reactor application.

Development Tests of Through-Tube Orifice-Type Flow Restrictors (F. A. Flint)

In order to maintain the temperatures of the EGCR experimental loop through-tubes within desired limits, it is essential that they be adequately cooled. This can be accomplished best by diverting a portion of the reactor coolant flow through the annuli formed by the through-tubes and the reactor core. This annulus flow must be controlled so that proper cooling is obtained without starving the surrounding fuel channels.

It has been proposed that orifice-type flow restrictors be placed in the annuli formed by the through-tubes and through-tube inserts at the bottom of the lower plate of the reactor core. Each restricting orifice would be designed to insure adequate coolant flow to the through-tube and to have a pressure drop approximately equal to that of a fuel channel through the core, thereby guarding against starving the coolant flow to the fuel channels. Because it would be extremely difficult to design these orifices by analytical methods, it has been proposed that they be developed experimentally.

The test will be conducted by passing air, at atmospheric pressure and ambient temperature, through a geometrically exact model of the through-tube annulus. Dynamic similarity between the model and the through-tube annulus will be maintained by passing the air at the weight rate necessary to make its Reynolds number equal to that of helium at design conditions. With dynamic similarity maintained, the dynamic pressure ratios between corresponding points on the model and the through-tube annulus will be constant. This relationship will make it possible

to calculate the pressure drop across the model required to give the desired pressure drop across the through-tube annulus. The orifice configuration, necessary to give the desired pressure drop in the reactor, will be determined by the cut-and-try method. Provisions are being made to test the orifice configurations developed by this method in helium at approximately reactor design conditions. The test system has been designed and fabricated.

Mechanical Joint Service Testing (J. C. Amos)

The mechanical joint tests conducted during this report period are described in Table 7.5. The test units have included 5-in.-IPS double-seal "Conoseal" joints and 6-in.-IPS double-seal "Grayloc" joints, both modified by the vendor to improve the sealing characteristics; a 3-in.-IPS single-seal "Grayloc" joint, a 1/2-in.-IPS union-type "Grayloc" joint, shown in Fig. 7.9; and a 1/2-in.-o.d.-tube union-type "Conoseal" joint.

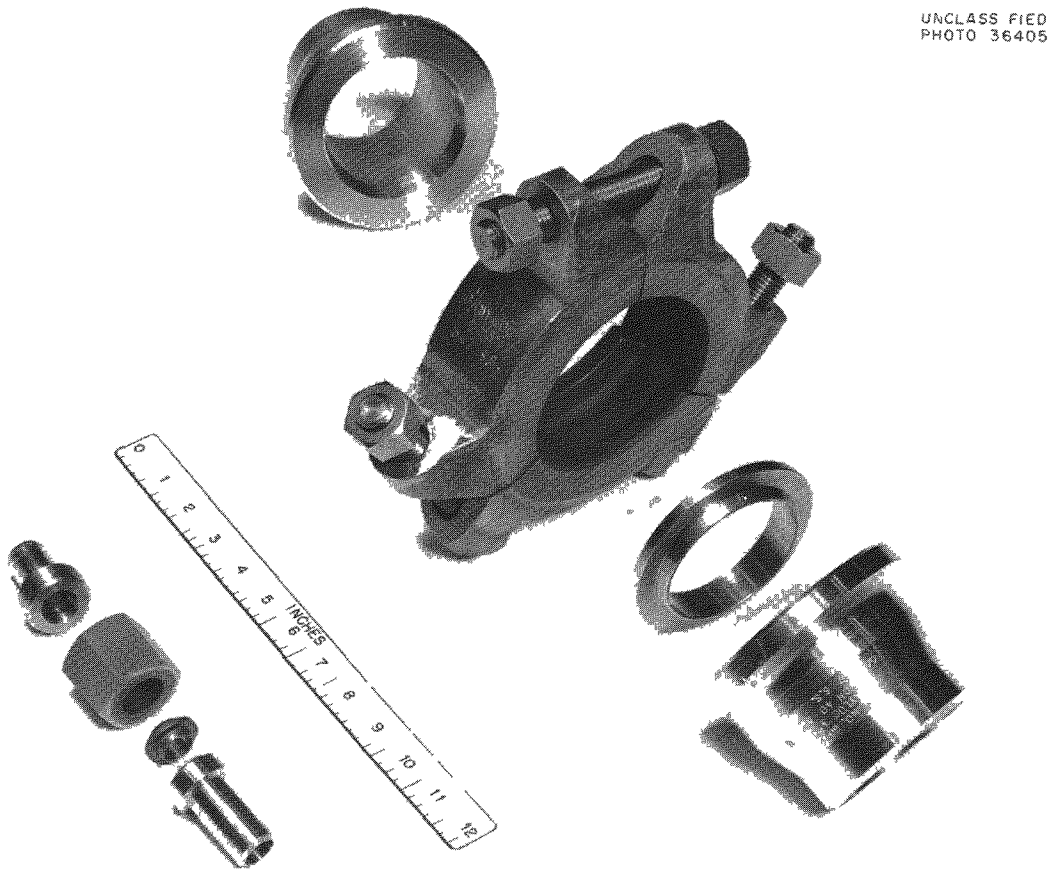

Fig. 7.9. Sample 3-in. and 1/2-in. sched.-40 "Grayloc" Pipe Joints Disassembled.

Table 7.5. Summary Description of Mechanical Joint Tests

Description of Joint	Test Conditions	Maximum Helium Leakage [cm^3 (STP)/sec]		Remarks
		Inner Seal	Outer Seal	
5-in.-IPS double-seal "Conoseal"[a] joint No. 1 (modified)	108 thermal cycles between room temperature and 700°F	2.8×10^{-8}	$\sim 7 \times 10^{-5}$	Unit was installed with an initial torque of 150 ft-lb and a final torque of 75 ft-lb; following the first two cycles the torque dropped to ~10 ft-lb and the torque was reapplied to 75 ft-lb; no loss of torque was detected during the balance of the test
	100 thermal cycles between 200 and 1000°F; internal pressure, 300 psig	3.1×10^{-7}	$\sim 7 \times 10^{-5}$	
5-in.-IPS double-seal "Conoseal" joint No. 2 (modified)	Room-temperature test after remote installation	$<1 \times 10^{-10}$	7×10^{-7}	Leak rates shown are for 75 ft-lb torque; outer seal helium leakage was $<1 \times 10^{-10}$ cm^3 (STP)/sec at 100, 150, and 75 ft-lb final torque
5-in.-IPS double-seal "Conoseal" joint No. 3 (modified)	Room-temperature test of joint as returned by vendor after 10 thermal cycles between room temperature and 700°F	$<1 \times 10^{-10}$	2×10^{-9}	Leak rates are essentially in agreement with those measured by vendor
6-in.-IPS double-seal "Grayloc"[b] No. 1 (modified)	40 thermal cycles between room temperature and 500°F at atmospheric pressure	2.4×10^{-7}	$<1 \times 10^{-10}$	Inner seal helium leakage dropped to $<1 \times 10^{-10}$ cm^3 (STP)/sec after first cycle; 300 ft-lb torque required to seal this joint
6-in.-IPS double-seal "Grayloc" No. 2 (modified)	Initial room-temperature test	1.3×10^{-5}	$<1 \times 10^{-10}$	
3-in.-IPS single-seal "Grayloc"	121 thermal cycles between room temperature and 500°F	1.2×10^{-5} (c)		Leakage dropped to $<1 \times 10^{-10}$ cm^3 (STP)/sec on first cycle and remained below this level until the seventh cycle between 200°F and 1200°F; at this point bolt torques were found to be zero; reapplication of torque did not reduce the leakage
	100 thermal cycles between 200 and 1000°F	$<1 \times 10^{-10}$		
	100 thermal cycles between 200 and 1100°F	$<1 \times 10^{-10}$		
	7 thermal cycles between 200 and 1200°F	$>2 \times 10^{-5}$		
	300-psig internal pressure during all tests			
1/2-in.-IPS union-type "Grayloc"	163 thermal cycles between room temperature and 500°F	$<1 \times 10^{-10}$		After completion of 1000°F cycling the unit was disassembled and reassembled with the same seal ring and found to be leaktight
	270 thermal cycles between 200 and 1000°F; internal pressure, 300 psig	$<1 \times 10^{-10}$		
1/2-in.-o.d.-tube union-type "Conoseal"	Thermally cycled at the following conditions with 300-psig internal pressure			
	No. of Cycles / Temperature (°F)			
	115 / 200–1000	$<1 \times 10^{-10}$		At completion of 1500°F cycling, the joint was disassembled and reassembled with a new gasket and had a leak rate of 5.5×10^{-8} cm^3 (STP)/sec
	105 / 200–1100	$<1 \times 10^{-10}$		
	106 / 200–1200	$<1 \times 10^{-10}$		
	101 / 200–1300	$<1 \times 10^{-10}$		
	57 / 200–1400	$<1 \times 10^{-10}$		
	107 / 200–1500	$<1 \times 10^{-10}$		

[a]"Conoseal" is an Aeroquip Corp. trademark. [b]"Grayloc" is a Gray Tool Company trademark. [c]Single seals.

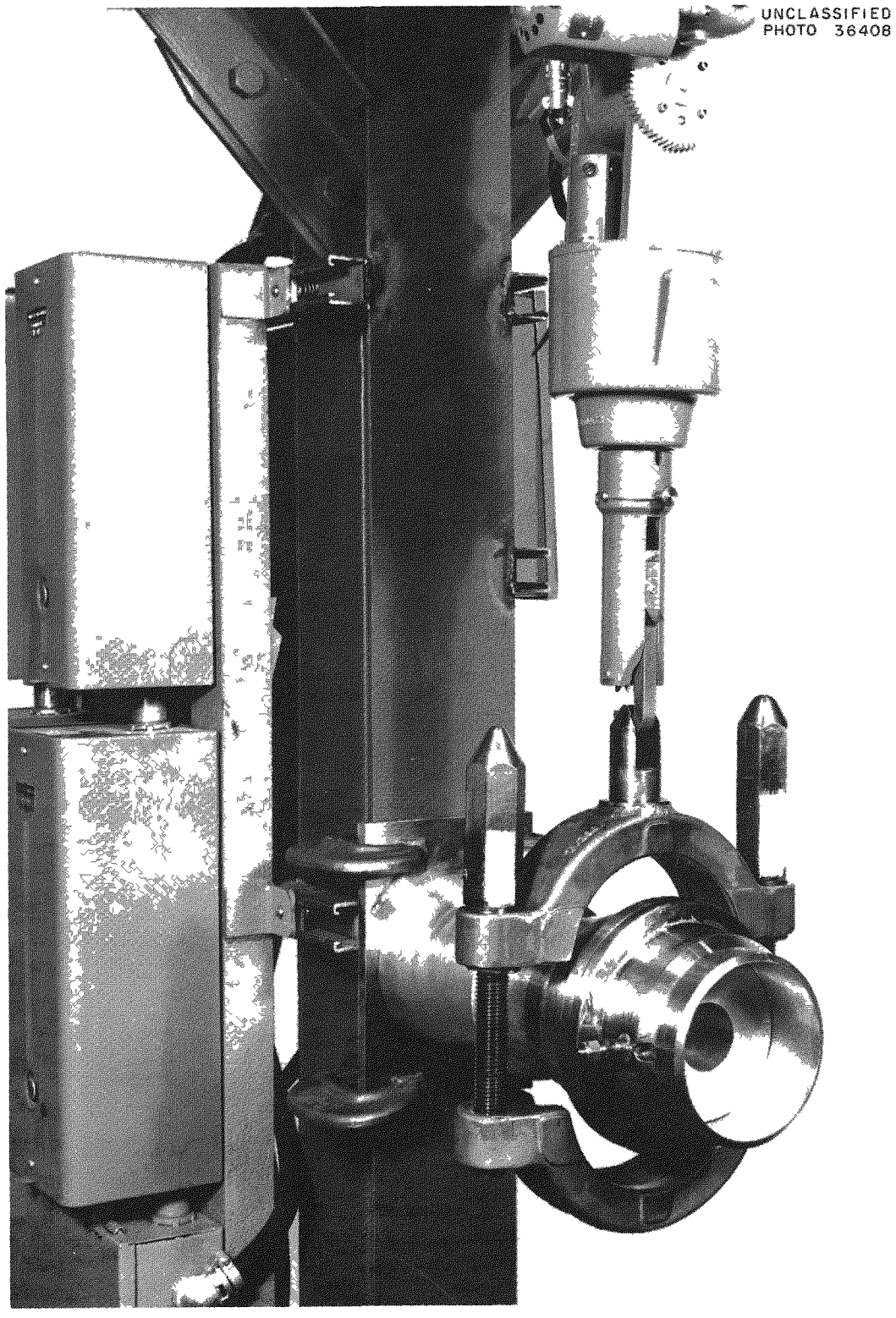

Fig. 7.10. Sample 5-in.-IPS "Conoseal" Clamp Being Positioned Remotely with a General Mills Model 100 Manipulator.

Modification of the 5-in.-IPS "Conoseal" joint included machining the clamps to closer tolerances and increasing the width of the gaskets. In addition to the thermal cycling tests being carried out on one of these units, assembly and disassembly of the joint by remote operation have been demonstrated. The clamp is shown being placed on the flanges with a General Mills one-arm manipulator in Fig. 7.10, and in Fig. 7.11 a motor-operated bolt runner is being removed after final tightening of the clamp.

Modification of the 6-in.-IPS "Grayloc" joint included remachining the flange sealing surfaces and silver plating the redesigned seal ring shown in Fig. 7.12.

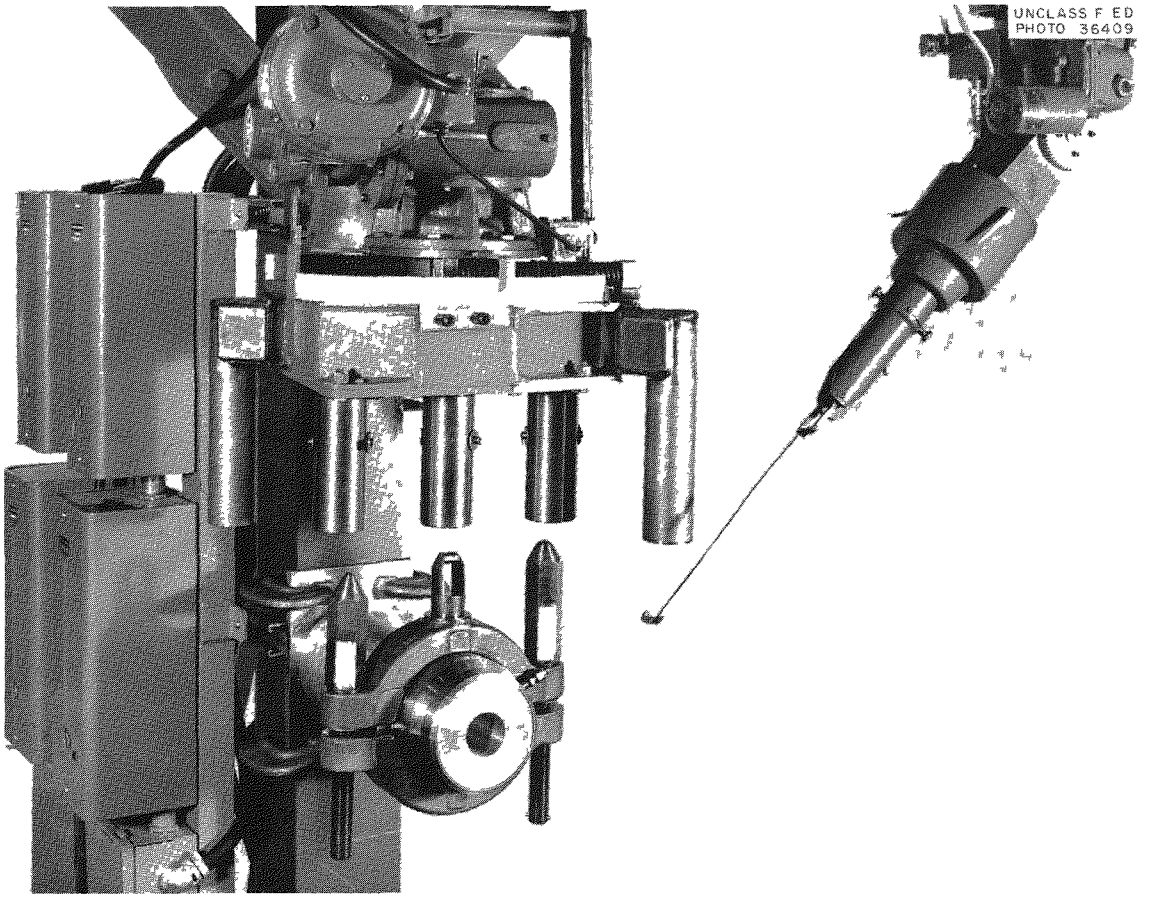

Fig. 7.11. Motor-Operated Bolt Runner Being Removed After Assembly of 5-in.-IPS Double-Seal "Conoseal" Joint.

Fig. 7.12. Sample 6-in.-IPS Double-Seal "Grayloc" Modified Seal Ring.

GCR-ORR Loop No. 2

J. Zasler

Loop Design and Construction (P. A. Gnadt, W. R. Huntley, T. S. Kress, J. LaGraff, E. E. Wade)

A sketch of the loop is presented in Fig. 7.13. The basic cell structure and cell liner are essentially complete. Temporary closures have been made for such of the cell penetrations as have not been installed, and a leak test of the cell is in progress. It is the purpose

UNCLASSIFIED
ORNL-LR-DWG-52934-B

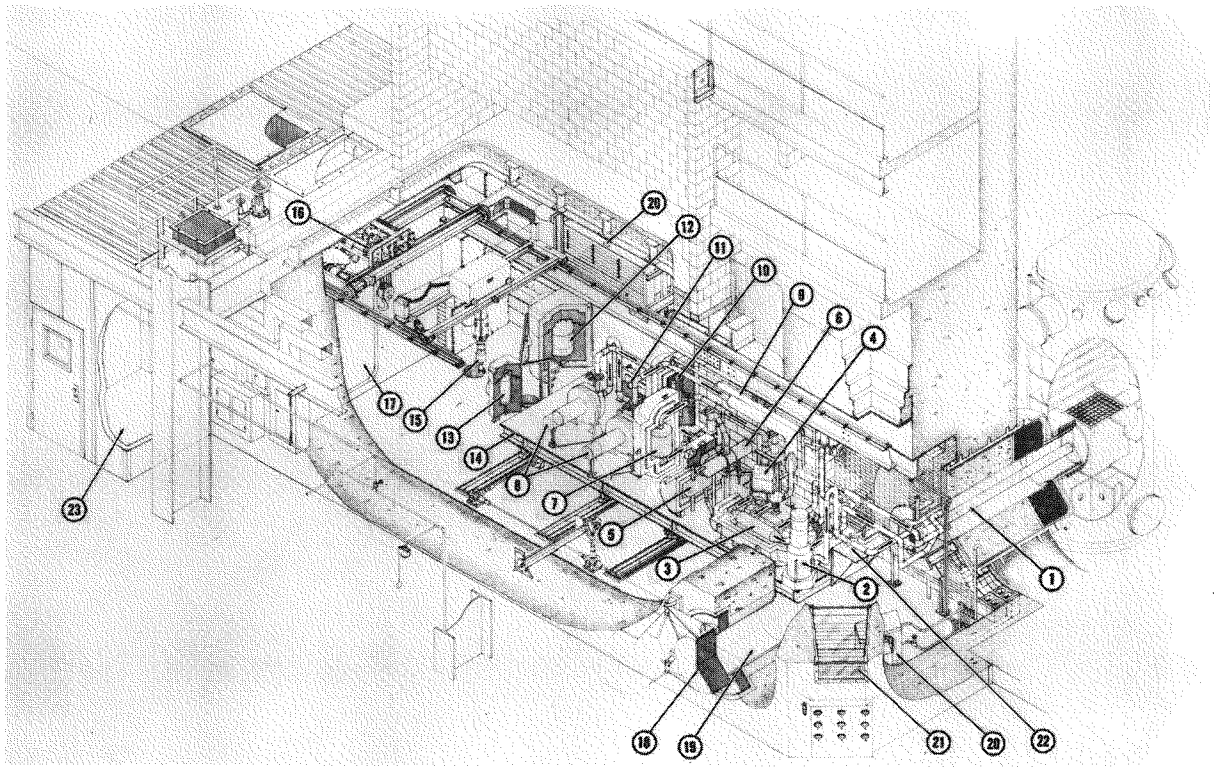

1. FUEL TEST TUBE
2. HEATER
3. REGENERATER
4. EVAPORATOR BY-PASS VALVE
5. EVAPORATOR
6. CONDENSER
7. FILTER
8. COMPRESSORS
9. SHELL COOLANT STREAM
10. CuO BED
11. SIDE STREAM COOLER
12. SIDE STREAM CARBON TRAP
13. MOLECULAR SIEVE
14. MOVABLE RACK
15. REMOTE MANIPULATOR
16. 5-TON CRANE
17. PERSONNEL ACCESS DOOR
18. EXTERNAL SHIELD DOOR
19. TEST PLUG REMOVAL SLEEVE
20. SPACE COOLERS
21. VIEWING WINDOW
22. MARMON SEAL FLANGE
23. AIR LOCK

Fig. 7.13. Sketch of GCR-ORR Loop No. 2.

of this test to find and repair all leaks in the liner and to establish the actual cell inleakage rate. The design of the loop calls for a maximum allowable inleakage of 40 ft^3/day with a pressure in the cell of 1 1/2 psi below atmospheric.

Drawings for parts of the main piping system are complete, and prefabrication of pipe runs is in progress. Material takeoffs have been made from the flow sheets in order for fabrication work to be started on the remaining portions of the main piping and all auxiliary piping systems as soon as the drawings are completed. In order to obtain better delivery dates on some materials, the materials have been ordered to standard ASTM specifications. Reactor-grade inspection procedures will be utilized to upgrade the standard material to reactor grade.

The status of the main loop major components is the following:

Item	Delivery Date	Comments
Evaporator	Complete	
Condenser	Complete	
Regenerator	Complete	
Filter	June 1	New filter elements being obtained
Heater	April 1	
Compressors		Delivery date uncertain because of vendor's gas-bearing development problems
Side-stream cleanup system (4 components)	Complete	
Component shields (7 required)	Complete	

The movable rack on which all the components will be mounted and its tracks and actuating mechanism have been delivered and are now being assembled for testing prior to installation at the reactor. The 5-in.-joint nut runner, the omniscope for remote cell viewing, and the fuel tube lifting tongs have been checked in the cell mockup, and all appear to function satisfactorily. A device to be used in conjunction with the manipulator

for remotely opening and closing small valves of the loop system is being built.

Subassembly drawings were completed for all shielded components that spell out thermocouple installation, flange attachments, and method of mounting within the lead shielding. These subassemblies are now being fabricated. Approximately 20% of the detail drawings of the main loop piping has been completed.

Design work has continued on the horizontal fuel test installation which was described briefly in the previous report. The shield plugs have been shortened so that the fuel test tube can be remotely withdrawn into the cell and the "cooling finger" remotely inserted if loop difficulties are encountered. The reactor can then go to power with the loop deactivated. A vertical cross section of the present design of the horizontal installation of a typical fuel element is shown in Fig. 7.14.

Shielding calculations now indicate that the streaming from the several annuli created by the concentric plugs will be low enough to allow limited direct maintenance at that end of the cell when the "cooling finger" is inserted in lieu of a fuel test tube (reactor at full power).

The high-efficiency (99.97% for 0.3-μ particles) main-stream filter was tested, and it failed under thermal cycling from room temperature to 700°F (see subsequent section for details). A specification has been prepared for another unit which will utilize the same filter pressure vessel and shield.

Criteria for the flange buffer gas system were prepared and equipment for the system has been ordered. Following the failure of the loop heater during preliminary testing, extensive redesigns were made. The new design specifies a four-pass cross-flow unit with a total of 60 cartridges. This heater is now in advanced stages of construction.

Experiments have been conducted with an experimental die on 1/2-in.-o.d., 0.065-in.-wall, types 304 and 347 stainless steel annealed tubing in order to establish the design of a die for remotely cutting and sealing a pipe in one operation. Helium leak rates of the order of 3×10^{-3} cm^3 (STP)/sec at 2 psig were measured for one severed end and 1×10^{-4} for

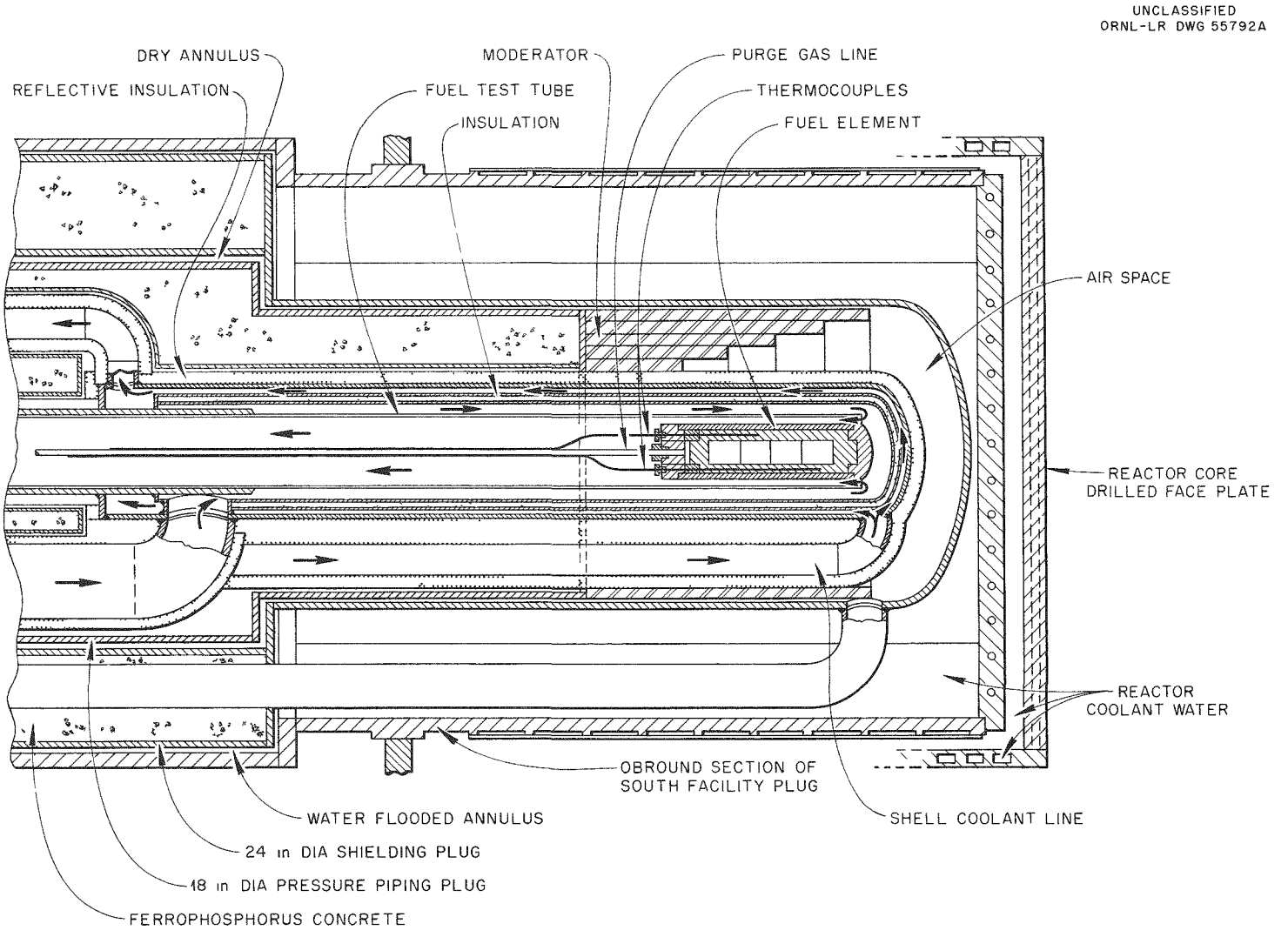

Fig. 7.14. Vertical Cross Section of Nose Piece for Horizontal Installation of Fuel Test Piece in GCR-ORR Loop No. 2.

the other. Test dies have been ordered for 2 1/2-in. sched.-160, type 347 stainless steel annealed pipe.

An IBM 7090 code has been used to study temperatures in the test plug following a loss of cooling water, with and without a reactor scram; loss of helium coolant, with a reactor scram or setback; and amount of cooling required to dissipate afterheat following an orderly shutdown. Since the design of the test section is not yet firm, the above studies may have to be repeated.

An IBM code was also used to determine the design of internal insulation for the Marman flanges to be used in regions of the loop with gas temperatures greater than 1000°F.

Temperature distributions for various cooling arrangements of the test plug were determined by electrical analogy. Conducting paper was used for the analog. The estimates of gamma energy deposited in the moderator were revised to consider the theoretical density variation of the moderator.

Investigations were started to analyze the case in which loss of helium coolant occurs and the reactor fails to scram. This temporal study involves a change-of-state of materials and will be coded for a digital computer to obtain solutions in a reasonable length of time.

The project schedule has been reviewed and modified to show the latest design, procurement, and installation plans. New information and revision of criteria have delayed completion of major portions of the design. Loop shakedown (without the test section) is now scheduled for the period of August through October 1961. The shakedown of the test section is scheduled for November and December 1961. A large portion of the field installation work will fall in the period June through August 1961.

Component Tests (F. A. Flint, R. E. MacPherson, A. M. Smith)

Multiple-Cylinder Experimental Slip Joint. A 2 1/2-in.-o.d. multiple cylinder slip joint being considered for use in the in-pile facility was fabricated and tested to determine the leakage characteristics of the proposed unit. The design of the unit is indicated in Fig. 7.15.

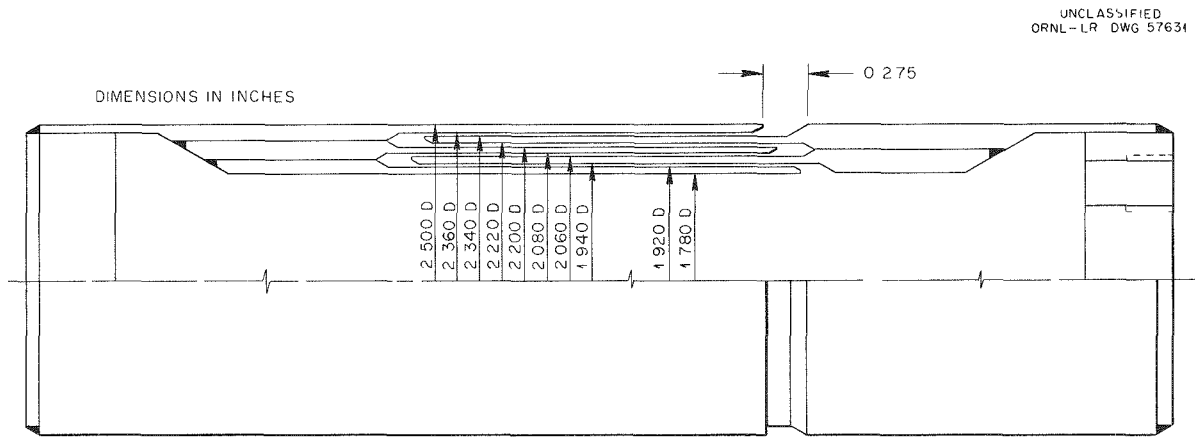

Fig. 7.15. Design of Multiple-Cylinder Slip Joint.

The tests were conducted using air, helium, and CO_2 over a pressure differential of 0.5 to 10.0 psig while maintaining the slip joint axially aligned with a gap of 0.275 ± 0.002 in. between the two halves of the joint. Results of the leak rate determinations for each of the three gases are shown in Fig. 7.16, and a general correlation for all three gases, assuming essentially incompressible flow, is shown in Fig. 7.17. In calculating the velocities and Reynolds numbers, average values for the area of the joint annuli and principal physical properties of the gases were used. Over the Reynolds number range investigated, the correlation appears to be useful in predicting the slip joint leakage where the ratio of internal to external absolute pressure is less than 2.

Coolant Filters. A series of efficiency and thermal-cycling tests were conducted on two specimens of a filter unit proposed for filtering the primary coolant in the in-pile loop facility. The filters tested were Flander's Airpure units constructed of glass filter paper and corrugated separators arranged in a high-surface-area geometry, as illustrated in Fig. 7.18. The filtering element was sealed to its casing with an adhesive composed of silica soda, ground silicate, fireclay, and asbestos fibers.

Results of efficiency tests run before and after thermal cycling are presented in Table 7.6. It may be seen that only one of two specimens demonstrated satisfactory performance (>99.9% efficiency in the "as-received" condition) and that this unit was damaged by subsequent thermal cycling. The posttest condition of unit 2 is shown in Fig. 7.19. The

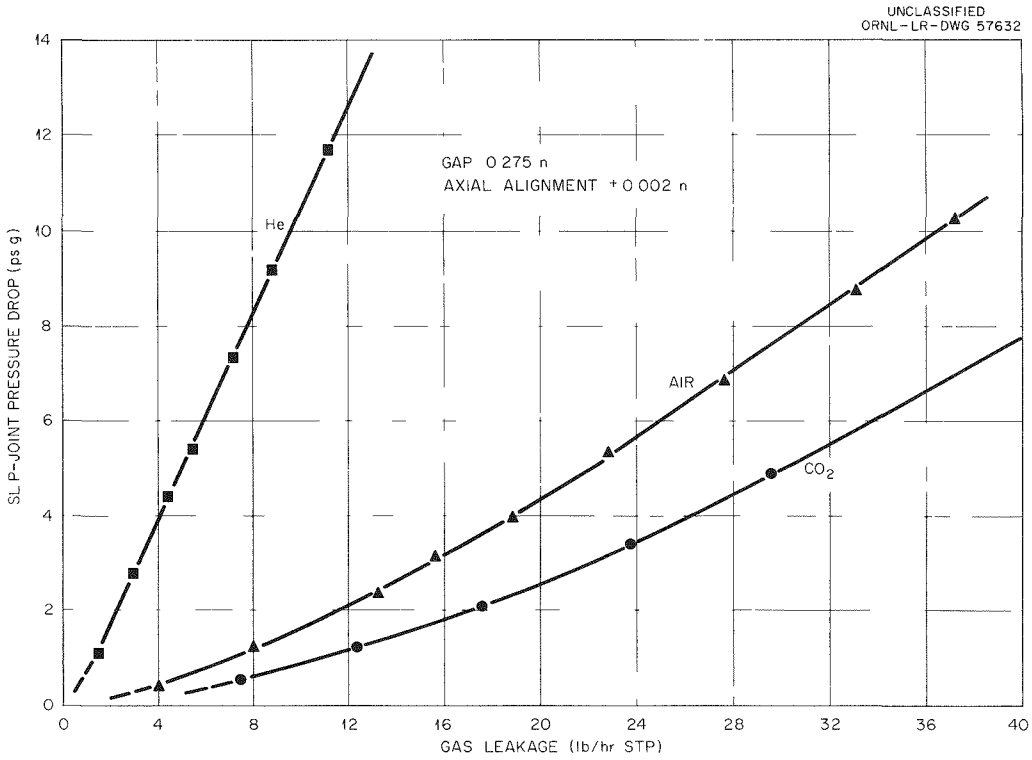

Fig. 7.16. Results of GCR-ORR Multiple Cylinder Experimental Slip Joint.

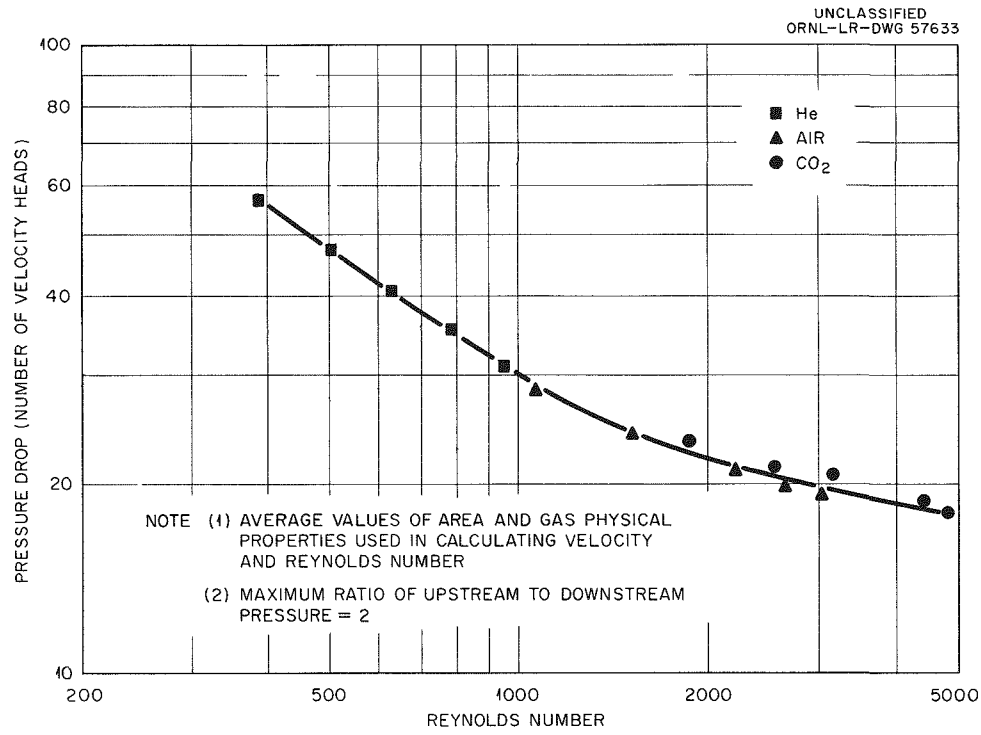

Fig. 7.17. Velocity Head Loss Versus Reynolds Number for Experimental Multiple-Cylinder Slip Joint.

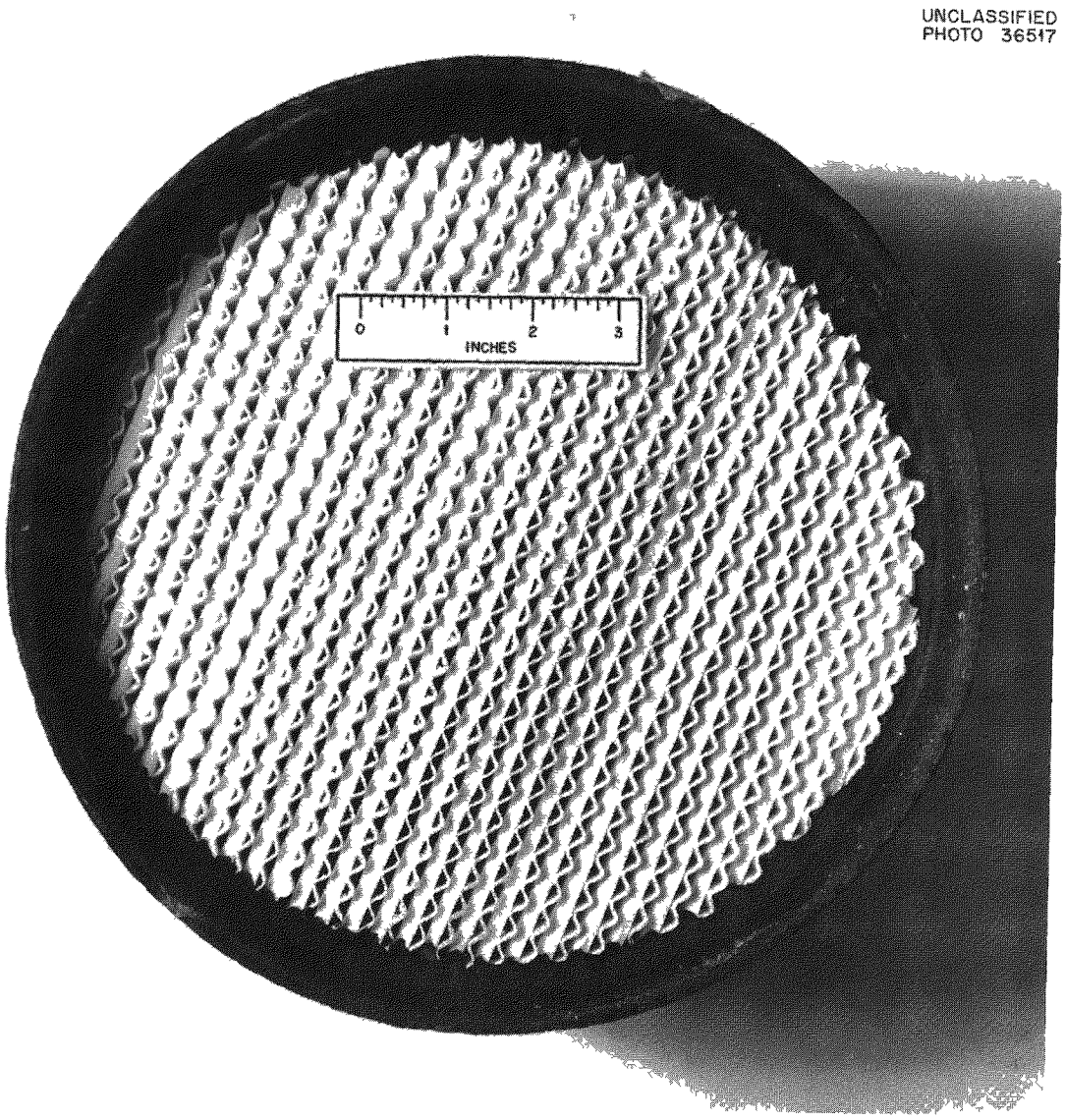

Fig. 7.18. Downstream End of Unmounted Filter Cartridge.

sealing adhesive between the filter element and the casing is cracked in several places; this could account for the failure to meet efficiency standards. Since the presence of moisture in the filters was noted during thermal cycling, it is possible that the release of adsorbed moisture and/or water of hydration from the adhesive resulted in shrinkage and

cracking. Results of these tests have indicated that the Flander's Air-pure filter is unsatisfactory for the GCR-ORR loop No. 2 application, and other filters are being investigated.

UNCLASSIFIED
PHOTO 36515

Fig. 7.19. Filter Unit No. 2 After Thermal Cycling and Efficiency Tests.

Table 7.6. Results of Filter Efficiency Tests Before and After Thermal Cycling

Filter Unit No.	Air Flow Rate		Pressure Drop Across Filter (in. H_2O)	Air Temperature (°F)	D.O.P.[a] Filter Efficiency (%)
	lb/hr	cfm			
			Before Thermal Cycling		
2[b]	522	133		132	99.995
1	572	145		130	86.00
			After Thermal Cycling		
2	287	71	0.75	125	86.00
2	405	101	1.3	125	
2	576	146	2.4	127	83.00

[a]Dioctylphthalate (0.6-μ particles).

[b]In order tested.

Out-Of-Pile Test Loop (F. A. Flint, R. E. MacPherson)

A new GCR-ORR loop No. 2 heater has been designed and is being fabricated to replace the original heater which failed during testing, as mentioned previously.[5] The out-of-pile loop for testing GCR-ORR loop No. 2 components is being modified to include the regenerator, a bypass around the regenerator, and a bypass around the evaporator.

The regenerator will be installed in the loop in such a way that the heater inlet gas will be preheated by the heater outlet gas. In addition to testing the regenerator, this arrangement will permit testing the heater at higher gas temperatures. The regenerator bypass will convey gas around the regenerator directly to the heater from the compressor. An orifice in the bypass will permit measuring the bypass gas flow. Valves in both the bypass and main loop will permit varying the bypass flow from no flow to total loop flow. The evaporator bypass will convey gas around the evaporator directly from the regenerator outlet

[5]GCR Quar. Prog. Rep. Dec. 31, 1960, ORNL-3049, pp. 335–7.

to the compressor inlet piping. An orifice in the bypass will permit measuring the bypass flow, which may be varied with a globe valve. The evaporator bypass will give a greater degree of control over the loop heat-rejection rate.

Special Compressors

Compressors With Grease-Lubricated Bearings (I. K. Namba)

The two regenerative compressors installed in the twin-turbine vessel of GCR-ORR loop No. 1 have continued to operate satisfactorily since the last report period. The compressors, which operate as two units in series, have logged a total of 3100 hr at speeds of 6000 to 12 000 rpm and temperatures up to 600°F. The last 2000 hr of operation was at 12 000 rpm with a helium-nitrogen mixture. Loop pressure has been limited to 45 psia.

A centrifugal compressor built by the AiResearch Company was operated for 5500 hr before it was removed from the loop in which it had been installed to permit repair of a leaking thermocouple hole. Examination of the bearings showed them to be in good condition, so this unit could probably have been operated for a considerably longer period. It is becoming apparent that it is possible to operate all the compressors equipped with grease-lubricated bearings for periods considerably in excess of the design specification of 2000 hr without relubrication.

An analysis of the designs that have been used for small gas compressors intended to operate at temperatures of 500°F, or above, has shown that a very large portion of the cost of such equipment is generated in cooling the motor and bearings to temperatures in the range of 150 to 200°F. Preliminary studies indicate that it may be possible to devise units which will effect an appreciable cost reduction in this area, and more detailed studies have been initiated. The use of reflux cooling appears to be attractive from the standpoint of simplicity of design and ease of providing proper containment; however, some designs using circulating water cooling are also under consideration.

Compressors with Gas-Lubricated Bearings (D. L. Gray)

Bristol Siddeley has continued to have difficulties with instabilities in gas-lubricated bearings applied to compressors operating at speeds above 11 000 rpm. However, the most recent reports indicate that a stripped-down version of the experimental compressor for ORNL was operated at speeds up to 15 000 rpm with only slight and intermittent touching.

In an attempt to ascertain the source of the instability, the compressor was operated through several tests using the same bearings. During the first of these runs the rotating assembly consisted of shaft, rotor, and circulating fan only. Touching was indicated at 10 575 rpm. A second run was made with the viscosity plate added to the previous rotating assembly configuration. Heavy journal touching was indicated at 11 000 rpm. A third run was made using the complete rotating assembly, and heavy journal touching was indicated over the speed range of 10 350 to 12 650 rpm. Capacity probe measurements indicated that the mode of whirl was half-speed shaft cylindrical.

An analysis of operating and measurement records received from Bristol Siddeley tends to indicate that some of their problems may stem from inadequate measurement techniques. The word "inadequate" is used here in a relative sense, since some of the Bristol Siddeley measurements appear to be accurate to about 0.00005 in. It appears that the chief difficulties probably occur in measurements of straightness, as opposed to roundness, of the bearings and shafts. It is known that at least one other commercial manufacturer of gas-bearing compressors has recently been able to find means of providing suitable bearing tolerances under even more rigorous conditions. Bristol Siddeley is therefore being encouraged and urged to increase their efforts in this particular area.

The installation of a test loop for gas-bearing compressors was completed, and the equipment was checked out. The GABE I compressor has been operated for a short period of time at atmospheric pressure and temperature, using a small flow of gas from an external source to relieve the load on the thrust bearings. An initial effort to operate it in the test loop was unsuccessful, and subsequent examination of the dissembled compressor revealed that the probable source of the difficulty was an excess

of external ("jacking") pressure which caused the rotating assembly to bind against a stop in the housing in the raised position. Several subsequent tests have been made in an open assembly stand to determine the best means of applying jacking pressure to start the compressor. Additional runs will be made before the compressor is reinstalled in the high-pressure test loop.

A contract was negotiated with the Continental Bearing Research Corp. of New York, N.Y., for the design, fabrication, and testing of a gas-lubricated bearing compressor utilizing a duplicate of the high-temperature motor used in the GABE I design. Phase I of this contract, which covers the design, fabrication, and testing of a prototype rotary assembly, is scheduled to be completed by the end of this fiscal year.

Compressors for GCR-ORR Loop No. 2 and EGCR Experimental Loops (H. C. Young)

Cracks were found in the main girth welds of two of the three pressure vessels for the GCR-ORR loop No. 2 compressors during reradiography by Bristol Siddeley. The vessels were returned to the supplier for repair. The motor, bearings, and shaft for the first compressor were assembled in the Meehanite carrier sleeve and operated for a short time at speeds up to 7000 rpm. All other parts of this unit, except the pressure vessel, are now ready for assembly, and it is understood that the pressure vessel may be completed to the point that experimental operation can be carried out at normal design pressures within a very short time. It will subsequently be necessary to replace this vessel with one modified to a configuration acceptable from the thermal stress viewpoint, but the proposed procedure should minimize delays in the initiation of the compressor test program.

Welding of the pressure vessels and fabrication of parts for the EGCR compressors are in progress.

Previous reports in this series are:

ORNL-2500	Parts 1-4, issued April 1, 1958
ORNL-2505	Issued June 19, 1958
ORNL-2510	Issued September 18, 1958
ORNL-2676	Period Ending December 31, 1958
ORNL-2767	Period Ending June 30, 1959
ORNL-2835	Period Ending September 30, 1959
ORNL-2888	Period Ending December 31, 1959
ORNL-2929	Period Ending March 31, 1960
ORNL-2964	Period Ending June 30, 1960
ORNL-3015	Period Ending September 30, 1960
ORNL-3049	Period Ending December 31, 1960

ORNL-3102

Reactor Technology
TID-4500 (16th ed.)

INTERNAL DISTRIBUTION

1. G. M. Adamson
2. S. A. Beall
3. R. J. Beaver
4. M. Bender
5. D. S. Billington
6. E. P. Blizard
7. A. L. Boch
8. C. J. Borkowski
9. W. F. Boudreau
10. G. E. Boyd
11. E. J. Breeding
12. J. C. Bresee
13. R. B. Briggs
14. W. E. Browning
15. F. L. Carlsen
16. C. E. Center (K-25)
17. R. A. Charpie
18. R. S. Cockreham
19. T. E. Cole
20. J. H. Coobs
21. J. A. Conlin
22. W. B. Cottrell
23. J. A. Cox
24. F. L. Culler
25. H. N. Culver
26. J. H. DeVan
27. D. A. Douglas
28. E. P. Epler
29. R. B. Evans
30. D. E. Ferguson
31. J. Foster
32. J. L. Fowler
33. A. P. Fraas
34. J. H. Frye, Jr.
35. A. E. Goldman
36. B. L. Greenstreet
37. W. R. Grimes
38. E. Guth
39. J. P. Hammond
40. W. O. Harms
41. T. Hikido
42. M. R. Hill
43. H. W. Hoffman
44. A. Hollaender
45. A. S. Householder
46. H. Inouye
47. W. H. Jordan
48. P. R. Kasten
49. G. W. Keilholtz
50. C. P. Keim
51. M. T. Kelley
52. J. J. Keyes
53. R. B. Korsmeyer
54. P. Lafyatis
55. J. A. Lane
56. J. L. Lamartine
57. R. S. Livingston
58. H. G. MacPherson
59. W. D. Manly
60. E. R. Mann
61. R. W. McClung
62. H. E. McCoy
63. H. C. McCurdy
64. H. F. McDuffie
65. C. J. McHargue
66. F. R. McQuilkin
67. H. J. Metz
68. A. J. Miller
69. R. S. Miller
70. J. G. Morgan
71. K. Z. Morgan
72. F. H. Neill
73. M. L. Nelson
74. L. G. Overholser
75. N. Ozisik
76. P. Patriarca
77. A. M. Perry
78. D. Phillips
79. C. A. Preskitt
80. M. E. Ramsey
81-82. P. M. Reyling
83. M. W. Rosenthal
84. G. Samuels
85. H. W. Savage

86. A. W. Savolainen
87. J. L. Scott
88. O. Sisman
89. E. D. Shipley
90. M. J. Skinner
91. G. M. Slaughter
92. A. H. Snell
93. I. Spiewak
94. E. Storto
95. R. D. Stulting
96. J. C. Suddath
97. C. D. Susano
98. J. A. Swartout
99. E. H. Taylor
100. D. F. Toner
101. W. C. Thurber
102. D. B. Trauger
103. C. S. Walker
104. J. L. Wantland
105. G. M. Watson
106. A. M. Weinberg
107. M. E. Whatley
108. J. R. Weir
109. J. C. White
110. E. A. Wick
111. G. C. Williams
112. C. E. Winters
113. J. Zasler
114-117. ORNL — Y-12 Technical Library Document Reference Section
118-187. Laboratory Records Department
188. Laboratory Records Department, ORNL R.C.
189-191. Central Research Library

EXTERNAL DISTRIBUTION

192-194. W. F. Banks, Allis-Chalmers Mfg. Co.
195-197. P. D. Bush, Kaiser Engineers
198. E. Creutz, General Atomic
199-201. R. B. Duffield, General Atomic
202. D. H. Fax, Westinghouse Atomic Power Division
203. T. Jarvis, Ford Instrument Co.
204. Richard Kirkpatrick, AEC, Washington
205-206. H. Lichtenburger, General Nuclear Engineering Corp.
207. J. P. McGee, Bureau of Mines, Appalachian Experiment Station
208. S. G. Nordlinger, AEC, Washington
209. H. B. Rahner, Savannah River Operations Office
210. Corwin Rickard, General Atomic
211. S. T. Robinson, Sanderson & Porter
212. M. T. Simnad, General Atomic
213. Donald Stewart, AEC, Washington
214. G. W. Tompkin, Mallinckrodt Nuclear Corporation
215. Philip L. Walker, Pennsylvania State University
216. R. E. Watt, Los Alamos Scientific Laboratory
217-218. W. L. Webb, East Central Nuclear Group, Inc.
219. Division of Research and Development, AEC, ORO
220-821. Given distribution as shown in TID-4500 (16th ed.) under Reactor Technology category (75 copies — OTS)